High Contrast Limitations of Slicer Based Integral Field Spectrographs

Graeme S. Salter
Hertford College

Department of Astrophysics
University of Oxford

Supervised by Prof. Niranjan Thatte

A thesis submitted for the degree of Doctor of Philosophy
in the University of Oxford.

Michaelmas Term 2010

To Mum & Dad
without whom I would not be where I am today.

Declaration

I declare that no part of this thesis has been accepted, or is currently being submitted, for any degree or diploma or certificate or any other qualification in this University or elsewhere. Except where explicit reference is made to the work of others, the work contained in this thesis is my own, and is not the outcome of work done in collaboration.

Graeme S. Salter

(December 2010)

Abstract

The viability of using a slicer based integral field spectrograph (IFS) for high contrast observations has been under scrutiny due to the belief that the one dimensional coherence that persists along the slice to the point of sampling at the detector will cause the creation of secondary speckles that will not have the same characteristics as normal speckles, thus stopping us from calibrating them out. It has also been previously assumed that a suitably low differential wavefront error when moving slice to slice was not guaranteed by design. It was for these reasons that slicer based IFSs were not selected for the current generation of planet finding instruments. As part of the EPICS (Exo Planet Imaging Camera and Spectrograph for the E-ELT) design study it was decided that slicers should be re-investigated due to results from on sky observations suggesting these limitations did not exist.

The purpose of this thesis was to determine whether there was validity to the concerns mentioned above and therefore to answer the question; Would implementing a slicer based integral field spectrograph limit the achievable contrast of an instrument designed for the direct detection of exoplanets?

Chapter 1 gives a brief introduction into the field of exoplanet research. Charpter 2 describes the noise limiting direct detection of exoplanets and the ways to get around it. Chapter 3 gives an overview of the two types of IFS under investigation by the EPICS consortium. Chapter 4 looks into details of the EPICS instrument and the IFS design study that came about. Chapter 5 shows simulations performed for the aim of achieving better contrasts via post processing methods and accurate data reduction as well as simulations of slicer based integral field spectrographs. Experimental tests using a slicer and a preoptics setup designed to simulate the limiting noise are described in Chapter 6. Chapter 7 looks at using SINFONI for high contrast observations and Chapter 8 details the conclusions drawn from the work presented in this thesis, as well as possible extensions to it.

The work performed in this thesis dispels the concerns about the continued one dimensional coherence up to the detecter and suggests that slicer based integral field spectrographs do not inherently limit the contrast achievable; Results from experiments fit well with the requirements for EPICS to achieve its goals. Simulations also supported the idea that secondary speckle noise should not be an issue for the slicer based IFS. This means that a slicer based IFS is a viable option for the EPICS instrument.

Acknowledgements

I would first like to thank my supervisor Niranjan Thatte for his excellent supervision throughout the duration even through some very hard times, his encouragement and insight have been invaluable. I am also extremely grateful for the financial support he was able to find during my final months at Oxford. I would like to thank Matthias Tecza who has always made the time to help, especially on optics design and helping with the speedy thesis corrections needed in the late stages, I hope your loyalty to the San Diego Padres never wavers. Thanks to Fraser Clarke for letting me pick his brain on many occasions, for proof reading parts of my thesis and for the company on many a work trip. Thanks to Ryan Houghton for the very useful discussions on IFS data cube reduction and interpolation errors and thanks to the EPICS consortium for letting me be a part of it all, especially Markus Kasper and Christophe Verinaud for the multiple useful discussions in relation to the IFS study.

I would like to thank all members of the Oxford Astrophysics faculty and all of the graduate students who have made my time here a far more enjoyable experience[1]. This includes the past and present Towerlings who have provided both fun times and the occasional intellectual discussion. In particular I would like to thank; Lisa Fogarty and Tim Goodsall for making the long days and nights in the lab more bearable, Millie Maier for putting me up and looking after me whilst I was observing in Chile, Natalie Christopher for the energetic distractions that kept me on the level in times of panic, Ben Fitzpatrick for the thoroughly inspirational text messages that came through at some of the toughest points in the write up and for being a great office mate (may the Tower be forever zombie free) and Emma Curtis-Lake for always being there to pick me up when I'm down, you've been a great friend these past years!

Finally I would like to thank my parents who have always provided me with unwavering support and encouragement.

[1] With special thanks to; Calum Brown, Ben Burnett, Alison Crocker, Timothy Davis, Sam Doolin, Cristina Fernandes, Sam Geen, Paul Goodall, Oliver King, Tony Lynas-Gray, Edward Macaulay, Richard Masters, Amy McQuillan, Sarah Miller, Nick Scott, Irene Sendra, Boon Kok Tan, Aprajita Verma

"When and if we find that other Earths are common and we see that some of them have signs of life, we will at last complete the Copernican Revolution - a final conceptual move of the Earth, and humanity, away from the center of the Universe. This is the promise and hope for the detection and characterization of habitable worlds."

S. Seager 2010

Contents

Chapter 1

Introduction

The area of exoplanet discovery and classification is a rich and fast moving field that has advanced extremely rapidly over the past 15 years. However, to put it into context we shall start from the beginning.

*Until the turn of the 17th century there were only 8 celestial bodies known amidst a field of "fixed stars"(the Earth, the Sun, the Moon, Mercury Venus, Mars, Jupiter and Saturn). It was believed that the Earth was at the center of everything and all other bodies were revolving around it. However, our view of the heavens was dramatically altered when Galileo first turned his telescope to the skies and by the end of the 17th century Copernicus's heliocentric theory had been widely accepted. William Herschel first discovered Uranus in 1781 and it was not until midway through the 19th century that Neptune was discovered by Adams and Le Verrier, having been previously mistaken for a star by Galileo. Pluto was discovered in 1930 by Tombaugh, although its classification was later demoted to that of a dwarf planet as it did not fit within the International Astronomical Union (IAU) definition of a planet† (its orbit passed through the Kuiper belt). Atmospheres of the planets have been observed from as early as the 19th century with observers noting that satellites and stars disappeared gradually, as opposed to instantaneously, when being occulted by the planet (Challis, 1863). The first spectroscopic observations of the planets revealed atmospheres that were very dissimilar to that of Earth's. Huge advancements were made in the field of the atmospheres of the solar system planets over the 20th century including the deficit of oxygen on Venus (Webster, 1927), the detection of methane on the giant planets (Adel & Slipher, 1934) and carbon dioxide on terrestrial planets Adel (1937).

*Dates drawn from nineplanets.org

†The IAU states that in the solar system a celestial body is only a planet if it is in orbit around the Sun, has sufficient mass to assume hydrostatic equilibrium (a nearly round shape), and has "cleared the neighbourhood" around its orbit.

For a long time mankind has wondered about the possibilities of worlds around other stars, however, this was all in the realm of science fiction until 1995[‡] when the confirmed detection of 51 Peg b, a peculiar Jupiter sized object orbiting a Sun like star, was announced (Mayor & Queloz, 1995). When thinking about the detection of an exoplanet it is natural for your mind to first jump to observing the planet directly, whereby photons emitted/reflected from the planet itself are detected. However, this first planet was found via the influence the planet has on the star it is orbiting, in particular the indirect method of detection called radial velocity (described in the following section). Over 500 planets have been detected to date and the vast majority of these have been detected via indirect methods. Figures 1.1 & 1.2 show respectively the methods of planet detection proposed to date (not all yet successful) and the number discovered per year.

The distinction that is made by the IAU should be noted here; The evolution of a celestial body that fuses hydrogen is very different to those that do not. The hydrogren burning limit, requiring a mass at least 80 times that of Jupiter (M_J from here on), is then imposed on objects being classified as stars. Objects with masses lower than $80M_J$ but still massive enough for deuterium fusion to take place in their cores, $13M_J$ are thereby classified as brown dwarfs. Finally, celestial bodies below the deuterium burning limit, $< 13M_J$ are classified as planets.

The first exoplanet detected directly via high contrast direct imaging was that of 2M1207b in 2004 and to date a total of 14 have been directly detected. Although the exoplanet community it somewhat divided on the legitimacy of many of the claimed exoplanets because estimating a mass from current observations is highly subject to uncertainty, as is discussed in Chapter 1.3, 2008 brought around the first bona-fide imaged planets which have been widely accepted as such.

[‡]The first detections prior to this were of 4 exoplanets discovered between 1992 and 1994, however, these were orbiting pulsars (detected via periodic timing variations)

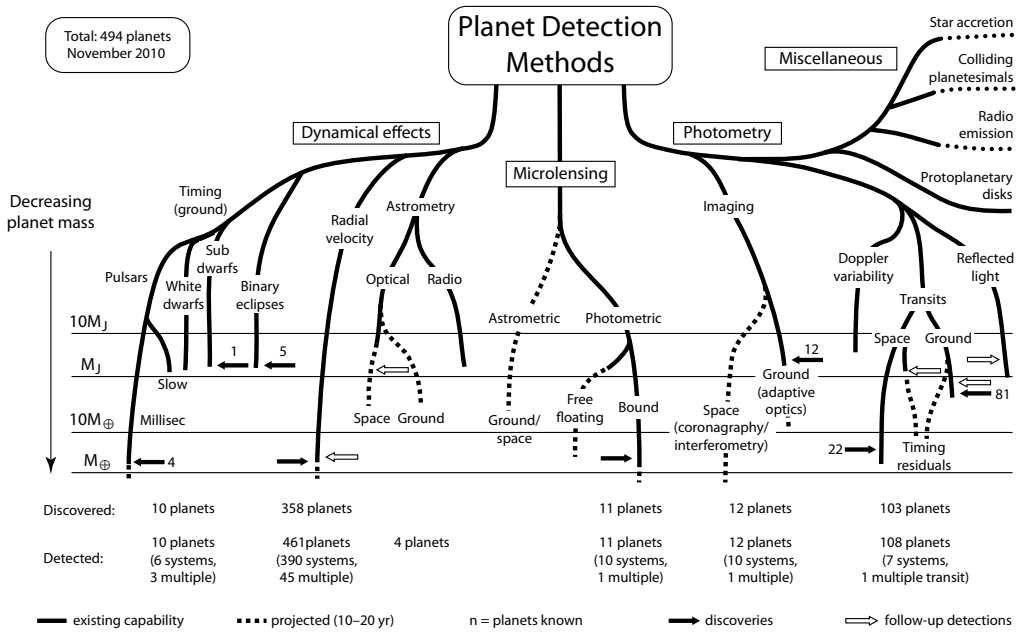

Figure 1.1: Diagram showing the different methods of detection of exoplanets. Image was created by M. Perryman and taken from the //exoplanet.eu website.

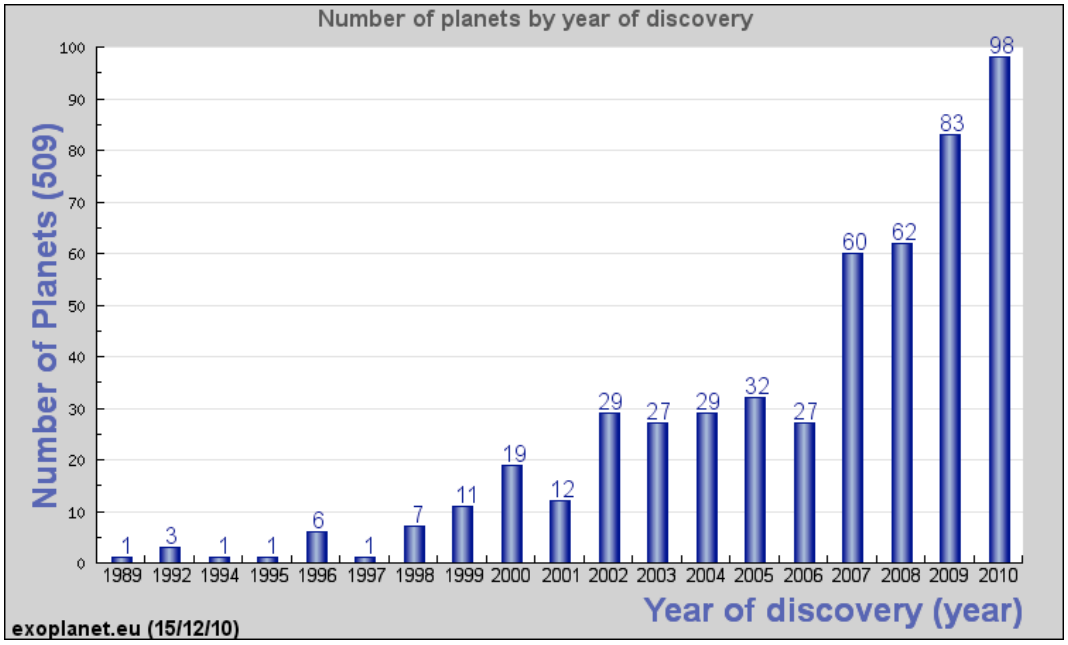

Figure 1.2: Plot displaying the number of planets descovered per year between the first detection in 1989 and the present year, 2010. This plot is taken from the //exoplanet.eu website.

1.1 Planet Detection Methods

In the following section I will describe the current methods of exo-planet detection. Different methods of observation can provide us with different information about the planetary companions. Here I also outline the properties we can determine from the different observational techniques and what we can achieve with current instrumentation.

1.1.1 Indirect Detection Methods

An indirect observation is one that uses the properties of one object being observed to infer the presence of another. In the case of exoplanets this means observing properties of the parent star that indicate the presence of a planet (with the exception of gravitational microlensing which uses a measurement of a background star). Each of the indirect methods of exoplanet detection will be explained here:

Radial Velocity

The radial velocity technique uses measurements of the Doppler wobble of the parent star induced as it and the planet orbit around their common centre of mass. By measuring this variation with time a determination of the period, P, semi-amplitude, K, and eccentricity, e, of the planets orbit can be made. With these properties, a minimum mass of the planet can be determined with the following relation;

$$\frac{(m_p \sin i)^3}{(M_\star + m_p)^2} = \frac{PK^3}{2\pi G}\left(1-e^2\right)^{2/3} \tag{1.1}$$

Where m_p is the mass of the planet, $M_\star$ is the mass of the star, P is the orbital period of the planet, e is the eccentricity of the planets orbit, i is the inclination of the planets orbit relative to our viewing, G is the universal gravitational constant and K is the semi-amplitude of the radial velocity variation.
By assuming a circular orbit and that $M_p \ll M_\star$ and by relating to the influence Jupiter has on the Sun we can write this in a more intuitively useful form:

$$m_p \sin i \simeq 1 M_J \left(\frac{K}{200\mathrm{ms}^{-1}}\right)\left(\frac{P}{\mathrm{day}}\right)^{1/3}\left(\frac{M_\star}{M_{\mathrm{Sun}}}\right)^{2/3} \tag{1.2}$$

The majority of the exoplanets detected have been via radial velocity measurements and the majority of these have been Hot Jupiters. This is of course a selection effect as these objects are $\sim$ Jupiter mass planets that are located very close to the parent star (<0.05AU) which, as can be seen from equation 1.2, has a large effect on the star.

Precise calibrations of the spectra obtained are necessary for the observation of any exoplanet but especially so when trying to probe into the Super-Earth regime. Here the use of calibration sources such as iodine cells and laser combs is essential to get you down to the $< 5\text{ms}^{-1}$ needed. With HARPS now routinely achieving an precision of $\sim 1\text{ms}^{-1}$ (Mayor et al., 2009) and with monitoring baselines of many years, both lighter planets and planets in wider orbits are being detected.

A project called ESPRESSO at the VLT is already underway (first light anticipated $\sim$ 2015) which will provide a high resolution spectrograph at its Coudé focus. This instrument is being designed to achieve an accuracy of $10cms^{-1}$ and a calibration stability that will be good for decades of subsequent observation. Further to this a similar instrument, CODEX is being proposed for the E-ELT which will aim for an precision of 1cms^{-1}.

However, the accuracy of the instruments used may not be the limiting factor to this technique as stars are asteroseismically active, meaning they provide their own radial velocity "jitter". On top of this the technique naturally requires a very large amount of telescope time for the detection of smaller and further out exoplanets.

Astrometric Perturbation

Just as in radial velocity, the effect of the movement of the star about the barycenter of the star-planet orbit due to the gravitational effect of the planet can be detected via astrometry. The path of star's orbit about this barycenter traces an ellipse with an angular semi-major amplitude, α, of;

$$\alpha = \left(\frac{m_p}{M_\star}\right)\left(\frac{a}{d}\right) \tag{1.3}$$

Where α is measured in arcsec, a is the semi major axis in AU, d is the distance from the Earth in pc and the masses are in the same units.

In the most favourable cases detection via astrometric perturbation requires accuracy on the microarcsec

scale, as shown in Figure 1.3. Future advances in this field include the PRIMA interferometric instrument for the VLTI, currently being commissioned, which will deliver an accuracy of 10μarcsec and GAIA, the μarcsec space based facility by ESA, see Figure 1.7 for GAIA's detection capabilities.

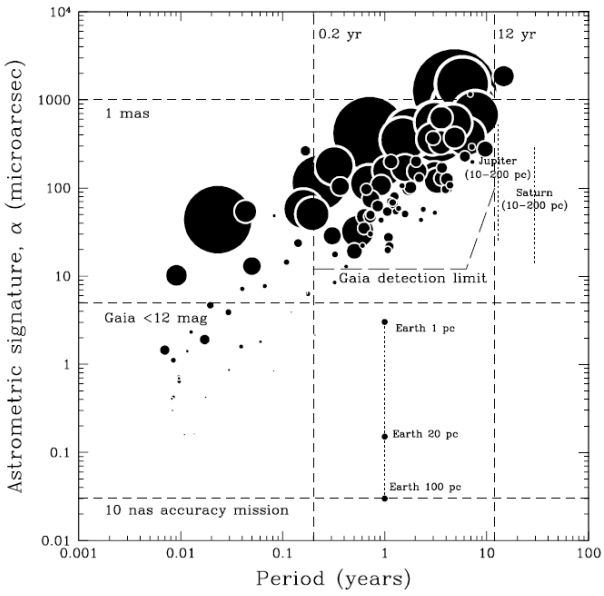

Figure 1.3: Figure 4 from Perryman et al. (2005) showing the Astrometric signature, α caused by orbiting planets, as a function of orbital period. The planetary systems detected as of 2005 are plotted with circles having radius proportional to $m_p \sin i$. The GAIA detection limits are over-plotted, showing that the longest period systems, with astrometric signatures of the order of micro-arcseconds are easily detected. Effects of Earth, Jupiter, and Saturn are shown at the distances indicated.

Transits

For every star-planet system there is a probability that the inclination of their orbits, with respect to our view point, will allow us to "see" the planet transit across the disc of the star. This probability, P, for a planet in a circular orbit is calculated as:

$$P = \frac{r_p + R_\star}{a} \tag{1.4}$$

where r_p is the radius of the planet, $R_\star$ is the radius of the star and a is the orbital distance of the planet.

As the planet moves across the surface of the star it will block out part of the flux radiated by the star. By

measuring this drop in flux, ΔF the radius of the planet can be determined as;

$$r_p \simeq R_\star \sqrt{\Delta F} \tag{1.5}$$

A primary eclipse or transit is when the planet passes in-front of the star and a secondary eclipse is simply the opposite of this, as shown in Figure 1.4.

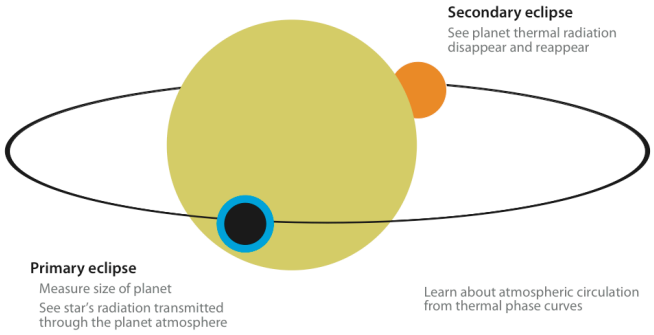

Figure 1.4: Cartoon depicting a transiting exoplanet being observed via the primary and secondary eclipses. Image is taken from Seager & Deming (2010).

Secondary eclipses give up information about the relative sizes and brightness of the planets. The planet's flux obtained from such eclipse observations provide information about the atmospheric composition and temperature gradient (at infrared wavelengths) or albedo (at visible wavelengths).

The inclination of the orbit is defined by the transit. With this knowledge in hand, measurements of the radial velocity signature of the planets can give very accurate determinations of the planet's mass. Once the mass and radius of the planet is known, we can estimate physical properties such as the average density and surface gravity of the planet.

The hot Jupiters mentioned previously obviously have a larger probability of transiting, due to their proximity to the parent star, and as such these are what most of the transit detections have been to date. However, the technique has not been limited to these objects as planets as small as 5 Earth masses (Super -Earths) have been detected via this method and with future missions expecting to achieve the accuracy to detect Exo-Earths.

The on-off nature of a transit and a secondary eclipse leads to an intrinsic calibration reference, which has

led to the success of instruments such as Spitzer that were not designed with detecting transiting exoplanets in mind.

Transiting observations provide a crucial role in the field of exoplanet research as they can provide an insight into their physical characterisation. Both primary and secondary eclipses can provide a large amount of information about the atmosphere of the transiting exoplanet, provided that the signals detected are > 1% of the overall flux from the system for the transit and >0.1% for the secondary eclipse (Lopez-Morales, 2010). The measurement of the atmosphere from a transit is made possible due to light from the star crossing the thin layer of the atmosphere of the planet during a transit thus providing a transmission spectrum. This spectrum is obtained by dividing through the spectrum observed during a transit to that observed prior to/after it. The characterisation of the atmosphere from a secondary eclipse is made via direct detection of the flux coming from the atmosphere of the planet.

The future of transiting observations look to new space based missions such as Kepler and JWST but also back on the ground. Ground based follow ups of secondary eclipses are starting to take place where by many targets are observed at the same time so as to obtain an intrinsic calibration of the atmospheric disturbances. By observing from the ground a new wavelength range is open to investigation.

Timing

The motion of a star around the star-planet barycenter causes a delay in the arrival of light emitted from the star. This is the case for all systems, but the effect can only be measured for systems with a regular period such as pulsars due to their intrinsic, extremely regular, periodic pulses. For a circular orbit the maximum amplitude of the delay, τ, in the arrival rate of these pulses is equated to the mass of the planet via;

$$\tau = \sin i \left(\frac{m_P}{M_\star}\right)\left(\frac{a_P}{c}\right) \tag{1.6}$$

Where a_P is the distance of the planet from the barycenter and c is the speed of light.

It was by this method that the first exoplanet was detected (Wolszczan & Frail, 1992) and determined to be of terrestrial and not Jovian mass.

Following the same methodology the presence of other planets can be found using the regular period of a transiting planet or a binary star.

Gravitational Microlensing

§Gravitational lensing is the apparent brightness variation of a background object due to gravity of an intermediate object bending space-time, thus focusing its light as viewed by us. Most dramatically, this effect can be observed when looking at distant galaxies. The term gravitational microlensing refers to the case where the images generated by the lens are too close together for their spatial separation to be observed. Microlensing occurs when a background star is lensed by an intermediate star (i.e. one that is typically a few Kpc from us). A perfect alignment of the two stars relative to us would produce symmetric images around the lensing star, known as the 'Einstein ring'. The Einstein ring radius is given by;

$$R_E = \left(\frac{4GM_{\star L}}{c^2} \frac{(D_B - D_L)D_L}{D_S} \right)^{1/2} \tag{1.7}$$

Where, $M_{\star L}$ is the mass of the lensing star, D_L is the distance to the lensing star and D_B is the distance to the background star. The microlensing magnification, that varies with time, t, is given by;

$$Q(t) = \frac{u^2(t)+2}{u(t)[u^2(t)+4]^{1/2}} \tag{1.8}$$

Where $u(t)$ is the projected distance between the image of the lensing star and the source star in units of R_E (Perryman, 2000). If a planet is in orbit around the lensing star its gravitational field will be distorted resulting in deviations from this amplification pattern. From these distortions measurements of the mass of the planet and the planet-lens separation can be deduced.

Note that the probability of alignment between two stars, even when looking at the Galactic center, is approximately one in 10^6, despite this planets have been discovered via the method including a system showing a Jupiter/Saturn Analog (Gaudi et al., 2008). However, the systems detected are currently unable to be followed up by any other method.

§Details have been drawn from Doyle (2008)

1.1.2 Direct Detection Methods

¶Direct detection is the intuitive way of thinking about detecting exoplanets, whereby you collect photons from the planet itself to determine properties about the planet, rather than inferring them from its influence on other bodies.

High contrast observations can be defined by the inner working angle (IWA), which is the closest separation from the star a planet can be detected, and the contrast at which the planet can be detected. The Sun-Jupiter example is often cited as a reference, showing a contrast of $\sim 10^9$ at an angular separation of 0.5" when viewed from 10pc. By this we mean, if we were to want to detect said Jupiter we would have to be able to select the one photon coming from the planet whilst getting rid of the 10^9 photons from the star. ‖ This is like trying to detect a firefly 10cm from a lighthouse at a distance of 26miles!. For comparison Figure 1.5 shows the absolute fluxes of the solar system planets, as compared to the Sun, at a distance of 10pc.

Being able to directly detect planets requires an understanding of the physics and behaviour of star light with real optics, as well as an ability to control optical and near-IR wavefronts to unprecedented precision. For these reasons direct imaging is trailing in the detection counts to date, however, should direct imaging be possible for an exoplanet a great wealth of information is provided which enables the us to physically characterise the planets being observed.

It is the contamination of residual starlight that limits high contrast detections. This contamination comes in the form of optical diffraction, redistribution of the light due to imperfect optics, and propagation of the light through the atmosphere. The result is a speckle noise pattern, an example of which can be seen in Figure 1.6. Therefore, if we wish to make these high contrast observations we must find a way around these factors. This is described in more detail in Chapter 2.

¶In this section I have drawn on the work of Oppenheimer & Hinkley (2009)

‖Assuming the Photinus Pyralsis firefly with a typical brightness of 1/40 candela (www.shgresources.com) and a modern day 500 million candela lighthouse

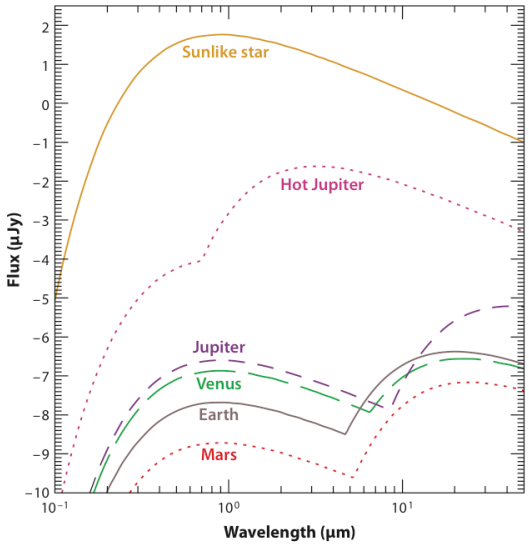

Figure 1.5: Figure 4 from Seager & Deming (2010) showing the black body flux of some Solar System bodies as "seen" from 10pc. The planets show two peaks in their spectra, the short-wavelength peak is due to sunlight scattered from the planet atmosphere and the long-wavelength peak is due to the planet's thermal emission. The hot Jupiter albedo was assumed to be 0.05 and the equilibrium temperature to be 1,600K.

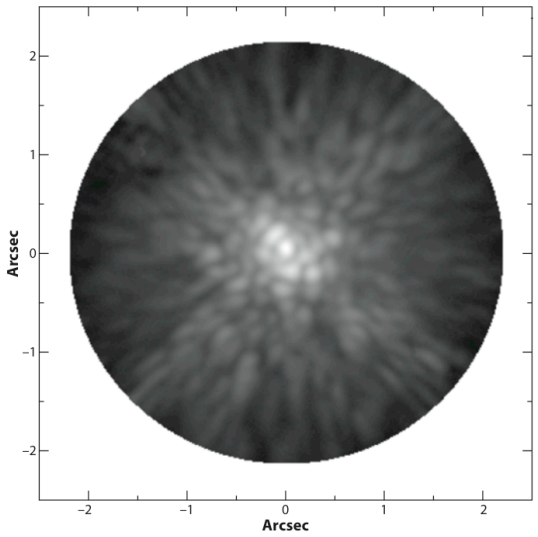

Figure 1.6: Figure and following caption from Figure 10, Oppenheimer & Hinkley (2009) ; Coronagraphic image of a nearby star demonstrating the prevalence of speckles even in extremely high-fidelity images. This H-band image is from the Lyot Project (Oppenheimer et al. 2003, Hinkley et al. 2007). The unocculted image has a point spread function with a Strehl Ratio $\sim$ 85%

Motivation

Following are some of the major advantages direct detection of exoplanets has over indirect methods.
By obtaining direct detections of an exoplanet at multiple epochs we remove the ambiguity in the inclination of the planetary system that plagues the mass estimation from the radial velocity technique. It also enables us to determine if multiple planet systems have a common orbital plane, such as is the case for our solar system, which is a crucial aspect for formation theories. The detection of planets around active stars is not possible via the radial velocity technique and significantly limited for that of astrometry and transits. This has no impact on the contrasts achievable with direct detection. Photometric colours of the planets enable tests on current atmospheric models and determination of the intrinsic brightness of the planets at different ages will give constraints on models of planetary system evolution. Detecting the planets with spectroscopy opens up a wealth of information including the chemical composition of the planets atmospheres, the presence of clouds and even properties such as surface gravity of the planet.

Direct Imaging

The use of adaptive optics to correct for the disturbance of light as it passes through the atmosphere is essential for high contrast observations, as too is the need for a way to suppress the diffracted light such as a coronograph. However, even when using both of these we find we are still limited by the speckle noise seen in Figure 1.6. Using a knowledge of the physical properties of the speckles we can devise methods to remove them. Such methods have shown great promise with many of the current directly detected exoplanets, described in the following section, having been detected via such methods. But for these methods to work great care must be taken in the design of the instruments to be used such that they do not modify the speckle pattern such that it is no longer characterisable. Current instruments are able to detect planets down to an effective temperature of $\sim 900K$ with a spectral resolution of $R \sim 50$, SNR=10 for $1-4\mu m$. The next generation of direct imaging instruments such as SPHERE (Beuzit et al., 2008), GPI (Macintosh et al., 2008) ,due to start commissioning in 2011, are boasting the ability to get down to temperatures of $\sim 300K$ and start to properly sample the self luminous gas giant exoplanet population. The future of planet finding instruments for the ELT era, such as EPICS (Kasper et al., 2010), are being designed with all of the previously explained factors in mind paying meticulous attention to possible sources of error so as to delve even further into the

high contrast regime and reach Super-Earth contrasts.

Interferometry

Interferometry is a very powerful technique, however it is still in its infancy in terms of high contrast imaging when compared to the capabilities of current coronographs. However, it does show great potential as, in theory, it contains the ability to destructively interfere all light coming form the star itself, thus leaving us only with signal from a companion. Add to this the possibilities of the reduction of inner working angle due to the large base lines such as CHARA, whose 300m base line would enable us to resolve even some hot Jupiters from their host stars, and we get some very powerful possibilities. Sadly current abilities in the field are showing contrasts of $\sim 10^2$ from the Keck II interferometer and MMT system. It is inevitably difficult to get down to higher contrasts from the ground due to the atmospheric turbulence. There have been proposals for space based missions that look promising, however, even these will suffer from the generally small collecting area that comes with space missions which will result in extremely long integration times.

1.1.3 Capabilities and Complementarity of Techniques

With radial velocity, astrometry and timing techniques we can derive a minimum mass, orbital period and orbital separation of the planet.
Observing planets via direct imaging or transits provide a greater wealth of information such as the following; The atmospheric temperature of the planet as a function of wavelength, or equivalently as a function of atmospheric height. The bolometric albedo (the fraction of flux incident on the planet from the star that is reflected back out into space) giving us information about the presence or absence of clouds. The energy redistribution factor, giving us information about how efficiently stellar energy incident on the day side is transported to the night side. But most importantly the chemical composition of the planet's atmosphere (Lopez-Morales, 2010).

It is possible for the spectral information of the same planet to be determined by both the transit and the direct imaging techniques and compared, however, this observation is extremely unlikely due to the reduced probability of transit of the objects observed at direct imaging separations, see Equation 1.4.

Using the knowledge of the orbits constrained via direct imaging or transit techniques, if we have radial velocity data for the objects also, we can negate the uncertainties in the mass determination. This provides an accurate, model independent, estimate of the planets mass.

However, there is currently no overlap of the parameter space where exoplanets are detectable from direct imaging and that of other techniques. See Figures 1.7 & 1.8, although future instrumentation for direct detection looks to change this.

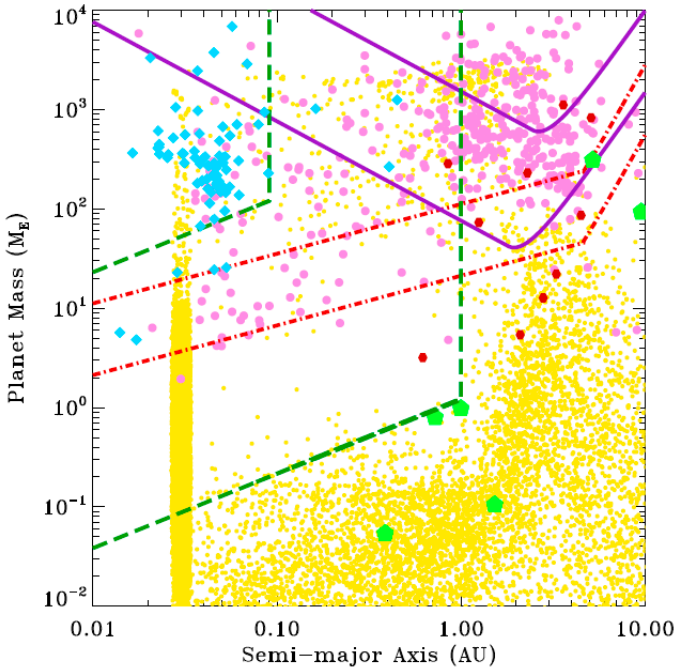

Figure 1.7: Figure 1 from Sozzetti (2010) showing the comparison of detectable limits for Gaia (purple curves) to Doppler (red lines) and transit (green lines) detection techniques. The overplotted symbols correspond to Doppler-detected exoplanets, as of May 2010 (pink filled circles), transiting systems (light-blue filled diamonds), microlensing detections (red hexagons), solar system planets (large green pentagons) and a theoretical distribution of masses and final orbital semi-major axes (Ida & Lin 2008).

1.2 Exo-planetary spectra

The goal is to physically investigate the exoplanets we find and, in order to do this, we need to obtain a spectrum of it. The best way, if possible, of doing this is via direct detection although determination of the physical properties of some exoplanets is possible via transits. By obtaining a spectrum of the planet we

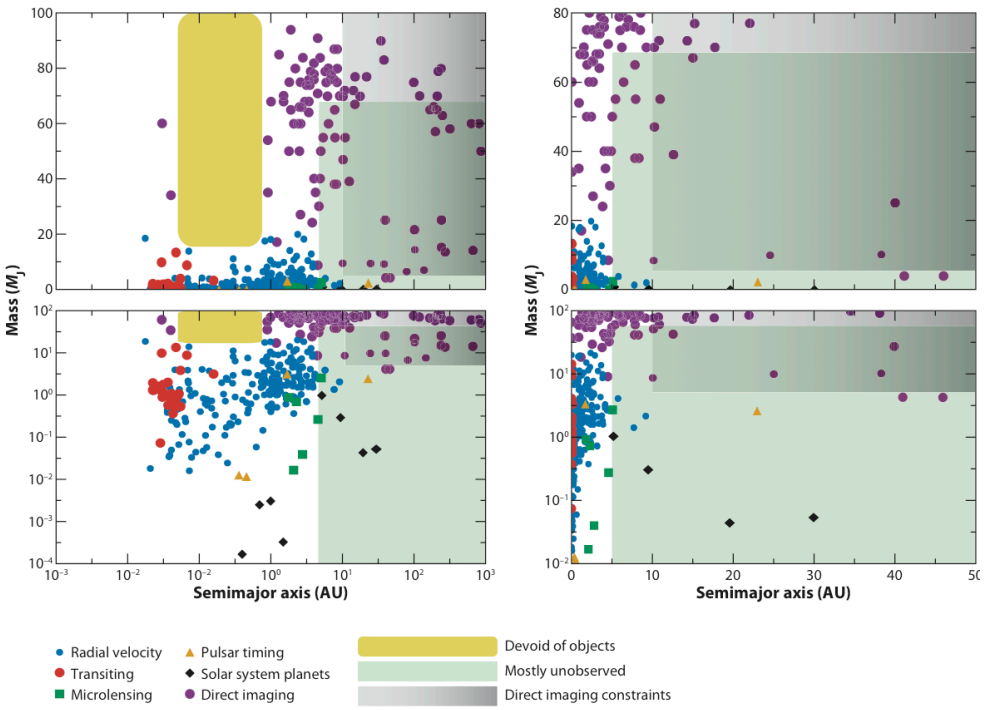

Figure 1.8: Mass versus semimajor axis for all known objects (as of 2008) in the mass range from $10^{-}4$ to$100M_J$ in orbit around nearby stars or brown dwarfs. Data are represented in four different versions of axis scaling to emphasize different aspects of the parameter space. The yellow region indicates the only region that is clearly devoid of objects based on sensitivities of various surveys (the brown dwarf desert). The green region is almost entirely unobserved except in a few cases for extremely young objects (and the Solar System). The gray regions show roughly where direct imaging surveys have placed some constraints on this parameter space, with darkness qualitatively representing completeness. Taken from Oppenheimer & Hinkley (2009)

can determine many properties some of the most prescient of which are detailed specifically below. The main aim, however, would be to determine the overall composition of the planet (namely the abundances of CO, C, H_2O, CH_4 & NH_3) and if possible surface gravity via the depths of narrow metal lines such as that of Sodium in the J-band, this requires a high spectral resolution which is difficult. Figure 1.9 shows the specturm of the hemispherically-integrated Earth as viewed by way of Earthshine measurements in the visible and near IR and in the mid IR as viewed by the Mars Global Surveyor.

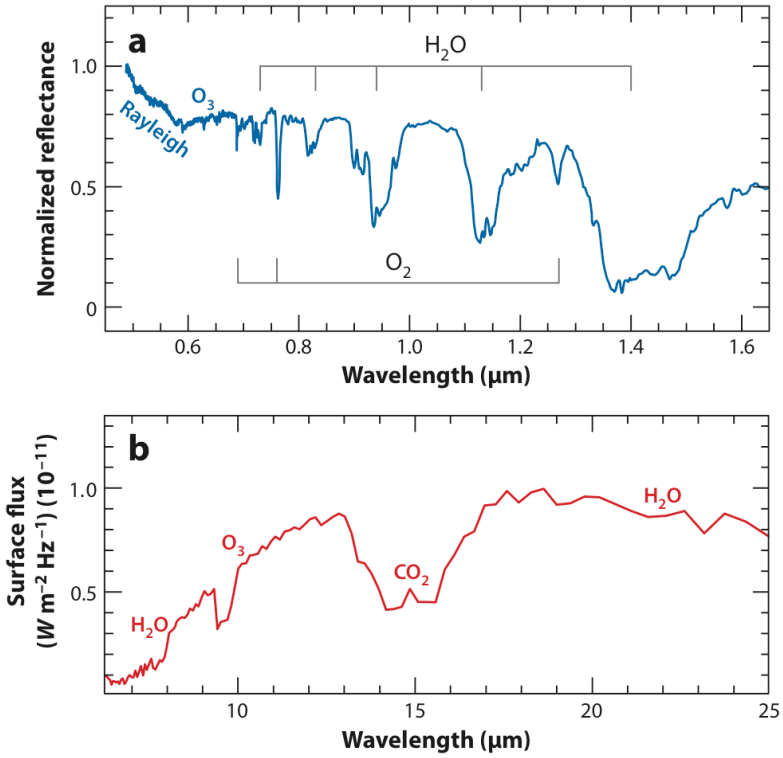

Figure 1.9: Earth's hemispherically averaged spectrum. (a) Earth's visible and near-IR wavelength spectrum from Earthshine measurements (Turnbull et al., 2006). (b) Earth's mid-IR spectrum as observed by Mars Global Surveyor en route to Mars (Christensen & Pearl, 1997). Major molecular absorption features are noted; Rayleigh means Rayleigh scattering. Taken from Seager & Deming (2010)

1.2.1 Major Detected Properties to Date

Transits

Hot Jupiters observed through transits have shown themselves to be both very hot but also very dark as they very effectively absorb in the visible (with albedos found of ~ 0.2, Rowe et al. (2008)) and emit in the IR wavelengths. Water vapour has been detected from the Hot Jupiters as is expected for a planet with an effective temperature of T >1000K and roughly solar composition. Other spectral features have also been detected; Na, CH_4, CO_2 and CO for the Hot Jupiters HD 209485b and HD 189733b (Seager & Deming, 2010), as shown in Figure 1.10. The validity of these detections of spectral features has however come into question by the exoplanet community (Gibson et al., 2010).

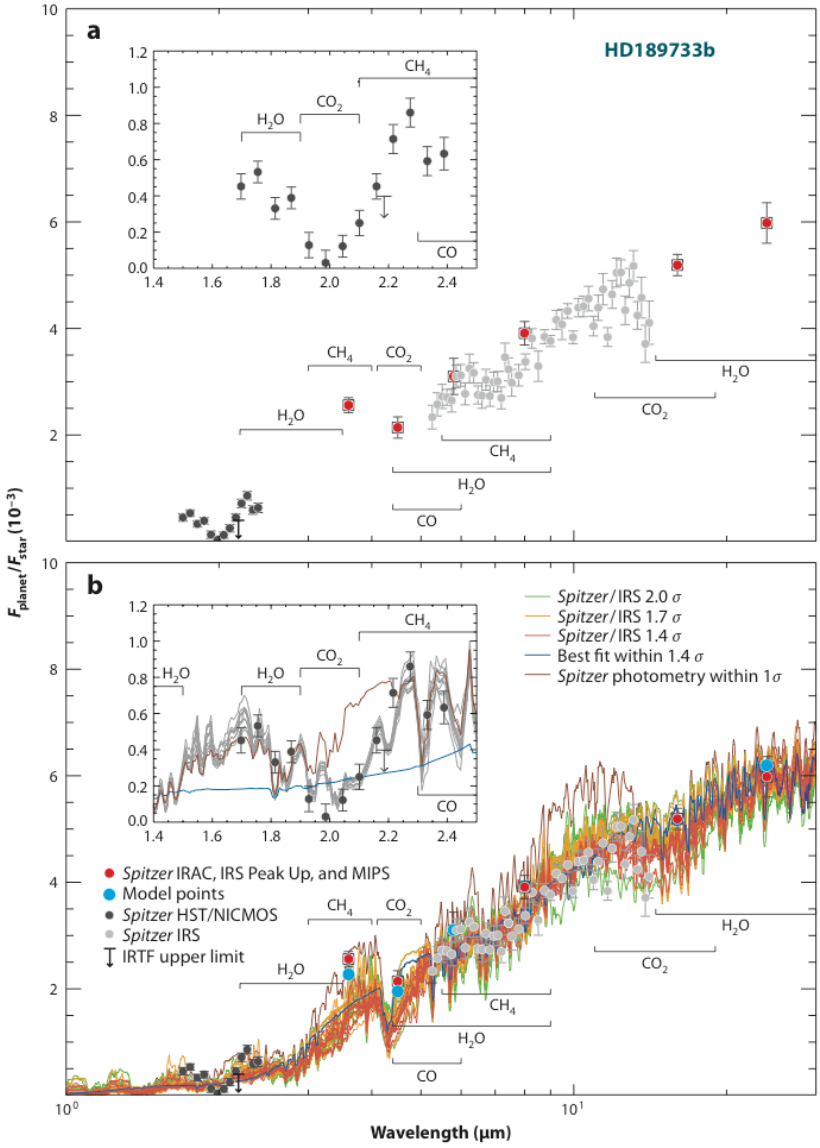

Figure 1.10: Figure and following caption from Figure 9, Seager & Deming (2010).; Thermal emission data composite for HD 189733 in secondary eclipse. (a) Data from Hubble Space Telescope/NICMOS (Near Infrared Camera Multi-Object Spectrometer) (black points), Spitzer Space Telescope/Infrared Array Camera (four shortest wavelength red points), Spitzer/Infrared Spectrograph "blue" Peak-Up Camera ($16\mu m$ red point), Spitzer/Multiband Imaging Photometer for Spitzer ($24\mu m$ red point), and Spitzer/IRS (Infrared Spectrograph) (gray points). (b) Models illustrate that the best fits to the Spitzer/IRS (red curves show fits within the $1.4\sigma errors$, on average; orange, 1.7σ ; green, 2σ ; and blue is one best-fit model within 1.4σ) and Spitzer photometry (brown curve within 1σ) do not fit the HST/NICMOS data (inset light gray curves within 1.4σ), possibly implying variability in the planet atmosphere from data taken at a different epoch or systematic errors in the NICMOS data that have not been correctly accounted for (Gibson et al., 2010).

The expected large temperature gradients from the tidally locked Hot Jupiters is also seen in their spectra with $\Delta T > 1000K$.

Atmospheric escape of atomic hydrogen from the highly irradiated Hot Jupiters is seen in some systems (Murray-Clay et al., 2009). A drop of upto 15% in stellar $Ly\alpha$ during a transit has been observed indicating a large cloud of hot hydrogen of upto 4 planetary radii surrounding the said planet.

Vertical thermal inversions have also been inferred and are thought to be indicative of absorption of the intense stellar irradience in a high altitude layer of the Hot Jupiters atmosphere (Madhusudhan & Seager, 2010).

There have also been some suggestions of variability in the observed spectra but nothing concrete has been published to date.

Direct Imaging

Low signal to noise spectra have been obtained for both HR8799 b & c, discussed in Section 1.3. Analysis of these results have suggested non-equilibrium chemistry, non-solar metalicities and intermediate clouds. These findings are, however, again not fully supported by the exoplanet community. This is a field that will be greatly advanced with the arrival of the new generation of planet finding instruments such as SPHERE and GPI, described in Chatper 3.

1.2.2 The Missing Methane Feature

Observations of field T-dwarf stars, with effective temperatures of $< 1200K$, show the defining feature of strong methane absorption in the H-band. This is opposed to the L-dwarfs where carbon is preferentially locked up in the form of CO. Our own gas giant planets also share this strong methane feature. For these reasons it was naturally expected that exoplanetary spectra would also contain this methane feature. Instruments were designed that use this methane feature to their advantage through a technique called spectral differential imaging, described in Section 2.3.1. However results from these instruments have shown very little sign of the methane absorption band to date. The reasoning behind this lack of methane is thought to be two fold; The planets currently able to be observed are much younger than our solar system planets, therefore making them hotter, also the effect of the radiation field produced from the primary star on the

composition of the exoplanets could cause the discrepancy that is being observed, this is obviously not a factor for the field T dwarfs for which the methane feature has been observed.
Note that the community is eagerly awaiting the discovery of the first "Y-dwarf" whereby the temperature of the dwarf ($< 550K$) is such that ammonia (NH_3) also becomes a defining feature, this is definitely something to look out for in exoplanetary spectra as well.

1.2.3 Biomarkers

**Biomarkers are defined as "detectable species, or sets of species, whose presence at significant abundance strongly suggests a biological origin" (Kaltenegger & Selsis, 2008). It has been stated by Lunine et al. (2008) that the evidence for biology is "simultaneous detection of O_2 or O_3 along with a reduced gas such as CH_4 or N_2O. This is a powerful diagnostic for a disequilibrium condition". We are moving into an era where the detection of biomarkers on other planets is going to move out of the realm of fiction as there are already high contrast instruments with the resolution needed to detect such features (R=30-40 in the near IR).

1.2.4 If We Had Enough Time

The direct observations we make of exoplanets are always of a diffraction limited point source, we never achieve a resolution across the surface of the planet. However, work done by the EPOXI team using Deep impact to look at the Earth has shown some amazing results (Cowan et al., 2009);
Deep impact's 30cm diameter telescope was used to observe the flux from the Earth in 7 wavebands (100nm wide bands centered on 350-950nm). Data was taken over a 24 hour period with hourly measurements of the 350, 750 and 950nm bands and measurements of the 450, 550, 650 and 850nm bands taken every 15min. Although this instrument provides the capability to resolve the Earth, observations were integrated over its entire disk to mimic data that will eventually be available from exoplanets. A spectrum obtained can be seen in Figure 1.11. Following PCA analysis they were able to determine that 98% of the changes in the colour of each observation was defined by the two principal eigencolors, as shown in Figure 1.12. They were then able to determine, from the time variability of the eigen colours, a longitudinally averaged map of the land

**In this section I have drawn on the work of Oppenheimer & Hinkley (2009)

distribution of Earth, as shown in Figure 1.13, very impressive! It should be noted here that this is food for thought and that we are quite a way off obtaining such maps of exoplanets due to, if nothing else, the length of observations needed to collect enough photons from the exoplanets.

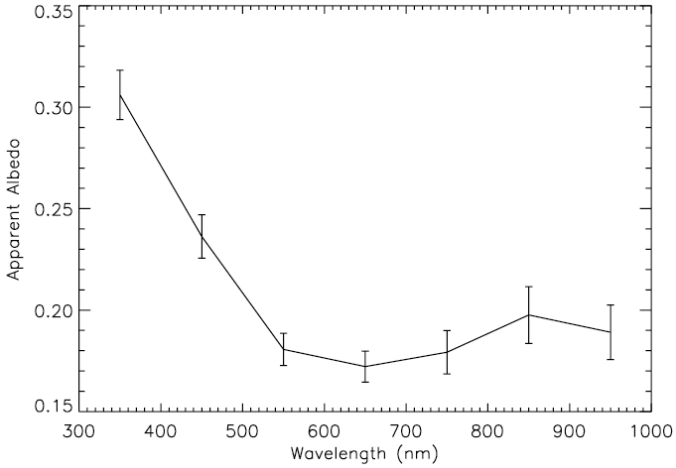

Figure 1.11: Figure 3 from Cowan et al. (2009) showing the time-averaged broadband spectrum of Earth, based on EPOXI observations.

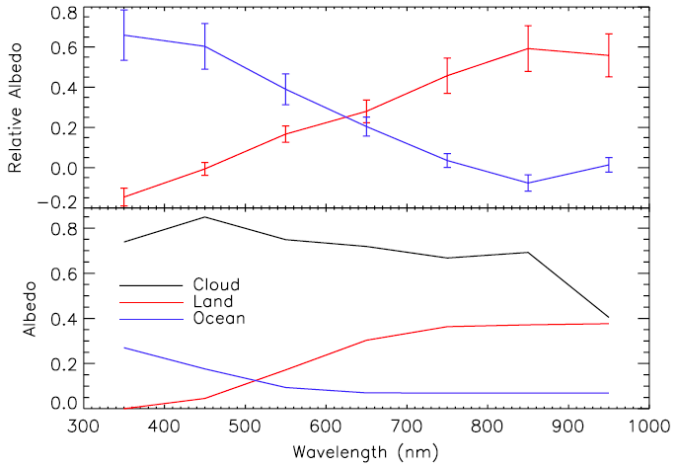

Figure 1.12: Figure 4 from Cowan et al. (2009) showing spectra for the two dominant eigencolors of Earth as determined by the EPOXI team. For comparison, the bottom panel shows actual spectra of clouds, soil, and oceans on Earth.

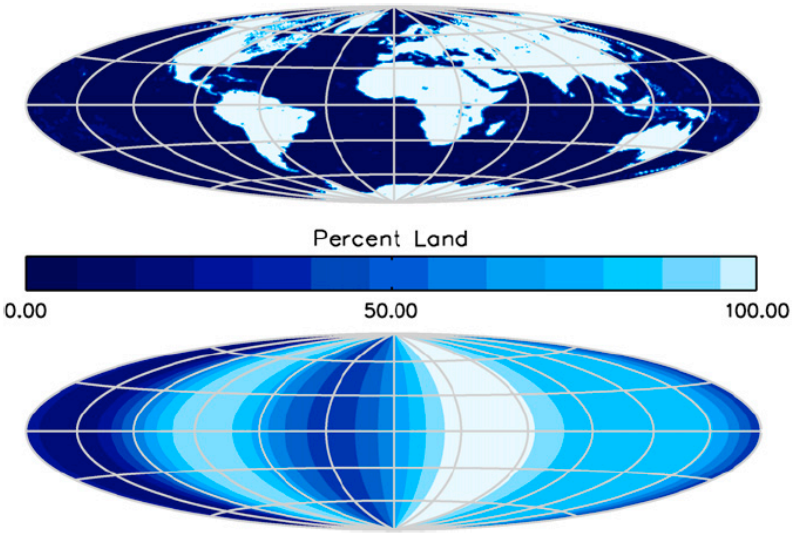

Figure 1.13: Figure 10 from Cowan et al. (2009) showing the land distribution on Earth (top panel) and the distribution of land as determined by the EPOXI light curves. The EPOXI map has no latitudinal resolution.

1.3 Current status of Directly Detected Exoplanets

* To date, only objects seen around Formalhaut and HR 8799 are widely accepted as being planets. For Formalhaut b this is because the mass is constrained by the dust distortions (Kalas et al., 2008) and for HR 8799 the convincing point is that there are four orbiting companions, the case of four (or even three) stars orbiting a central star has never been seen before, and the orbital motion of these companions has been observed for several years. Other objects that claim to be planets have had their mass inferred by models using their brightness and age to constrain the fit. The determined age of the system has a large affect on these models and is the limiting factor when trying to get an accurate result. It is this determination of the mass from models that worries some of the community and is the reason these objects have not been more widely accepted. For the above reasons the following section will give more detail of what we have learnt from Formalhaut b and HR8799 b, c, d & e and only a brief overview of the other planetary mass objects detected via direct imaging.

*Properties of the stars and their companions detailed in the following sections have been taken from //exoplanet.eu unless otherwise stated.

1.3.1 Fomalhaut b

† The debris disk of Formalhaut was first imaged using HST, with its coronograph, by Kalas et al. (2005), see Figure 1.14(a). The center of this debris disk was determined to be offset from the location of Formalhaut. This along with the sharp cut off of the inner edge of the debris disk led to much speculation about the possibility of there being a planetary companion and many possible candidates were located in the HST images. Determination of the common proper motion of the candidate sources was made using Keck II (2005) and HST (2006). In 2008 Formalhaut b was determined to be physically associated with the star and an orbit was deduced. Follow up observations were consequently made at $3.8\mu m$ using Gemini. The companion was observed to move at a rate of $0.82 \pm 0.1 AU\,year^{-1}$ over the 2004-2006 datasets, see Figure 1.14(b). Assuming the planet is coplanar with the dust belt this gives a semimajor axis of the orbit of Formalhaut b to be $a \approx 115AU$. The use of dynamical models of how a planet at the location of Formalhaut b would sculpt the debris disk enabled an accurate determination of the mass of the companion, which was determined to be $3^{+0.5}_{-1.3}M_J$. Keck observations in the CH_4 passband and the H band, Gemini observations in the L'band and HST observations with the F814W filter all fall nicely in line with the atmospheric models of Fortney et al. (2008) simulating a $1-3M_J$ planet wiht an age of 200My, T=400K, gravity=46ms^{-2} and radius=$1.2R_J$. Measurements of the companions flux for all of the observations mentioned above can be found in Figure 1.15.The offset of the HST observations from the models are inferred to be due to reflected stellar light from a circumplanetary dust disk or ring system. A plot of the spectrum from such a dust disk (with a radius of $20R_J$ and a constant albedo of 0.4) is seen to fit these offset data points nicely, also shown in Figure 1.15. A brief summary of the properties of Formalhaut and its planetary companion can be seen in Table 1.1.

†In this section I have drawn on the work of Kalas et al. (2008)

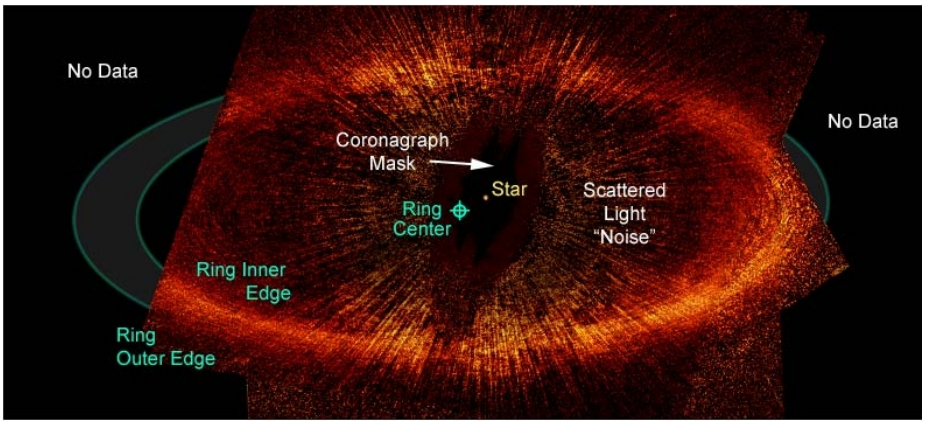

(a)

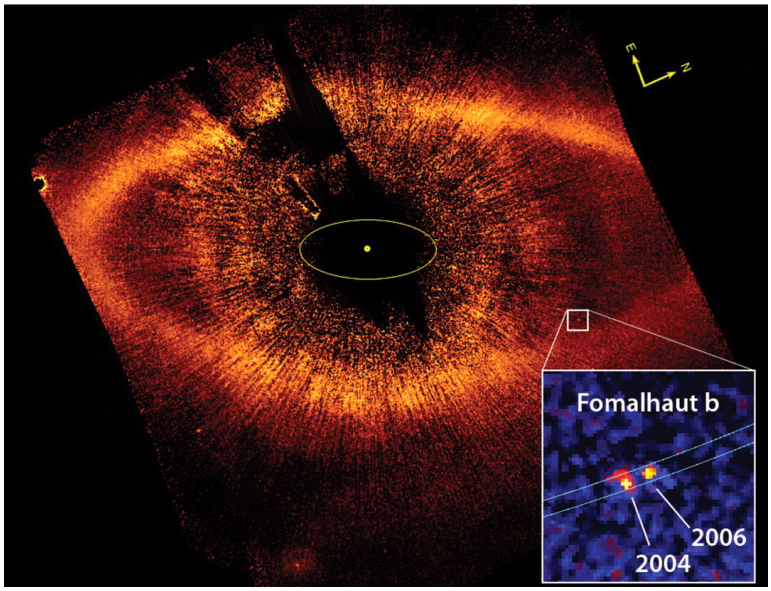

(b)

Figure 1.14: Images of Formalhaut: (a) shows a HST coronographic image taken in 2005 of the Formalhaut system annotated to point out the offset of the star from the center of the debris ring. Adapted from Kalas et al. (2005). (b) Figure 1 from Kalas et al. (2008) showing the HST coronagraphic image of Fomalhaut at $0.6\mu m$. The white square shows the position of Fomalhaut b, at a radius of 12.7 arc seconds from the star (the position of which is shown by the yellow circle), just within the inner boundary of the dust belt.

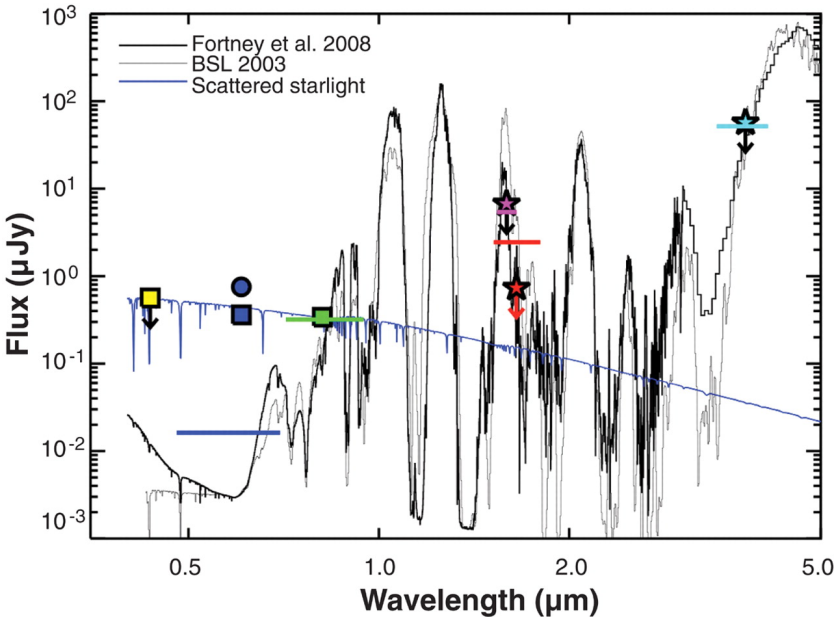

Figure 1.15: Figure 3 from Kalas et al. (2008) shows the photometry of Fomalhaut b through different passbands (arrows show the measurements that gave upper limits) and the fitted planet atmosphere model from Fortney et al. (2008) (heavy solid line). The solid blue line represents light reflected from a circumplanetary disk (radius $20R_J$ and a constant albedo of 0.4).

Formalhaut A		Formalhaut b		
Distance	$7.7pc$	Discovered	2008	Kalas et al. (2008)
Spectral Type	A3 V	Instrument	HST	
Mass	$2.06M_{sun}$	Mass	$3^{+0.5}_{-1.3}M_J$	
Age	$0.2 \pm 0.1Gyr$	Separation (proj.)	$115AU$	
Radius	$1.82 \pm 0.06R_{sun}$	Orbital Period	320000 days	
		Eccentricity	$0.11^{+0.02}_{-0}$	

Table 1.1: Properties of Formalhaut A and its companion Formalhaut b

1.3.2 HR 8799 b,c,d and e

‡ Companions HR8799 b & c were first seen in Gemini NIRI data from 2007 and companion d was first detected using Keck NIRC2 in 2008 (Marois et al., 2008). All these observations were analysed using the angular differential imaging (ADI) technique whereby the intrinsic field of view rotation of the telescope is used to de-couple the planets signal from that of optical artefacts, see Section 2.3.2 for more details. Re-analysis of earlier non-ADI Keck data also revealed the b & c companions. The presence of the fourth planet in the system, HR8799 e, was found from Keck data taken in 2009 and 2010 after again following the ADI technique, see Figure 1.16 (Marois et al., 2010).

Photometric analysis of a, b & c show them to lie at the base of the L-dwarf spectral sequence, shown in Figure 1.17, and their colours are comparable to those of free floating $\sim 11 M_J$ Pleiades brown dwarfs, where the mass has been determined through evolutionary models (Casewell et al., 2007). However the age of this system of is thought to be younger than these Pleiades brown dwarfs which would give a lower mass as determined from the models. The age of the HR8799 system has recently come under question; originally determined to be around 60Myr old, it has now been shown, in two independent investigations, that HR8799 is very likely to be a part of the 30Myr old Columbia Association (R.Doyon *et al.* & B.Zuckerman *et al.* in prep). This new, younger age determination leads to a lower mass estimate of the planets by approximately $3 M_J$, as is shown in Figure 1.18. An overview of the known properties of HR8799 and its planets can be seen in Table 1.2.

Work by Bowler et al. (2010) shows a spectrum for HR8799 b (see Figure 1.19) determined from OSIRIS integral field spectrograph data after implementing an ad-hoc version of the ADI technique. They determine the planet to have a spectral type consistent with L5-T2 dwarfs although the SED is seen to be different to most field objects. They note that no individual model was able to fit the whole data set, however, models including non-equilibrium chemistry, non-solar metalicities and intermediate clouds did provided the best results. Similar results have also been seen for HR8799c (Janson et al., 2010). Broadband photometry of planets b, c,& d also provide strong evidence for significant cloud coverage. Not enough spectral informa-

‡In this section I have drawn mainly on the work of Marois et al. (2008), Marois et al. (2010) & Bowler et al. (2010)

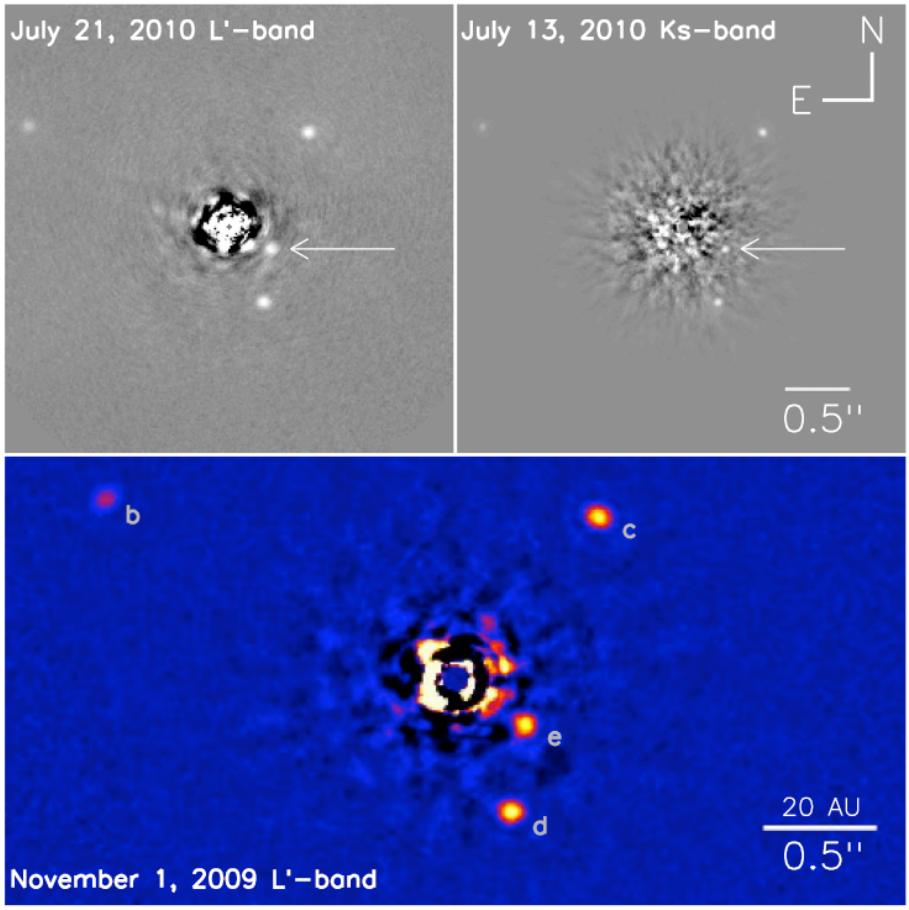

Figure 1.16: Figure 1 from Marois et al. (2010) showing images of the HR8799 planets acquired using the Angular Differential Imaging technique (ADI). This keeps the point spread function in a static orientation while allowing the field-of-view to rotate with time as the star is tracked across the sky. The newly detected planet, e is indicated with an arrow in the top two panels and all four planets are labelled in the bottom panel.

tion is yet known about HR8799 e to give any insight into its atmospheric properties but its near-IR colours are similar to those of the other three planets suggesting a similar cloud cover and chemistry.

The presence of the fourth planet in the system poses many difficulties for the formation models. Formation by the process of in situ bottom up accretion is a possibility for planets d & e however, this is not the case for b & c. The collisional time scale at the orbital radius of b and c is thought to be too low for core accretion to form giant planets before the system's gas is depleted. Formation via in situ gravitational instability fragmentation in the disk could be the formation process of b, c and possibly d, however, it is

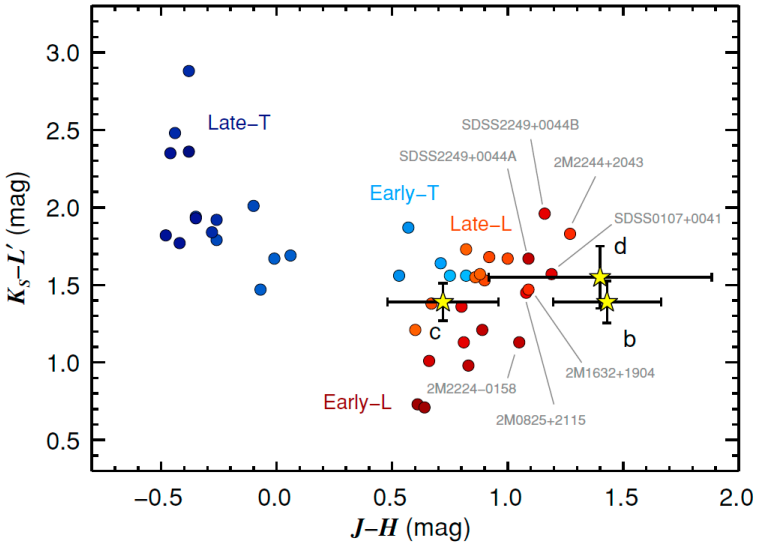

Figure 1.17: Figure 8 from Bowler et al. (2010) showing the colour-colour diagram for L and T-type dwarfs from Leggett et al. (2010) (filled circles) compared to three of the HR 8799 planets (yellow filled stars). The planets are seen to lie at the base of the L-dwarf spectral sequence.

HR8799				
Distance			$39.4 \pm 1 pc$	
Spectral Type			A5V	
Mass			$1.5 \pm 0.3 M_{sun}$	
Age			$0.06^{+0.1}_{-0.04} Gyr$	
	HR8799 b	HR8799 c	HR8799 d	HR8799 e
Discovered	2008	2008	2008	2010
	Marois et al. (2008)			Marois et al. (2010)
Mass (for 60Gyr age)	$7^{+4}_{-2} M_J$	$10 \pm 3 M_J$	$10 \pm 3 M_J$	$9 \pm 4 M_J$
Radius	$1.1 \pm 0.1 R_J$	$1.3^{+0.1}_{-0} R_J$	$1.2^{+0.1}_{-0} R_J$	
Separation	$68 AU$	$38 AU$	$24 AU$	$14.5 \pm 0.5 AU$
	1.73”	0.95”	0.63”	
Orbital Period	$170000 days$	$69000 days$	$36500 days$	$\sim 18000 days$
Eccentricity	<0.4	<0.4	<0.4	
T_{eff}(K)	800-900	1000-1100	1000-1100	
Contrast(mag) from Kasper et al. (2009)				
ΔJ	13.8	12.2	12.9	
ΔH	12.6	11.6	11.6	
ΔK	11.8	10.9	10.9	10.7 ± 0.22
ΔL	10.5	9.5	9.4	9.37 ± 0.12

Table 1.2: Properties of HR8799 A and its companions HR8799 b, c, d and e.

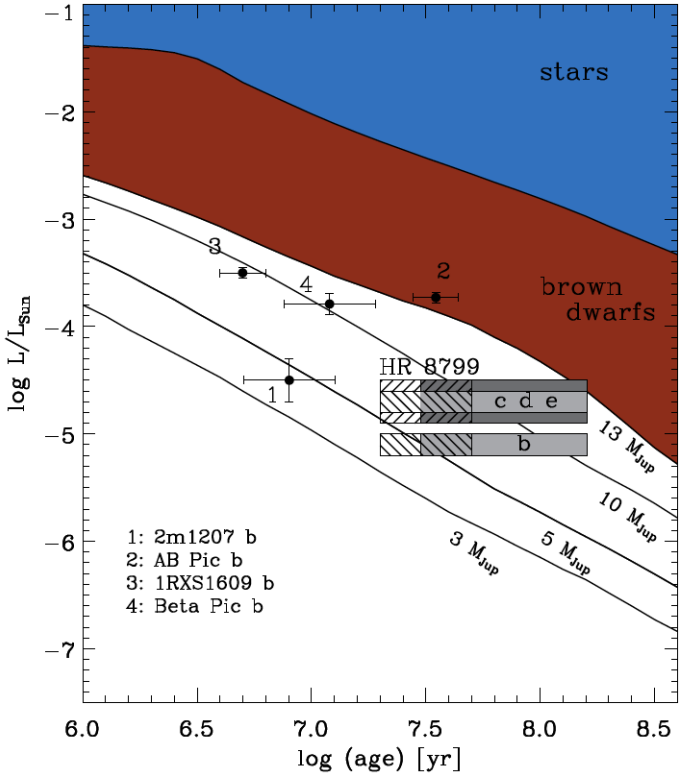

Figure 1.18: Figure 3 from Marois et al. (2010) showing the masses of the HR 8799 planets derived from the age-luminosity relationship. The solid lines are luminosity-versus-age tracks for planet evolution models. The cross hatch areas and grey boxes show the adopted luminosities (1 sigma error bars) with the cross hatch showing the age-range of 20-50Myr and the grey boxes showing the 30-160Myr age-range (see text for details of different age determinations). The darker shading/opposite hatch show the larger luminosity measurement errors for planet e.

very difficult for this to happen at a radius <20-40 AU from the primary (Dodson-Robinson et al., 2009) which rules out this being the formation process of HR8799 e. It is possible that a combination of the two formation processes has occurred in the system, however, it is unlikely due to the similar masses and dynamical properties of the planets. The HR8799 system contains a very dense debris disk. The planets could therefore have formed by either of the two processes before migration to their current locations via interactions with the debris disk.

The HR8799 system is also reminiscent of a scaled up version of our own solar system, with all of the giant planets located past the system's estimated snow line and the debris belts located at similar equilibrium temperatures, as shown in Figure 1.20

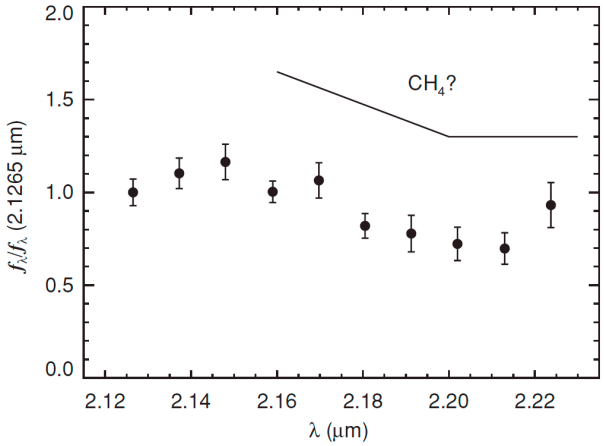

Figure 1.19: Figure and following caption from Figure 3, Bowler et al. (2010); Telluric-corrected OSIRIS spectrum of HR 8799 b. The mean S/N per spectral bin is 11. The data are normalized to 2.1265μm and the error bars are derived from our analysis of injecting and extracting artificial planets. Weak CH_4 absorption is suggested by the data from the negative slope between 2.15 and 2.22μm, but strong 2.2μm absorption is absent. We note, however, that the apparent dip at 2.18μm is offset from the nominal 2.20μm CH_4 band head.

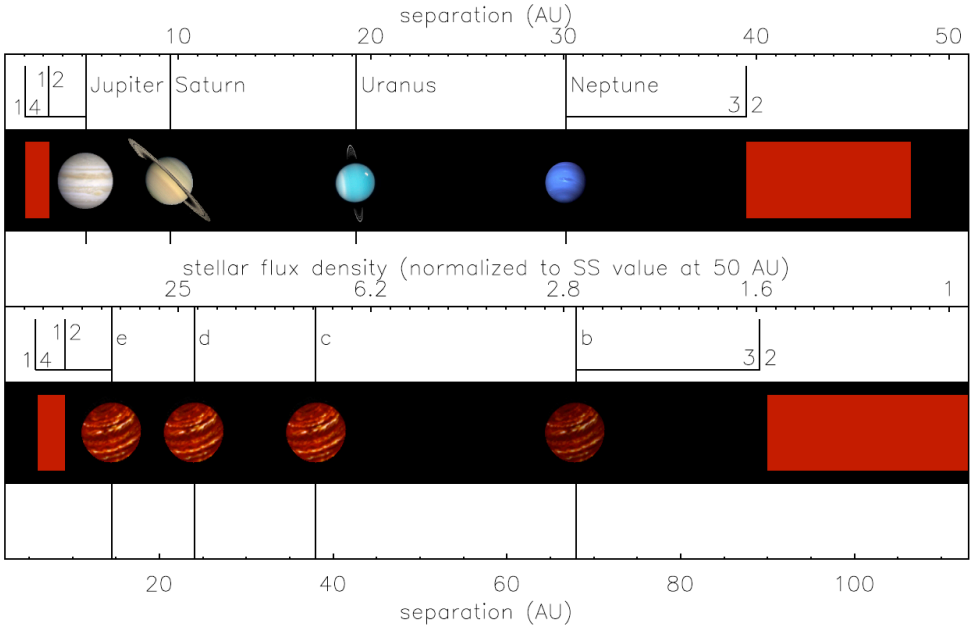

Figure 1.20: Figure 4 from Marois et al. (2010) showing the solar system (upper panel) compared to the HR 8799 system (bottom panel). The horizontal-axis of the HR 8799 plot is compressed by the square root of the ratio of the luminosity of HR 8799 to that of the Sun, thereby showing each system over the same equilibrium temperature range. The red shaded regions represent the inner and outer debris belts in both systems.

1.3.3 Overview of other planetary objects discovered via Direct Imaging

The following tables and figures cover all of the other directly detected companions that are classified as possible planets under the IAU regulations. We will not go into any detail about the individual planets but it is worth noting the range in mass and separation of the planets that have been directly detected to date.

2M1207A		2M1207b		
Distance	$52.4(\pm1.1)pc$	Discovered	2004	Chauvin et al. (2004)
Spectral Type	M8	Instrument	VLT-NaCo	
Mass	$0.025M_{sun}$	Mass	$8\pm2M_J$	Mohanty et al. (2007)
Age	$0.008^{+0.004}_{-0.003}Gyr$	Separation (proj.)	$46\pm5AU$	
			0.77"	
		Radius	$1.5R_J$	
		Contrast (mag)	$\Delta J=7$	Kasper et al. (2009)
			$\Delta H=5.7$	
			$\Delta K=5$	
			$\Delta L=3.6$	
AB Pic A		AB Pic b		
Distance	$47.3(\pm1.8)pc$	Discovered	2005	Chauvin et al. (2005)
Spectral Type	K2 V	Instrument	VLT-NaCo	
Age	$0.03Gyr$	Mass	$13.5\pm0.5M_J$	
		Separation (proj.)	$275AU$	
GQ Lup A		GQ Lup b		
Distance	$140(\pm50)pc$	Discovered	2005	Neuhäuser et al. (2005)
Spectral Type	K7eV	Instrument	VLT-NaCo	
Mass	$0.7M_{sun}$	Mass	$21.5\pm20.5M_J$	
Age	$0.001\pm0.001Gyr$	Separation (proj.)	$103\pm37AU$	
			0.73"	
		Radius	$1.8R_J$	
		Contrast (mag)	$\Delta H=6$	Kasper et al. (2009)
			$\Delta K=6.2$	
			$\Delta L=5.8$	
UScoCTIO 108 A		UScoCTIO 108 b		
Distance	$145(\pm2)pc$	Discovered	2007	Béjar et al. (2008)
Spectral Type	M7	Instrument	WHT-AUX	
Mass	$0.057\pm0.02M_{sun}$	Mass	$14^{+2}_{-8}M_J$	
Age	$0.0055\pm0.0005Gyr$	Separation (proj.)	$670AU$	

Table 1.3: Properties of 2M1207, ABPic, GQ Lup, UScoCTIO 108 and 1RXS169 systems

1RXS1609 A			1RXS1609 b	
Distance	$145(\pm 20)pc$	Discovered	2008	Lafrenière et al. (2008)
Spectral Type	K7V	Instrument	GEMINI North	
Mass	$0.73 \pm 0.05 M_{sun}$		NIRI & ALTAIR	
Age	$0.005 Gyr$	Mass	$8 M_J$	
		Separation (proj.)	$\sim 330 AU$	
		Radius	$1.7 R_J$	
β Pic A			β Pic b	
Distance	$19.3(\pm 0.2)pc$	Discovered	2008	Lagrange et al. (2009)
Spectral Type	A6V	Instrument	VLT-NaCo	
Mass	$1.8 M_{sun}$	Mass	$8^{+5}_{-2} M_J$	
Age	$0.012^{+0.008}_{-0.004} Gyr$	Separation (proj.)	$12 \pm 4 AU$	
			0.41"	
		Orbital Period	$\sim 6000 days$	
		Contrast (mag)	$\Delta L = 7.7$	Kasper et al. (2009)
CT Cha A			CT Cha b	
Distance	$165(\pm 30)pc$	Discovered	2008	Schmidt et al. (2008)
Spectral Type	K7	Instrument	VLT-NaCo	
		Mass	$17 \pm 6 M_J$	
		Separation (proj.)	$440 AU$	
		Radius	$2.2^{+0.81}_{-0.6} R_J$	
		Contrast (mag)	$\Delta Ks = 6.3$	
2M J044144A			2M J044144b	
Distance	$140 pc$	Discovered	2010	Todorov et al. (2010)
Spectral Type	M8.5	Instrument	HST-WFPC2	
Mass	$0.02 M_{sun}$		& GEMINI North	
Age	$0.001 Gyr$		NIRI & ALTAIR	
		Mass	$7.5 \pm 2.5 M_J$	
		Separation (proj.)	$15 \pm 0.6 AU$	
GSC 06214-00210A			GSC 06214-00210b	
Distance	$145(\pm 14)pc$	Discovered	2010	Ireland et al. (2010)
Spectral Type	M1	Instrument	Palomar 200" - PHARO	
Mass	$0.6 M_{sun}$		& Keck - NIRC2	
Age	$0.005 Gyr$	Mass	$13.5 \pm 1.5 M_J$	
		Separation (proj.)	$\sim 320 AU$	

Table 1.4: Properties of β Pictoris, CT Cha, 2M J044144 and GSC 06214-00210 systems

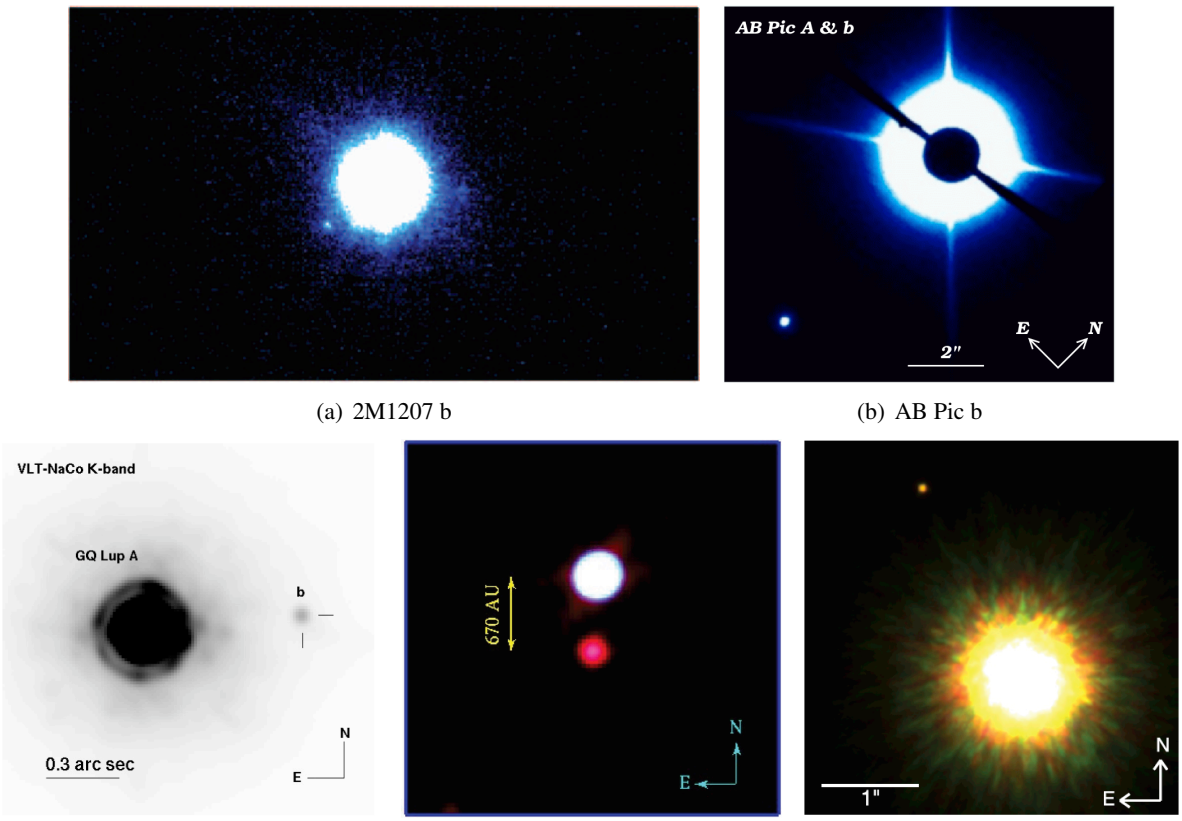

(a) 2M1207 b (b) AB Pic b

(c) GQ Lup b (d) UScoCTIO 108 b (e) 1RXS1609 b

Figure 1.21: Images of directly detected exoplanets:
(a) J band Image of 2M1207A and its companion 2M1207b taken with VLT- NACO . 2M1207A is the central bright source, 2M1207B the bright dot to its immediate lower left, at a separation of $769 \pm 10 mas$. Taken from Mohanty et al. (2007).
(b) A Ks band coronagraphic image of AB Pic A and b with an occulting mask of diameter 1.4". Taken from Chauvin et al. (2005).
(c) VLT-NACO Ks band image of GQ Lup and its 6 mag fainter companion candidate 0.7325 ± 0.0034" west. Taken from Neuhäuser et al. (2005).
(d) Composite-color IZK image (19.5" x 19.5") of UScoCTIO 108 A and b (I=blue, Z=green, K'=red). IZ images are from the AUX instrument on the William Herschel Telescope, and the K' image is from NICS on the Telescopio Nazionale Galileo. All images were convolved with a Gaussian to a spatial resolution of 1.1". Taken from Béjar et al. (2008).
(e) Composite image of 1RXS1609 A and its companion. Blue, green, and red represent images taken in J, H, and K , with intensities scaled such that they are proportional to the photon rates inferred from the 2MASS magnitudes of the primary. Taken from Lafrenière et al. (2008).

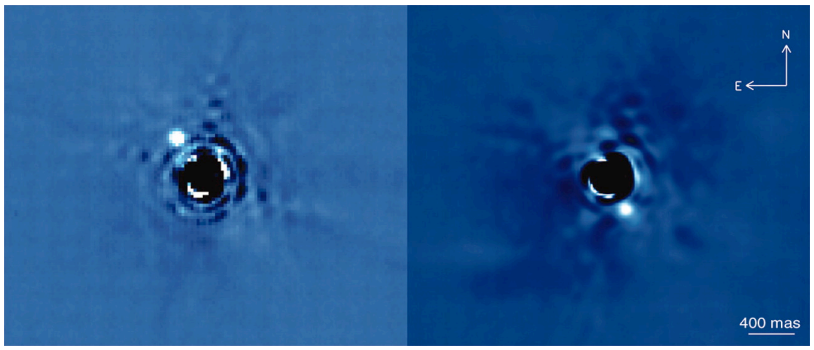

(a) β Pictoris b

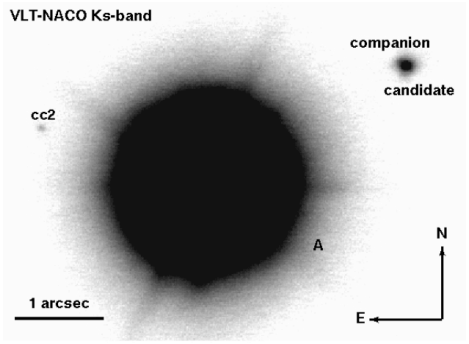

(b) CT Cha b

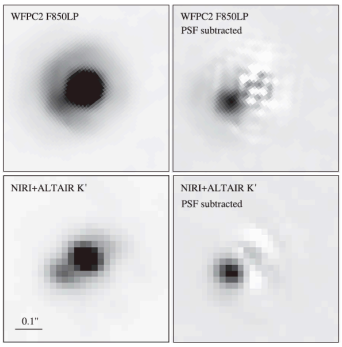

(c) 2M J044144 b

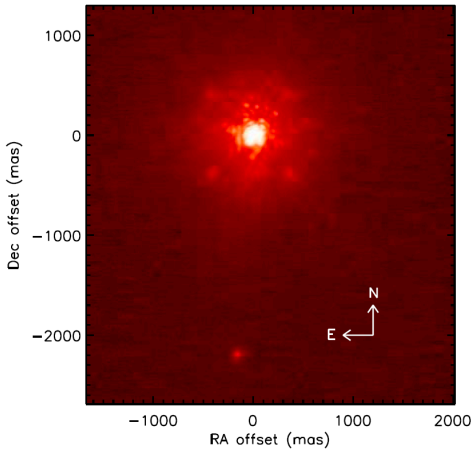

(d) GSC 06214-00210 b

Figure 1.22: Images of directly detected exoplanets:
(a) β Pictoris imaged at L band with the VLT/NaCo instrument in November 2003 (left) and the fall of 2009 (right). Images of the comparison star HR2435 were used to estimate and remove the stellar halo. Taken from Lagrange et al. (2010).
(b) VLT-NACO Ks-band image of CT Cha A and its 6.3 mag fainter companion candidate (2.670 ± 0.038" northwest) from 2007 March 2. The object marked as "cc2" was found to be a background object. Taken from Schmidt et al. (2008).
(c) WFPC2 and NIRI+ALTAIR images of the young brown dwarf 2M J044144 before and after PSF subtraction (0.6" x 0.6"). Taken from Todorov et al. (2010).
(d) Image of GSC 06214-00210 taken in the Kp filter, with a log stretch. The faint companion can be seen as at an RA offset of $\sim 200 mas$ and a Dec offset of $\sim 2200 mas$. Taken from Ireland et al. (2010).

Chapter 2

Limitations of High Contrast Imaging and Spectroscopy

As mentioned earlier the ultimate achievable contrast of direct detection experiments is limited by so-called quasi-static or super speckles. Speckles are residual starlight created when the light passes through the earth's atmosphere, and by imperfections in the telescope and instrument optics. In order to understand the methods used to directly image exoplanets we must first understand the noise itself and hence where it comes from.

2.1 Properties of Speckles

*If we assume we are observing a star with a telescope such that we cannot resolve it and that it is hence diffraction limited the wavefront from this star resembles a perfect plane and the telescope simply acts as a Fourier transform of this plane multiplied by the telescope's pupil shape and thus we are left with a perfect Airy pattern. We can take this pupil shape to be the primary mirror (negating the effects of the secondary mirror and support structure on the shape of the pupil). Any deviation from the perfect plane wave front at the entrance pupil will cause a modification to this PSF.

By considering the simple case of an added, low amplitude, sinusoidal phase to the plane wave front we can

*Description of the origin of speckles and their noise properties have been drawn from Oppenheimer & Hinkley (2009), Racine et al. (1999) Sparks & Ford (2002) & Hinkley et al. (2007).

see that the corresponding Fourier components in the image plane are faint copies of the original PSF but offset by an angle proportional to the sinusoids frequency across the pupil. As we are using the example of a sinusoidal wave front there will be a symmetric set of spots on either side of the primary PSF. This is essentially our speckle noise, however, in reality the speckles are not made from perfect sinusoidal waves but by complex random wave fronts which result is sub sections of the pupil interfering coherently to produce the speckles. We can see that two such coherently interfering sub sections of separation D will constitute a two beam interferometer for which the PSF produced will have a width of λ/D. As was mentioned the location of these patches of coherence are random and as such we see that their position is more likely to be around the edge of the pupil (due to the larger annular area). This characteristic size of the speckles, λ/D is the same as that of the diffraction limited PSF (D is essentially the pupil diameter). As a consequence a speckle in the image plane would look exactly the same, at any given wavelength as a real object and hence a huge problem for direct detection.

Minor changes in the wave front cause the speckles to move around, disappear or produce new speckles. This results in a highly variable, non-smooth background noise which cannot be easily calibrated out.

The first source of speckles to consider is the turbulent atmosphere the light has to pass though to reach our telescopes. These speckles are typically short lived and, due to their random nature, they can therefore be averaged out via long exposure times. Our main problem comes from the longer lived speckles that can not be averaged out but that still vary enough for us to be unable to calibrate them out. Such speckles can be produced from the semi-static wave front errors of imperfect optics in the instruments and telescopes being used, these speckles are called super speckles or quasi-static speckles. An example of this can be seen in Figure 2.1, where two images taken with NACO are shown each separated by 1 hour illustrating how the speckle pattern changes with time. Figure 2.2 shows a typical map of short and long speckle lifetimes as determined from hundreds of sequential images taken through a coronagraph behind an AO system.

2.2 Methods of Reducing Speckle Noise

2.2.1 Extreme-Adaptive Optics

By using prior knowledge that the object we are trying to observe is a point source we are able to determine what phase changes are needed in the pupil to give the original point source. Adaptive Optics systems do

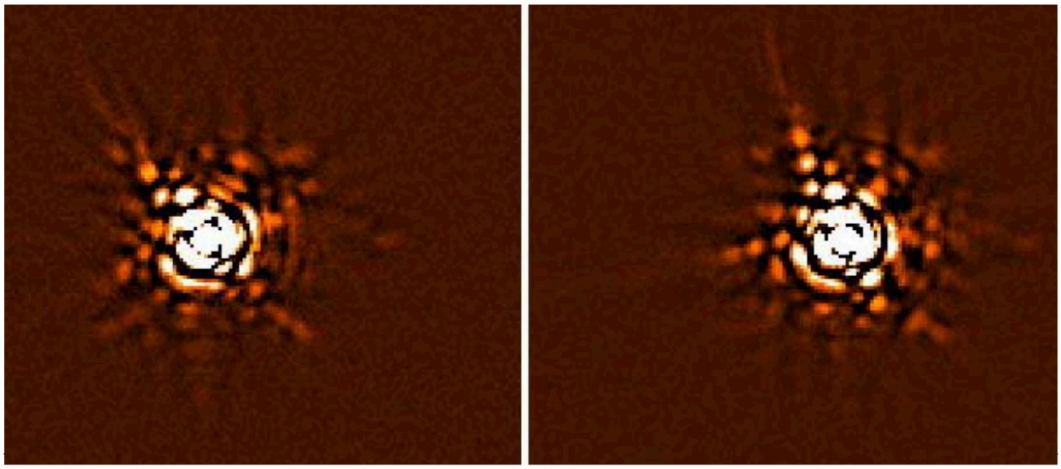

Figure 2.1: Observations of the quasi-static speckle pattern taken using NACO on the VLT. Images are separated by $\sim 1hr$. It should be noted that the field of speckles has rotated due to the pupil de-rotation needed to keep the field stable, however, changes in the speckle pattern can also be seen on top of this rotation. Taken from Vérinaud et al. (2006).

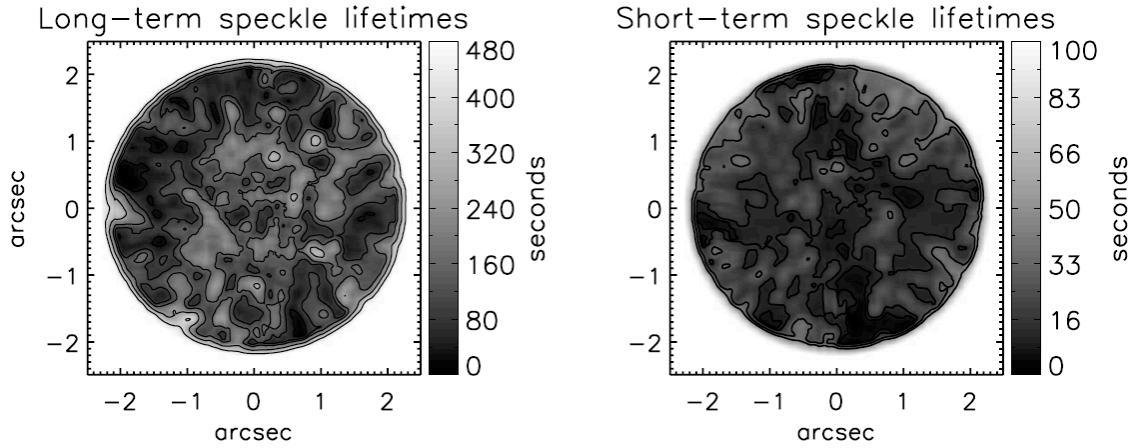

Figure 2.2: Speckle lifetimes as determined from hundreds of sequential images taken through a coronagraph behind an AO system. Taken from Hinkley et al. (2007).

exactly this, they sample the wave front and apply the necessary changes to a deformable mirror. These changes have to be calculated and performed incredibly fast, up to a few thousand times a second (Oppenheimer & Hinkley, 2009), and as such guide stars used to perform the correction of must be suitably bright. To summarise the aim of Adaptive Optics is to produce a diffraction limited image by flattening out the wave front using the star as a reference. Most AO systems to date work in the 20-60% Strehl range (where

Strehl is the ratio of the peak of the actual PSF to that of the perfect PSF), however, new Extreme Adaptive Optics systems are being produced that have the ability to push the achieved correction into the $> 90\%$ Strehl regime.

Adaptive optics, although essential, is not the only thing we need if we are going to get down to exoplanet contrasts. The AO system produces an almost diffraction limited image with which diffraction suppression techniques can be applied, as described in the next section, however, even with this greater Strehl the residual speckles are still the limiting noise.

2.2.2 Coronagraphs and Apodizers

With our diffraction limited image from the adaptive optics it is now time to tackle the diffraction itself. The field of coronagraphy is highly extensive and not one I am going to go into much detail about. The three main types of coronagraph you should be aware of are;

Classical Lyot Coronagraph Whereby the core of the star is masked with a simple stop in the focal plane and the diffracted light is subsequently masked with a stop in the pupil plane.

Apodised Lyot Coronagraph Whereby the diffraction effects are lessened by inserting a gradual or apodised transmission function into the pupil plane prior to the focal plane mask.

Four Quadrant Phase Masks Whereby two quadrants of a transparent mask have additional phase added such that the light from the star it is centered on destructively interferes.

Again even after the improvement of the coronagraphs we are still limited by the speckle noise. We shall now move on to what we can do to remove the remaining speckle noise left after such reduction methods have been implemented.

2.3 Methods of Removing Speckles

The following methods of speckle removal use the intrinsic properties of the speckles or the planets to remove them; Simultaneous Differential Imaging (SDI) uses a prior knowledge of the planetary spectra, Spectral Deconvolution (SD) uses the wavelength dependence of the speckles and Angular Differential

Imaging (ADI) relies on the temporal stability of the speckles. SDI and ADI have been amply performed on sky with speckle rejection levels around the one to two magnitude regime a regular occurrence and in the case of Marois et al. (2006) even three to four magnitudes. Spectral deconvolution is in its infancy in this respect, having no detections of exoplanets to its name. However, this is due to the lack of instrumentation available to correctly employ the method and spectral deconvolution is actually expected to be the best method of speckle rejection out of all three. As such, all new planet finding instruments are being designed with the capability of exploiting this very powerful speckle rejection method.

2.3.1 Simultaneous Differential Imaging

In this method pairs of images are taken simultaneously in adjacent wavelength bands so that their speckle patterns are almost identical. A spectral range is chosen where the planetary and stellar signals are very different, such as a methane absorption band. The method takes the two signals as described in Equations 2.1 & 2.2 where $S(\lambda)$ is the total signal for a fixed position around a star where a planet is located, $s(\lambda)$ is the stellar signal at this position and $p(\lambda)$ is the planetary signal.

$$S(\lambda_1) = s(\lambda_1) + p(\lambda_1) \tag{2.1}$$

$$S(\lambda_2) = s(\lambda_2) + p(\lambda_2) \tag{2.2}$$

Assuming λ_2 is located within an absorption feature of the companion we get;

$$p(\lambda_2) = 0 \text{ and } s(\lambda_1) = s(\lambda_2) \tag{2.3}$$

Therefore, when we subtract the images we are left with only the companion signal;

$$S(\lambda_1) - S(\lambda_2) = p(\lambda_2) \tag{2.4}$$

Images need to be rescaled before subtraction due to the speckles being chromatic.
The change in Strehl Ratio and stellar spectrum with wavelength results in residuals still limiting the possible detection with this method. A slight modification to this technique, called Double Difference, has been

developed to try and get rid of some of the residual speckles left by the SDI technique. This method takes 3 images, $S(\lambda_1), S(\lambda_2)$ and $S(\lambda_3)$, at adjacent wavelength bands, $\lambda_1 < \lambda_2 < \lambda_3$, with only one located in the absorption feature. The double difference is;

$$dd = (S(\lambda_1) - S(\lambda_2)) - k(S(\lambda_1) - S(\lambda_3)) \tag{2.5}$$

$$k = \frac{SR_1 - SR_2}{SR_1 - SR_3} \tag{2.6}$$

Where SR denotes the Strehl Ratio at each wavelength. This method takes into account the global variation of the PSF with wavelength (Marois et al., 2000).

SDI has a few dedicated instruments; TRIDENT (Marois et al., 2003), NACO (Lenzen et al., 2004), NICI (Toomey & Ftaclas, 2003), and SPHERE-IRDIS (Beuzit et al., 2006). TRIDENT was the first and did not provide the contrasts expected. This was due to telescope aberrations and the non-common path errors due to the 3 different optical paths within the instrument. Data showed 130nm rms instrument aberrations and $\sim$100nm of this was due to the different optical paths (Marois et al., 2005). The instruments that followed were far stricter with the amount of optical path difference and have been showing impressive results especially when combined with the angular differential imaging technique described in the following section.

A significant disadvantage of SDI is that you need to have a prior knowledge/expectation of the planetary spectra and select your wavelength bands accordingly. There is also the additional need for follow up observations to confirm the nature of the object, through determination of a common proper motion with the parent, and for characterisation of the companion.

2.3.2 Angular Differential Imaging

Angular differential imaging (ADI) is the most successful method to date, having been used to remove speckles and discover the planets around HR8799 (see Section 1.3.2). The method takes advantage of the rotation of the speckle pattern with respect to the sky, when viewing on a non-equatorially mounted telescope, caused by the rotation of the primary mirror with respect to the sky. By instead fixing the primary mirror w.r.t. the sky this can be flipped around such that the speckles now stay still and the sky rotates,

thus converting any companions into an arc. From this one can determine what is stationary and what is not enabling a rejection of the speckle pattern and leaving you with any companions that may be present. ADI relies on the temporal stability of the quasi-static speckle pattern and there in lies its limitation as to why it can not achieve perfect contrasts, as the speckle pattern is not time independent. Figure 2.3 shows the power of the ADI technique as performed by the Gemini NICI instrument observing the PZTel system.

The angular differential imaging method can in principle be combined with either that of spectral deconvolution or SDI to provide an added contrast improvement and thus is the intent for many instruments. Figure 2.4 shows contrast curves for such an application with Gemini's NICI instrument performing a combination of SDI in the H band as well as ADI

2.3.3 Spectral Deconvolution

It has been amply demonstrated by several authors (e.g. Sparks & Ford (2002), Thatte et al. (2007)) that all the information available in an IFS data cube can be used to identify and eliminate long lived quasi-static speckles (also called super speckles) which otherwise define the speckle noise limit in high contrast imaging spectroscopy applications. In a way, using the spectral deconvolution method represents a generalisation of the Simultaneous Differential Imaging (SDI) technique, see Section 2.3.1, which uses information at other (neighbouring) wavelengths to identify and subtract quasi-static speckles from a high contrast image. Hav-

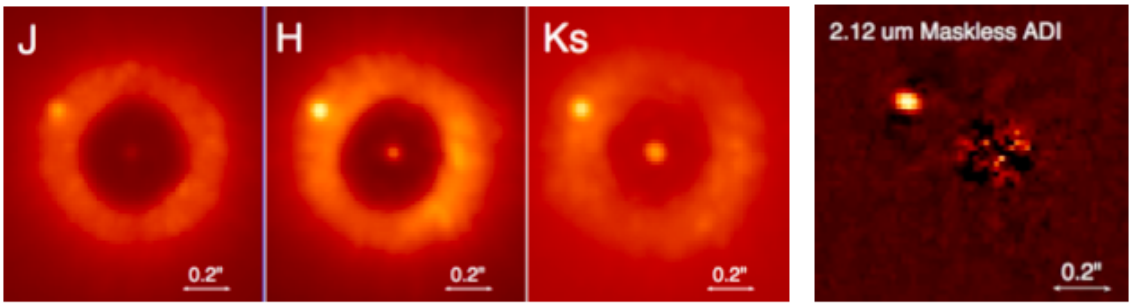

Figure 2.3: Figure showing the ability of Gemini-NICI to detect faint companions via the angular differential imaging technique. The left three panels show images of the PZ Tel system taken in the$J, H\&K_s$ bands with the NICI instrument in direct imaging mode. The Primary star is located at the center of the partially translucent 0.22" radius focal plane mask. The confirmed companion is at 0.36" separation with flux ratios of $\Delta J = 5.4 \pm 0.13$, $\Delta H = 5.38 \pm 0.09$, and $\Delta K_s = 5.04 \pm 0.10$mag. The right hand image shows the result of maskless ADI at $2.12 \mu m$. From Biller et al. (2010)

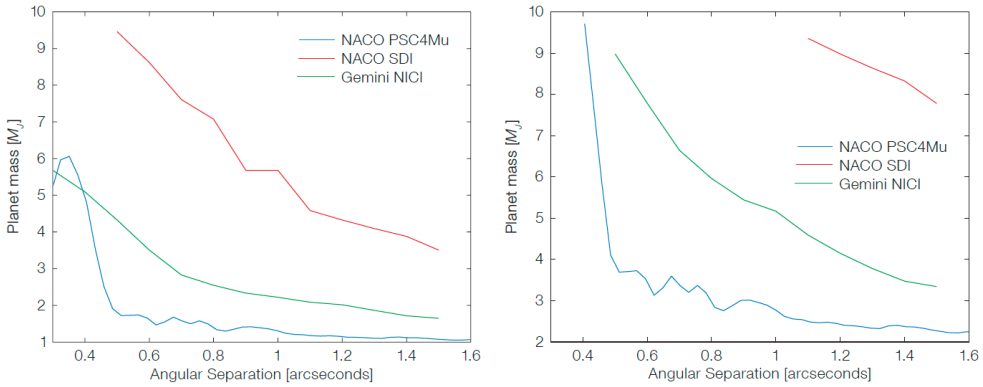

Figure 2.4: Plots showing 3σ detectability, in terms of planet mass (assuming a K0 host star), using modelled exoplanet spectra of a age 100Myr (left) and 316Myr (right) of currently operational instruments; VLT-NACO in normal SDI mode (H-band), the improvement using a pupil stabilised coronagraphic mode (NACO PSC4Mu in the L-band) and Gemini-NICI in joint H-band SDI-ADI mode. From Kasper et al. (2009)

ing access to multiple wavelength channels, as is typical in an IFS data cube, allows this more sophisticated technique for identifying and eliminating quasi-static speckles to be employed.

The spectral deconvolution technique uses the fact that the position of almost all features arising from the parent star (including the Airy pattern and speckles) scales linearly with wavelength. Take the Airy pattern as an example, the first null is always at $1.22\lambda/D$ from the parent star. However, a physical object's location is, obviously, not dependent on wavelength. If we were to look at the the location of the companion and move through in wavelength we would see the intensity rise and fall as the airy pattern (and other features) moved across it, drowning out the signal from the companion. We, however, use this wavelength dependence to our advantage. The method of spectral deconvolution was first proposed by Sparks & Ford (2002), and is essentially an extension to the SDI technique described in 2.3.1. The following description assumes a data cube (whereby the third dimension is wavelength) has already been obtained, i.e. through the use of an integral field spectrograph (for a more in depth description of integral field spectrographs please see Section 3.1);

1. Each wavelength channel of a datacube is scaled with respect to wavelength such that if the datacube was of a noise free point source each channel would be identical after scaling (i.e. the Airy pattern of the point source seen in one channel would exactly match that seen in every other channel). Doing this spatially lines up all of the speckles so that they appear at the same place in every wavelength

channel whereas the location of the companion signal now appears to be wavelength dependent. This is depicted graphically in Figure 2.5. Figure 2.6 shows simulations of a data cube, before and after this scaling, that has been collapsed along the wavelength direction.

2. The data cube is divided through by the spectrum of the parent star as all artifacts arising from the parent star should have the same spectrum.

3. Once the stellar spectrum has been removed and the wavelength channels have been scaled so that the speckles are lined up on respective spaxels[†] we can make a fit to their spectra. The companion signal is faint and now smeared across multiple spaxels causing it to appear as a low intensity, high frequency bump in the spectra of the speckle. For this reason a low order polynomial fit to each spatial pixel can almost completely take into account the speckle signal but leave the planet signal almost untouched, see Figure 2.7.

4. This fit is then removed from its respective spaxel and the parent spectrum is multiplied back into the data so that we are just left with the planet signal radially smeared out across multiple spaxels.

5. Each wavelength channel of the datacube is then re-scaled to its original dimensions turning the radially smeared out planet back into its original form.

By using the an integral field spectrograph and applying the spectral deconvolution method we are able to obtain not only a detection of a low mass companion but also its spectrum in one go, thus also negating the need for follow up observations to confirm the nature of the object detected. This is, therefore, a very powerful technique and one that all new instrumentation for the direct detection and characterisation of exoplanets are being designed to exploit.

To date, there is only one integral field spectrograph in operation that has been designed for high contrast applications, Project 1640 at the 200" Hale Telescope in Palomar. Two others are also nearing completion; SPHERE on the VLT and GPI on Gemini. All of these instruments are described in Chapter 3. Currently the best demonstration of this technique would have to be the work of Thatte et al. (2007) on AB Dor C, whereby they achieved a contrast of 9 magnitudes at 0.2" and 11 magnitudes at 0.5" with the SINFONI instrument that was NOT designed for high contrast observations. This work is described in Section 7.2.

[†]By spaxel we mean a pixel that spans the entire wavelength range of the integral field spectrograph data cube.

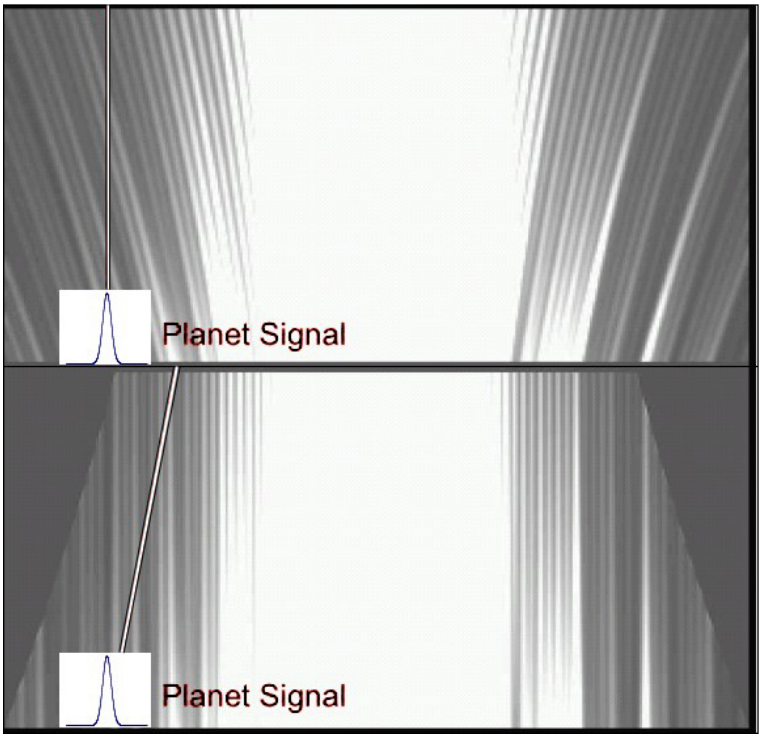

Figure 2.5: These images show cuts through a datacube with one spatial and one spectral dimension, lines representing the planet flux have been overlaid on top. In the top image, the raw datacube, the speckles diverge outward with wavelength. The bottom image shows the cube after it has been scaled w.r.t. wavelength. The location of the speckles is no longer dependent on wavelength so they form straight lines running vertically in the plot (modified from Figure 27 in Sparks & Ford (2002))

Bifurcation Radius

[‡]The bifurcation radius is a limit on the inner working angle of the spectral deconvolution technique as determined by the maximum movement of the speckle due to the limited wavelength coverage. Outside the bifurcation point the speckle pattern at a given wavelength can be reconstructed (and eliminated) using regions unaffected by the planet image. If the maximum movement of the speckle with wavelength is less than the width of the first airy null of the diffraction limited PSF it can be understood that any companion located within such a radius will be partially fit out by the spectral deconvolution method. To determine the bifurcation point it is helpful to consider it from the point of view of the scaled data cube. Here the

[‡]Here I draw on the work of Thatte et al. (2007)

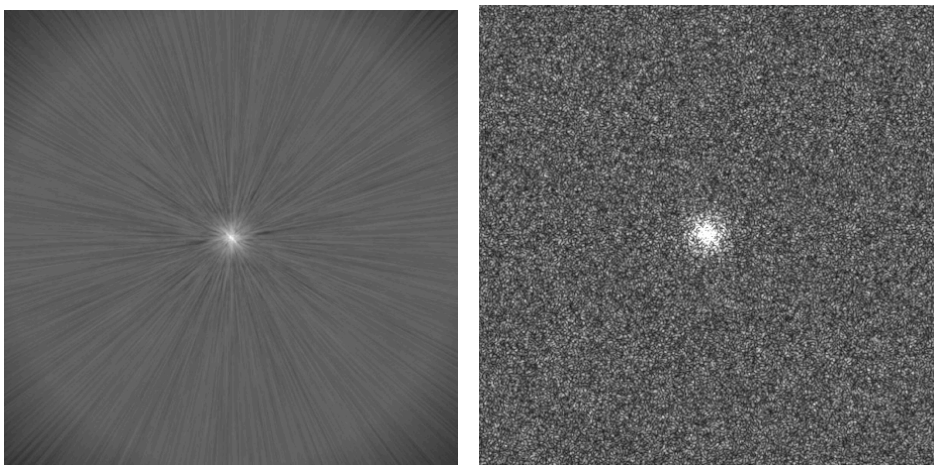

(a) Unscaled (b) Scaled

Figure 2.6: EPICS simulation data (described in Section 5.2) (left) Raw data cube (right) Data cube after scaling w.r.t. wavelength. Both are collapsed along the wavelength axis.

movement of a real companion is given by;

$$\Delta r = r - r\frac{\lambda_{min}}{\lambda_{max}} = r\frac{\Delta\lambda}{\lambda_{max}} \tag{2.7}$$

where, r is the radial distance to the companion from the star, λ_{min} is the shortest wavelength and λ_{max} is the longest.

Due to the scaling, the physical extent of the companion, Θ is now a constant;

$$\Theta = 2 \times 1.22\lambda_{min}/D \tag{2.8}$$

The bifurcation point is then given by;

$$\Delta r = r\frac{\Delta\lambda}{\lambda_{max}} = 2 \times 1.22\lambda_{min}/D \tag{2.9}$$

It has, however, been amply demonstrated by Thatte et al. (2007) that if the location of the companion is known an iterative implementation of the spectral deconvolution method can be performed to enable us to still be able to extract the spectra of companions at a distance of the bifurcation radius.

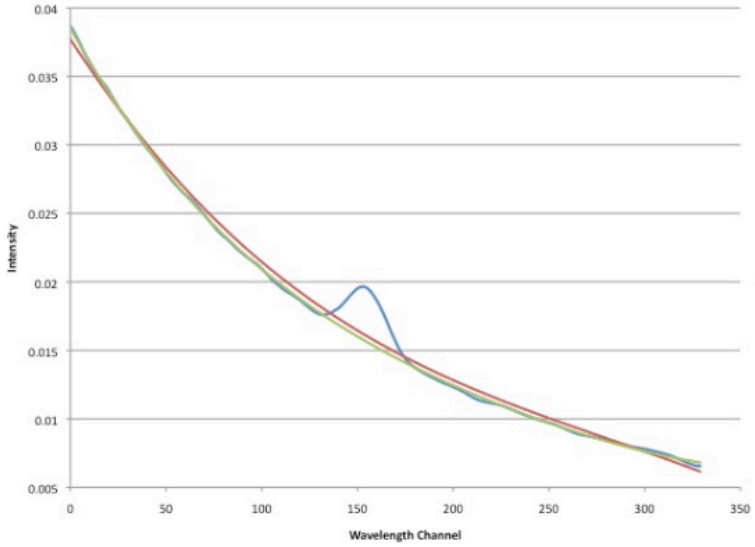

Figure 2.7: Simulated data of a low order polynomial fitting to speckle spectrum after scaling. The blue curve is the intensity of the speckle after scaling, the red curve is the initial polynomial fit and the green curve is the fit after + sigma clipping (described in more detail in Section 5.2). The bump in the centre is where the planet signal, now a radial smear, crosses over the speckle.

Speckle Smearing

[§]Additional to this lack of speckle movement at small separations, the movement of the speckles at large separations can be too great for the spectral resolving power supplied by the instrument resulting in a smeared speckle signal moving between wavelength channels. As mentioned the position of a speckle scales proportionally to wavelength, i.e. a speckle located at an angular distance, θ, from the star at the central wavelength, λ, will move spectrally at the rate of $d\lambda/d\theta = \lambda/\theta$. Therefore a speckle of width $\delta\theta_s = \lambda/D$ will correspond to a spectral speckle of width;

$$\delta\lambda_s = \frac{\lambda^2}{\theta D} \tag{2.10}$$

In order to be Nyquist sampled we require two sample points per speckle spectral width. This corresponds to a two pixel spectral resolution of;

$$R > \frac{\lambda}{\delta\lambda} = \theta\frac{D}{\lambda} \tag{2.11}$$

[§]Here I have drawn on the work of Antichi et al. (2009) & Salter et al. (2008).

This criteria is fulfilled within an angular distance from the star, θ_{Ny}, that is referred to as the Nyquist radius;

$$\theta_{Ny} = R\frac{\lambda}{D} \tag{2.12}$$

For an integral field spectrograph covering the wavelength range $\lambda_{min} - \lambda_{max}$ with a central wavelength λ_c, the Nyquist radius is defined by;

$$\theta_{Ny} = \frac{R}{D}\frac{\lambda_{min}^2}{\lambda_c} \tag{2.13}$$

Figure 2.8 shows the result of collapsing a data cube of low spectral resolution. The result of the Nyquist radius not being fulfilled can be seen as the radial smearing of the speckles furthest from the star.

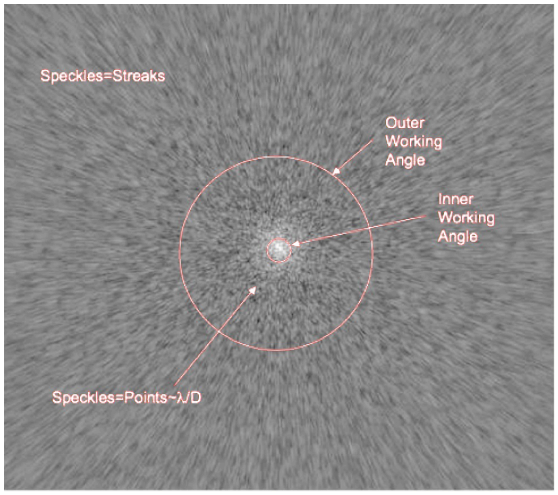

Figure 2.8: Simulation of a flattened, scaled data cube of low spectral resolution. Image shows the inner working angle dictated via the bifurcation radius and the outer working angle dictated via speckle smearing of the spectral deconvolution method. The transition of the speckles from points $\sim \lambda/D$ in size to radial streaks with increasing distance from the source is clearly seen. From Salter et al. (2008)

Chapter 3

Instrumentation for High Contrast Imaging and Spectroscopy

All new instruments being designed for high contrast applications are including an integral field spectrograph so as to be able to take advantage of the wavelength dependance of the speckle noise and therefore remove it. For such an instrument the ability to obtain wavelength information for every point in the field of view simultaneously is essential as the speckle pattern varies with time.

3.1 Types of Integral Field Spectrograph

For the purposes of this thesis only two main types of integral field spectrograph (IFS) will be discussed as they are the only ones that have been implemented in planet finding instruments to date* or that are being investigated for future instruments, these are;

3.1.1 Lenslet

TIGER

TIGER is the original type of lenslet IFS, as seen in Figure 3.1, it samples the focal plane using a mosaic of lenslets, the pupil images formed by these lenslets (smaller in extent than each lenslet) are then dispersed

*Note that fibre fed IFU's are not investigated due to their low throughput. High throughput of the system is vital due to the very low signals trying to be detected.

along the spaces between the pupil images. This type of integral field spectrograph design has been implemented by the GPI and Project 1640 instruments described in the following sections.

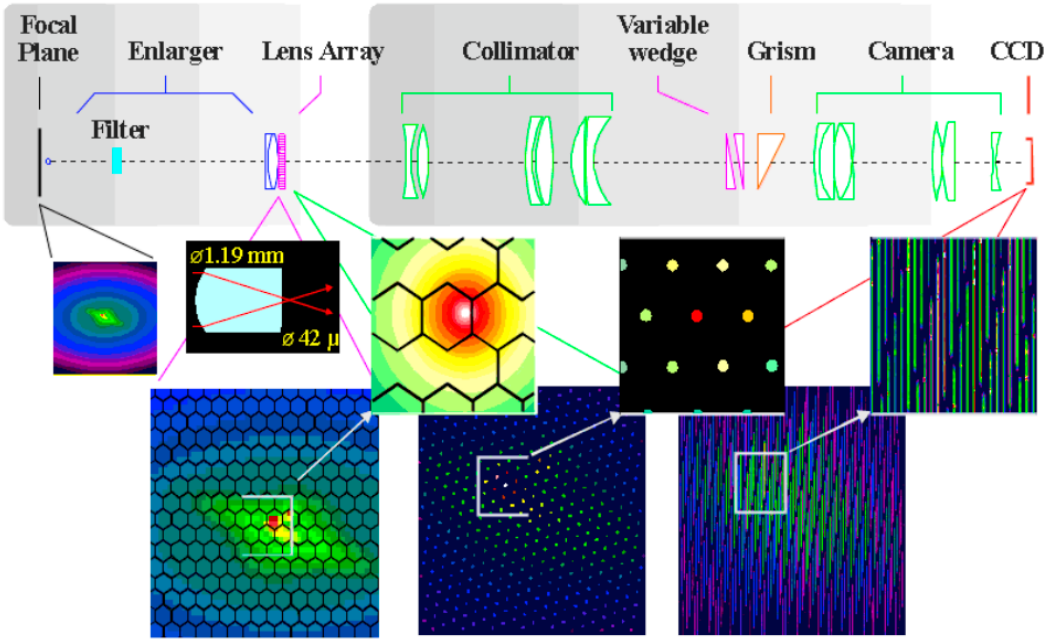

Figure 3.1: TIGER: The optical design of the SAURON instrument (de Zeeuw et al., 2000). Figure taken from Bacon et al. (2001)

The pupil produced by the lenslet array is small and can essentially be taken to act like a point source, the image of the micropupil is then in this case dominated by the PSF of the microlens, which is an Airy pattern for a circular aperture. The wings of this PSF do not decay rapidly resulting in a cross talk between lenslets which in turn adds in an error to our produced data cube which can be detrimental to high contrast imaging and spectroscopy. A way around this is to analyse the cross talk produced by each lenslet individually. Then, with this map of cross talk, you can re-calibrate your data accordingly although the accuracy of this method is not fully trusted.

BIGRE

BIGRE is a modified version of the TIGER design. It employs a second lenslet with a much shorter f-ratio than the first, that produces a demagnified focal plane image. This lenslet captures alot more of the diffracted

PSF from the first lenslet and therefore reduces the amount of cross talk. A schematic of the BIGRE lenslet design is shown in Figure 3.2. SPHERE the new planet finding instrument for the VLT includes a BIGRE type lenslet integral field spectrograph.

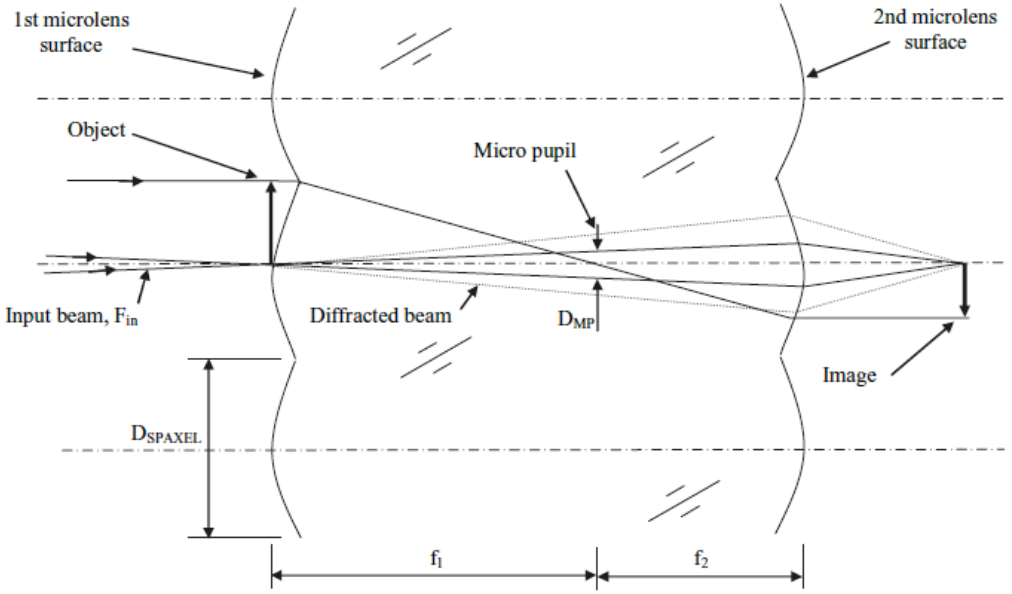

Figure 3.2: Schematic of the BIGRE concept from Antichi et al. (2009)

3.1.2 Slicer

Using a stack of long thin mirrors, each with a different tip and tilt angle, located in the focal plane of the telescope (the slicer stack) the two dimensional field of view is sliced up into a number of slitlets. Each of these slitlets is redirected to an array of corresponding mirrors which arranges the slitlets into the desired format, that of a pseudo-longslit, which can then be dispersed just as a single long slit would be. This method is shown graphically in Figures 3.3 & 3.4.

No high contrast instrumentation has been designed to date that includes a slicer based integral field spectrograph due to the worry that a one dimensional coherence persists along the length of a slice which could introduce modifications to the speckle noise that would be detrimental to high contrast imaging and spectroscopy. However, the slicer based design has been brought back to the attention of the instrument designers after a very impressive result by Thatte et al. (2007) on the SINFONI instrument (described in Chapter 7) even though the SINFONI instrument was never designed with high contrast applications in mind.

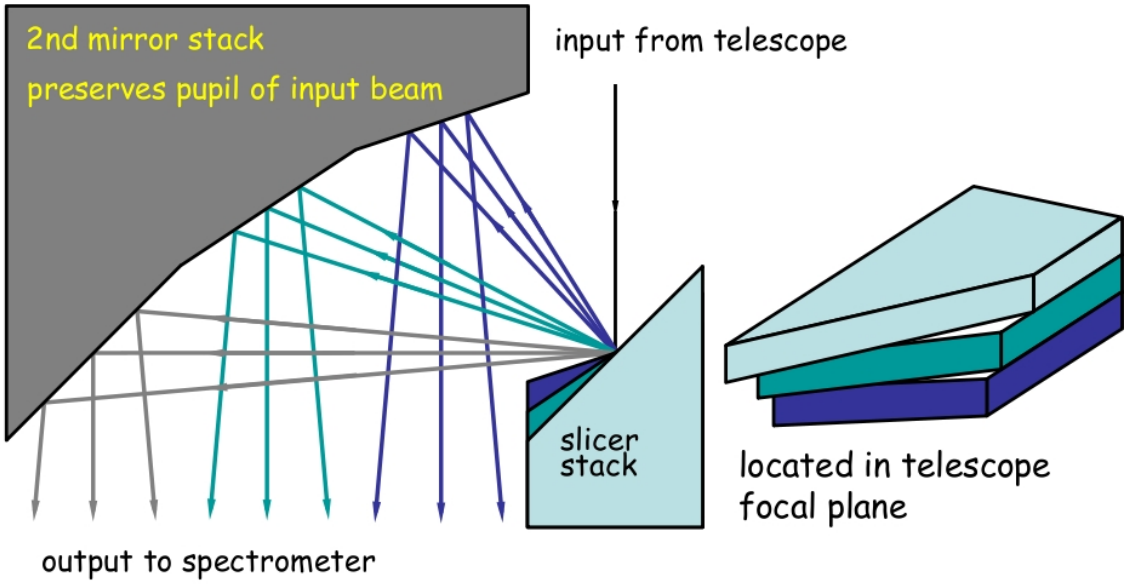

Figure 3.3: Principle of the image slicer integral field spectrograph. Courtesy of M. Tecza

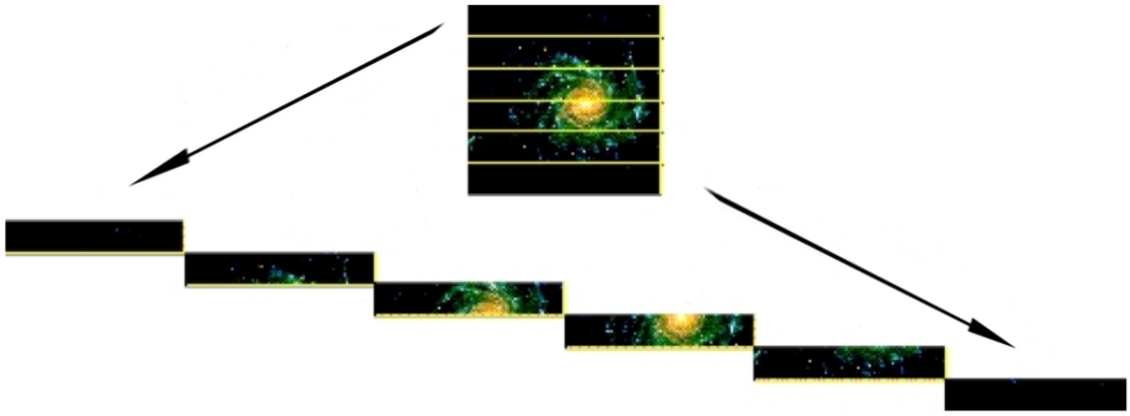

Figure 3.4: Creation of a psudo-long slit using a slicer based IFS. Courtesy of M. Tecza

3.2 Project 1640

†Project 1640 is a TIGER lenslet integral field spectrograph designed for high contrast observations at the Hale 200" telescope at Palomar Observatory, shown in Figure 3.5. The aim of the instrument is to measure low resolution spectroscopy of brown dwarfs and young Jupiter mass planets orbiting stars within 50pc of the Sun. The spectrograph provides imaging in 23 channels over the J and H bands (from $1.06 - 1.78\mu m$), therefore a spectral resolution of R=35-58. The TIGER lenslet array is made up of 200x200 microlenses each of which sample the telescope focal plane at 19.2 mas which gives critical sampling of the diffraction limited PSF at the shortest wavelength. The instrument boasts an apodized-pupil Lyot coronograph (shown in Figure 3.6) and the entire system sits behind the Palomar adaptive Optics system. The current AO system is PALAO that uses a 241-actuator mirror however an upgrade to the AO system is currently underway and the new PALM3K AO system will boast an additional 3388-actuator mirror. This will be the highest resolution AO corrector of its kind. Current performance of the PALAO system combined with the apodized pupil Lyot coronograph have shown contrasts being reached of $\sim 2 \times 10^{-4}$ at a separation of 1". However, the system was designed to take advantage of the ADI technique, described in Section 2.3.2, which has shown an additional factor of 10-20 improvement giving an achievable contrast of $\sim 2 \times 10^{-5}$, shown in Figure 3.7 .

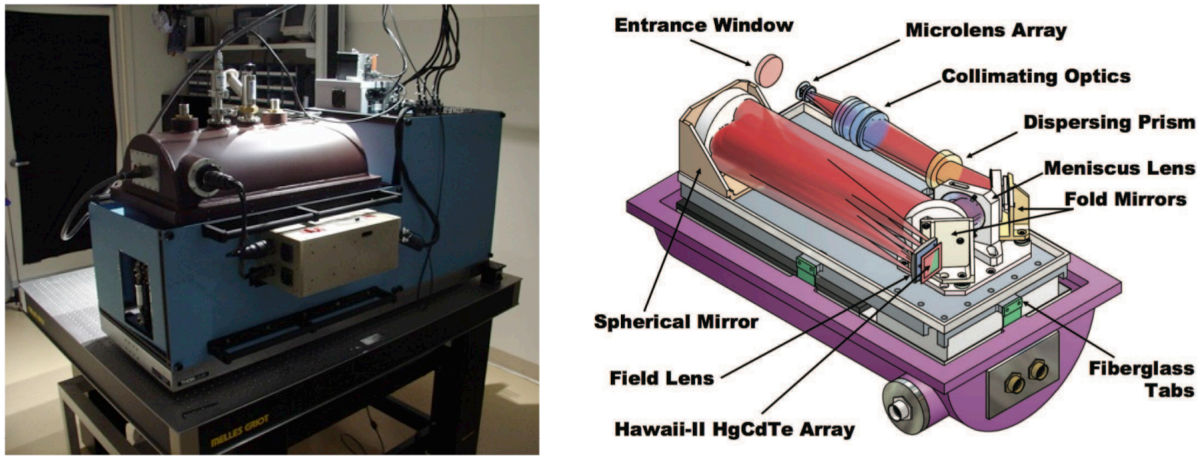

Figure 3.5: (left) Photograph of the P1640 instrument (Hinkley et al., 2008) (right) CAD drawing showing the layout of the instrument with the dewar lid and aluminium heat shield removed (Hinkley et al., 2009)

†In this section I have drawn on the work of Hinkley et al. (2009)

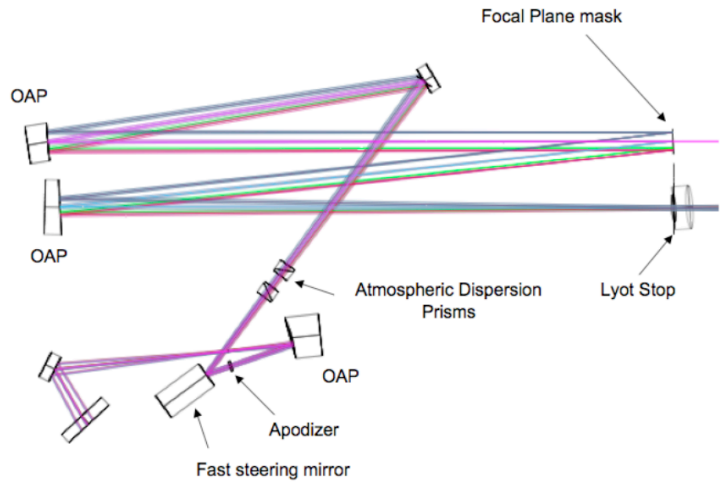

Figure 3.6: Layout of the apodized pupil Lyot coronograph (Hinkley et al., 2008)

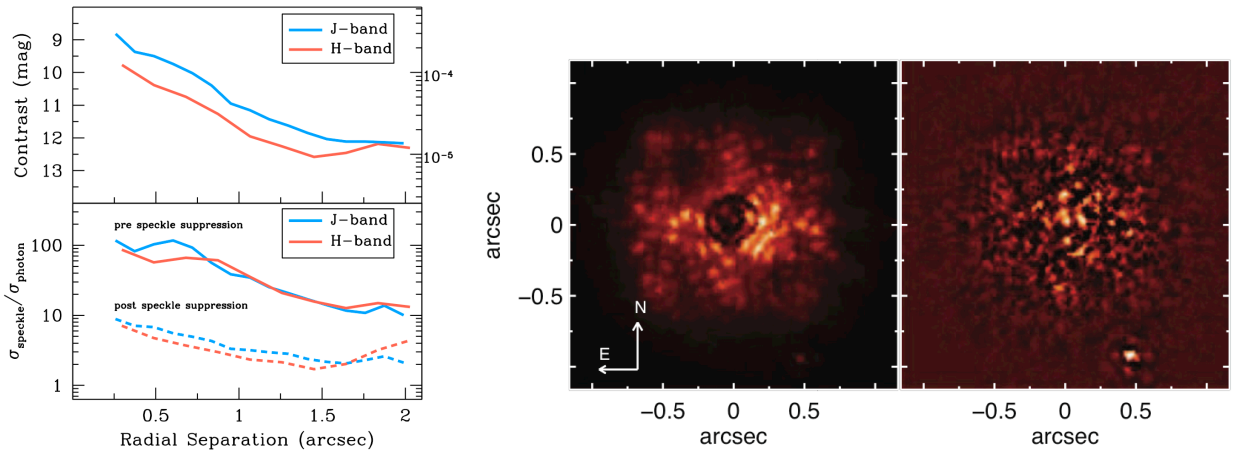

Figure 3.7: Contrasts achieved by Project1640: (left) Contrasts curves after application of ADI -top panel- and plot of the gain in sensitivity by applying the ADI method -bottom panel-. (right) Images illustrating the capabilities of Project 1640; Image before ADI -left- and after -right- of the star Alcor and its companion in the bottom right (Hinkley et al., 2009)

3.3 Gemini Planet Imager

‡The Gemini Planet Imager is the new instrument under construction for the Gemini South 8m telescope. It is again a TIGER based integral field spectrograph with a microlens array of 200x200 lenses. Each lens subtends an angle on the sky of 0.014" giving a total field of view of 2.8"x2.8". The spectrograph disperses with an average spectral resolution of ~ 45 over the Y,J,H and K bands $(1 - 2.4\mu m)$. The instrument combines

‡Details have been drawn from Macintosh et al. (2008)

a high order AO system and an apodized pupil Lyot coronograph much in the same way as Project 1640. However, GPI also has a high accuracy IR interferometer calibration system (CAL) that is able to measure the pre-coronographic wavefront and send this data back to the AO once a minute for correction. In this way GPI's requirement of 1nm RMS wavefront error at mid spatial frequencies is achievable. The instrument also includes a polarimetric mode whereby a the spectral prism is replaced by a Wollaston prism which serves to split the two orthogonal polarizations from each lenslet onto the detector. An optical schematic is shown in Figure 3.8 and a mechanical design of the instrument can be seen in Figure 3.9. The instrument is designed for imaging and spectroscopy of young $(100-1000M\text{yr})$ massive $(1-10M_J)$ self luminous planets with scientific requirements demanding a contrast of 10^{-7} and an inner working angle of 0.13". Figure 3.10 shows a simulation of the expected capabilities of GPI.

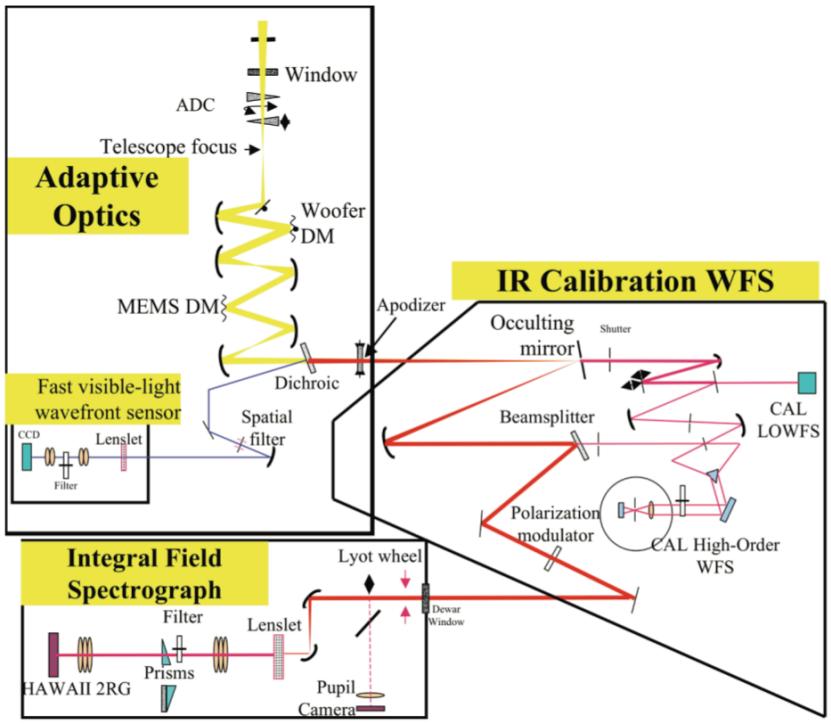

Figure 3.8: Schematic of the optical path through the Gemini Planet Imager (Macintosh et al., 2008)

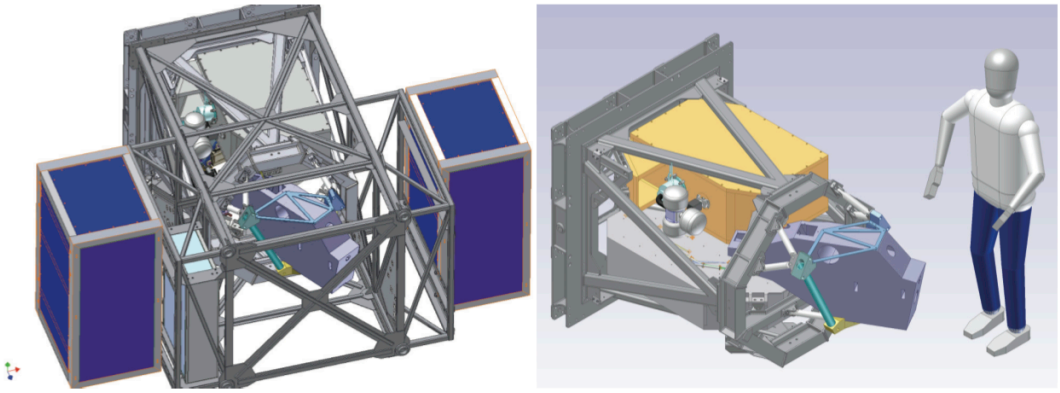

Figure 3.9: Mechanical design of the Gemini Planet Imager. Left: GPI with its covers removed, showing the external frame structure and electronics racks and the inner flexure sensitive structure. Right: Flexure sensitive structure with the optical subsystems. The IFS is the yellow dewar at top; the CAL interferometer is inside the blue box at right; the AO subsystem is mounted on the grey optical bench at bottom. The square plate on the left mounts to the Gemini Cassegrain instrument support structure. Taken from (Macintosh et al., 2008)

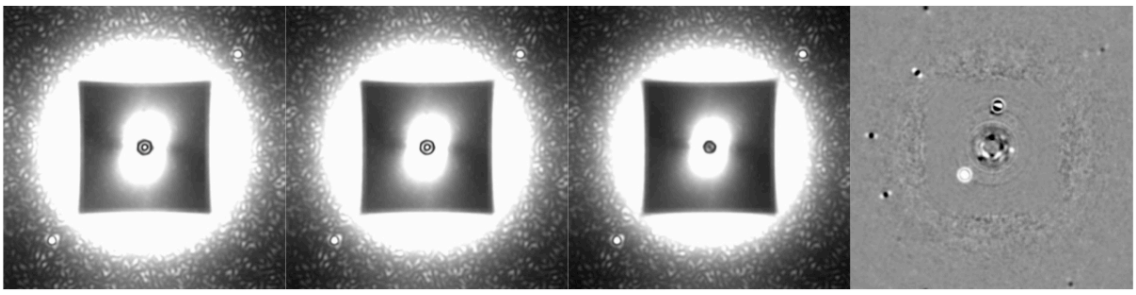

Figure 3.10: From Left to Right; Simulated 1-hour exposure GPI images at 1.48, 1.57, and 1.78μm and a simulated PSF after SDI processing with point sources added. This final image is shown with a linear gray scale between -5×10^{-7} and 5×10^{-7} of the PSF peak. Taking North to be up in the image; the object north of the star is a background object, the object located south-east of the star is a $4M_J$ with $T_{eff} = 580K$ planet and the object west of the star is a $1M_J$ with$T_{eff} = 330K$ planet. Dark spots outside the dark hole are dust artifacts. Taken from Macintosh et al. (2008)

3.4 SPHERE

[§]Spectro-Polarimetric High-contrast Exoplanet Research (SPHERE) is the new exoplanet detection instrument under construction for the VLT. Its top level goals include the ability to ; detect planets at a contrast of 10^{-6} at separations of 0.5", have access to angular separations of 0.1-3" from the host star, have optimal performance for targets upto 9th magnitude in the visible, have the ability to follow up detected objects with low resolution spectroscopy ($R \sim 30$) and have a sensitivity to extended sources down to a contrast of $\sim 10^{-7}$. In order to achieve these goals the instrument is made up of many sub-systems, see Figure 3.11. There is a differential imaging camera, IRDIS (InfraRed Dual Imaging Spectrometer), which works on the principle of SDI, see Section 2.3.1, a visible imaging polarimeter, ZIMPOL (Zurich Imaging Polarimeter) and a BIGRE design integral field spectrograph, IFS. All of these systems sit behind the SAXO adaptive optics system and visible and near-IR coronographic devices. ZIMPOL shares the visible path light with the wavefront sensor, the IFS covers the wavelength range $0.95 - 1.65\mu m$ over a 1.8"x1.8" field of view. With the IFS working up to the J band, the H band is then left to IRDIS which is able to perform SDI (the instrument can also perform low to medium resolution long slit spectroscopy). Multiplexing in this way optimises the observational efficiency of the instrument. The instrument will provide a suite of coronographs to chose from including a four quadrant phase mask, a classical Lyot coronograph and an apodized pupil Lyot coronograph. IRDIS is expected to achieve a 5σ contrast of 2×10^{-5} at 0.1" and 5×10^{-7} at 0.6". The 5σ contrast of the IFS is expected to be between $10^{-6} - 10^{-7}$ at 0.5". The expected performance of ZIMPOL depends on the polarisation of the planet being observed, however, simulations show that they are expected to reach close to the photon noise limit (Beuzit et al., 2008). At this limit they expect to be able to detect a 25% polarized Jupiter-sized planet at 0.3" from the host star with 5σ confidence and the same planet at 0.1" with $\sim 50\sigma$ confidence.

[§]Details have been drawn from Beuzit et al. (2008)

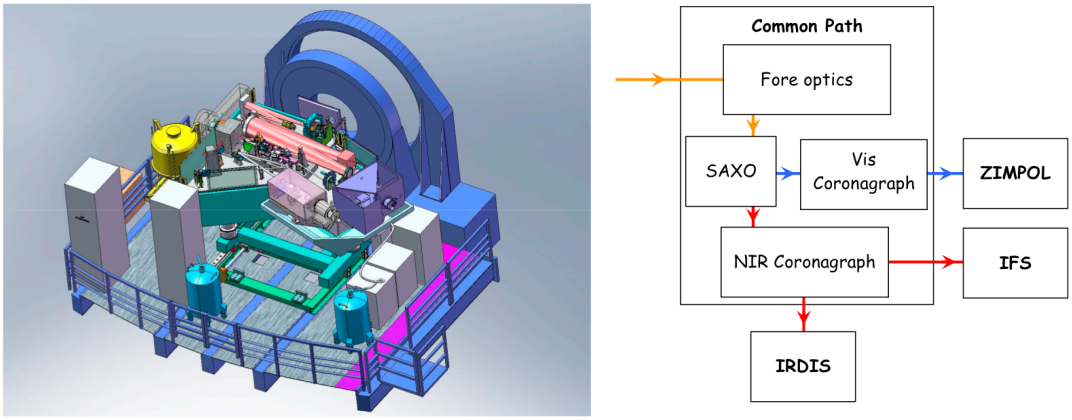

Figure 3.11: SPHERE: (left) a representation of SPHERE at the Nasmyth platform of the VLT, (right) Schematic of the optical path through SPHERE to each of its sub-systems, orange denotes common optical path, blue is visible and red is near-IR. (Beuzit et al., 2008)

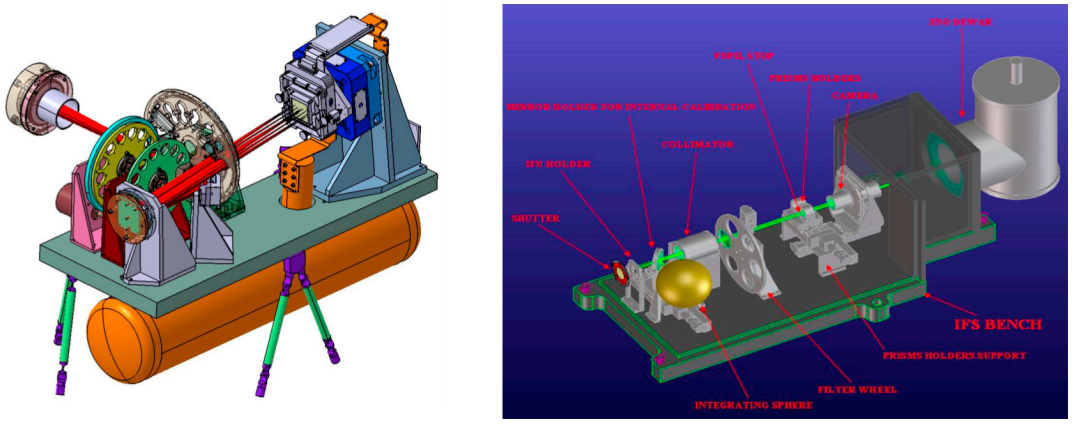

(a) (b)

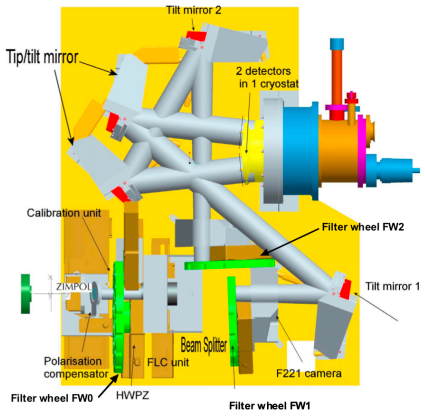

(c)

Figure 3.12: SPHERE sub-systems: (a) IRDIS, (b) IFS (c) ZIMPOL (Beuzit et al., 2008)

Chapter 4

EPICS and the Future of Planet Finding Instruments

*The main drive for the investigations into Slicer based integral field spectrographs that is described in this thesis, has been the PhaseA study for the Exo-Planet Imaging Camera and Spectrograph (EPICS) for the E-ELT (see Figure 4.1). In this Chapter details about the EPICS instrument and what it is being designed to achieve will be looked into.

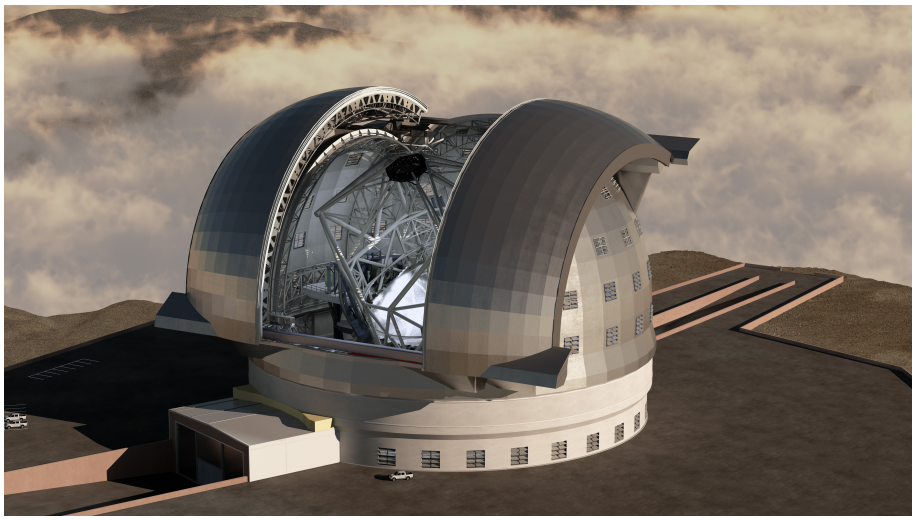

Figure 4.1: Rendering of the 42m E-ELT atop Cerro Armazones. Taken from eso.org

*Details and Figures in this Chapter have been drawn from the EPICS Phase A review documents; Salter et al. (2010a), Verinaud et al. (2010a), Verinaud et al. (2010b) ,Kasper & Gratton (2010) & Gratton et al. (2010) unless otherwise stated

4.1 Exo-Planet Imaging Camera and Spectrograph (EPICS) for the E-ELT

4.1.1 Science Goals

The Exo-Planet Imaging Camera and Spectrograph (EPICS) is an instrument being designed for the direct imaging and characterisation of extra-solar planets with the European Extremely Large Telescope (E-ELT). It has recently concluded its Phase A study and is being designed with the hope of becoming one of the first generation instruments of the E-ELT.

New instruments for the 8m class telescopes, SPHERE and GPI described in the previous Chapter, should allow detection of a few tens of planets (essentially Giant Planets) around a few of the closest young objects. While this would be by itself of great interest, the much higher sensitivity of EPICS will allow us to observe far fainter planets, that are both less massive and/or older as well as enabling us to explore with high sensitivity regions very close to the parent star. Figure 4.2 shows a comparative, predicted achievable contrast plot of the 8m class instruments and the contrasts achievable by the instruments being designed for the next generation of extremely large telescopes.

Even though the field of exoplanet detection and characterisation is expected to advance greatly in the time

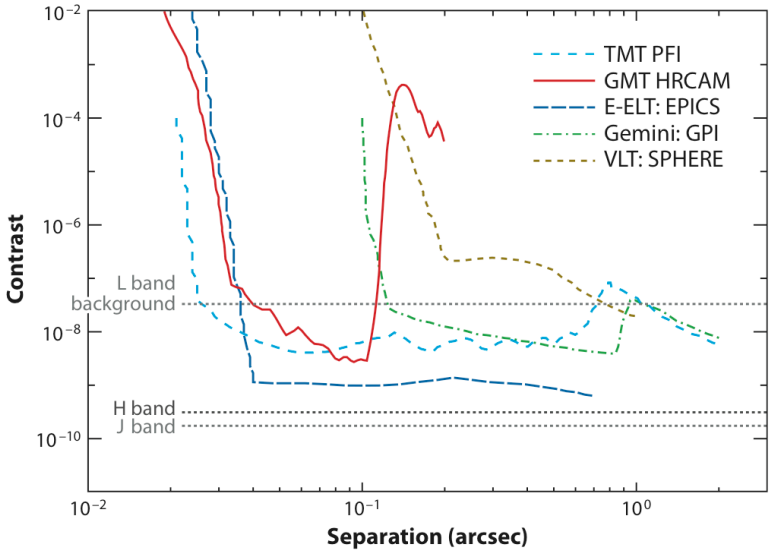

Figure 4.2: Comparison of the expected achievable contrasts and angular separations of the new (VLT-SPHERE and Gemini-GPI, described in Chapter 3) and next (E-ELT-EPICS, TMT- PFI & GMT-HRCAM) generation instruments. Dotted lines dictate the sky background for a one hour integration for the GMT on a Sun like star at 10pc. Taken from Seager & Deming (2010).

leading up to the completion of the EPICS instrument it is still foreseen that EPICS will be able to have a major impact on a few areas;

1. Detection of low-mass planets up to the habitable zone and giant planets beyond the ice-line.
2. Characterisation of Exoplanets down to rocky planets by direct imaging, spectroscopy and polarimetry.
3. Observation of very young planets ($\sim 10^7 yr$ or less) close to the ice line.
4. Intermediate and high resolution spectroscopy modes will provide the opportunity to turn quantitative studies provided by other instruments into direct physical insight.

The top level requirements of the EPICS instrument show an achievable contrast, for observations of a 5th magnitude star, of 2×10^{-9} at 30mas to 5×10^{-10} at 300mas, which will degrade (due to adpative optics efficiency) to contrasts of, 10^{-8} at 30mas and 10^{-9} at 300mas for a 7th magnitude star and 10^{-6} over the field of view for 9th magnitude stars. Figure 4.3 shows the simulated achievable contrasts of the two EPICS science instruments, described in the following section. Through the use of Monte Carlo simulations of a large sample of nearby stars a rough estimate of the planets we would be likely to detect with the instruments is shown in Figure 4.4. On top of this a high photometric and astrometric precision, of 0.05mag and $100\mu m$ respectively, must be achieved.

4.1.2 Concept

To achieve the contrast requirements stated in the previous section, excellent correction of the dynamic and quasi-static wavefront aberrations, introduced by the Earth's atmosphere and the telescope/instrument respectively, are needed;

- Dynamic wavefront aberrations produced by the atmosphere are corrected using a high order (or extreme) adaptive optics system (XAO) which will provide a very high correction bandwidth. The XAO system is estimated to produce a contrast of 10^{-5} at small angular separations up to better than 10^{-6} at the larger separations.

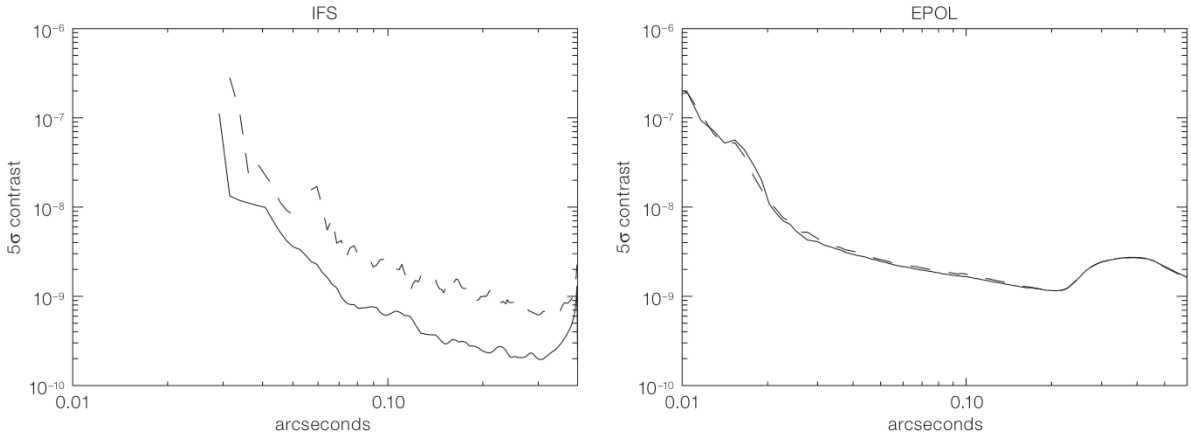

Figure 4.3: Expected achievable contrast of the two EPICS science instruments (left) IFS (right) EPOL from detailed simulations producing 2D contrast maps. Cuts in the x (solid line) and y (dashed line) are shown assuming a stellar magnitude of 2.3 and a 10hr exposure time including effect of field rotation. Differences in the x and y directions are due to diffraction effects caused by the spider arms holding the secondary mirror (Kasper & Beuzit, 2010).

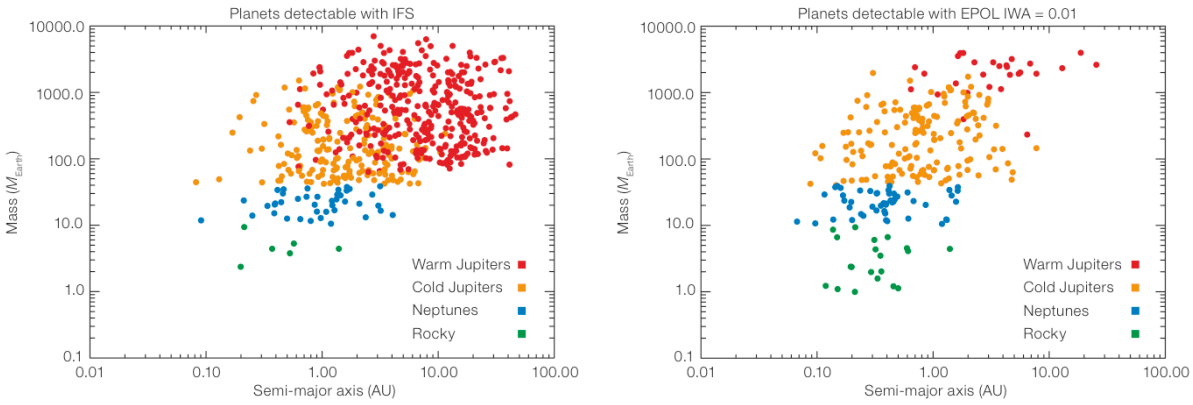

Figure 4.4: Expected planet detection rates of the two EPICS science instruments as calculated be Monte Carlo simulations of a large population of nearby stars.(Kasper & Beuzit, 2010)

- All moving optics such as the atmospheric dispersion compensators and optical de-rotators are placed in the common path before the XAO system such that EPICS will provide excellent temporal stability of instrumental aberrations.

- Non-common path optical aberrations are calibrated using focal plane wavefront sensing techniques (SCAO) that are offloaded back to the XAO system. Diffraction pattern suppression techniques will also be employed, as described in Section 4.2.1 and as a result EPICS will deliver a high quasi-static PSF contrast of better than 10^{-6}.

- This high contrast beam is then passed to two instruments, IFS and EPOL, where residuals are further calibrated and removed via instrumental and data analysis techniques such as spectral deconvolution and differential polarimetry respectively. These techniques will then provide the required contrasts of the order 10^{-8} at 30mas and better than 10^{-9} at larger separations. Note this is an upper limit on the speckle rejection factor needed by the instruments as the stated contrast achieved prior to them is quite a pessimistic case and we will also benefit from field vs pupil rotation allowing a greater contrast to be achieved via rotational smearing of the residuals.

The breakdown of EPICS into its subsystems is shown in Figures 4.5 & 4.6.

A rendering of the two EPICS science instruments is shown in Figure 4.7.

EPOL is the coronagraphic imaging polarimeter in EPICS. It is being designed for the visible wavelength range (600-900nm) with a 2"x2" field of view sampled with 1.5mas spaxels (Nyquist sampled at the minimum wavelength).EPOL removes differential aberrations by simultaneously observing both polarization states from each of the polarization modulation phases.

The top level requirements of the IFS are that it should have a field of view greater than 0.79" x 0.79" that is Nyquist sampled at the minimum wavelength (2.33mas pixel scale). It should cover the wavelength range of $0.95\mu m - 1.65\mu m$ and should provide 3 grades of 2 pixel spectral resolutions; low R$\sim$ 100, medium 1500 < R < 4000 and high R$\sim$ 20000. The efficiency of the IFS must also exceed 55%.

The lower number of photons available for EPOL when compared to the IFS (due to smaller spectral bandwidth and the dependance on the polarization of the planet) as well as the increase in AO residuals at visible wavelengths results in a lowered sensitivity of EPOL over the IFS. The shorter wavelength and the efficient

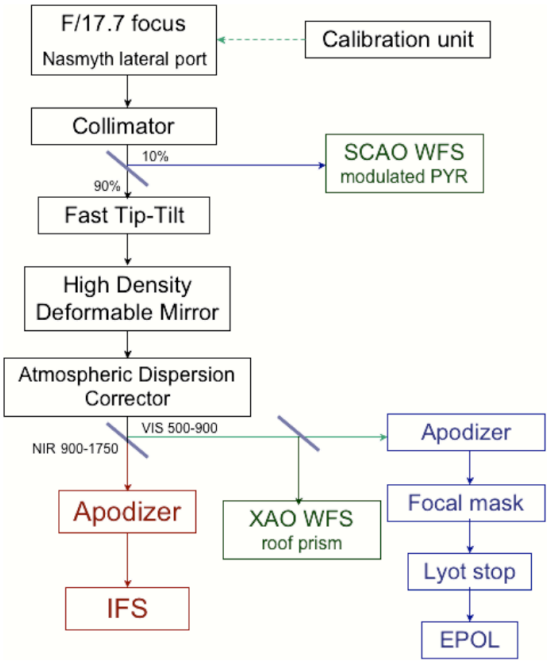

Figure 4.5: Box diagram of the EPICS subsystems

apodized Lyot coronagraph, however, serve to allow EPOL to achieve high contrasts at the smallest angular separations ($\sim 10mas$).

The predicted contrasts and possible detections for the two instruments are shown in Figures 4.3 & 4.4.

4.1.3 IFS Design study

The baseline for the instrument has been to use a BIGRE type IFS design. The choice of the BIGRE for EPICS IFS concept is not based on a complete trade-off analysis. The main reasons of this choice were;

- The experience gained from SPHERE development (also a BIGRE type IFS), see Section 3.4.
- The more advanced opto-mechanical design of BIGRE at this stage of the study.

Nevertheless, the SLICER concept has several advantages;

- potentially offers a larger field of view
- can provide a higher spectral resolution still in an integral field mode (not possible for a BIGRE design)

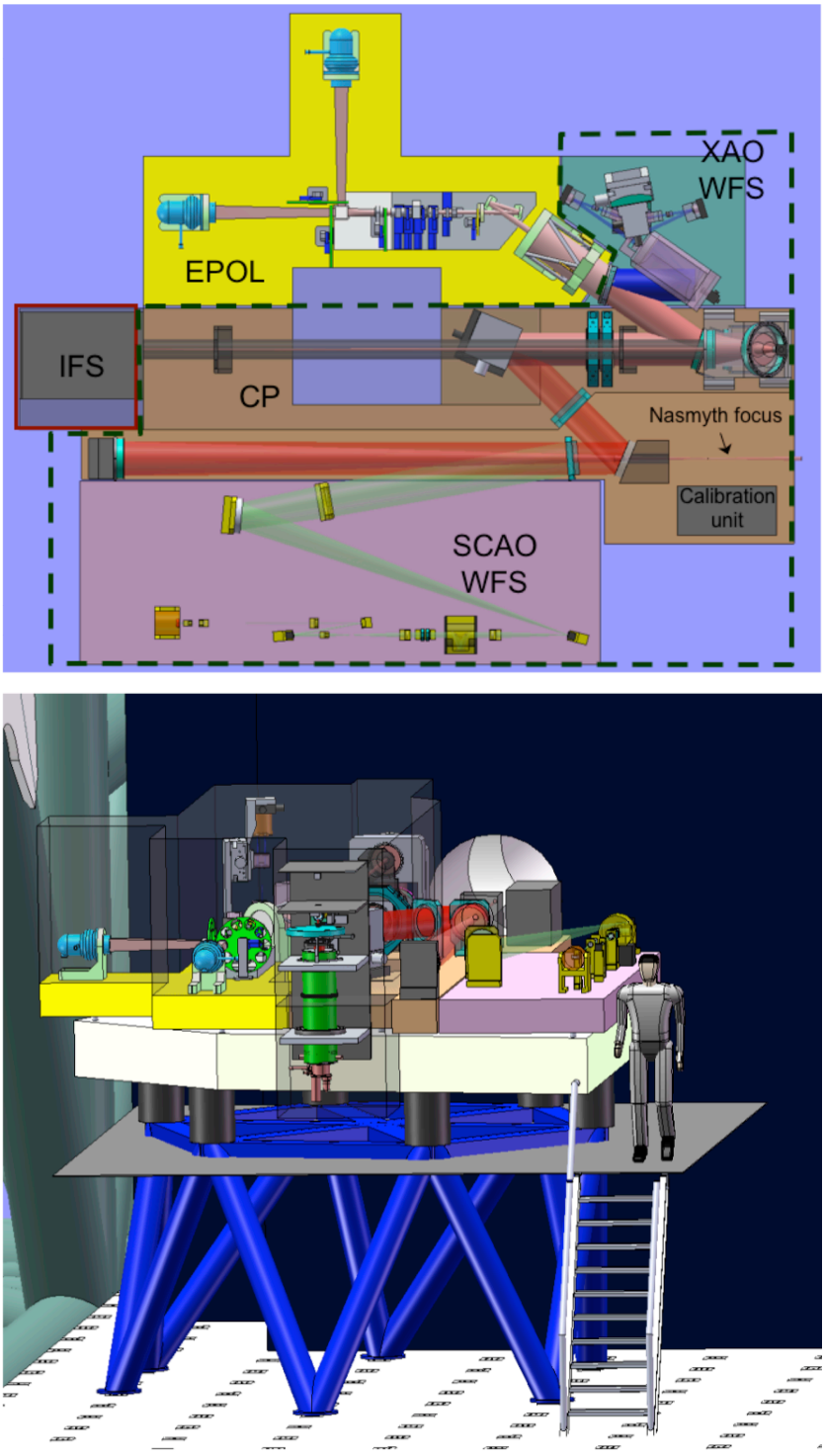

Figure 4.6: The EPICS concept: (top) schematic view of the EPICS instrument with subsystems labelled, (bottom) 3D representation of the EPICS instrument at the lateral focal station of the E-ELT

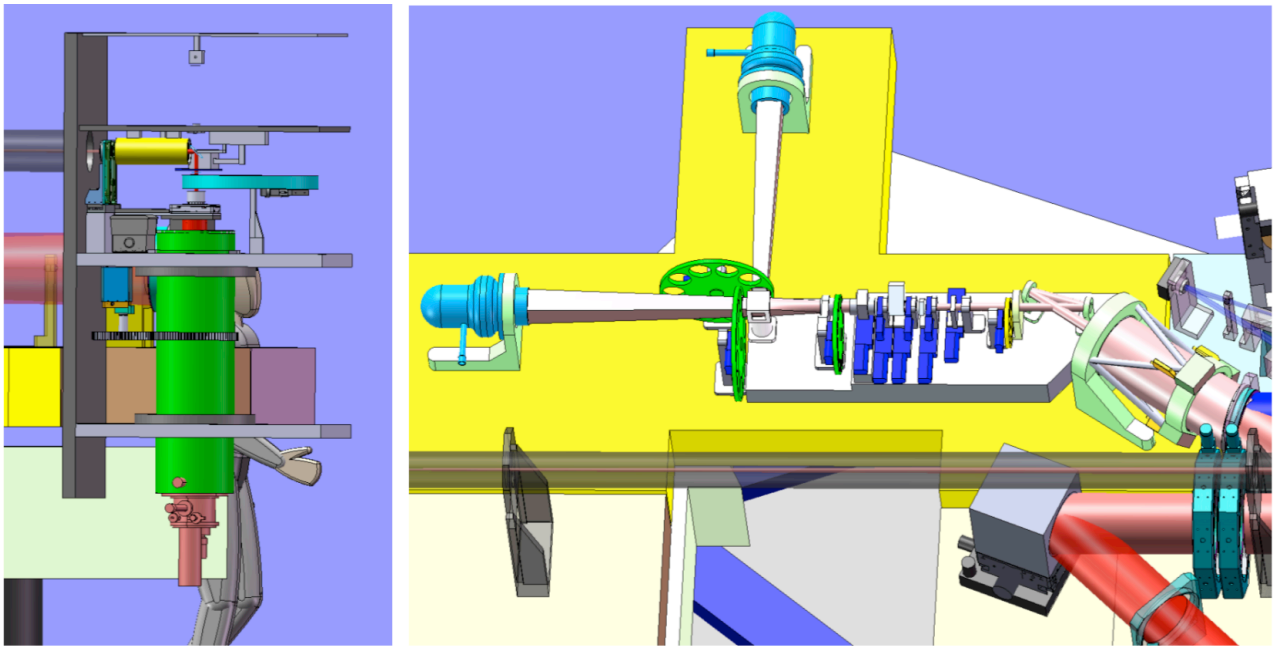

Figure 4.7: Rendering of the EPICS science instruments; (left) IFS (right)EPOL

- spectra can be packed closer together on the detector providing a better detector fill factor
- slicer based design provides a higher efficiency than the BIGRE design.

As has been mentioned the current generation of IFS instruments for high contrast applications (SPHERE and GPI) have not chosen a slicer based IFS in their designs. We will now look at why that has been the case and why it was decided that slicer based integral field spectrographs should be re-investigated for the EPICS design;

Potential Limitations of Slicer Based IFS

As part of the design study for the Planet Finder instrument for the VLT (the precursor study to SPHERE), an analysis of the post coronagraphic non common path (differential) WFE was carried out for an SDI instrument. The detailed results of the analysis are presented in Mouillet & Beuzit (2004), which came to the conclusion that the two channels of an SDI instrument needed to have differential WFE no larger than 10 nm rms, with 2 nm rms being quoted as the desirable number (their result is shown in Figure 4.8). In Dohlen & Beuzit (2004), the impact of the non common path WFE was analysed, leading to a decision to not propose

an IFS as part of the VLT PF instrument. The arguments put forward in the system analysis report (Dohlen & Beuzit (2004) on page 22) are reproduced below for convenience;

"2.3.5 Why the IFS is not proposed

An important system-level decision made towards the end of the phase A study was that of not finally proposing the Slicer IFS for the baseline instrument. Further analysis and a deeper comprehension of the problems involved, in particular with respect to dual-band imaging, has led us to realize that the differential aberrations advantage is not valid, at least not across the entire FOV.

Dual band imaging relies upon measurement of the stellar surroundings (planet plus speckle pattern produced by residual atmospheric turbulence and fixed instrumental aberrations) at two different wavelengths, one of which corresponds to an absorption feature in the expected planetary spectrum. Subtraction of the two images is shown to yield the required speckle reduction when differential aberrations between the two wavelength bands are sufficiently low (∼2nm rms). For IRDIS, which is expected to achieve 10nm rms differential aberrations, a technique referred to as double difference, involving a second star, must be employed to achieve the goal speckle reduction. The slicer IFS was thought to give essentially zero differential aberrations, hence avoiding the use of a second star.

In fact, the slicer IFS has virtually zero differential aberrations between two nearby spectral channels of the same pixel (i.e. the same slice) because the photons follow nearly identical optical paths through the instrument. However, since the spatial scale of the residual speckle pattern varies with wavelength, the images to be subtracted must be scaled, and so spectral information from one slice must be compared with information from a different slice. Differential aberration performance at a level significantly below that of more classical dual band imaging is then no longer guaranteed by design, and achievement of the required 2nm performance is unlikely.

2.3.6 What we do propose

The phase A conclusion is therefore to remove the IFS option in its present form from the instrument baseline"

Essentially the worry is that the differential wavefront error going from slice to slice is not naively guaranteed by design to be low. An additional worry to this is the fact that one dimensional coherence is preserved along each slice which allows the possibility of secondary speckles to be produced via the light contained

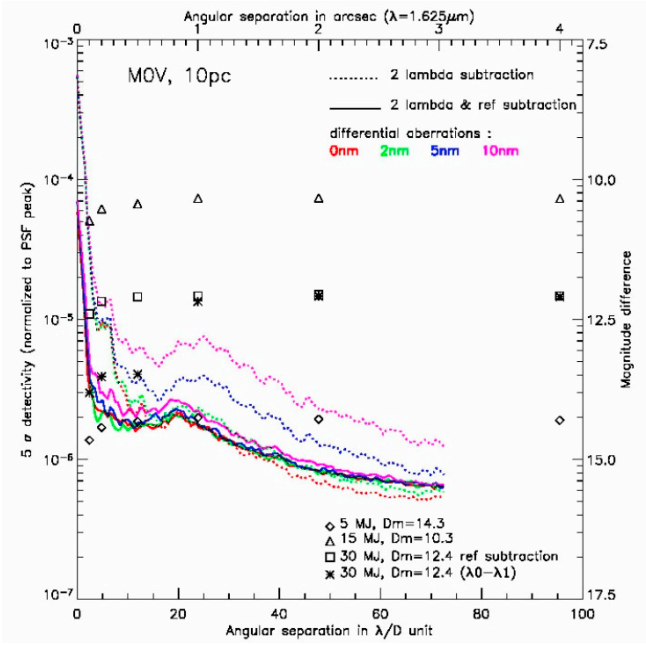

Figure 4.8: Results from the planet finder study showing that a differential wavefront error of ∼2nm is needed between spectral channels. (page48 Mouillet & Beuzit (2004)).

within the slice interfering coherently with itself. This would produce new speckles that would not behave in the characteristic way, i.e. their separation from the primary star would not be directly proportional to wavelength.

Re-analysis of a slicer based IFS

As part of the EPICS phase A study, it was decided to re-analyse the potential limitations of a slicer based IFS mentioned above, for a variety of reasons.

1. The on-sky high contrast imaging performance obtained by Thatte et al. (2007) using the VLT SINFONI instrument (for which no specification was placed on the slicer or spectrograph in terms of differential WFE) showed that a slicer based instrument can be successfully used in high contrast applications, and can achieve a performance comparable with that achieved by current on-sky SDI systems (discussed in Section 7.2). These results speak against a fundamental limitation to contrast arising from the slicer technology.

2. The conclusions of the VLTPF feasibility study reports were based on an extrapolation of the per-

formance requirements for an SDI instrument to an image slicer based IFS. No actual simulation of an image slicer based IFS was carried out. Although such a simulation is quite complex to carry out correctly, it was felt that an IFS specific analysis of potential contrast limitations should be carried out before making any design decisions for EPICS, given the multiple advantages of slicer based systems over competing IFS technologies, as described previously.

3. An image slicer IFS samples the post-coronagraphic focal plane only in one dimension (across slices), while within each slice (along a slice) the light proceeds coherently through the slicer and spectrograph and is sampled only at the final detector plane. Although this leads to the potential problem that the instrument performance between slices could vary considerably, leading to a modification of the post-coronagraphic speckle pattern, in actual fact the PSF of the spectrograph is very tightly controlled, dictated by the need to produce a clean image of each slit at the detector, so as to retain the designed spectral resolution. Thus, a detailed analysis of an actual slicer IFS design should be carried out before any reasonable conclusions can be drawn regarding contrast performance.

4. Even if the slicer IFS and spectrograph do modify the speckle pattern in some way, the etendue of the spectrograph is necessarily larger than that of the incoming light by a factor of at least 3-5, so as to correctly account for the diffraction effects at the slicer. Thus, it may very well be possible to disentangle effects to the speckle pattern arising prior to the IFS from those arising within the IFS, thus leading to a suitable algorithm that may be used to eliminate the (additional) speckles created by the IFS, if indeed this is the case.

For these reasons, and others, it was decided to carry out a detailed analysis of a slicer based IFS to determine if the technology posed any limitations to the achievable contrast in high contrast applications. This is the topic of this thesis.

Proposed Course of Action

While most of the questions raised about technology limitations to the contrast achieved by a slicer based IFS could be answered through carrying out appropriate simulations, it was already clear at the start of the EPICS Phase A study that any such simulation would be quite complex, and due to limitations inherent in the

simulations themselves, the conclusions drawn from the simulations would have limited applicability. Thus, it was decided to take a two pronged approach, involving both simulations and actual laboratory measurements. On the one hand, the simulations could try to address many critical issues, such as the dependence of ultimate achieved contrast on the choice of spectral resolution, or spaxel size and the characteristics of secondary speckles as could be produced by a simulated wavefront error in the pupil plane. On the other hand, effects such as scattered light, Fresnel diffraction, or non-pupil-plane wavefront errors, which could not be well simulated, would be measured with a test set-up in the laboratory. The simulations are detailed in Chapter 5 and the laboratory tests are described in Chapter 6. These tests are crucial, as no image slicer based IFS coupled with a high contrast AO system has been implemented in an instrument to date, thus, no experimental data of the on-sky performance are available. As described previously, in the EPICS IFS accessible FOV (30-mas to 400-mas angular separation) the systematic speckles halo level will be at a contrast of about 10^{-6} to 10^{-7}. In order to attain a 5-sigma level of residuals imposed by the top level requirements (10^{-8} to 10^{-9}) the speckle rejection must be in the range 100 to 1000 (with the factor of 1000 assuming a very pessimistic performance of the EPICs instrument up to the IFS). It is this level of speckle rejection that was to be investigated by the laboratory experiments.

4.2 Additional Problems that Future Instruments Need to Address

In this section we are going to address some of the factors that have been of lesser importance for designs of the current generation of planet finding instruments but that are crucial if the contrasts suggested by the planet finders for the ELTs are to be achieved;

4.2.1 Chromaticity of Speckles

The power of the spectral deconvolution method, described in Section 2.3.3, has been noticed by the direct detection community. Thus the next generation of planet finding instruments are being designed with application of spectral deconvolution in mind, which means ensuring the optical beam passing through the system stays as achromatic as possible. This is essential as any chromatic effect of the speckles will result in noise on its fit and, therefore, a limit to the achievable contrast. The main contributors to this speckle chromaticism are the coronagraph and Fresnel diffraction throughout the system;

Coronagraph

Almost all coronagraphs are tuned to specific wavelengths meaning they are chromatic. Simulations performed by the EPICS consortium proved that this inherent chromaticity is large enough to limit the achievable contrast via spectral deconvolution to something higher than the top level requirements of the instrument. Instead, it was therefore decided by the consortium that an apodized pupil should be used to suppress the diffraction wings of the PSF and no focal plane mask should be implemented. Instead a mask should be placed on the integral field spectrograph itself at the point of sampling. In the case of a BIGRE design this would mean blanking out a few of the lenslets and for the slicer design a few of the slices. This ensures that the core of the PSF is rejected and that the instrument also guarantees a very achromatic diffraction rejection. The design of the apodized solution can be seen in Figure 4.9. Initial tests with the apodizer have shown a 2 orders of magnitude rejection of the airy rings for angular separations greater than 30mas.

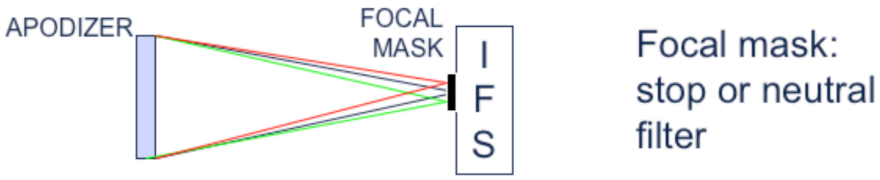

Figure 4.9: Schematic of the apodizer solution for EPICS.

Fresnel Diffraction

Future instruments designed to take advantage of the speckle pattern's characteristic positional wavelength dependance by applying spectral deconvolution, must take into consideration the chromatic effects of Fresnel diffraction when designing the optical system.

The following description shows that, even if all optical elements in a system are fully achromatic, there is no guarantee that the optical beam relayed by the optics will remain achromatic;

Figure 4.10 depicts graphically what happens when a beam, constant over the aperture on the left, is aberrated by one Fourier component (sine wave) with a small wave front error amplitude. The right hand side of the image shows that Fraunhofer diffraction dictates at infinity and we see a main bright component in

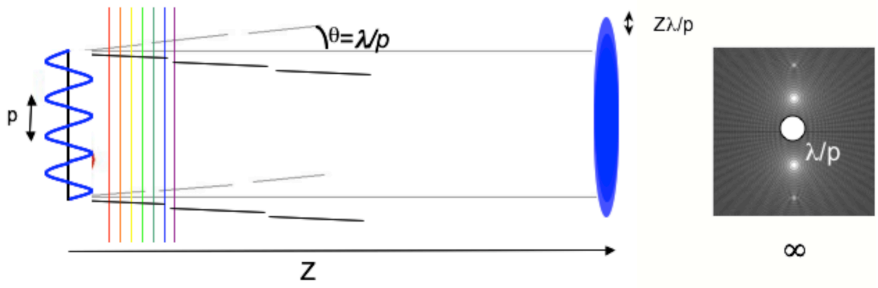

Figure 4.10: Fresnel Diffraction, explained in the text. From Verinaud et al. (2010a)

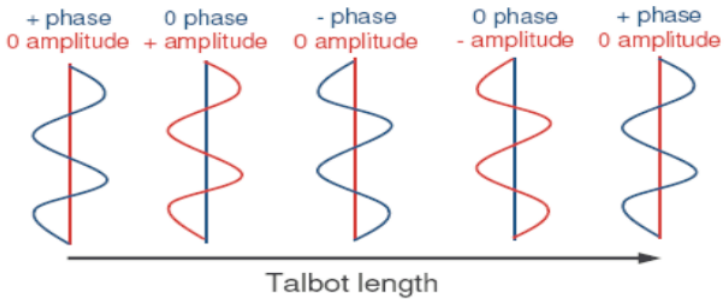

Figure 4.11: The Talbot effect: mixing between phase and amplitude, From Macintosh et al. (2008)

the center and 2 speckles on each side, separated from the centre by a distance λ/p where p is the period of the original wave front error aberration. Each component of the PSF at infinity can be considered to be a collimated beam that has propagated from its origin (left) to the screen at infinity with a given angle. The central component is very bright and on axis, the other 2 components are faint and have the angles $\pm\lambda/p$. At a distance, z, from the original aperture the footprints corresponding to each component are displaced from each other by a distance $z\lambda/p$. From this we can see that the displacement, and the angle with which the components of the beam reach the plane at z will depend on wavelength.

Furthermore, the pure phase aberration introduced in Figure 4.10 can become a pure amplitude aberration at a different position along the optical axis, and back to pure phase observation, see Figure 4.11. This is called the Talbot effect, and the period of the oscillation is the Talbot length $L_\tau = 2p^2/\lambda$. Note that this too is wavelength dependant. The point to take away is that these effects are both wavelength and spatial period dependant and can result in an added phase error's components in amplitude and phase becoming highly chromatic. For us this means an added chromaticism of the speckles that would be detrimental to the

spectral deconvolution method.

To avoid such effects there are two options;

- Use an optical design whereby optical elements are as close as possible to a pupil conjugate.
- Use optics that have extremely low wave front error and cleanliness.

4.2.2 SNR of Data

The role of the IFS is to produce a very high signal-to-noise spectrum of the light falling in each spaxel. The response for each spaxel must be calibrated to a very high precision to avoid a differential response, as this would then become the limiting factor. This means errors, such as interpolation errors, need to be meticulously calculated and carried through each step of the data reduction. With such high rejection factors of the speckles needed, the flat field and dark calibration data have to be extremely accurate to avoid limiting the achievable contrast.

As described in Section 2.1 speckle noise is correlated and adds coherently, therefore if we are trying to accurately measure the speckles in order to remove them, the noise associated with the speckle signal could be the limiting factor for the spectral devonvolution method. Just as any other correlated signal, there is photon noise associated with the speckle signal. Following is a brief calculation of the exposure time that would be needed to provide a SNR of the speckles high enough for them to be rejected to the level of 10^9 by the EPICS instrument;

Taking Vega as our source to begin with, we know that the number of photons arriving to us in the J-band;

$N_\gamma \approx 2 \times 10^6 \gamma s^{-1} m^{-2} \text{Å}^{-1}$ (Cox & Pilachowski, 2000).

Considering the 42m E-ELT as our telescope (ignoring obscuration by the secondary and supporting structure) we calculate the number of collected photons;

$N_\gamma \times \frac{42^2 \pi}{4} = 2.8 \times 10^9 \gamma s^{-1} \text{Å}^{-1}$

Assuming a 30% efficiency of the telescope and instrument as a whole and that the EPICS adaptive optics system and apodizer will deliver a contrast of 10^6 (under-estimate);

$8x10^2 \gamma s^{-1} \text{Å}^{-1}$ photons per second per angstrom at the detector.

With a spectral resolution of R=100 at a wavelength of $1 \mu m$ we have 10Å wide channels which gives;

$8000 \gamma s^{-1}$ photons per second per wavelength channel.

Now assuming we are observing a 6th magnitude star (i.e. $10^{-6/2.5}$ Vega intensity);

Speckle intensity per second$\sim 32\gamma s^{-1}$

We now need to reject speckles by a factor of 1000 to get to a contrast of 10^9. Assuming the noise on the speckle is purely photon noise we have the requirement;

$SNR_{Speckle} = \frac{S_\gamma}{\sqrt{S_\gamma}} = \sqrt{S_\gamma} \geq 10^3$ where S_γ is the total number of speckle photons collected

$\therefore S_\gamma = 10^6\gamma$

This mean the integration time needed to have speckles with a signal to noise ratio of 1 in 1000 for a 6th magnitude star using EPICS on the E-ELT is; $T_S(6mag) \sim 8.7hrs$ A table of a range of magnitudes and equivalent calculations for a rejection factor of 100 is shown in Table 4.1.

	Speckle Rejection Factor	
Stellar Magnitude	100	1000
0	1sec	2min
2	8sec	13min
4	50sec	1.4hrs
6	5min	8.7hrs
8	33min	55hrs
10	3.5hrs	347hrs

Table 4.1: Table of integration times needed for a speckle rejection factor of 100 and 1000 when observing stars ranging from 0th to 10th magnitude using EPICS on the E-ELT (assuming a modest rejection factor of 10^6 from the instrument)

This is a problem due to the limited life time of a speckle, as described in Section 2.1. We may integrate for the amount of time required but the speckle may not exist long enough for us to get a measurement with a high enough SNR.

If instead we assume all of our speckles last for 20 minutes (optimistic!) we can back track to find out what the achievable contrast would be, using the same assumptions as before, results can be seen in Table 4.2. To summarise, the speckle pattern is only stable for ∼10-20 minutes (see Section 2.1), and so over hundreds of exposures, they will be randomly distributed. Therefore, the degree to which spectral deconvolution can reject them will establish the noise floor for the planet detection. This is a problem due to the limited life time of the speckles; We may integrate for the amount of time required to theoretically detect a given planet but the speckles observed may not exist long enough for us to get a measurement with a high enough SNR.

Therefore, it may not be the type of IFS design that limits the speckle rejection factor but rather the photon noise of the speckles themselves.

	XAO & Apodizer Performance			
	10^6		10^7	
Stellar Magnitude	Speckle Rejection	Contrast	Speckle Rejection	Contrast
0	3100	3×10^9	980	1×10^{10}
2	1200	1×10^9	400	4×10^9
4	500	5×10^8	150	1.5×10^9
6	200	2×10^8	60	6×10^8
8	80	8×10^7	25	2.5×10^8
10	30	3×10^7	10	1×10^8

Table 4.2: Table of maximum theoretical speckle rejection factor and hence achievable contrast for a range of stellar magnitudes and a combined XAO+apodizer performance of 10^6 & 10^7. Assumptions; all speckles have a lifetime of 20min which is also the integration time, achievable speckle rejection is determined by photon noise on the speckle

Chapter 5

Simulations of Slicer Based Integral Field Spectrographs in the High Contrast Regime

In this chapter simulations of how a slicer based integral field spectrograph modifies the speckle pattern and the effectiveness of the spectral deconvolution method are described. The way these simulations are carried out means that there are no inaccuracies introduced from the reconstruction of the datacube, this is not the case in real life due to the limited accuracy of the interpolations required for the reconstruction. Interpolation accuracy can also be the limiting factor of the effectiveness of the spectral deconvolution method. For these reasons, we first investigate the accuracies of the interpolations required.

5.1 Interpolation accuracy

*Interpolations are a necessity in both the reduction of data from an integral field spectrograph into a data cube and in the post processing methods needed for removeal of speckles (in our case for spectral deconvolution). Here I present a description of the advanced methods of interpolation undertaken to reduce errors as well as the limits the methods faced.

*In the following section I have drawn upon the work of Marois (2004) where the implementation of Fourier techniques for image scaling and translating have been investigated for use with SDI, see Section 2.3.1.

5.1.1 Interpolations for creating a Datacube

When producing the data cube from the output frames of the detector one must be wary of the interpolations used to reduce the data. Errors get added every time the data is interpolated and thus the number of interpolations should be kept to a minimum to avoid too much degradation of the data. The type of interpolation method used can also have just as much impact as the number of interpolations to be performed. I make reference here to the work of Ryan Houghton (*in private communication*) who has performed simulations to show the affects of single and multiple interpolations when using IRAF for the reconstruction of datacubes from IFSs. His plots, shown in Figure 5.1, clearly show the degradation of the data as multiple interpolations are performed and the preference for interpolating with IRAFs bicubic spline algorithm over the bilinear fitting. It was for this reason that care was taken to select the best interpolation method and reduce the number of interpolations made when creating data cubes from the slicer experiments detailed in Chapter 6, where the IRAF package was also used for the data cube creation.

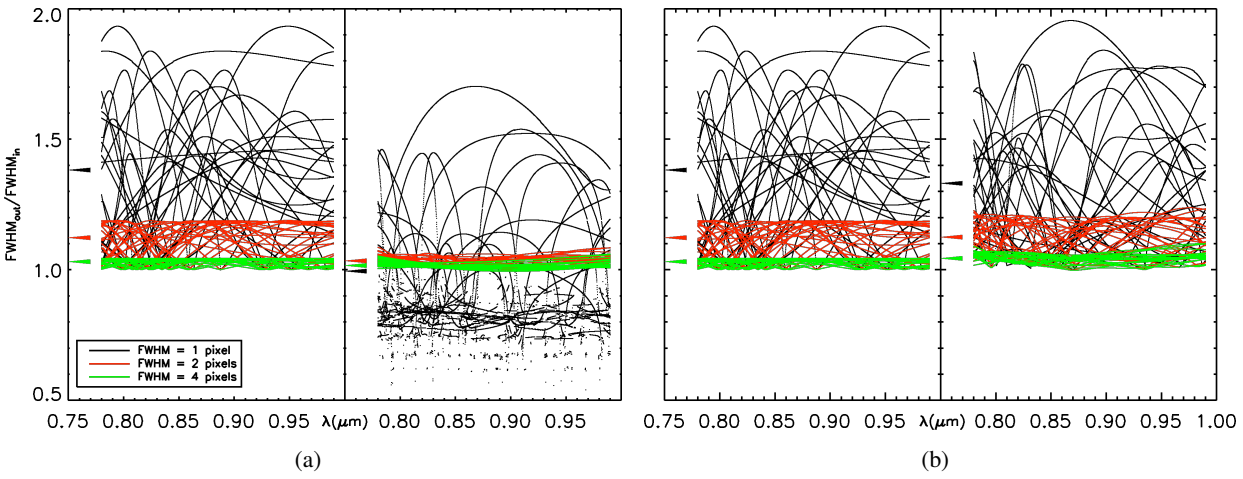

(a) (b)

Figure 5.1: Degradation of data through interpolation type and the use of multiple interpolations. Multiple realisations of values for the ratio of the FWHM after interpolation to the FWHM of the input PSF are plotted for the input cases of 1,2 and 4 pixels per FWHM (2 pixels representing the Nyquist sampled case). The left hand plot of both (a) and (b) show the results after the input is interpolated 3 times right hand plots show shows the results after having combined the 3 steps into just a single interpolation. (a) : Results using IRAFs bicubic spline fitting algorithm. (b) : Results using IRAFs bilinear fitting algorithm. From these plots, when having to use multiple interpolations it would seem that the type of interpolation would not play much of a role, however, you can clearly see the benefit from using a single interpolation in the case of the IRAF bicubic spline algorithm. Images are courtesy of Ryan Houghton (*private communication*)

5.1.2 Interpolations with Fourier Transforms

Any method of interpolation of an image with limited sampling will undoubtedly propagate additional noise and when working in such high contrast regimes this noise is a worry. For example a Nyquist sampled PSF contains very sharp changes from pixel to pixel that regular interpolation methods would find hard to fit accurately. It should, however, be possible for the Fourier transform of a Nyquist sampled image to retain all of the information contained within it thus allowing a far more accurate result. The use of Fourier transform interpolations can be applied easily enough for the scaling and translating of images, which is needed for the application of spectral deconvolution, however, the prospect of using this method for the creation of the data cubes themselves has not been investigated here as the interpolations needed here are generally not as simple as an overall scaling or shift.

Results from an investigation into the performance of Fourier methods for the scaling of images, performed by Marois (2004), is shown in Figure 5.2. The method followed was to generate two images of a Nyquist sampled PSF at different scales. One is scaled via various methods and subtracted from the other. The residuals are then convolved with a 2 pixel (ie. λ/D) per FWHM Gaussian function to remove interpolation noise at spatial frequencies smaller than that of the PSF. The noise attenuation factor, $\Delta N/N$, is then calculated as the median over an annulus of the ratio of the absolute value of the intensity in the difference image to its absolute value in the original image for each pixel. The results show that the Fourier technique of scaling provides the best accuracy within $30\lambda/D$ at which point its performance is similar to that of the IRAF 2D sinc algorithm.

The scaling of each wavelength slice is performed through Fourier transforms by adding the correct amount of zeropadding in the image and in Fourier space. By changing the amount of zeropadding in the Fourier transform of the image, as compared to the zeropadding in the image itself, we are changing the ratio of the optical transfer function dimension to the PSF cutoff frequency. In doing this we are not affecting the frequency information of the focal plane but we are changing the sampling of the frequencies in the image plane.

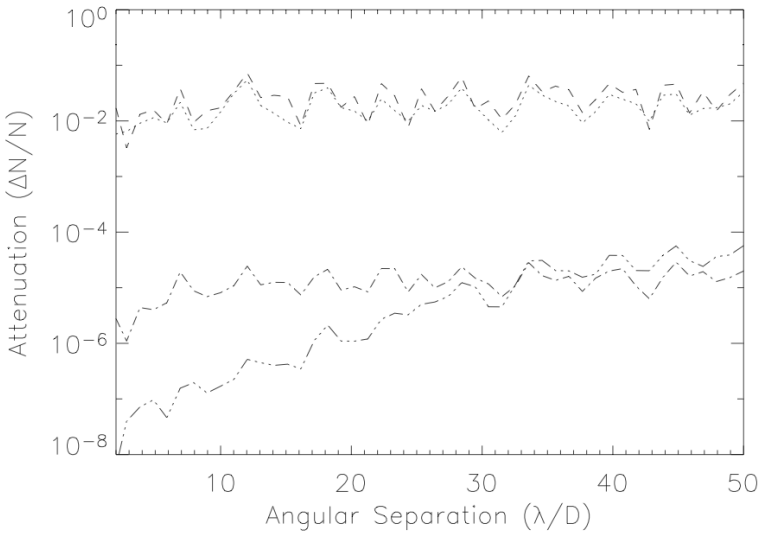

Figure 5.2: PSF noise attenuation obtained from different scaling algorithms: IDL cubic algorithm (dashed line), the IRAF cubic spline algorithm (dotted line), the IRAF 2D sinc algorithm (dot dashed line) and the FFT algorithm (triple dots dashed line). Taken from Marois (2004)

In order to achieve the required scaling the zeropadding sizes must satisfy the following:

$$Zpad_{Fourier} = Zpad_{image}\frac{\lambda_{scale}}{\lambda_i} \tag{5.1}$$

Where λ_{scale} is the wavelength we wish the image to be scaled to, λ_i is the wavelength of the image we are dealing with, $Zpad_{image}$ is the image space zeropadded dimension and $Zpad_{Fourier}$ is the Fourier space zeropadded dimension. Note $\frac{\lambda_{scale}}{\lambda_i}$ is the scaling factor required.

The amount of zeropadding obviously has to be an integer number of pixels, to avoid large errors in the amount the image is scaled by, values of $Zpad_{image}$ and $Zpad_{Fourier}$ should therefore be found that are as close to integer values as possible. Using larger zeropadded images will help in this endeavour, however, it is at the cost of computing time and the maximum size of the zeropadding will be limited by the computing power available to you. For the work done in this thesis a search of zeropad values up to a maximum of 6000x6000 pixels was performed as this was the limit of my computing power. The resultant sizes after zeropadding also have to be divisible by 2 in order for the FFTs to work. An example of this scaling would be the following:

Problem - Scale a Nyquist sampled PSF with original dimensions of 256x256 needs to be scaled from a wavelength of $1.62\mu m$ to $1.5\mu m$

Solution - Zeropad the 256x256 image to 2538x2538. Calculate the optical transfer function through IDL's `FFT` routine. Crop the Fourier space zeropadded image down to 2350x2350 and Fourier transform back.

For the above example it was possible to find an integer solution within the limits of computational ability, however, this is not always the case. It is possible to perform multiple scalings of the same image to get to the required result however, this is not ideal as multiple interpolations will build up noise in the result. Figure 5.3 shows the resultant sizes of the zeropadding needed for the case of the prototype slicer data described in Chapter 6. The straight lines seen in the figure are a result of the set $\Delta\lambda$ of the wavelength sampling giving giving preferential Fourier plane zero padding values. The error due to the scaling inaccuracy is determined as the maximum offset of each sample point determined from this scaling relative to its ideal value, measured in pixels. As can be seen in the figure the error values are very small, with a maximum offset of 0.0006 pixels at the furthest point from the centre of scaling (where the affect of the imperfect scaling is largest). This error is still going to be far smaller than the error on the centring of the image and so all of the wavelength slices scaled in this way can be used. However, supposing that we found ourselves in the situation where there were a few slices that had very large scaling errors, we could in this case just discard these slices and run spectral deconvolution treating them as missing data.

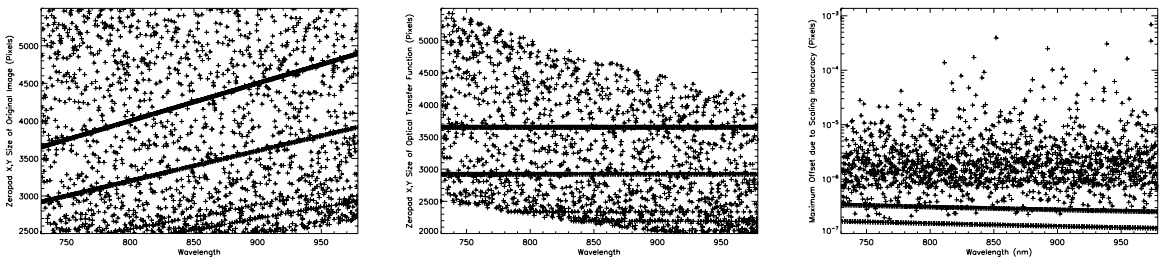

(a) (b) (c)

Figure 5.3: Zeropadding sizes and resultant scaling errors for a data set obtained from the experiments described in Chapter 6. The data set spanned the wavelength range $730-980nm$ in $0.1nm$ slices and was scaled to $730nm$. Padding sizes were restricted to be between 6000-2000 pixels on a side. (a) shows the calculated zeropad needed in the image, (b) shows the amount of zeropad needed in the Fourier-space image. (c) shows the error due to the scaling inaccuracy, determined as the maximum offset of each sample point relative to its ideal value. The straight lines seen in the figures are a result of the set $\Delta\lambda$ of the wavelength sampling giving giving preferential Fourier plane zero padding values

Sub pixel translations are also commonly needed in the data reduction, in the case of spectral deconvolution they are needed in order to centre the point of scaling and for on-sky data to correct for atmospheric dispersion. These translations will also benefit by using Fourier transforms, this operation can be performed at the same time as the required scaling so as to reduce the number of interpolations required. A translation of the data is performed by adding a linear phase to the Fourier transform of the image in question. The slope of the linear function is proportional to the ratio of the shift required to the image dimension. A comparison of the accuracy of shifting images using 3 standard interpolation techniques and the Fourier technique are shown in Figure 5.4, taken from Marois (2004). In this investigation two identical PSFs of a Nyquist sampled point source are generated with a 0.5 pixel shift relative to each other. One is then shifted to the position of the other via the method stated and subtracted from it. The errors on this difference image are calculated in the same way as stated above for Figure 5.2. This investigation showed that the Fourier shifting was the most accurate method of performing sub pixel shifts within the central $15\lambda/D$ at which point its performance was comparable to the IRAF 2D sinc algorithm.

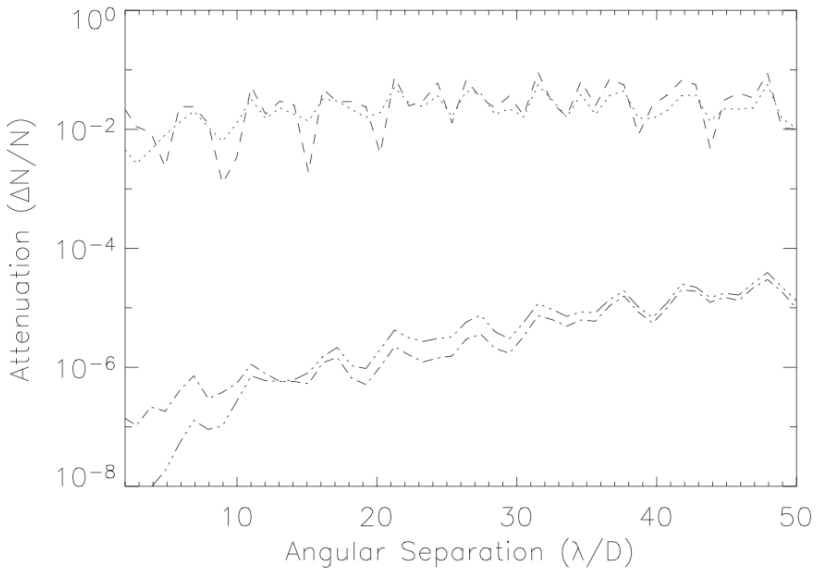

Figure 5.4: PSF noise attenuation obtained from different shifting algorithms: IDL cubic algorithm (dashed line), the IRAF cubic spline algorithm (dotted line), the IRAF 2D sinc algorithm (dot dashed line) and the FFT algorithm (triple dots dashed line). Taken from Marois (2004)

5.1.3 Interpolations with Real Data

The scaling or shifting of an image of infinite dimension using Fourier transforms should be accurate to its numerical precision. However, in reality image dimensions are finite which means some fraction of the PSF information will fall outside of the field of view. The information that is lost results in it not being possible for the Fourier fit to perfectly represent the PSF of the original image. Modifications of the Fourier plane image (ie. for scaling or adding in a shift) will therefore introduce noise into the resampled image. This noise can, theoretically, be reduced by increasing the size of the field of view. Marois (2004) claim that an increase in image size from 512x512 to 1024x1024 will result in 3 magnitudes lower residuals in the Fourier noise and an increase to 2048x2048 will give 6 magnitudes lower residuals. However, in practise this can only be true where you are not limited by the noise in the image, as this can dominate over the weak signal of the PSF in the now extended parts of the field of view and prevent you from achieving a more accurate result. It should be noted that as long as the Fourier noise is well below the random noise floor of the image there is no need for it to be improved further as we will not gain as a result.

In the application of high contrast imaging we often have to deal with large dynamical ranges in images, when not working with a central obscuration for example. This can also pose a problem for image manipulations with Fourier transform as any inaccuracies in the fit will result in ringing throughout the image due to the incorrect fit to frequencies not sampled well enough by the image. For a relatively bright source in the image this ringing may be strong enough to wipe out the signal you are trying to detect from a companion. To try and get around this problem, a fit can be made to the radial average intensity from the center of the primary source. The data can then be padded out to a larger size by generating fake data with this fit. This will only help, however, if there is still significant signal from the primary source outside the FoV. If you are dominated by noise at the edges of your image you will not reduce the Fourier noise of the primary source by embedding it in fake data. This will, however, reduce the ringing produced at the edges of the FoV which is typical of Fourier methods.

In an attempt to get around the dynamic range problem the central core of the very intense source can be replaced by an analytic function, this will of course mean losing any information within this core. However, in the case of spectral deconvolution, if it is within the bifrucation radius (described in Section 2.3.3) we are not going to be loosing anything of value.

5.2 Improving Spectral Deconvolution through EPICS Simulations

† Improvements have been made to the method of spectral deconvolution and have been tested using EPICS simulation data. These include:

- Better interpolation methods have been used for scaling
- Clipping of the data points used in the polynomial fitting has been implemented

5.2.1 EPICS Simulation

The goal of this simulation was to generate a data cube representing the output of a perfect IFS behind a perfect coronagraph with purely achromatic phase aberrations and to test signal extraction with spectral deconvolution to see what contrasts could be reached in an ideal case.
Simulation details:

- Field of View: 2.4 arcsec
- Number of pixels: 1024x1024
- Spectral range: $\sim$0.95-1.735μm
- Spectral resolution: R$\sim$500-900
- Static aberrations only: 62-nm rms
- Seven exo-planets with various contrasts and separations have been integrated into the images (see Figure 5.5)

5.2.2 Improved Interpolations for Scaling

The normal method of spectral deconvolution, as described in Section 2.3.3, was followed whereby after scaling, a low order polynomial is fit to the intensity distribution of each spatial pixel with respect to wavelength. The planet signal is faint and now smeared across multiple spaxels causing it to appear as a small

†Information in this Section has been drawn from Salter et al. (2008)

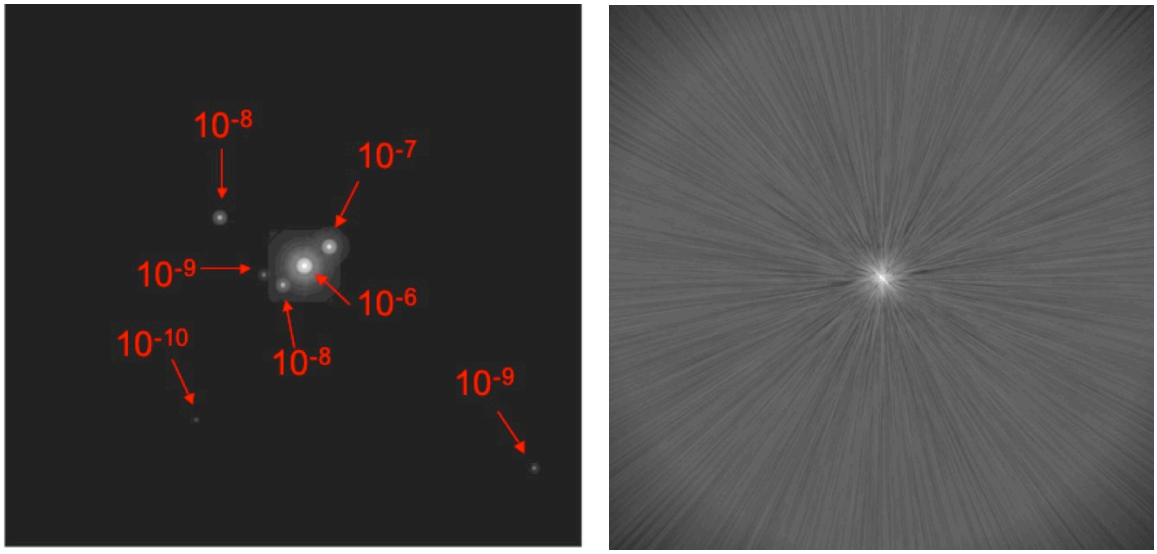

(a) (b)

Figure 5.5: EPICS simulation data - (a) Planets integrated into the central 512x512 pixels before noise has been added. Corresponds to 1.2"x1.2". FoV (b) data cube after noise addition, collapsed along the wavelength direction. Planet signals cannot be detected without some post processing to remove the speckle noise. Corresponds to 2.4"x2.4" FoV.

bump in the spectra of the speckle. For this reason a low order polynomial fit to each spatial pixel can almost completely take into account the speckle signal but leave the planet signal almost untouched. Figure 5.6 shows the results from scaling the data cube using IDL's `INTERPOLATE` function, fitting and removing a low order polynomial from each spatial pixel. The noise pattern seen in this image is thought to be due to the non-ideal interpolations made during scaling, as well as a possible slight centring offset during scaling.

In contrast, Figure 5.7(a) shows the result from following the same method of fitting low order polynomials but this time using FFTs to perform the interpolation for the scaling, see Section 5.1.2 for details. The results are greatly improved, detecting some signal from all 7 planets as opposed to the 3 planets seen in Figure 5.6. This very loosely translates to an improvement of ~ 2 orders of magnitude as the highest contrast detection after scaling with IDL's `INTERPOLATE` function was the 10^{-8} planet to the upper left of the central star whereas the new method was able to detect the 10^{-10} planet to the bottom left of the central star (the separations of the two are different so it is hard to make a direct comparison). The dark radial stripes are a tell tale sign of the planets presence and are formed from the spreading out of the planet signal when the datacube is scaled. These 'tiger stripes' are artifacts from the polynomial fit fitting not just the speckle spectra, but part of the planet signal as well.

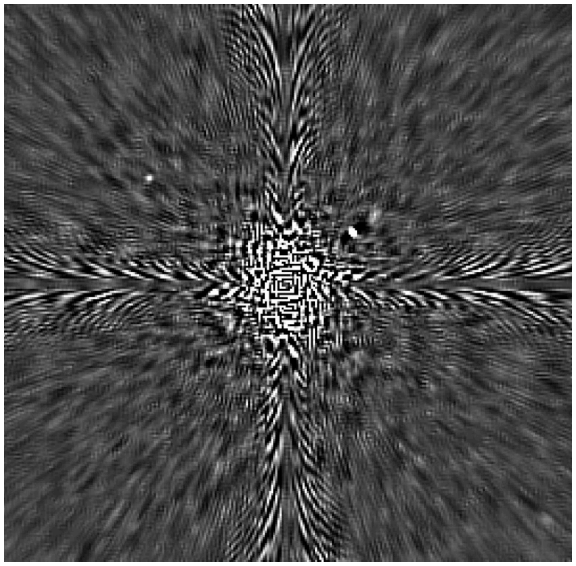

Figure 5.6: EPICS simulation data - Post Spectral Deconvolution that has had the scaling performed using IDL's `Interpolate` routine.

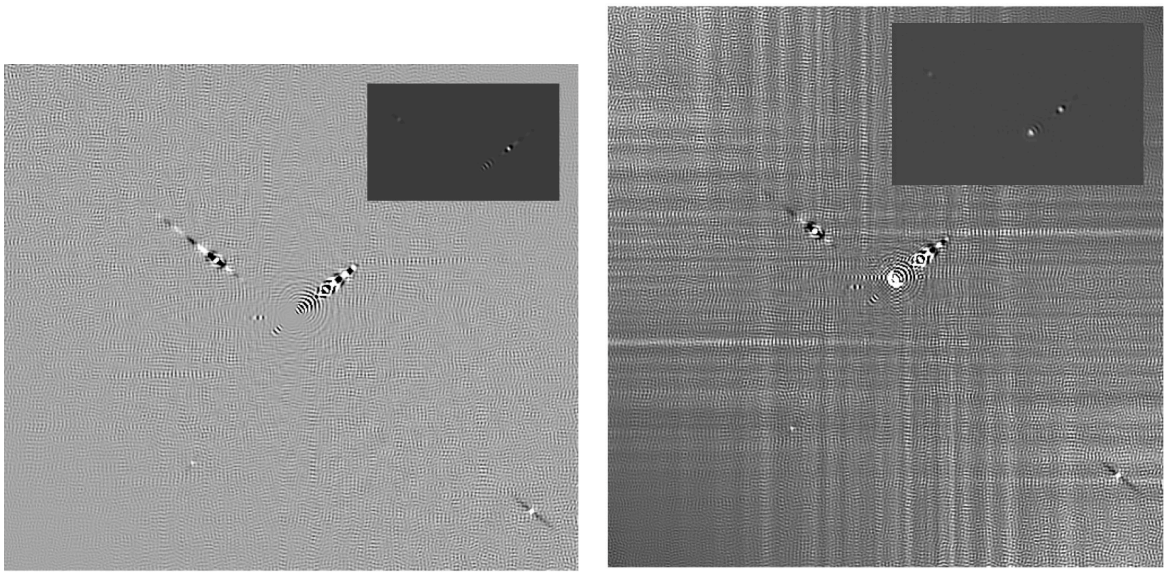

(a) (b)

Figure 5.7: EPICS simulation data - (a) Post Spectral Deconvolution that has had the scaling performed using FFTs.(b) Post Spectral Deconvolution that has had the scaling performed using FFTs and speckles have been iteratively fit with clipped polynomials. Top right is a better cut for viewing the brighter, close-in, planets.

5.2.3 Clipped Polynomial Fitting

The polynomial fitting method was improved by using an iterative process of fitting the speckle spectra, rejecting points lying $> 3\sigma$ above or $> 10\sigma$ below from the fit. An example of this method of fitting a scaled spaxel with an overlapping companion signal is shown in Figure 5.8. The improvement of the simulation result after performing this clipping can be seen in Figure 5.7(b), it shows increased contrast, reduced 'tiger stripes' and the brighter inner planet is now clearly detected.

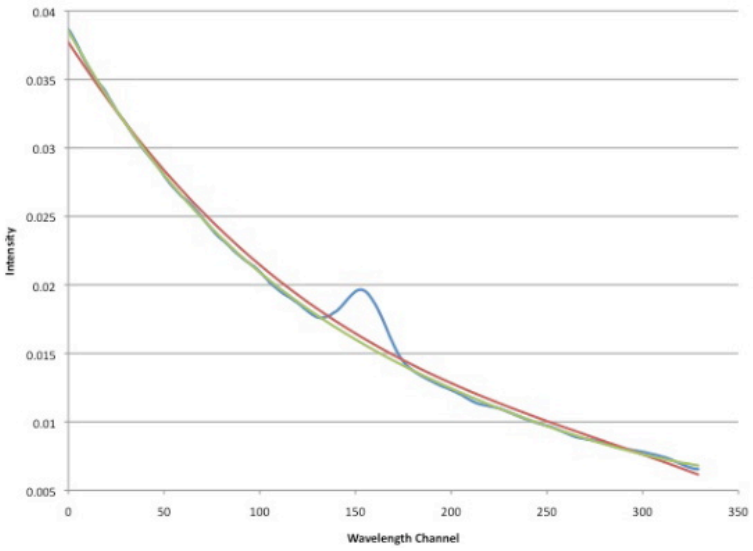

Figure 5.8: Simulated data of a low order polynomial fitting to speckle spectrum after scaling. The blue curve is the intensity of the speckle after scaling, the red curve is the initial polynomial fit and the green curve is the fit after sigma clipping. The bump in the centre is where the planet signal, now a radial smear, crosses over the speckle.

5.3 Simulations of a Slicer based Integral Field Spectrograph

‡ This section describes in detail the simulations performed to identify any potential limitations imposed by an image slicer based IFS to the achievable contrast in an exo-planet direct detection (and characterisation) instrument. The principal goal is to determine whether the one-dimensional coherence, retained along the slice as the light passes through the spectrograph, causes the speckle pattern to be modified in a way that cannot be correctly accounted for using spectral deconvolution on the resultant data cube. In particular, differential non-common path errors between adjacent slices (which could be large in the spectrograph) could potentially affect the speckles in this way. This is described in detail in Section 4.1.3.

5.3.1 Description of Method

The method for simulation of the IFS performance is as follows:

1. The AO modeling group, led by Christophe Verinaud (LAOG), provided complex amplitudes (E field) for a range of wavelengths at the post-apodizer focal plane. These contained typical errors expected from the extreme AO system and common path optics, including all elements up to the image slicer focal plane. Many wavelengths were simulated, so that the spectral deconvolution (SD) algorithm could be applied to the end product.

2. The focal plane E field distribution is truncated to the geometry of each slice of the image slicer. The resulting complex amplitude will be propagated to the pupil plane, using Fourier techniques. Note that with a slice width of $\lambda/2D$ at the shortest wavelength, significant diffraction is to be expected at the slicer. This diffracted pattern is truncated by the finite pupil size of the spectrograph optics (typically oversized in a slicer IFS by a factor of 3 to 5 relative to the geometrical pupil size).

3. At the pupil plane the wavefront error appropriate to that slice will be applied to the complex amplitude. Expected design errors are very small and can be ignored in comparison to the random errors introduced by manufacturing. One can add typical manufacturing errors expected for the optical components, with a magnitude determined by the type of optical polishing to be performed, and with a

‡Information in this section has been drawn from Salter et al. (2010b)

spatial frequency behavior that decays as $1/f^2$, typical of many different sorts of errors in optics production. Note that as only one set of errors can be applied for each slice, any field dependence of the wavefront errors within the slice cannot be taken into account. We realise that this is a fundamental limitation of the simulation technique, but are unable to provide a field dependent error simulation. Also, all errors are applied in the pupil plane, even if they may occur elsewhere.

4. The resulting complex amplitude, after applying the wavefront error from the slicer IFS for that slice, is then transformed back to the focal plane to provide the intensity distribution for that slice at the detector. This is done for as many wavelengths as desired.

5. The focal plane intensity for all the slices are truncated to the slice width, and concatenated to produce the full focal plane illumination at the slicer IFS detector plane, the process is repeated for many wavelengths. Each focal plane is then binned to the sampling that would be provided by a real system (calibrated for 2 pixels per λ/D at the shortest wavelength) giving in effect the final IFS data cube.

6. The SD algorithm is applied to the resulting data cube to try and recover as much of the initial contrast as possible, by detecting, suppressing and eliminating speckles. The results are compared to those generated by applying the SD algorithm at the slicer input focal plane, to determine the degradation, if any, to the contrast, resulting from the use of a slicer based IFS.

This process is depicted graphically in Figure 5.9.

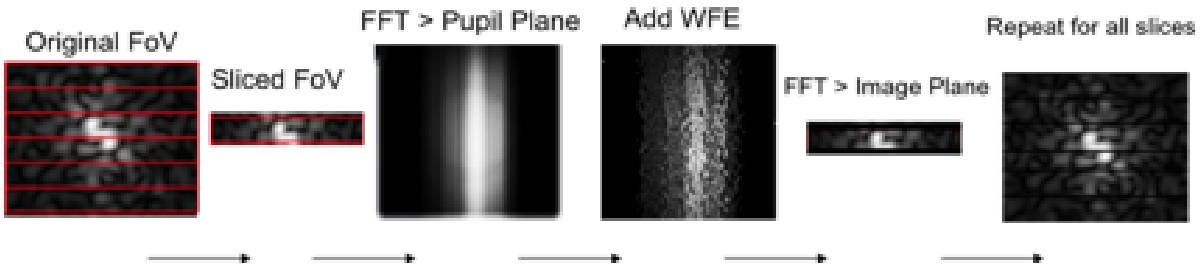

Figure 5.9: Schematic showing the sequence of steps performed during the slicer simulations. From left to right, the focal plane is truncated to slitlets, propagated to the pupil plane where wave front error is added, propagated back to the image plane and put together with the rest of the slitlets to form a complete wavelength channel.

5.3.2 Generation of Post-Apodizer Complex Amplitudes

The AO simulation code developed at LAOG was used to generate a data cube of complex amplitudes to carry out these simulations. The following parameters describe the data set:

- 512 x 512 spaxels (spatial pixels) in each wavelength channel
- 440 channels, starting $\lambda = 0.950\,\mu$m, ending $\lambda = 1.765\,\mu$m, $\Delta\lambda = 0.00186\,\mu$m
- Sampling of 10 pixels per λ/D at the shortest wavelength
- Apodiser transmission of 43%
- Static aberrations of 14*nm* rms, with a flat power spectral density.

5.3.3 Random Wave Front Error Addition

As described in the previous section we add the wave front error as a phase difference in the pupil plane. Currently we are only adding the wave front error corresponding to manufacturing errors (ie. having a $1/f^2$ frequency profile) as the expected design errors are very small and can be ignored in comparison to these random errors introduced by manufacturing. In a real slicer IFS the wave front error changes slowly with wavelength for each slice, and discontinuously when moving across slices. Currently we add errors that are completely discontinuous from slice to slice but without any variation with wavelength. This means that simulation predictions are overly pessimistic across slices but optimistic in the spectral dimension. We plan to rectify this in the future. We also intend on adding in errors inherent to the design of the IFS, obtained using Zemax, although as previously stated this should not have a large effect on the result.
There have been four simulation runs so far using added wave front error maps with RMS values of 1 nm, 20 nm, 100 nm and one set that has had no effects of the slicer added (no diffraction from slicing, no additional pupil plane errors, no cropping of the pupil), this is meant as a reference point to help us understand the results.

5.3.4 Removing the Central Bright Region

The input data assumes an apodizer, rather than a coronograph (as is the current baseline for the instrument (Kasper et al., 2010)), this is in an effort to reduce the chromaticity of the speckle pattern. However, unlike

the real instrument design, the simulations do not have a masked out central region. This is needed as near-IR detectors do not have sufficient dynamic range for the central region to be imaged without substantial attenuation. Having this bright central region present in the simulations has a few repercussions: The Fourier transforms needed to scale the data during the application of the spectral deconvolution method causes large amounts of ringing around the bright region that gravely effects the rest of the data. The bright central core also dramatically increases the intensity of the secondary speckles produced.

In order to get around the Fourier ringing produced by the central core we decided to mask it out, however, one cannot simply replace it with zero values as this step change in the data would also produce ringing of its own. Thus we used a smoothly varying function, tapering to zero at the center, with an extent of $7\lambda/D$ at the shortest wavelength, this can be seen in Figure 5.10. By modifying the data in his way we are making that region unusable but it reduces the ringing significantly so as to make the rest of the data useful.

We also intend on improving this by fitting an Airy pattern to the data that will be subtracted but that can also be analytically scaled such that it can be added back to the data after the Fourier transforms have been performed. The idea is that this would then remove the high signals that ruin the rest of the data during the transforms due to Fourier ringing but then we can add it back to the scaled data (without additional noise) so as to retain the validity of the data in the central region.

Note that this removal of the central core is performed after the addition of the wave front error in the pupil plane, i.e. the light is contained will have already interfered to produce secondary speckles elsewhere on the slices that would not have been generated had the light been occulted at an earlier point.

5.3.5 Simulation Results and Discussion

Figure 5.11 shows a single wavelength channel for each of the 4 simulation runs described in Section 5.3.3, the corresponding residuals after performing spectral deconvolution are seen to the right of each image. The bright rings which can be seen in Figure 5.11 are a result of edge effects from the limited size of the function we use to reduce the central bright peak, as described in Section 5.3.4. The range over which the function is applied has been made to scale with wavelength so as cover the same fraction of the Airy pattern and therefore affect the same area of the scaled cube (when performing spectral deconvolution). However, the slight discrepancies at the edges modify the speckle spectra sufficiently to cause large residuals to be left over. In

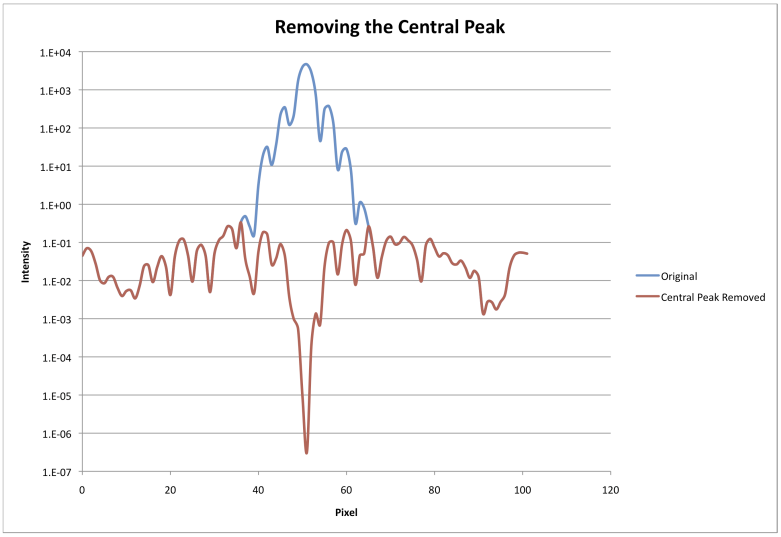

Figure 5.10: Suppression of the central region using a smoothly varying function, tapering to zero at the center, with an extent of $7\lambda/D$ at the shortest wavelength

the current application of the spectral deconvolution method the differencing between the data and the fits is performed in the scaled plane. This means the residuals have to be rescaled (using Fourier transforms). It is a combination of this re-scaling with the ringing present from the forward scaling of the bright central source that causes the cross shaped noise pattern seen in the final data set. This noise is a limiting factor for a large region of the FoV and the regions containing it have to be masked when determining the contrast achieved.

The contrast achieved for the same dataset as Figure 5.11 are shown in Figures 5.12, 5.13 & 5.14. They are for a single wavelength channel. Figure 5.12 is for the case of an ideal IFS (0nm wave front error added) and shows the comparison between a radial profile of the data before spectral deconvolution to that after SD, as well as the result after masking off the region affected by Fourier ringing. Figures 5.13 and 5.14 show the post spectral deconvolution results for all 4 simulation runs with the noisy cross left in and masked out respectively. The right hand axis (named contrast, central region removed) assumes that we reduce the maximum intensity by a factor of 100-1000 using an obscuring focal plane mask, which should also reduce the secondary speckles by an equivalent factor. Since secondary speckles are the limiting factor here it is reasonable to assume the contrast curves would therefore improve accordingly.

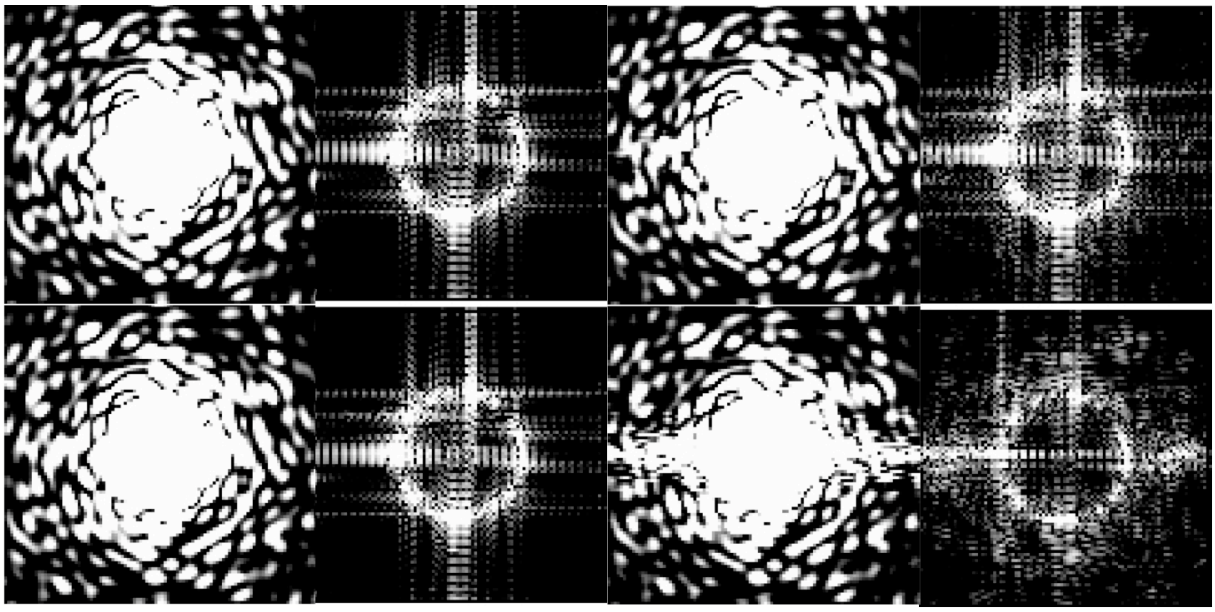

Figure 5.11: Simulation result for a single wavelength channel. Pairs of images: Left hand images are the focal plane intensities after having been passed through the slicer and the right hand images are the residuals after the spectral deconvolution method has been performed. Going from top left to bottom right , 0nm, 1nm, 20nm, and 100nm of differential wavefront error have been added in the pupil plane.

5.3.6 Simulation Limitations

We are only considering Fraunhofer propagation and therefore all errors are applied in the pupil plane, even if they occur elsewhere. Consequently a fundamental limitation of the simulation technique is that the field dependence of the wave front errors cannot be taken into account.

We currently do not include errors inherent to the design of the IFS, as can be determined using Zemax. The current method of wave front error addition is overly pessimistic across slices, but optimistic along slices, as described previously. This is something we plan to rectify in the future. The angular size of the FoV of current simulations is very small, due to the large computational time needed to produce the complex amplitudes. Future simulations will provide a larger FoV which should enable us to achieve greater contrasts as the spectral deconvolution method works better the further from the parent.

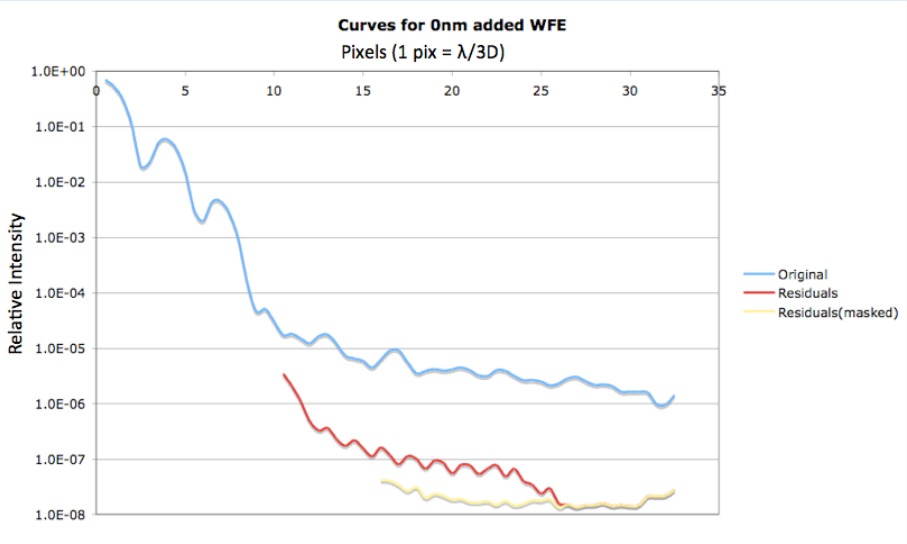

Figure 5.12: Radial contrast plots from a single wavelength channel of the simulation results (see Figure 5.11). Curves for the case where 0nm wave front error was added, simulating an ideal slicer. The top blue curve is the mean radial profile before performing spectral deconvolution. The red curve is the RMS residual after SD. As can be seen from Figure 5.11, here we have been dominated by the Fourier noise from the transforms needed when scaling the data during the SD process. This ringing of the data limits the achievable contrast. In an effort to prevent this affecting the results, a cross-shaped section covering this region with large amounts of Fourier noise is masked out. The RMS residuals after masking are shown by the yellow curve.

5.3.7 Shapes of Secondary Speckles

The size of a speckle is defined by the distance between the patches of the pupil interfering coherently to produce it. Speckles generated classically are therefore $\sim \lambda/D$ in size due to the higher probability of the coherent patches being close to the edge of the telescope pupil. However, as light passes through the slicer the light gets diffracted perpendicular to the slitlet, due to the slicing of the focal plane, see Figure 5.15. The probable location of the interfering patches are still within the core of this diffracted pupil however the core is now a lot larger in the direction perpendicular to the slice than parallel to it. This should result in the shape of speckles created past the slicer being elongated in the direction of the slice. This is a characteristic that could possibly be used to identify them and remove them from the data. Figure 5.16 shows the result of a simulated slice, centered on the primary star being viewed with an apodizer, the left image shows the result from applying 1nm of wave front error, it is seen to have little effect and the noise above and below the slice is just due to diffraction of the cropped pupil. The image on the right shows the case where 100nm of wave

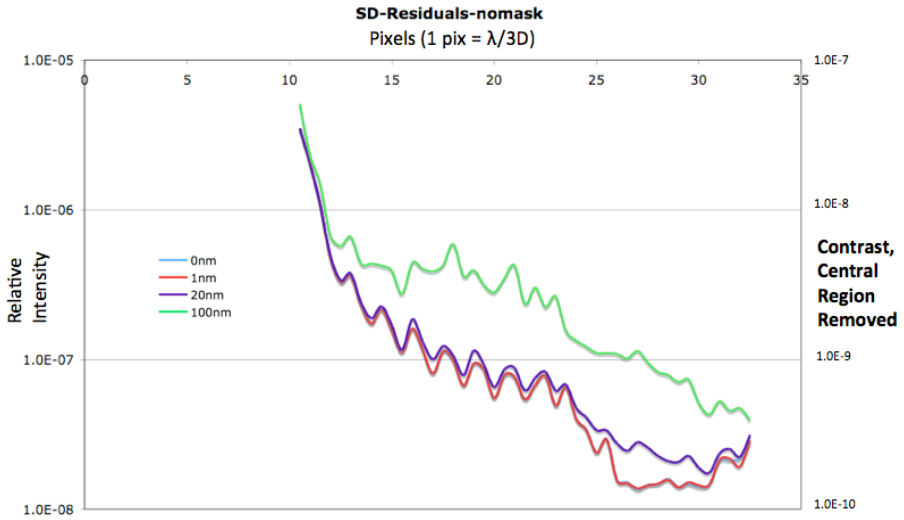

Figure 5.13: RMS radial profile residuals after the application of spectral deconvolution for all 4 simulation runs. The contrast curves have been limited by the Fourier ringing, seen as the cross pattern in Figure 5.11.

front error is added. A sea of secondary speckles is produced over shadowing the noise due to diffraction seen in the left image. The elongated shape of these seconday speckles is clearly seen in this image.

Possible Modifications to the SD Algorithm

The determination of technology dependent contrast limits cannot be carried out independently of the algorithms used for speckle suppression. If the technology modifies the speckle pattern in a well-defined way, it may be possible to devise an algorithm that can identify and eliminate the modified speckle pattern, in a manner similar to the unmodified speckle pattern. Identification of the characteristic shape of secondary speckles produced by the IFS may give us a way to identify them and thus remove them.

5.3.8 Simulations Conclusions

Through simulations we have determined that slicer based IFS are unlikely to limit the achievable contrast. The main limitation of these simulations is that the central region of the apodized PSF has been left in. This is unrealistic as near-IR detectors do not have sufficient dynamic range for the central region to be imaged without substantial attenuation. EPICS proposes to have the central region obscured, transmitting only a small fraction of the light from this bright region. Since secondary speckles are produced from the light

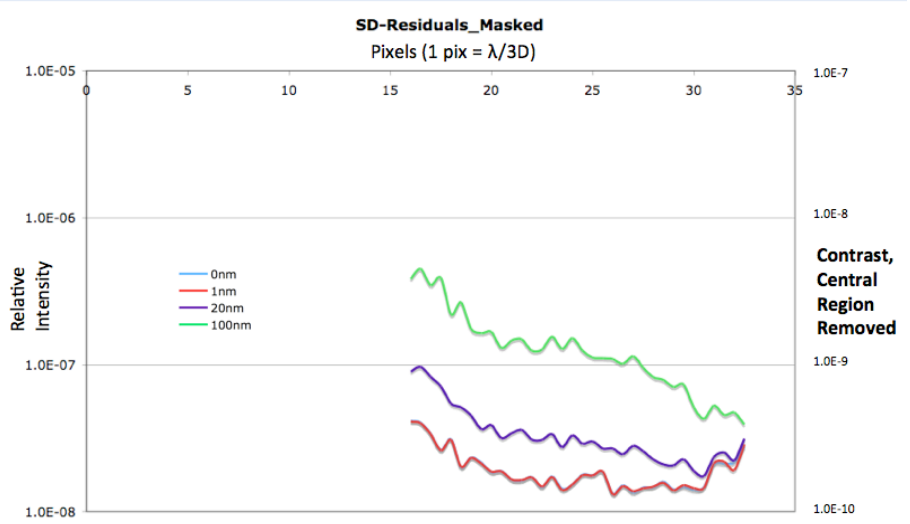

Figure 5.14: RMS radial profile residuals after the application of spectral deconvolution for all 4 simulation runs. Here the central noisy cross seen in Figure 5.11 has been masked out to enable us to determine the achieved contrast.

incident on the slitlets and the results above show that we are limited by the secondary speckles, if the maximum intensity of the incident flux is reduced by a factor of $\sim$100 (equivalent to an occulting spot $2\lambda/D$ in radius) we would expect that the secondary speckles are also 2 orders of magnitude lower in intensity. The achievable contrast would then improve by the same amount (as plotted on the right hand axis of Figures 5.13 & 5.14). We intend to incorporate an occulting spot in our next set of simulations.

The simulations show that significant secondary speckles are formed only when a large amount of differential wave front error is added. In contrast to the 100nm of wave front error needed to bring out the secondary speckles in the simulations, spectrographs built for this purpose will be diffraction limited and therefore, by definition, they should have no more than $\lambda/14$ of RMS wave front error.

The AO modelling group at LAOG will be preparing some new simulations that will have a larger FoV (as the current one is very small) and will include a more realistic E-ELT pupil (i.e. containing spider arms and artefacts from the gaps between mirror segments) We intend on making the added wave front errors more realistic by using those calculated from the optical design and adding in an additional wave front error for each slitlet that varies slowly with wavelength.

As mentioned previously, we intend on tailoring the method of spectral deconvolution so as to produce the

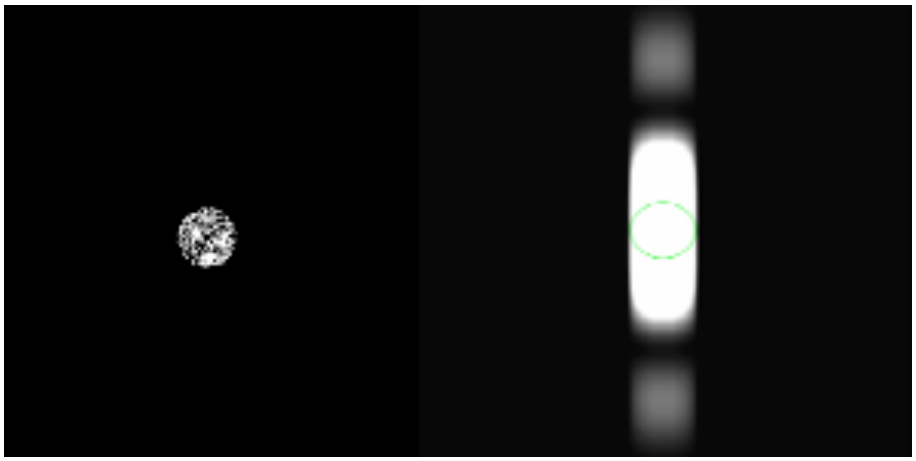

Figure 5.15: Left: Original telescope pupil. Right: Diffracted pupil after having passed through the slicer. A circle is drawn on the diffracted pupil to show the relative size of the original telescope pupil (geometric pupil)

best results for slicer based integral field spectrographs. These modifications will likely involve filtering out secondary speckles that have been created past the slicer (these will be identifiable due to their characteristic shape). Once the new AO simulations are available, and we are confident we are no longer being dominated by Fourier noise we intend on using the simulations to probe the parameter space by increasing the range of errors added to the system and also to determine the optimum spectral and spatial resolutions required to produce the best results.

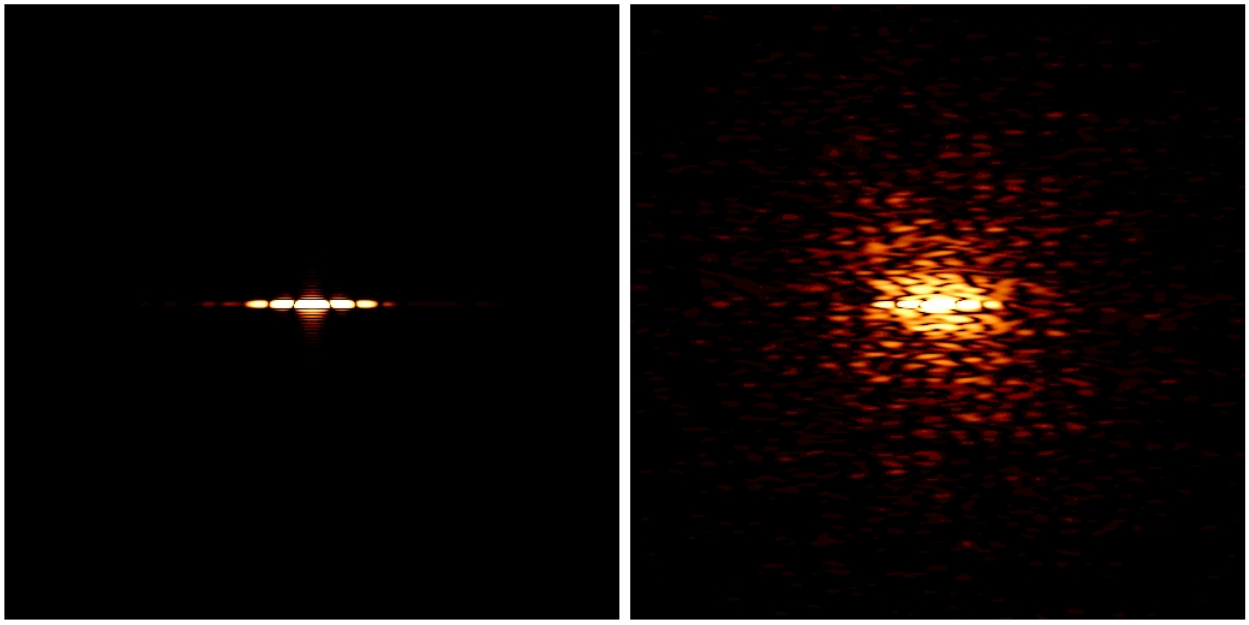

Figure 5.16: Simulation result of a single slice, centered on an apodized star; Left: 1nm of wave front error has been added, noise above and below image is due to diffraction from the cropped pupil. Right: 100nm of wave front error is added, a sea of secondary speckles is seen each with an elongated PSF.

Chapter 6

Determining Contrast Limitations of Slicer Based Integral Field Spectrographs: Experiments

As part of the EPICS (Exoplanet Imaging Camera and Spectrograph for the European ELT) Phase A study, we planned to determine whether the choice of a particular technology for the IFS imposes a limitation on the ultimate contrast achievable by the EPICS instrument. If such technology dependent contrast limits do exist, it would be the driver for the choice of IFS technology. Since speckle noise, and not photon noise, determines the ultimate contrast achieved by extreme AO systems, any inherent limitations in combating the speckle noise (i.e. speckle suppression) are to be investigated. In this respect, the key issue to be studied is whether the IFS modifies the post-coronagraphic speckle pattern in any way, and if so, to quantify the impact that these modifications have on the ability to identify and eliminate the speckles in the high contrast data cube. However, it should be kept in mind that any determination of technology dependent contrast limits cannot be carried out independently of the algorithms used for speckle suppression, as, if the technology modifies the speckle pattern in a well defined way, it may well be possible to devise an algorithm that can identify and eliminate the modified speckle pattern in a manner similar to the unmodified speckle pattern. While most of the questions raised about technology limitations to the contrast achieved by a slicer based

Much of the first sections of this chapter have been drawn from the SPIE conference precedings Salter et al. (2010c) and from EPICS Phase A Review document Salter et al. (2010a)

IFS could be answered through carrying out appropriate simulations, it was already clear at the start of the EPICS Phase A study that any such simulation would be quite complex, and due to limitations inherent in the simulations themselves, the conclusions drawn from the simulations would have limited applicability. A two pronged approach was thus devised, involving both simulations and actual laboratory measurements. The simulations would address many critical issues, such as the dependence of ultimate achieved contrast on the choice of spectral resolution, or spaxel size and the characteristics of secondary speckles as could be produced by a simulated wavefront error in the pupil plane. On the other hand, effects such as scattered light, Fresnel diffraction, or non-pupil-plane wavefront errors, which could not be well simulated, would be measured with a test set-up in the laboratory.

This chapter details the laboratory experiments performed to measure the contrast achieved by an image slicer based IFS. These tests are crucial, as no image slicer based IFS coupled with a high contrast AO system has been implemented in an instrument to date, thus, no experimental data of the on-sky performance are available. The simulations are detailed in Chapter 5.

6.1 Experimental Set-up

A dedicated IFS working at near-infrared wavelengths was not available to carry out these tests, even if we were to accept the longer timescale and higher level of difficulty associated with carrying out the tests at cryogenic temperatures. Furthermore, the cost of constructing a custom-built image slicer for these tests was prohibitively high, and the timescale was also beyond the scope of the Phase A study. Consequently, we decided to perform the experiment with a prototype image slicer, based on the slicer for the SWIFT instrument, which has been recently built at the University of Oxford (Thatte et al., 2006; Tecza et al., 2008). It was possible to manufacture a prototype slicer based on the SWIFT slicer within 6 months, and at low cost. Spectrograph optics had also been designed for the SWIFT instrument, and these could be adapted easily for the high contrast tests. Thus, the design for laboratory testing could be realised within a time scale of 12 months, making it feasible to obtain results from these tests within the scope of the EPICS Phase A study. As the SWIFT instrument was expected back in Oxford during 2010, due to the upgrade of the PALMAO system to PALM3K, we planned to switch the prototype slicer for the one in SWIFT. This was, in theory, a very quick change to the experimental setup as both slicers are mounted onto identical base plates

and the prototype slicer could be replaced without having to dismantle any of the other optics. This upgrade is described in more detail in Section 6.4.

The primary objective of these tests was to probe errors that cannot be accurately simulated easily, such as Fresnel diffraction, scattered light, and optical component manufacturing errors. Thus, the prototype IFS spectrograph, based on the Oxford SWIFT design, would allow us to make the necessary measurements, although its operating wavelength range was in the red visible ($\sim$ 0.7 - 1 μm). This made the experimental setup easier as well.

6.1.1 Pre-Optics

The pre-optics does the job of producing the speckle with the required size (as the speckle is diffraction limited, the pupil size controls the speckle's angular extent) and magnification, so as to image its FWHM on to a minimum of two slices of the prototype image slicer at the shortest wavelength (Nyquist sampling criterion). It also provides the necessary calibration light sources (and path) to calibrate the integral field spectrograph. The following sub-sections describe the set-up of the pre-optics. A schematic layout, showing the focal lengths and separations of all components, is shown in Figure 6.2.

Specifications

The Pre-Optics needed to provide the following;

- A focused image on the slicer stack with a pupil located 162mm past it (due to the constraints of the slicer IFU, described in Section 6.1.2.
- A diffraction limited point source that would be Nyquist sampled at the slicer and that would move, as a function of wavelength, across at least 2 slices over the wavelength range of 0.7-1μm. Thus simulating a speckle.
- The appropriate calibration mechanisms for characterising the instrument.

Speckle Generation Using a Diffraction Grating

First plans for this experiment used a phase screen in the pupil plane to produce the required speckles. However, given the small size of the pupil, the phase screen would have to be very small. In addition, the limited imaging capability of the prototype slicer required a speckle to be produced at a certain distance and orientation w.r.t. the central source. A sinusoidal pattern on the phase screen of the desired frequency and amplitude would produce the desired speckle pair.

However, we recognized that this is conceptually equivalent to a diffraction grating, which could be purchased for a small fraction of the cost of the phase screen, with the required line density. Furthermore, the grating would be blazed for a particular order, which would make the speckle brighter than the central source, making it easy to observe. Subsequently, this proved to be a benefit, as the small pupil size required a very bright light source to produce adequate photon counts in the dispersed spectrum at the detector. The pre-optics set-up was designed so that a commercial off-the-shelf diffraction grating (35 l/mm) could be used.

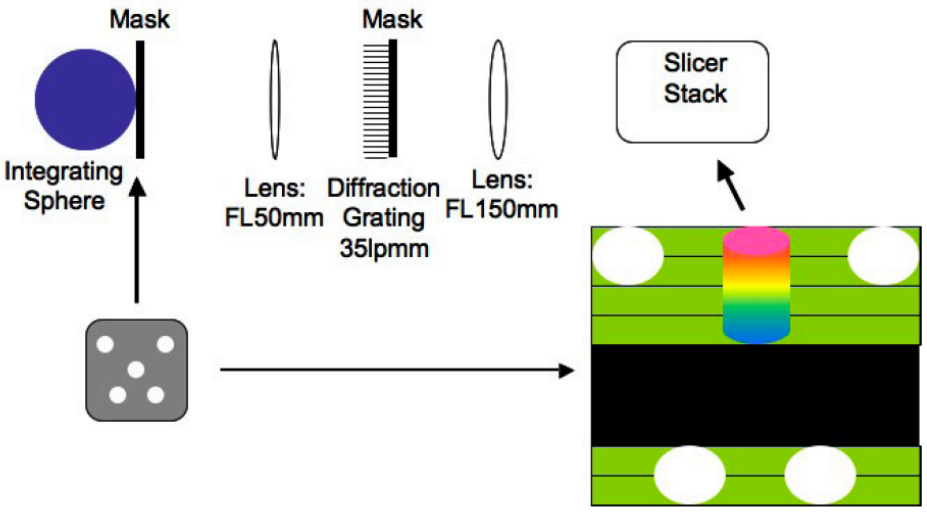

Figure 6.1: Preoptics Design: A focal plane mask is placed in front of the exit port of the integrating sphere, this mask contains 5 pinholes. The first order diffraction spot of the central pinhole (after passing through the preoptics) is the speckle produced for the tests, and is an Airy pattern with a FWHM of 2 pixels (at λ = 700nm) that moves across the outer 4 active slices over the wavelength range $0.7 - 1\mu m$. The other four point sources are used for calibration tests such as measuring the magnification of the preoptics.

Optical Design

The optical design of the Pre-optics was intended to be as simple as possible, using off the shelf components we were able to reduce lead time and cost but still have a system that provided what we need. The design has been developed through collaboration with Dr. Matthias Tecza and a full prescription can be found in the Appendix.

It was decided that an integrating sphere with a halogen lamp and the appropriate focal plane mask would be used to create a point source. A lens is then needed its focal length away from the mask to collimate the beam. To create the diffraction limited point source we want, a pupil stop has to be inserted into this collimated beam. We require the point source to move as a function of wavelength and in order to do this a diffraction grating is placed behind the pupil stop so that we can use the 1st order of diffraction as our point source. The beam needed for the input of the slicer has to be focused on the slicer stack and also have a pupil located 162mm behind it. We were able to do this with just one lens by placing it at its focal length away from the Slicer stack (thus providing the focus from the collimated beam) and ensuring its distance from the pupil stop was such that the pupil was in the correct position through the use of the Gaussian Lens Formula seen in equation 6.1.

$$\frac{1}{s_o} + \frac{1}{s_i} = \frac{1}{f} \tag{6.1}$$

Where s_o denotes the object distance, s_i is the image distance and f is the focal length of the lens.

By using only one lens in this way the magnification of the system is also now defined. We decided on a 50mm collimating lens and a 150mm field lens (this focal length needed to be larger than the distance to the edge of the slicer base plate) both of which were available as catalogue off the shelf lenses with the appropriate anti reflection coating. In order for the diffraction limited point source to be Nyquist sampled at $0.7\mu m$ by the Slicer stack the pupil stop size was calculated to be $115\mu m$, this stop was made in house by the photofabrication lab by etching thin brass foil and measured to be $\sim 114\mu m$ which is accurate enough for our needs. By using the grating equation, see Equation 6.2, it was determined that an off the shelf diffraction grating with 35 l/mm was able to satisfy the criteria that the diffraction limited point source has to move over at least 2 slices over the wavelength range available.

$$d \sin \theta_m = m\lambda \tag{6.2}$$

This is the grating equation, where d is the spacing between lines, m is the order of principal maxima, θ_m is the angle subtended by the principal maxima m.

Also, the diffraction grating is blazed at an angle that will make its first order a lot brighter than the zeroth order. This is of benefit to us as we are already throwing away a lot of the halogen lamp flux with the small focal and pupil plane masks.

The integrating sphere was also fitted with an Argon Arc lamp for calibration of the spectrograph.

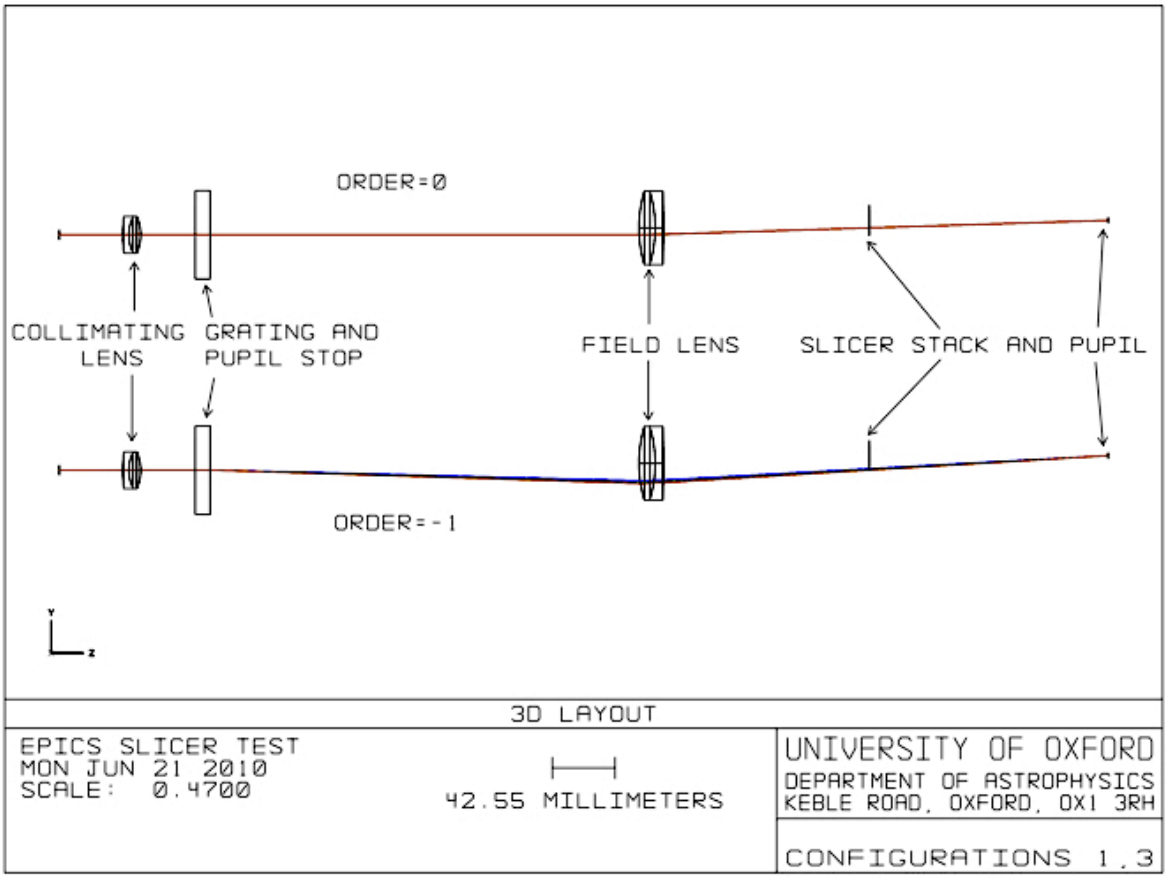

Figure 6.2: Layout of the pre-optics for the experimental test set-up with the 0th and 1st diffracted orders of the central pin hole depicted. The diffraction grating is used as a phase screen to generate the speckle (the 1st order). The pin hole mask at the integrating sphere forms the input focal plane on the left.

The focal plane mask was designed to have two usable positions, the first was a grid of 5 pinholes and the second was a large open window that would fully illuminate the slicer stack. Of the 5 pin holes, the central one would be used for the main experiment (to create our speckle). The other four were used for necessary

calibration tests of the instrument, such as the calculation of the system magnification and the alignment of the slices, and would be blocked out using a baffle located directly after the focal plane mask (see Figure 6.3) so as to reduce the stray-light contamination that may arise from these additional sources. The only constraint on the sizes of the 5 pin holes were that they were not too large so as to dominate the PSF after being diffracted by the pupil stop. The focal plane mask was also made in house by the photofabrication lab and measured sizes of the 5 pin holes were $\sim 62\mu m$. This finite size results in a PSF of an Airy pattern produced by the pupil stop that is convolved with a top hat of the size of the pin hole. As a result the width of the FWHM is 1.7% wider than the Airy pattern on its own at 730nm and 1% larger at 980nm. This effect is not large and varies smoothly with wavelength which means is should not be a problem for the spectral deconvolution. The integrating sphere was mounted on an XYZ stage (see Figure 6.4) which enabled us to select which of the two sections of the focal plane mask we wanted to use by accurately moving the integrating sphere vertically up and down.

A mount was made that enabled the focal plane mask to be fit directly onto the integrating sphere but also allowed a filter to be put in place behind it. A narrow band, laser line filter put in place for the calibration tests of the pre-optics set up and an RG610 filter (cutting out all wavelengths shorter than 610nm) was left in place after the pre-optics has been calibrated. This filter was needed in order to avoid contamination from the other orders in the spectrograph.

The diffraction grating was fitted into a mount that enabled it to be flipped into and out of the beam which was is needed for calibration images such as flat fields.

A pupil mask holder was designed such that the mask inserted could be repeatably switched from a larger 1mm pupil mask, used for calibration of the spectrograph and alignment of the slicer, to the $114\mu m$ mask used for the experiment.

The entire system was enclosed in a purpose built light tight baffling to avoid stray light affecting the results.

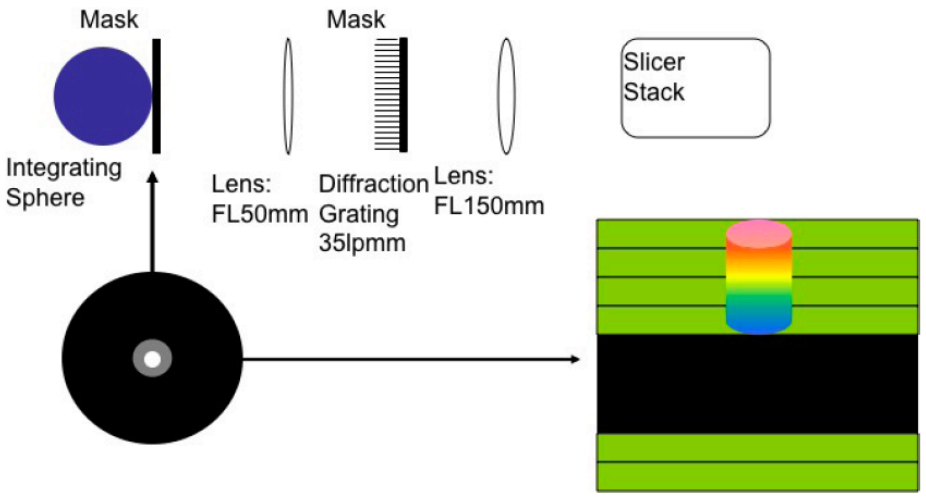

Figure 6.3: The 4 outer pin holes are masked off to just leave the speckle that moves across the 4 outer active slices.

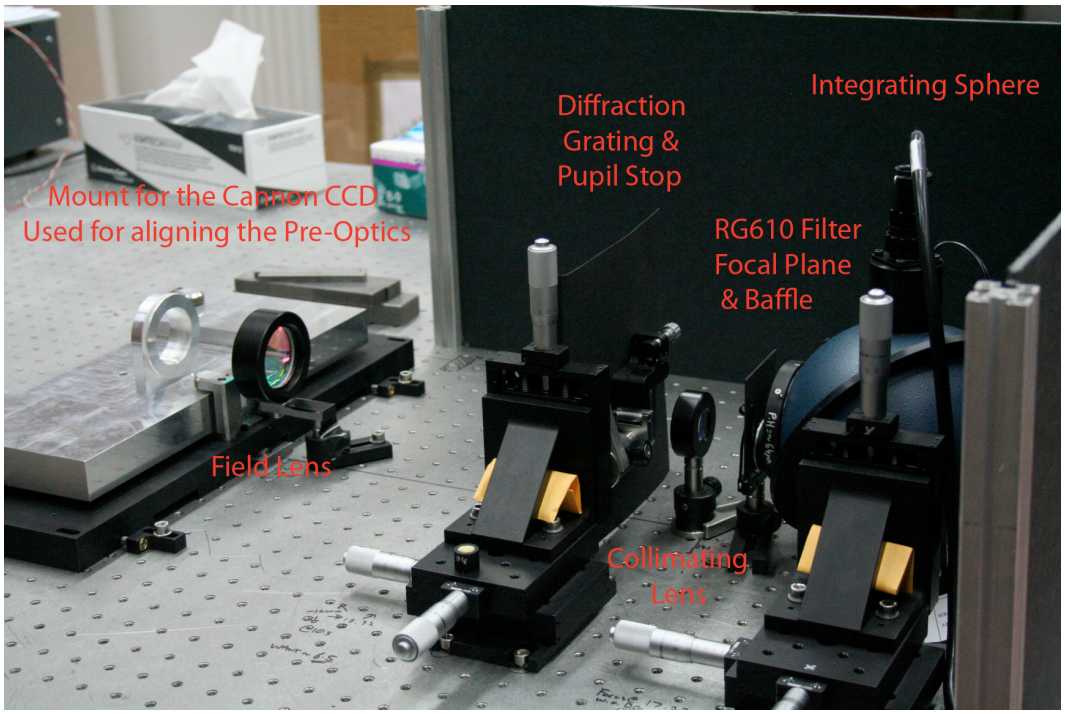

Figure 6.4: Photograph of the test setup showing the pre-optics. The integrating sphere (blue) is visible on the right, while the bare aluminium plate on the left is the mount for an SLR camera, used to verify the location of the slicer focal and pupil planes. The XYZ stage in the centre holds the pupil stop and diffraction grating.

Footprint of the 5 Pin holes

The footprint of the 5 pin hole mask on the two lenses in the preoptics (the collimating and field lenses) is shown in Figure 6.5. This figure also shows the footprint of the 5 point mask and our simulated speckle on the slicer stack. Note that in practise the integrating sphere can be translated vertically so that we can position the image where we want, however, this can lead to some vignetting of the two furthest apart pin holes by the field lens mount.

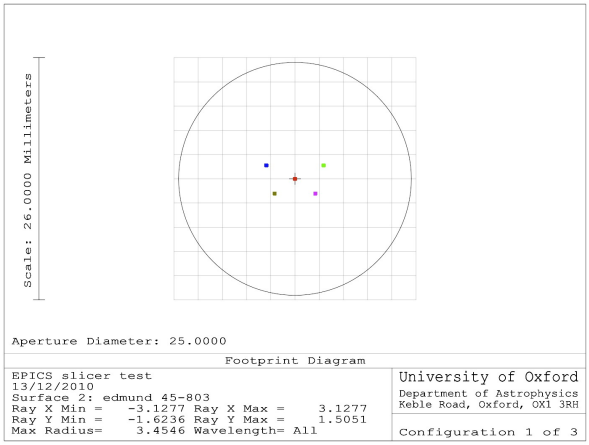

(a) Collimating Lens: 5 point mask

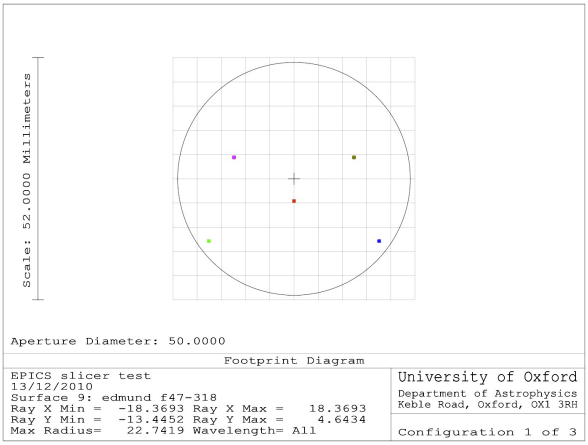

(b) Field Lens: 5 point mask

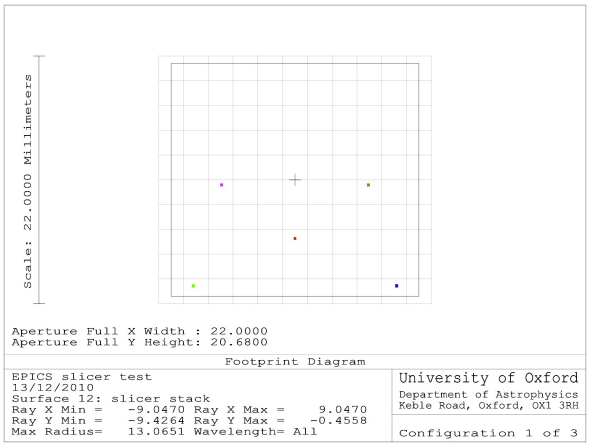

(c) Slicer:5 point mask

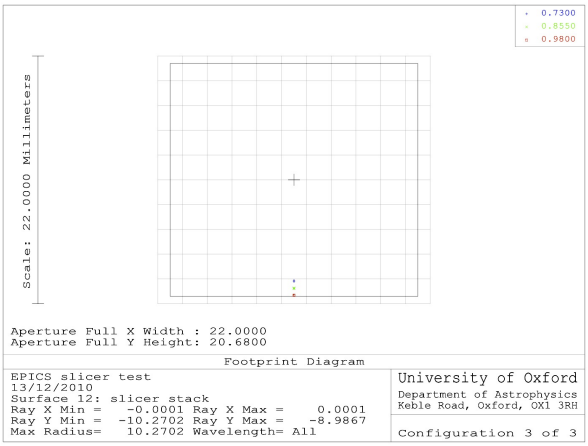

(d) Slicer:Speckle

Figure 6.5: Footprint of the 5 pin hole pattern on the collimating lens, the field lens and the slicer stack. The footprint of the speckle on the slicer stack in shown also.

Assembly and Alignment

Assembly and alignment of the pre-optics was performed with the aid of a Canon SLR CCD camera. The camera was mounted using a mock slicer base plate (seen in Figure 6.4), which in turn was mounted on a stage that allowed the CCD to be located at both the slicer focal plane and the slicer input pupil, 162 mm behind the slicer focus (an explanation of the slicer pupil can be found in Section 6.1.2). All other components were placed at their nominal position. By performing a set of "through focus" scans at both the focal and pupil planes of the slicer, the position of each component of the pre-optics was adjusted so that the focal plane was located at the slicer stack, and the pupil located precisely 162 mm beyond the slicer, along the optical axis. Tests were performed to ensure correct alignment, measure the system magnification, verify the alignment of the grating and the locations of the diffracted orders. Figure 6.6 shows the zeroth and first orders of the diffraction grating, as viewed at the slicer focal plane, but with a large pupil only the red channel of the Cannon CCD has been displayed in this Figure to avoid confusion.
Figure 6.7 shows the images at the slicer focal plane, taken with the small ($114\mu m$) pupil, showing the diffraction limited zeroth and first orders created by the transmission grating. The spot size and location changes with wavelength, as expected. The Canon camera used is a three colour SLR CCD with red, green and blue sensitive pixels, see Figure 6.8(b). This is the reason for the three distinct circles seen in the image.

Magnification

By measuring the separation of the 5 pin holes in the focal plane mask using a microscope, the magnification of the system was able to be calculated by comparing the separations of points in the real mask to those measured on an image of the mask taken by the Canon CCD a the location of the slicer stack, shown in Figure 6.8(b). The system magnification was designed to be 3.0 and we get a measured value of 2.97 which is within our requirements.

Diffraction Limited Size

Using a the RG610 filter we were able to get a measurement of the FWHM of the first diffracted order of our pre optics setup at $\sim 610nm$. It was calculated to be $916\mu m$, comparing this to the designed value of $846\mu m$ at 610nm, shows it to be slightly larger, which is fine for our experiment. The value is large is due

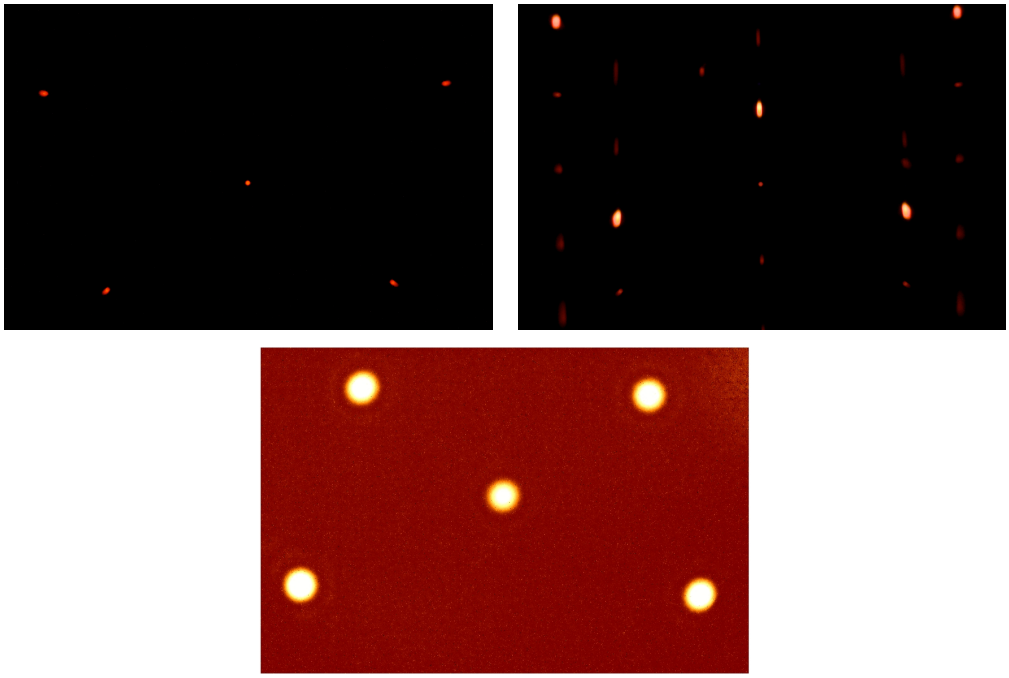

Figure 6.6: Images from a Cannon CCD placed at the location of the slicer stack with the 5 pin hole mask imaged without (top left) and with (top right) the diffraction grating in place. Note that the diffraction grating is blazed so that the first order diffraction is brighter than the zeroth order. The bottom image is from not having the diffraction grating in place but with the small pupil. For this test the RG610 filter was in place.

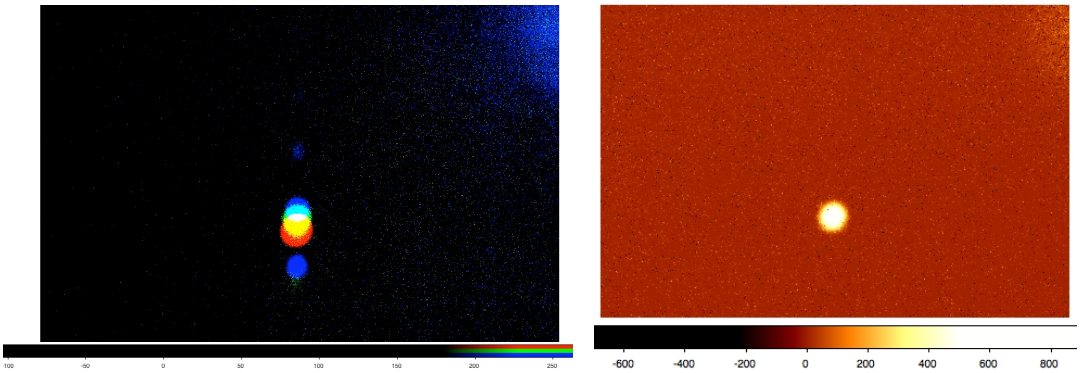

(a) SpeckleRGB (b) SpeckleR610

Figure 6.7: Images of the central spot, taken at the location of the image slicer using a Canon SLR CCD, with the diffraction grating inserted in the pre-optics. The left hand panel shows the blue, green and red spots from the grating's first order diffraction. The 0th order spot can also be seen, as can the second order in blue light. Note that the diffraction limited spot size changes with wavelength, as expected. The right panel shows the image after inserting the 610nm cut-in filter, that overlaps the Canon CCD sensitivity only in the red band. Detail of the RG610 filter and Canon RGB bands can be seen in Figure 6.8

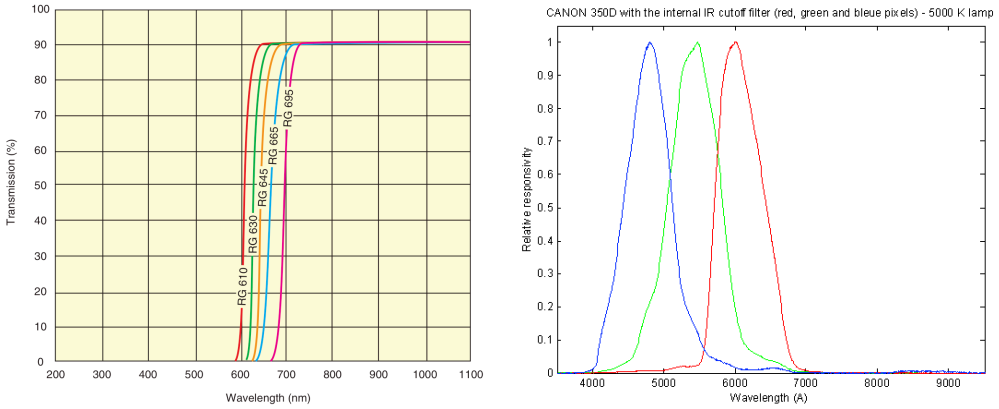

Figure 6.8: (a) shows the transmission efficiency of the RG610 filter, (b) shows the location and relative responsivity of the RGB spectral bands of the Canon CCD used, note that the peak response of each spectral bands is normalized to unity. The relative response is therefore not conserved in this plot

to all of the light long-ward of 610nm being observed up to the tail off in the Cannon camera's QE.

Location of the First Diffracted Order

Using the 830nm laser line filter we were able to measure the location of the zeroth and first orders of the diffraction grating at the location of the slicer stack. The separation was found to be $4.34mm \approx 9.23slices$. This is acceptable for our tests.

6.1.2 Slicer Integral Field Unit

As the prototype slicer that was built was based on the SWIFT slicer it makes sense for us to first describe the specifications of the SWIFT instrument before moving onto the design of the SWIFT slicer and the specification of the prototype slicer.

SWIFT

The Short Wavelength Integral Field specTrograph (SWIFT) is an AO assisted I & z band IFS that was designed and assembled at Oxford University and commissioned for the Palomar 200" Hale telescope in October 2008, shown in Figure 6.9. SWIFT has 44 slices each of which is sampled by 89 spatial pixels at the detector thus allowing the simultaneous observation of ~ 4000 spectra. The preoptics of the instrument gives an anamorphic magnification of 2:1 along the slicer giving it a rectangular field of view. A choice of

three pixel scales are also provided by the instrument, for details see Table 6.1. The instrument was designed to have a very high throughput, $\sim 35\%$ (Thatte et al., 2006), and to be very compact, so as to fit behind the PALMAO system at the Cassegrain focus or the Hale telescope.

Parameter	Value
Wavelength Range - Dichroic 1	$650 - 1050nm$
Wavelength Range - Dichroic 2	$750 - 1050nm$
Spectral Resolving Power	4000
Field Format (spaxels)	44 x 89
Field of View (0.235" per spaxel)	10.3" x 20.9"
Field of View (0.160" per spaxel)	7.0" x 14.2"
Field of View (0.080" per spaxel)	3.5" x 7.1"

Table 6.1: SWIFT specifications

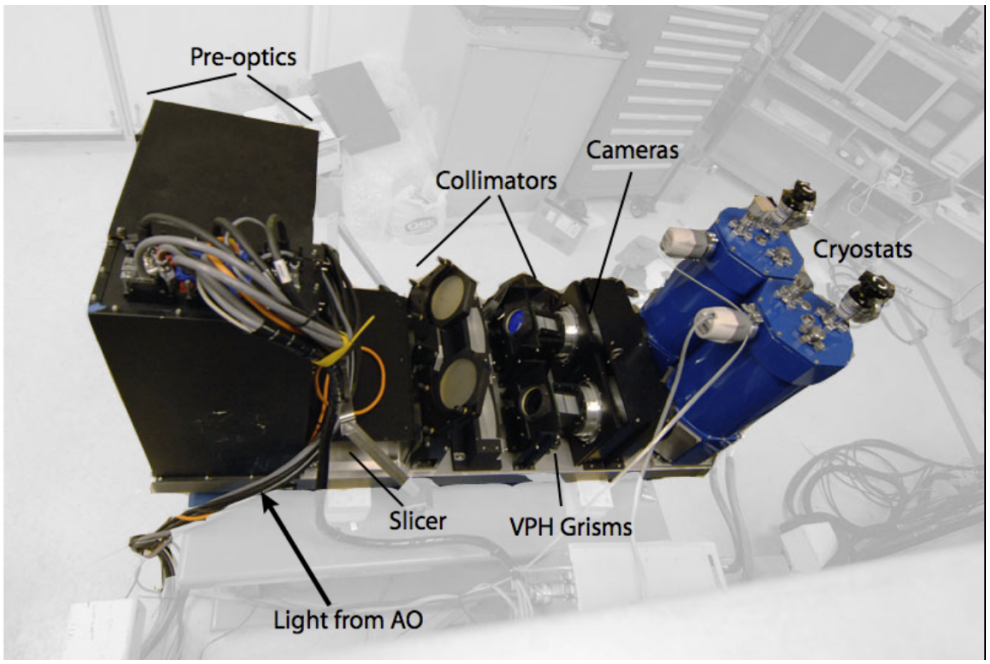

Figure 6.9: Annotated photograph of the assembled SWIFT instrument

SWIFT Slicer Design

In order to achieve the compact configuration needed for the SWIFT image slicer, while still using flat, conventionally polished slicing mirrors, the "standard" design such as that of SINFONI (Eisenhauer et al., 2003), see Section 7.1, had to be modified. The new design still uses two sets of flat mirrors for the slicing and re-arranging of the input field, but additionally uses a mosaic of identical small lenses to de-magnify the input field thus creating a shorter exit slit (see Figure 6.10 for an illustration of the principle of the slicer). By using conventionally polished optical surfaces a much higher grade surface finish is achieved leading to less scattered light and higher throughput than diamond turned surfaces, especially at the SWIFT wavelengths ($0.65-1.05\mu m$). A cartoon showing the path of the light through the slicer can be seen in Figure 6.10 and a photograph of the SWIFT slicer is shown in Figure 6.11.

* The entrance pupil location is 162mm beyond the slicer focus and at the optimum slice width of 0.47mm the entrance pupil diameter is 4.1 mm. The focal length of the mini lenses is 38.88 mm, and the de-magnification is 0.24.

The individual slice length in the slicer stack is $0.5 \times 0.47mm \times 89 = 20.915mm$, leading to a slitlet length in the exit slit of $0.24 \times 20.915mm = 5.0196mm$. The factor 0.5 accounts for the anamorphic magnification of the pre-optics, which is needed to achieve Nyquist sampling of the spectra on the detector.

Including the gaps of $4 \times 0.235mm \times 0.24 = 0.2256mm$ between them, the slitlets in the exit slit have an equidistant spacing of 5.2452mm, the total exit slit-length for one slicer subset is $22 \times 5.0196mm + 21 \times 0.2256mm = 115.1688mm$.

Each mini-lens has a diameter of $2 \times 5.2452mm = 10.4904mm$, the stagger in dispersion direction between neighbouring slitlets due to the close-packing of the mini-lenses is $10.4904mm \times 0.5\sqrt{3} = 9.0850mm$.

The centre-to-centre distance between the exit slits is 230mm, corresponding to a gap between the two slits of 114.8312mm.

A key element of the SWIFT slicer is the location of the slicer entrance pupil. The entrance pupil is located a relatively short distance beyond the slicer stack, i.e. the rays past the slicer stack "converge" towards a mini-pupil 162 mm past the slicer. It is this position of the exit pupil which allows the compact layout with built-in de-magnification.

*Slicer parameters have been drawn from EPICS Phase 1 review documents

The exit pupil created by the slicer is telecentric, both within each slice, and across all slices. This allows a normal spectrograph geometry. The exit focal plane has a staggered slit, with a zig-zag pattern in the dispersion direction. This is essential to retain all the light, and prevent vignetting within the slicer.

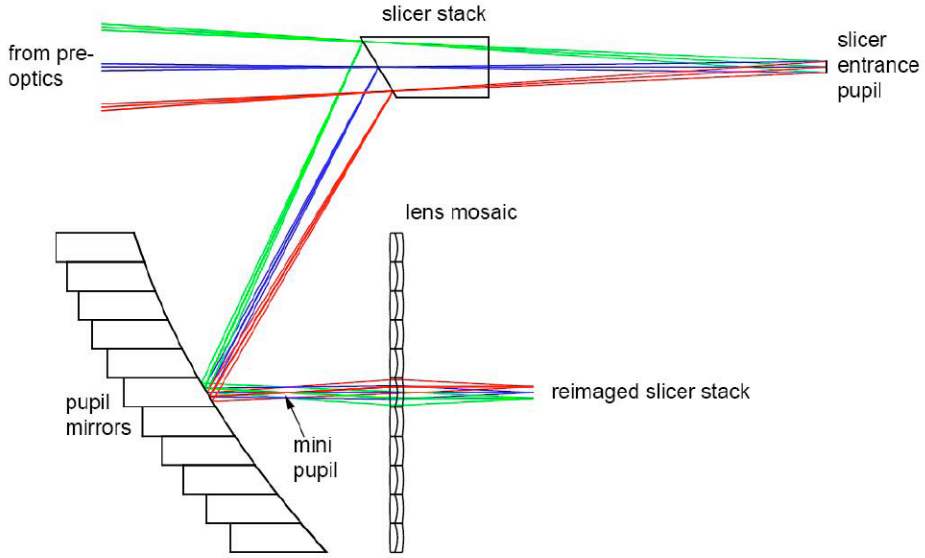

Figure 6.10: The principle of the SWIFT image slicer (the prototype image slicer shares this design) is illustrated here. Two sets of flat mirrors (slicer stack and pupil mirrors) re-format the input field, while the lens mosaic provides the required de-magnification and a telecentric exit slit

Prototype Slicer

The SWIFT slicer contains 44 slices. Of these, only four at the bottom edge of the field, four at the middle of the field, and four at the top of the field are active in the prototype slicer, the rest of the focal plane is occupied by spacer blocks of Zerodur. The reasoning behind only manufacturing a few active slices was to save cost. Within this overall layout, the SWIFT image slicer consists of two subsets of identical image slicers. Each subset re-arranges half of the input field (22 slices) and forms a long exit slit. As only one spectrograph is implemented in the prototype IFS, only six active slices are available within the field of view.

The entire slicer including the baseplate and spacers, except the doublets, is made from Zerodur, a glass ceramic that is easily polished to high surface quality. The individual mirrors, baseplate and spacers are

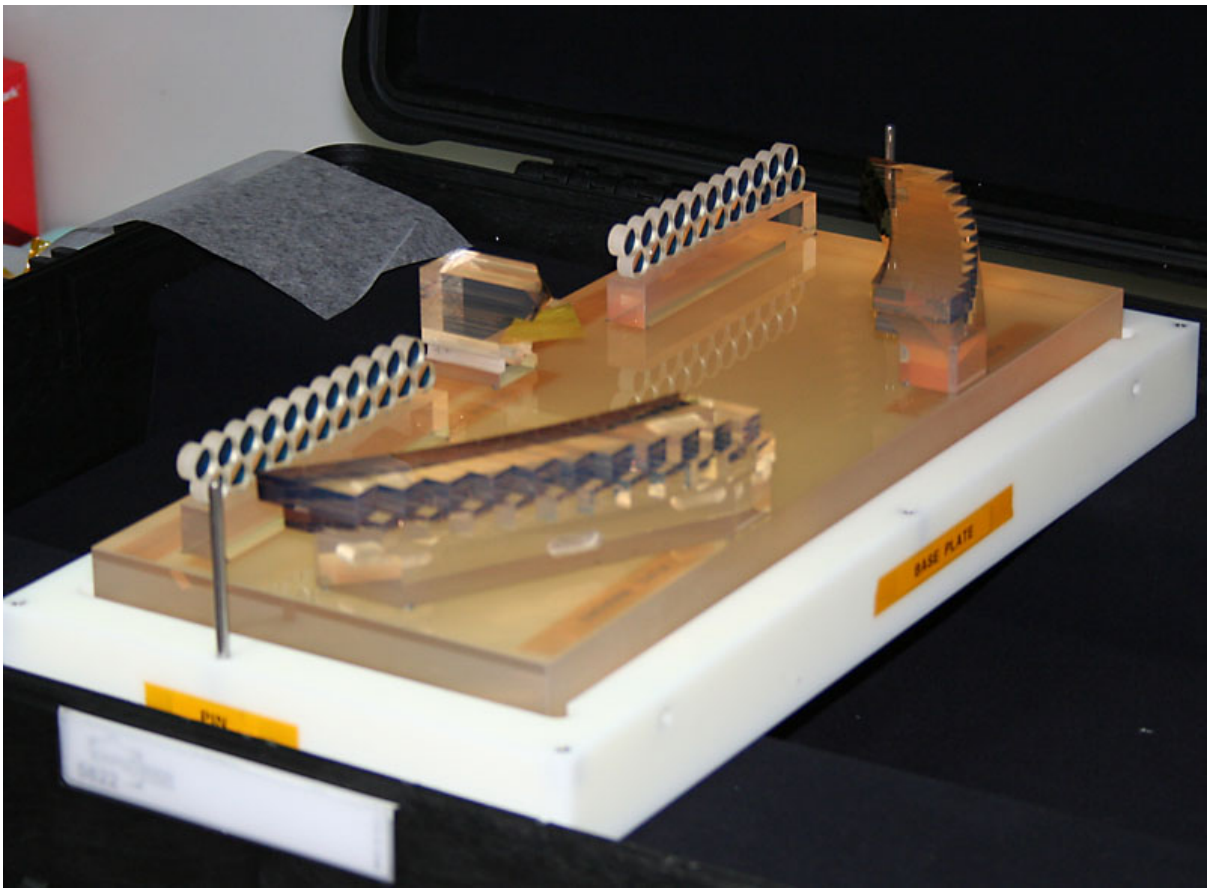

Figure 6.11: Photograph of the SWIFT slicer when it was delivered by Winlight Optics in 2007.

held together by optical contacting only, this contact is virtually impossible to break. The lens mosaics are glued to the spacer that is optically contacted to the baseplate.

To have adequate image quality the lens mosaic is made from cemented doublets, which provide the necessary colour correction and have almost no aberrations.

The prototype image slicer, with 12 active slices (6 in each half stack), was built by Winlight Optics S.A., following the same design prescription as the slicer for the SWIFT spectrograph (Tecza et al., 2008). Figure 6.13 shows a photograph of the prototype slicer, as delivered to the University of Oxford. The slicer underwent full system acceptance tests at the manufacturer, prior to shipping. The relevant form errors were in the range 11 to 20 nm rms for the lens doublets (operating in transmission), between 0.05 and 0.17 λ rms for the pupil mirror array, and between 0.12 and 0.28 λ rms for the slicer mirrors. Due to the limited number of slices present in the prototype image slicer (a consequence of cost limitations), it is not possible to image

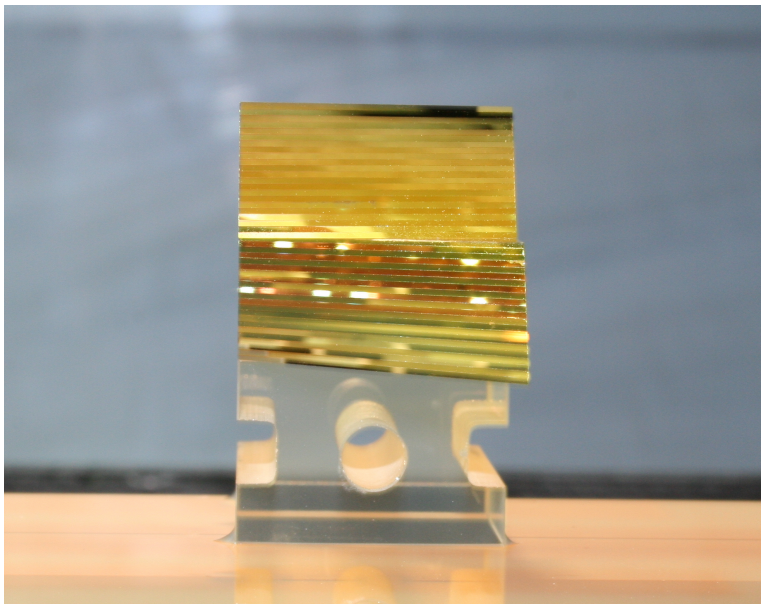

Figure 6.12: Close up of the SWIFT slicer stack.

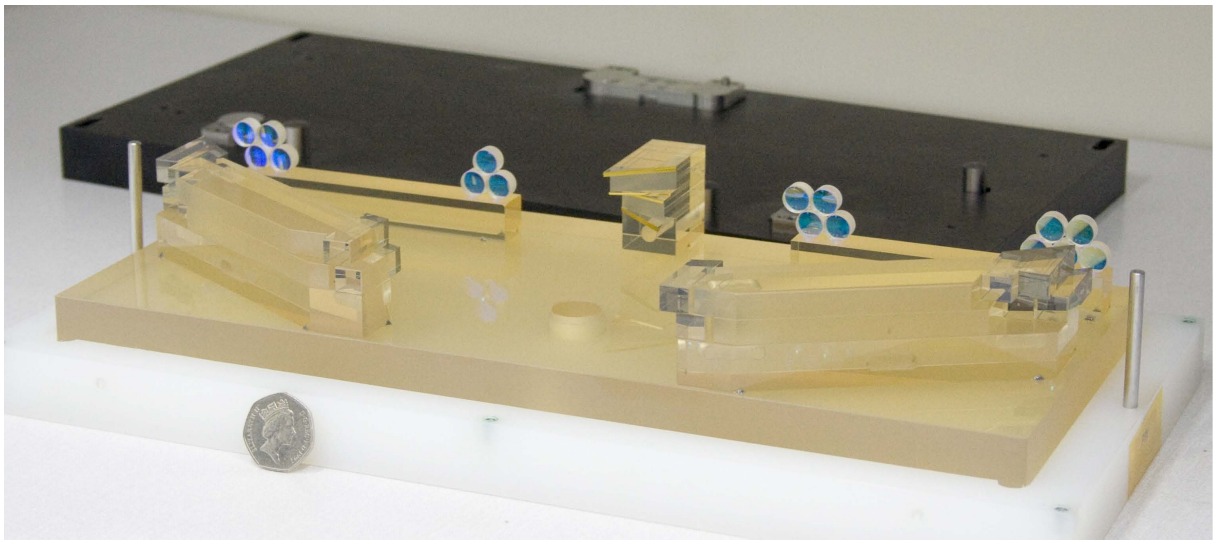

Figure 6.13: Photograph of the prototype image slicer, showing the active slices and the active mini lenses. The mounting plate (black anodized aluminium) can be seen in the back. A UK 50p (equivalent in size to a 2 Euro coin) coin provides the scale.

both the speckle and the central source at the same time. Instead, we mosaic 5 sets of observations together to produce a 16 slice datacube (one slice of each set is redundant) which contains both the diffracted spot and the central source.

Wave Front Error by Design

By design the performance of each slice is identical. Figure 6.14 shows the RMS WFE seen by different wavelengths at the slicer. With a maximum of $\sim 5 \times 10^{-5}$waves the wave front error introduced by the slicer will be negligible by design. In reality manufacturing errors will have a larger effect.

6.1.3 Spectrograph

The speckle is sliced by the image slicer, and the light from each slit is dispersed on to the spectrograph detector, a schematic view of the spectrograph and an Inventor rendered view can be seen in Figures 6.15 & 6.16 respectively. SWIFT is designed to accept an anamorphic focal ratio of 2:1 (as is introduced by the SWIFT pre-optics). The etendue of the slicer-spectrograph system is larger than the geometrical etendue of the input beam by a factor of 16 across the slices and a factor of 32 along the slices. Thus ensuring that over 99% of the light is transmitted through the spectrograph optics, even though there is substantial diffraction at the slicer (located in a focal plane). The dispersion of the SWIFT spectrograph is much higher than required for an exo-planet application ($R \sim 4000$ instead of $R \sim 500$), so we planned to bin 10 wavelength channels to produce the final data cube, simultaneously improving the photon counts in this way.

Colimator

The collimator is a catadioptric design, composed of two cemented doublets, and a spherical mirror. Less than half of the larger doublet is used (it is operated off-axis), and thus only a half lens is required. The collimator can also allow for magnification correction in the as-built spectrograph.

Disperser

The disperser in the spectrograph is a VPH grating sandwiched between two prisms. The prisms disperse more at blue wavelengths, while the grating dispersion is larger at longer wavelengths. The two effects partially cancel each other, leading to a smaller variation of dispersion with wavelength (a flatter dispersion curve). In addition, the prisms have the advantage that they flatten the grating efficiency curve, although the effect is small in our design. The spectrograph has a mean resolving power $R \sim 4000$ over the wavelength range of $0.65 - 1.05 \mu m$

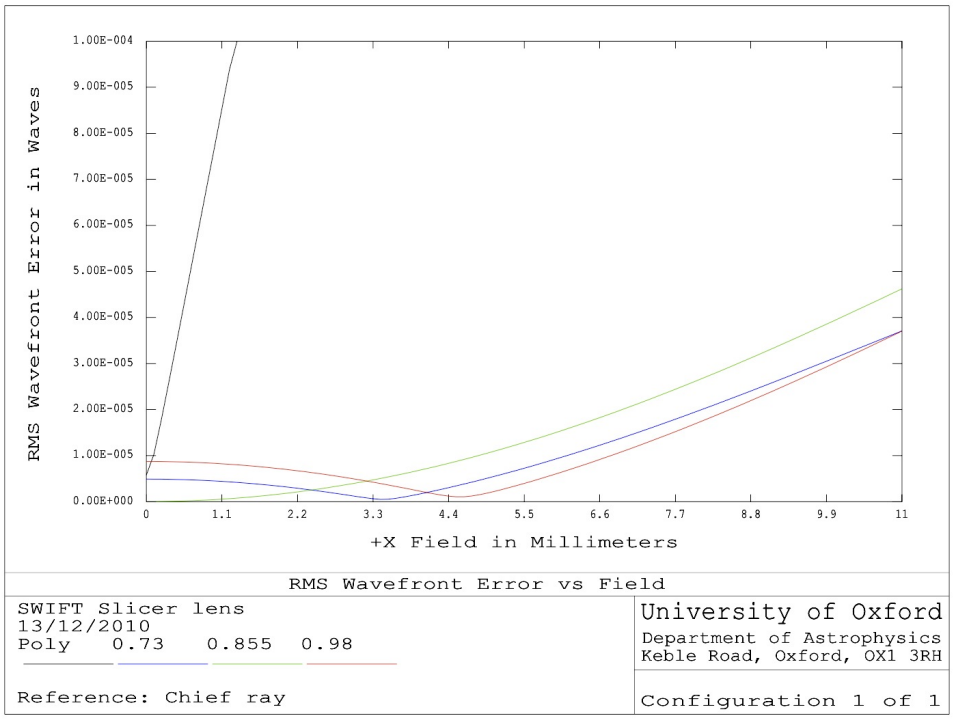

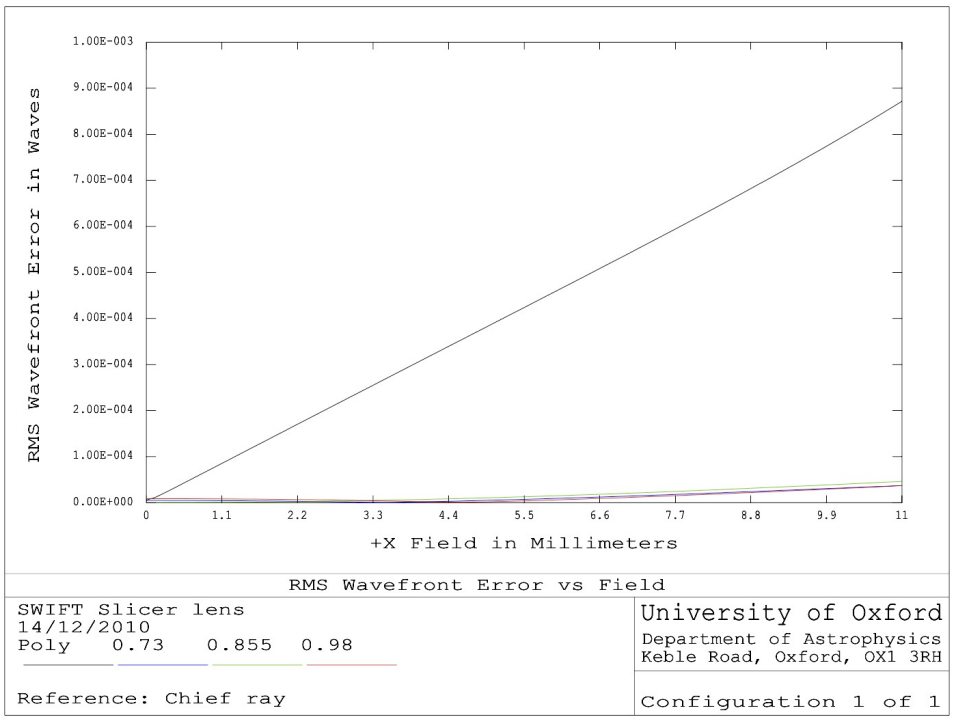

Figure 6.14: RMS wavefront error as a function of position of the slice for three wavelength that cover the wavelength range of our tests.

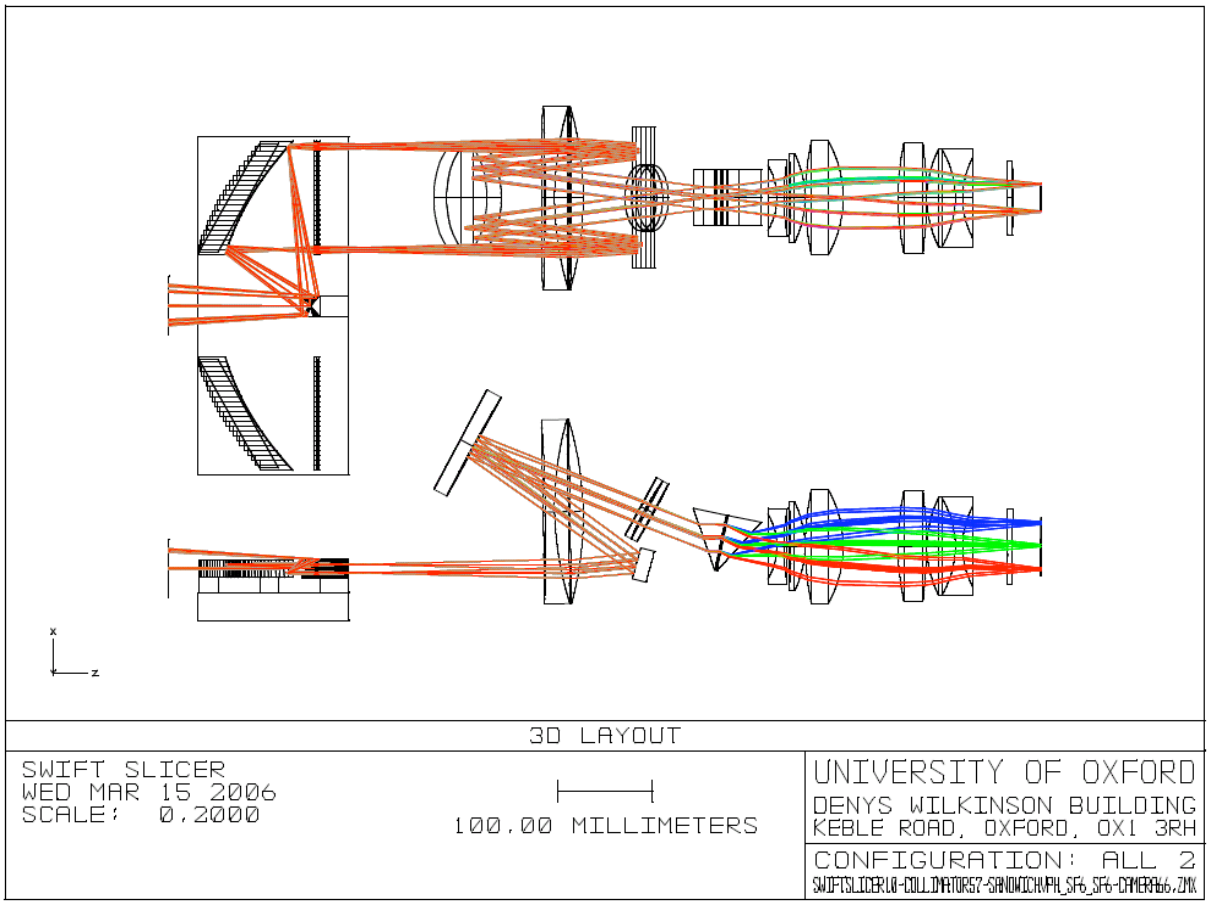

Figure 6.15: Schematic view of the image slicer with one spectrograph. The first collimator lens is shown full size, but only a segment (lower third) is used in practice.

Camera

The spectrograph camera is a fully transmissive design, comprised of lenses with only spherical curvatures. This makes it relatively cheap and easy to manufacture. The camera lens comprises 6 lenses in 5 elements, and provides excellent performance, with over 80% ensquared energy per detector pixel. It also provides almost straight spectra at the detector, with a maximum deviation of only ± 0.9 pixels over the entire slit length and wavelength range.

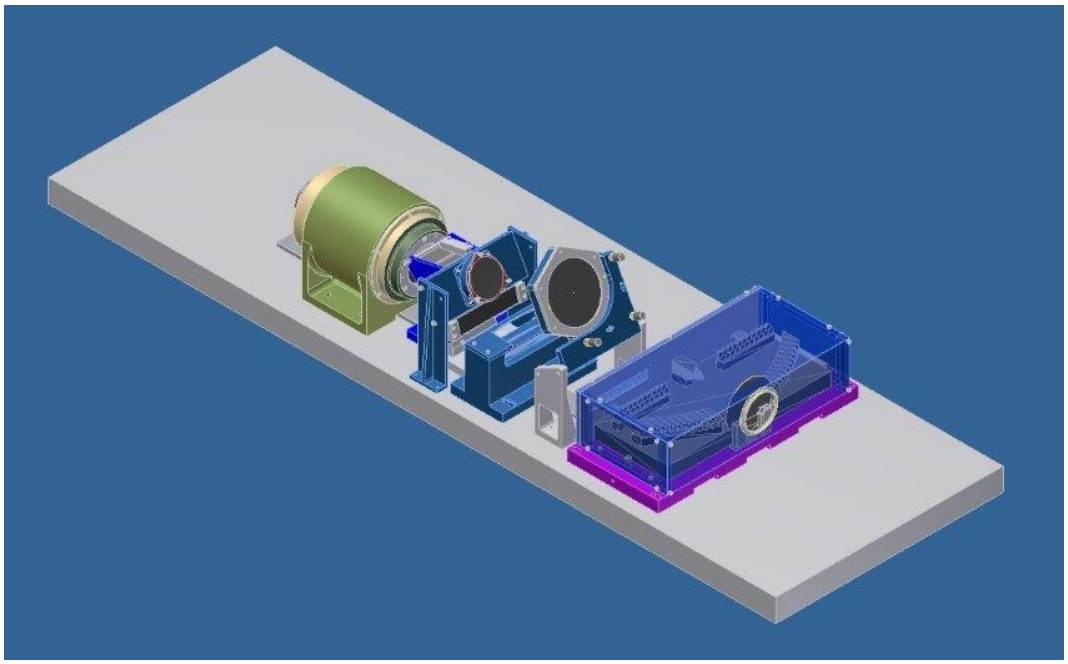

Figure 6.16: An Inventor rendered view of the slicer and spectrograph.

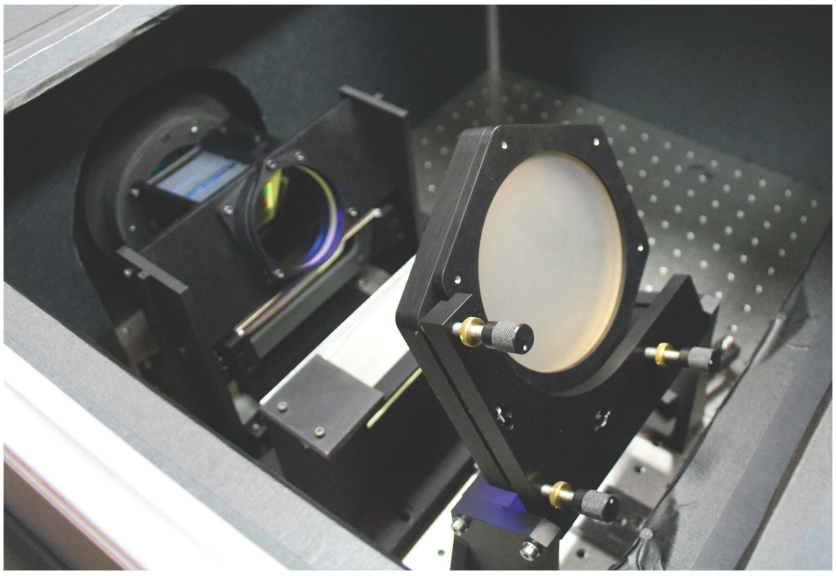

Figure 6.17: Photograph of the assembled spectrograph. In this view you can just see the first lens of the camera barrel on the left. The Slicer is just out of view on the right hand side.

Wave Front Error by Design

The wavefront error that is introduced by the spectrograph will have a greater effect than that of the slicer, it is this that was thought could compromise the high contrast performance of the IFS. However, as is shown in Figure 6.18, the WFE by design of the spectrograph is $\sim$ 5nm RMS for slice 11, with a much smuller differential wavefront error between slices of $<$ 1nm. Thus we will likely again be limited by manufacturing errors rather than design.

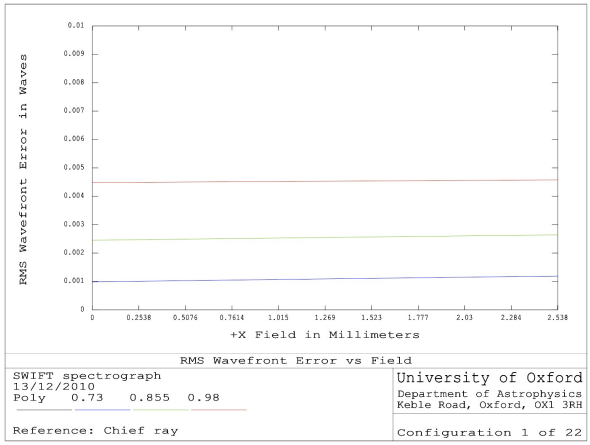

(a) Slice1

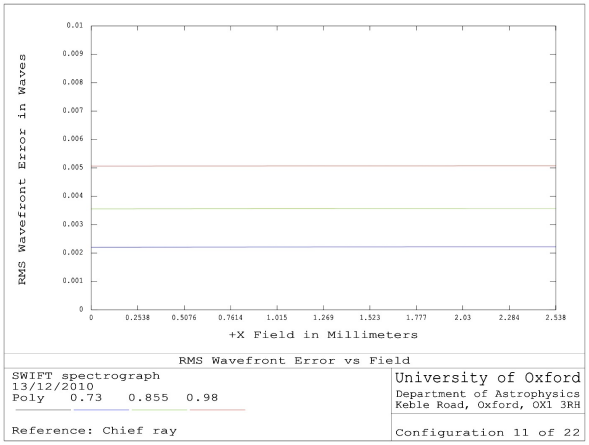

(b) Slice11

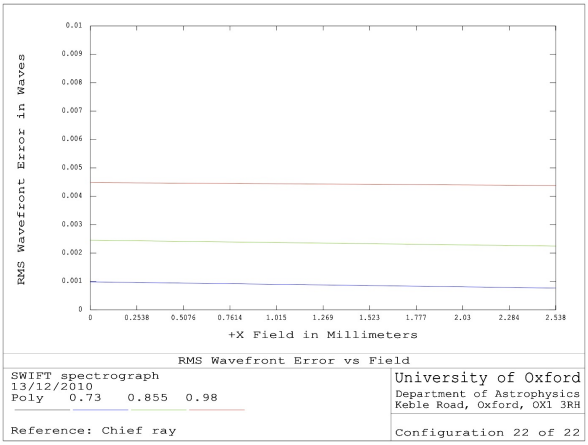

(c) Slice22

Figure 6.18: RMS wavefront error introduced by the spectrograph as a function of field points along the single slitlets for three wavelengths covering the wavelength range of our experiment

Assembly and Alignment

The camera lenses were assembled in their barrels, with the help of Dr. Matthias Tecza, following the same procedure as for the SWIFT spectrograph optics (using a CMM to confirm the centering of the lenses). Each lens has been centred to $10\mu m$ or better in its mount. The other elements of the spectrograph (collimator and disperser) were aligned, also following the prescription for the SWIFT spectrograph, which includes capabilities for adjusting the magnification (via collimator element spacings).

The spectrograph focus governs the image of the pseudo-slit at the detector, and thus controls the spectral resolution, as well as the image quality along one spatial dimension of the image. The image is sampled at the slicer in the other dimension (across slices), so that the spectrograph image quality has no influence in that dimension.

6.1.4 CCD

Laboratoire d'Astrophysique de l'Observatoire de Grenoble (LAOG) lent us the CCD used for the experiment, it was a 3K x 3K Apogee ALTA U9000 which had an inbuilt forced air, thermoelectric cooler capable of cooling to $45°C$ below ambient temperature with a stability of $\pm 0.1°C$. The CCD was controlled using a piece of commercial software (Nebulosity). As can be seen in Figure 6.19 the quantum efficiency of the CCD drops from $\sim 50\% - 10\%$ over the wavelength range we are interested in. This will result in a significant decrease in signal to noise at the long wavelength end of our data.

The CCD has a purpose built alignment stage containing linear, tip/tilt and gimbal stages. This was designed and built by Matthew Brock and Fraser Clarke. The CCD was focused by using an Argon Arc lamp in the integrating sphere with the 5 pin holes illuminated, this produced a grid of point sources that could be moved to different slices by moving the integrating sphere up and down. Through focus scans of these point sources could then be performed using the CCD alignment stage to find the best focus. The depth of focus of the detector is $\sim 1mm$ which is very easily achievable with the micrometer adjusters of the alignment stage.

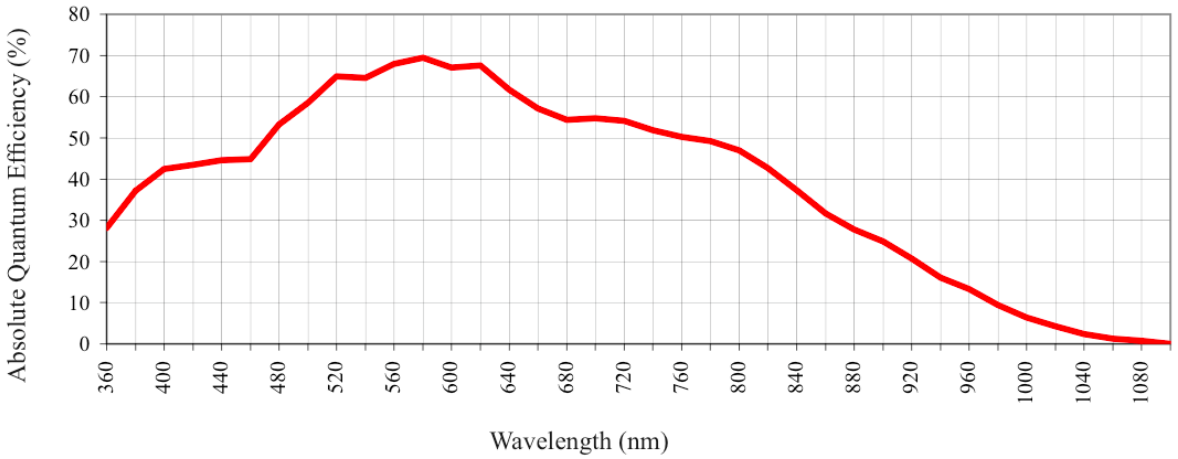

Figure 6.19: Quantum efficiency of the Apogee ALTA U9000 3K x 3K CCD as provided by the CCD datasheet.

Camera Name	Apogee ALTA U9000
CCD	Kodak KAF-09000
Array Size (pixels)	3056 x 3056
Pixel Size	12 x 12 microns
Imaging Area	36.7 x 36.7 mm (1345mm^2)
Linear Full Well	79K electrons
Dynamic Range	84 dB
Digital Resolution	16 bits at 1 MHz
System Noise	9.9 e- RMS at 1 MHz
Exposure Time	30 milliseconds to 183 minutes (2.56 microsecond increments)
Cooling (typical)	Thermoelectric cooler with forced air. Max 45°C below ambient
Dark Current (typical)	<0.6 e-/pixel/sec (-25°C)
Temperature Stability	$\pm$ 0.1°C
Gain	1.2 (electrons per count)
Bias level	1345 (counts)

Table 6.2: Details of the Apogee ALTA U9000 3K x 3K CCD taken from the CCD datasheet and camera test report supplied with the camera.

6.1.5 CCD Characterisation

Bad Pixel Detection and Removal

Multiple dark exposures are taken with an integration time of 20 minutes (two times longer than the longest integration time of any of our measurements). These images were clean meaned[†] together thus removing any cosmic rays and reducing the relative dark and read noise.

Firstly all bad columns identified by eye are masked out manually. A 2 sigma upper and lower cut is then made on the data to remove the strongest outliers. Then a 15 pixel wide box car smoothed image is removed to take out any global variations in the dark. An itterative sigma clip is performed. All pixels identified are considered bad and the resultant bad pixel mask can be seen in Figure 6.20. Total number of bad pixels found, including bad columns is $\sim 3\%$ of the whole detector. Bad pixels are interpolated over using the IRAF `FIXPIX` routine.

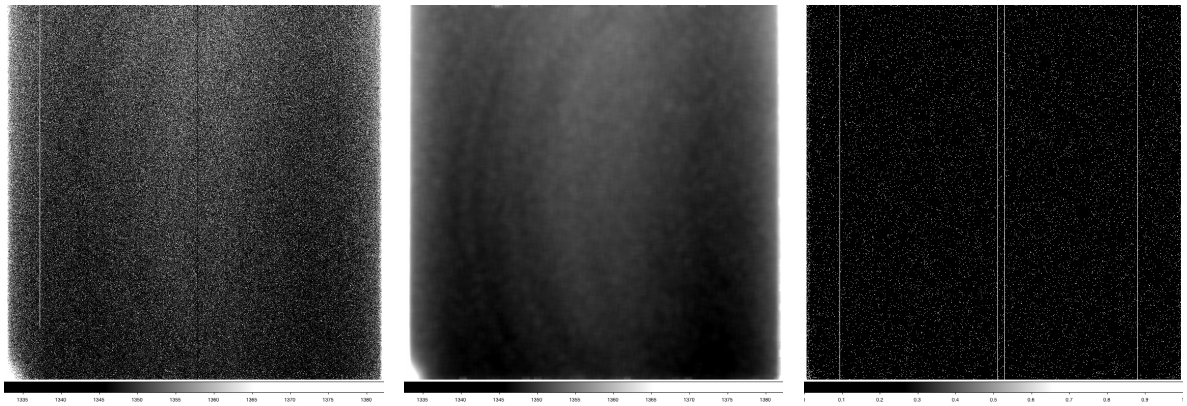

(a) Combined 20min dark exposures (b) Box car smoothed image (c) Found bad pixels (in white)

Figure 6.20: Method of bad pixel finding

Linearity

With the limitations of our experimental setup we can not uniformly illuminate the CCD. Instead, to investigate the CCD's linearity, we use a series of flat fields at different exposure times. Pixels are binned according to their intensity at the longest exposure time. Taking into account bad pixels, 20 such bins have been made spanning the range 33,000ADU - 53,000ADU at 60 seconds exposure time in 1,000ADU inter-

[†]For each detector pixel, the stack of exposures are sorted, the lowest and highest value are rejected, and the rest combined (using a mean) to form a master frame.

vals, the maximum read out given by the analogue to digital converter is 65,535ADU. Each bin contains between 150,000 to 250,000 pixels. The mean value of the intensities is found for each bin at each exposure time and the results can be seen in Figure 6.21(a). Figure 6.21(b) shows the same data divided by exposure time to give the mean intensity per second. There is a significant hump around the 5 second mark that was slightly worrying, however looking at Figure 6.21(c) which has had each bin divided by its mean value, we can see that the affect is roughly constant for all bins and should not cause us a problem. The hump appears to be an imperfection of the CCD controller software, possibly coupled with an affect of the finite shutter speed. There is also a dip at 45 seconds which we again think must be due to the controlling software as it is an identical dip for each of the bins (possibly a timing error of the control software). Figure 6.21(d) shows the previous plot normalised to the lowest intensity bin showing the slight non linearity of the CCD when going to the higher intensities. Intensities of exposures taken should, therefore, not be so high so as to be affected by this very slight non-linearity. For the case of our experiments the maximum intensity of the speckle in any single exposure is $\sim 6000 ADU$. By relating this to the highest intensity curve in Figure 6.21(d) shown (53,000ADU at 60sec) this suggests that the data around the 7 second mark would give the relative non-linearity, which is very small.

Gain

To calculate the gain a set of 30x10sec exposures were used. Each had a dark frame removed from it. Bad pixels found previously and all pixels below a set threshold were flagged not to be used in this calculation. For every "good" pixel a mean and standard deviation value was determined and hence the gain was calculated via Equation 6.3, assuming the noise on the signal should follow Poisson statistics plus the read noise, N_R. We then determine the mean value of the calculated gains.

$$\textbf{gain} = \frac{Signal}{\sigma^2 - N_R^2} \tag{6.3}$$

By this method, and the following calculation of the read noise, the Gain was calculated to be $1.23 e^- / ADU$. This is a good match to the manufacturers determination of $1.2 e^- / ADU$, shown in Table 6.2

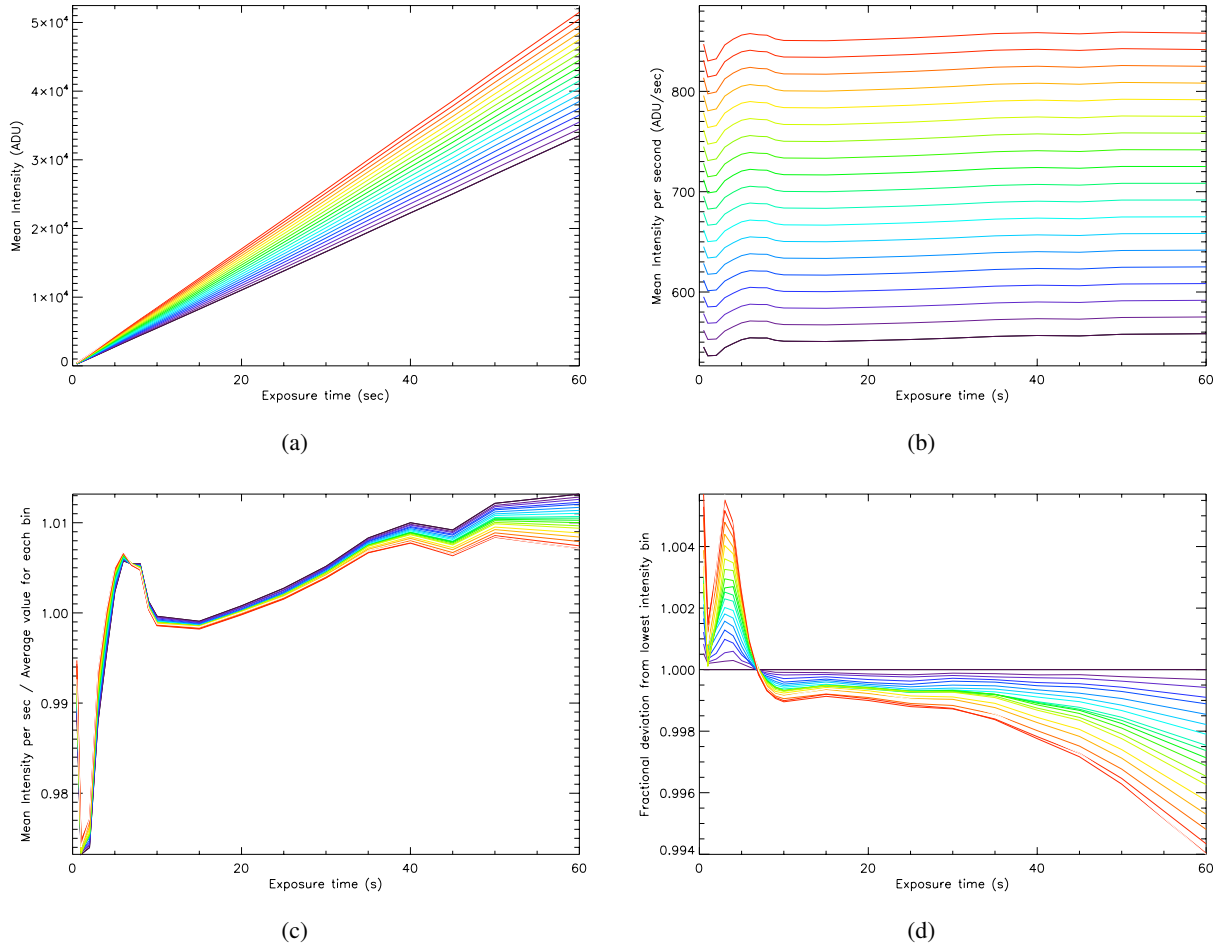

Figure 6.21: Linearity of the CCD: Sets of flat fields were taken at different exposure times, the pixels in theses exposures are binned according to their intensity at the longest exposure time. Bins range from 33,000ADU - 53,000ADU at 60sec in 1,000ADU intervals. (a) shows the mean values of the intensities of each bin at each exposure time. (b) shows this result divided by the exposure time of each image, giving a mean intensity per second. (c) shows the result of each bin, at this stage, being divided through by its mean value. (d) shows the previous curves divided by the lowest intensity bin curve, giving the fractional deviation from the lowest intensity bin.

Read Noise

Two frames of zero exposure length were taken and differenced, by doing this we remove any overall gradients in the bias frame and are left just with the structure of the noise. A typical region was identified covering 100k pixels and the standard deviation was found $\sigma = 11.1 ADU$, the read noise can then be calculated by dividing by $\sqrt{2}$, as two frames with read noise have been subtracted from each other. The read noise is therefore found to be $N_R = 9.5 e^- / pix$, using our previous measurement of the gain, as compared to the $9.9 e^- / pix$ RMS noise as quoted from the data sheet in Table 6.2.

Dark Current

To determine the dark current of the CCD at the operating temperature for our experiment $(-12°C)$ a set of dark frames taken at different exposure times are taken. Each has a bias frame subtracted from it and all known bad pixels corrected. A typical region covering 100k pixels was identified that was free of cosmic rays, bad columns etc. The mean value of this region was then determined and the resultant curve can be seen in Figure 6.22. The CCD has a calculated dark current of $\sim 1.0 ADU / min$ per pixel, for our 10 minute science exposures this gives us a dark current of 10ADU/pixel. Given that the gain is $1.23 e^- / ADU$, as calculated previously, this gives us 12.3 electrons of dark current per pixel. Assuming Poisson noise this will leave us with a dark current noise of $\sqrt{12.3} = 3.5 e^-$ for a 10 minute exposure.

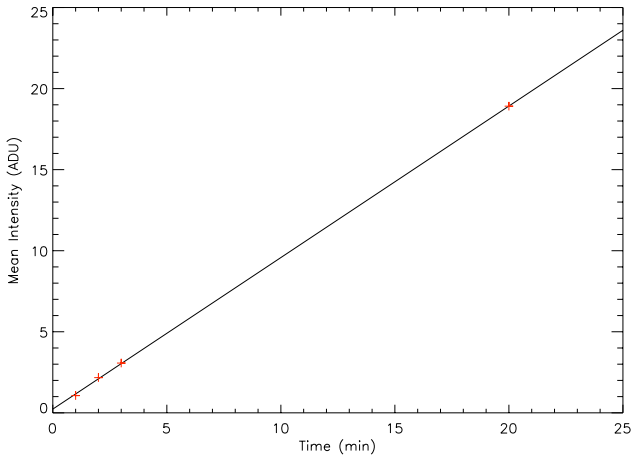

Figure 6.22: Mean intensity (ADU) of a typical region of dark frames with different exposure times

6.2 Implementation of the Spectral Deconvolution Method

The way spectral deconvolution is performed has a huge impact on the result. It is necessary here to justify some of the subtleties of the method that has been used as it is important to show that we are fitting the speckle in a manner that could be used with on-sky data and in a way that would not also remove the signal of a companion. The determination of the achieved contrast can be made in many ways, including some that may give the reader the impression that a far better rejection has been achieved, compared to reality. Our calculation of the speckle rejection factor is also explained at length in the following section.
It should be pointed out that the purpose of the following experiment has not been to look at the characteristics of the simulated speckle we have produced. Our simulated speckle is a special case as it has no central star from which it has been formed, instead it has its associated zeroth diffraction order. Characteristics of the speckle, needed for spectral deconvolution, that are normally calculated from the primary star itself need to be computed differently and an accurate way of measuring such characteristics, without affecting the result of the experiments, needs to be determined. The methods we have followed are discussed here.

6.2.1 Method of Scaling

It has been shown that a greater accuracy can be preserved by performing the scaling using Fourier techniques, described in Section 5.1.2. This is the method that was employed here, however, due to our limited field of view the Fourier transforms can produce larger amounts of noise than that previously described. This is due to the loss of the fraction of the PSF information falling outside of the field of view. There are a few ways of manipulating the data so as to help reduce the Fourier noise, as described in Section 5.1.3. For the analysis we present we have used an embedding of the real data in a set of fake data containing radial averages centered on the speckle, this is then embedded in a smooth function that tapers to zero. Other manipulations such as the removal of an Airy pattern that could be analytically scaled and added back in the scaled plane were also tried but this embedding seemed to produce the best results.

6.2.2 Centroid of Scaling

As our speckle is made from the first diffracted order of a diffraction grating its location compared to the location of the zeroth diffracted order should scale perfectly with wavelength. However, as long as the simulated speckle moves over a sufficient number of slices and its movement can be accurately accounted for, the accuracy of this dependance has no influence on our measurements. The wavelength dependance of our simulated speckle may be distorted due to effects such as the tilt of the diffraction grating or in the case of the tests using the SWIFT slicer where the FoV is imaged onto the whole slicer stack in one go, see Section 6.4, the footprint on the field lens is quite large, see Section 6.1.1 and the zeroth order position may get slightly distorted due to passing through near to the edge of the lens. In order to avoid such effects we decided to centre the data on the simulated speckle itself. This was also of benefit to us as it would provide a more accurate estimate of the centring, this is because there is a higher signal to noise on the first diffracted order than the zeroth order, due to the efficiency of the diffraction grating, and the placement of the zeroth and first orders in our data sets puts the zeroth order very close to the edge of the field of view (sometimes with the central core of the zeroth order partially outside of the field of view) which makes it difficult to centre on.

6.2.3 Spectrum of the Speckle

In every application of spectral deconvolution the data cube needs to be normalised by the spectrum of the parent star. The speckles that have been produced from the stellar flux should have the same spectrum as the star itself which needs to be taken out to leave us with speckles that have a flat spectrum that can be fit out. However, in the case of our experimental set up we do not have a central source from which our simulated speckle is made. The spectrum of our simulated speckle is a combination of the lamp spectrum in the preoptics, the throughput of the slicer integral field spectrograph and the efficiency of the diffraction grating for its first diffracted order. The efficiency of a diffraction grating is different for each of its diffracted orders, this prevents us from using a measurement of the zeroth diffracted order as our normalising spectrum.
We were able to generate a theoretical efficiency curves for both the zeroth and the first diffracted orders of our diffraction grating using the PCGrate program, with the assistance of Matthias Tecza. These curves are shown in Figure 6.23(a). The high frequency ripples seen around 750*nm* and 850*nm* are thought to be

a numerical artefact from the PCGrate software. The ratio of the two orders varies quite smoothly with wavelength, which is a property that can be quite well fit by spectral dconvolution, however, there are a number of small wiggles in the spectrum, see Figure 6.23(b), which may not look like much but they are by far large enough to cause problems when trying to fit the speckle and would thus cause a limit to the achievable speckle rejection factor. It is thus justifiable to use a spectrum determined from the simulated speckle itself. The spectrum is calculated over a section of the field of view that covers at least the core of the speckle and its first Airy ring at all wavelength but does not contain any flux from the zeroth order (apart from the very faint Airy rings hidden in the noise). We believe we are getting a true representation of the simulated speckle's spectrum. In doing this we are not calibrating out any effects of the slicer itself as the speckle is imaged onto multiple slices at any wavelength, all of which are used to calculate a single spectrum.

6.2.4 Order of Polynomial Fit

When fitting a polynomial to the speckle spectrum one has to be sure to fit the correct order. Too high an order of fit can end up fitting out any companion signal that may also be present. The order of polynomial you can legitimately fit varies according to the distance you are from the primary source. This is because the further away a speckle is from the primary star the more it moves radially outwards with increasing wavelength. However, in the following experiments the centroid or our generated speckle only moves a distance of ~ 2.5 slices over the entire wavelength range observed, i.e. the speckle is at a distance not that much larger than the bifurcation radius of the set up (see Section 2.3.3). It is therefore unreasonable to fit a polynomial any higher than second order to the speckle spectrum. We have used a second order polynomial in all of our analysis.

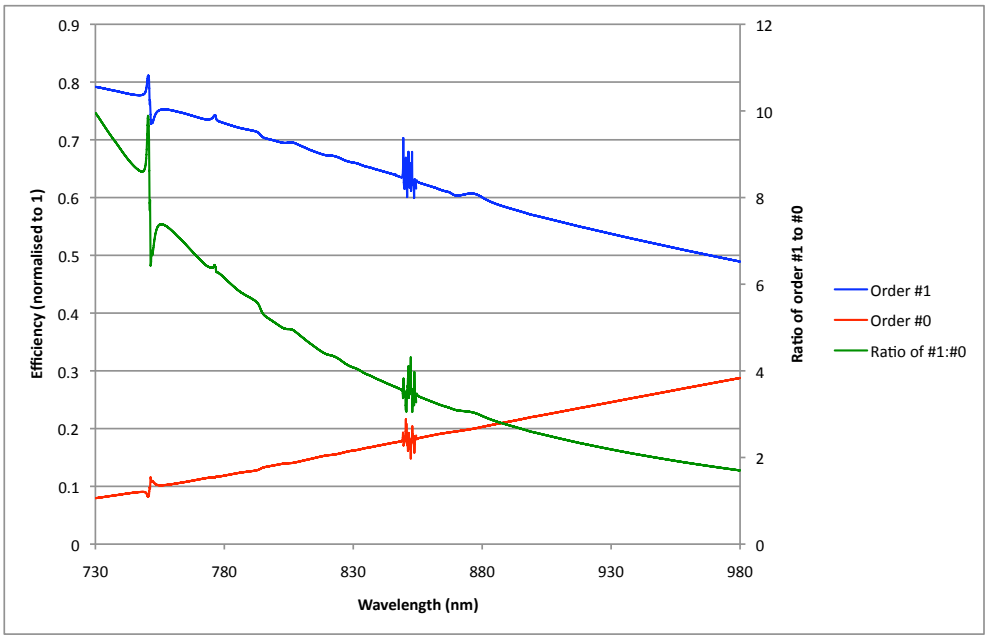

(a)

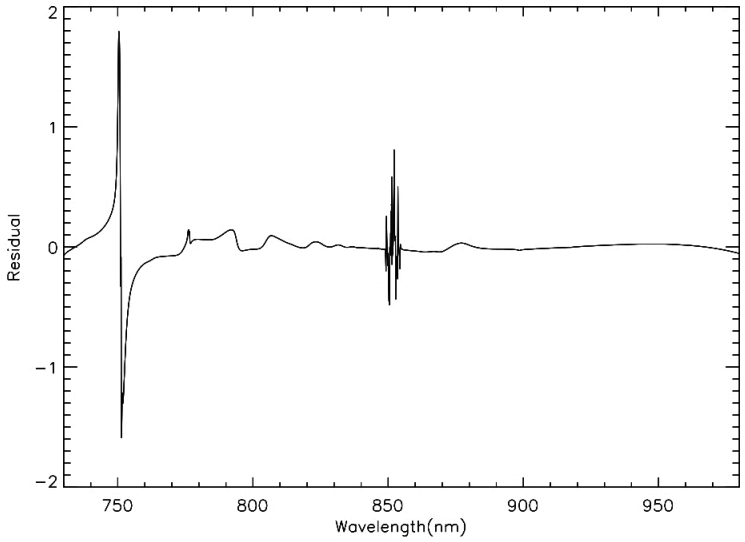

(b)

Figure 6.23: Predicted spectrum of the different diffraction grating orders as calculated using the PCGrate software. (a) Efficiency curves of the zeroth and first diffracted orders of a 35 lpmm ruled transmission diffraction grating made out of BK7 with a blaze angle of 2.2°. (b) Ratio of the first order spectrum to the zeroth order with a smooth low order polynomial subtracted.

6.2.5 Calculation of the Speckle Rejection Factor

The data is inspected in 3 ways to determine our achieved speckle rejection factor:

Visual Inspection

After reducing the data to the form of a data cube it should be visually inspected before and after scaling to determine if there are any noticeably bright [‡]secondary speckles that have been produced. Any ghost images should be noted also so that they can be correctly addressed at later stages. The determination of what is a ghost and what is a secondary speckle is quite general. The wavelength dependance of the artefact in question should be examined, if it is not stationary but moves out radially from the speckle with wavelength, at a rate different to that of the Airy rings of the speckle, it is quite likely to be a secondary speckle. It should not, however, move across slices as secondary speckles are produced within a slice after coherence is lost in this dimension. However, if it moves with wavelength in exactly the same way, but offset from, the speckle it is far more likely to be a ghost. A ghost image (if produced prior to the silcer) will also have a physical extent both along and across slices.

One Dimensional Horizontal, Vertical and Diagonal Cuts across the Field of View

Secondary speckles on a slice can only be made from light incident on that slice. For this reason we do not expect to see any secondary speckles produced on slices other than that containing the core of the speckle (or in the case of real data the host star). A good determination of the level of secondary speckle noise is then to make a comparison of the intensity along a slice centred on the core to the intensity of a cut centred on the core but at some angle such that it covers slices not contaminated by the core of the speckle. We suggest a comparison to a cut at 45° instead of a vertical cut across the slices as it would be dominated by signal from the zeroth order and possibly Fourier noise artefacts. A vertical cut should be made for this reason, so that we can look into any Fourier noise present.

[‡]Secondary speckles are those produced after slicing by the coherent interference of the light incident on the slice produced as a result of wavefront error in the IFS

Speckle Rejection of the Core of the Speckles PSF

The main aim of the experiment is to determine to what level we can reject a speckle. By performing the centring described in Section 6.2.2 and after scaling each wavelength slice accordingly in order to perform spectral deconvolution the speckle will be the same size and centred on the same four pixels at all wavelengths. Since it is in this scaled frame of reference that the fitting and rejecting of the speckle takes place we propose that this is where the calculation of the speckle rejection factor should be determined and should be done by looking at the RMS value of the four pixels spanning the core of the speckle both before and after spectral deconvolution. This value can then be determined for three different binnings:

- Using the data as is: Speckle rejection factor per spectral channel
- After binning up the data cube such that it represents a spectrograph with a lower spectral resolution, such as will be the case for future planet finding instruments: Speckle rejection factor per low R spectral channel
- Flatten the entire cube along the wavelength axis, in doing this we lose the spectral information about any companion but it will give the highest possible achievable contrast for detection of companions: Speckle rejection factor for the flattened cube

As we are looking for the rejection factor of our single simulated speckle this binning should also be performed in the scaled plane otherwise its signal would be smeared out.

Using Prior Knowledge to Improve the Result

We know that any signal from a real object will have an extent of a minimum of 2 pixels per FWHM. We can therefore say that any signal with a spatial extent smaller than this is of no interest to us. Using this prior we then convolve the results of the spectral deconvoltuion with a Gaussian function with a FWHM of 2 pixels. In doing this any signal smaller than 2 pixels will get heavily smoothed but the effect on a real signal will be far less due to its spatial extent. The speckle rejection factor can then be calculated again in the manner previously described.

6.3 Tests Using the Prototype Slicer IFU

6.3.1 Observations

Observations of the speckle were carried out over several sets of exposures taken during Jan 2010. Each exposure was 90 seconds, and 11 images were taken for each set. The small pupil size results in a weak illumination intensity, requiring long exposures. However, overheating of the halogen lamp proved a limitation to the maximum exposure length.

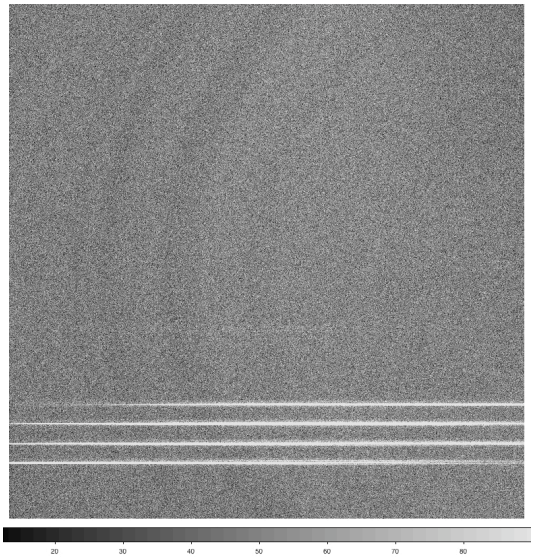

Figure 6.24: Full CCD frame showing the four active slices illuminated by the speckle. Only a small fraction of the detector is used for the dispersed spectra from the prototype IFS.

Mosaicing of Fields

Although the instantaneous field of view of the prototype image slicer (4 contiguous slices) is sufficient to fully image the speckle, the movement of the speckle centroid by two slice widths over the wavelength range implies that the spot is not fully imaged at all wavelengths. Thus, we had to mosaic several fields of view, in order to ensure adequate spatial coverage. This was done by moving the light source (pinhole) by precisely 3 slice widths, and obtaining another set of exposures. In total, we obtained 5 sets of data, covering the image of the speckle at all wavelengths, and including the "central star" image (0th order of the grating) as well. The mosaiced field of view is 16 slices, after accounting for the one slice overlap between sets.

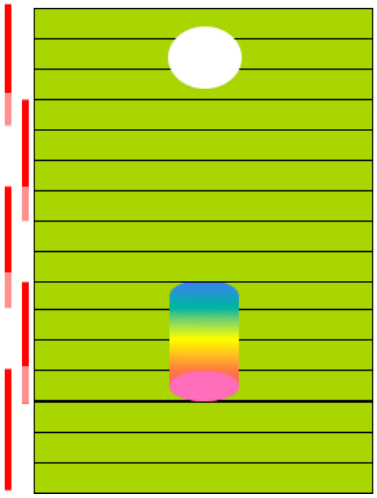

Figure 6.25: Cartoon depicting the mosaicing of the fields. The zeroth order is the white circle at the top of the image and the rainbow cylinder is meant to represent our simulated speckle. On the left hand side, in red, you can see the individual fields of four slices each with one redundant slice.

6.3.2 Calibration Observations

A complete set of calibration observations were also made, so as to be able to remove the instrumental signature from the data to the highest level of accuracy.

Darks

Sets of dark and bias frames were obtained to measure the background level on the CCD. 10 exposures were taken to ensure adequate signal-to-noise in the calibration exposures. Figure 6.26 shows the dark exposures, the low level structure seen in the dark is from a very low level light leak in the baffle of the spectrograph (post image slicer).

Wavelength Calibration

Arc lamp frames, covering the full field of view spatially, were obtained for wavelength calibration purposes. The Argon lamp was used as the source, as shown in Figure 6.27, which shows the region covering the four active slices at the edge of the slicer FoV. The zig-zag pattern (offset between neighbouring slices in the spectral direction) is clearly visible, as is the slit curvature.

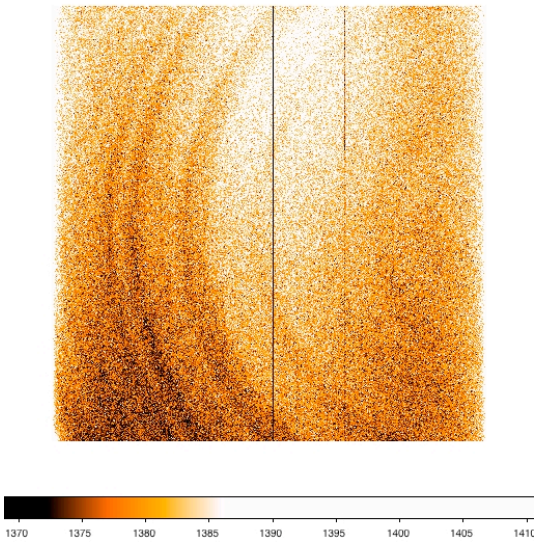

Figure 6.26: Dark exposure covering the entire CCD detector array.

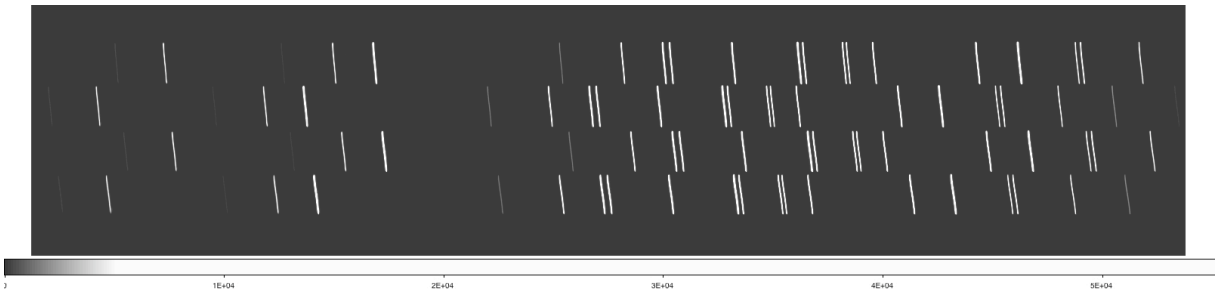

Figure 6.27: View of the arc line exposure for the four lowest slitlets. The zig-zag pattern is clearly visible.

Flat Fields

Flat fields were obtained by illuminating the entire FoV with the halogen lamp (see Figure 6.28). The $114\mu m$ pupil stop was used, to ensure that the flat field had the same focal ratio as the real data. The exposure time was 6 seconds, with a 10W halogen lamp at full intensity.

Slitlet Positions and Traces

Trace correction is required to remove any spectral curvature present in the spectrograph. Although the spectral curvature is small, we obtained spectra of pinholes located on each of the active slices, so as to be

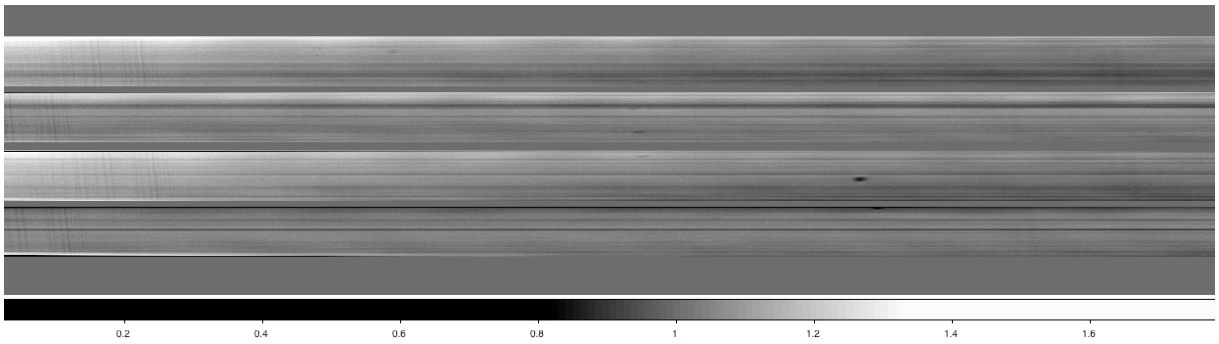

Figure 6.28: Flat field covering the four bottom slices. The flatfield has been normalized to unity. The structure that you can see as a constant along the dispersed axis (left-right) is from dust on the slicer mirrors.

able to do a trace correction. In fact, as shown in Figure 6.29, the pattern of five pinholes was moved back and forth across the FoV during a long (10 sec) exposure, so as to produce a set of spectral traces. This exposure also provides data for one additional calibration needed by slicer based IFS - it provides the centre to centre spacing between slices, so that they can be correctly stacked one on top of the other, to reconstruct the two dimensional image. As the distance between the pinholes in the pattern is also accurately known, this calibration also allows the plate scale to be measured.

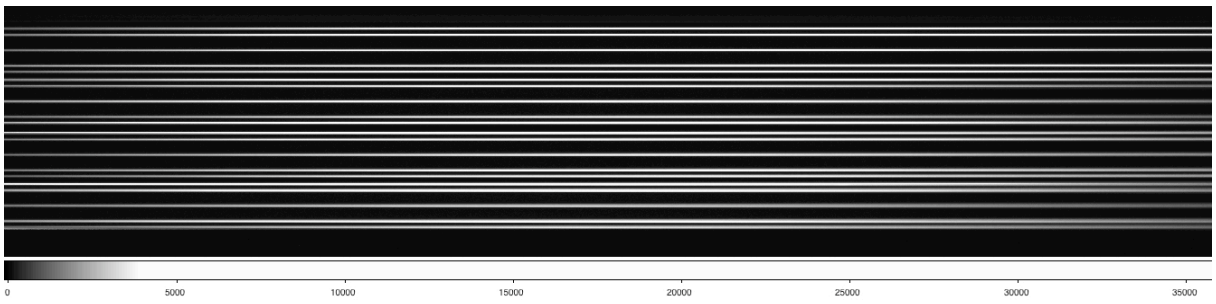

Figure 6.29: Flat field covering the four bottom slices. The flatfield has been normalized to unity.

6.3.3 Data Reduction

The data reduction and analysis for the experimental set-up followed the same procedure typically used for analyzing data from integral field spectrographs. The data reduction involves removing the instrumental signature from the data, and produces a 3-D data cube. This is followed by a second step, applying the spectral deconvolution algorithm to the data cube, so as to eliminate the speckle as best possible. Both steps

are described in some detail below. Given the rather special nature of these data, and as there were only four active slices, we used the IRAF package `twodspec` (in conjunction with IDL) to remove the instrumental signature.

Preparing Frames

A number of dark exposures, with the same exposure time as the speckle data, were clean meaned[§] together and subtracted from the speckle data to remove dark noise and CCD bias.

Flat fielding for IFS data can be quite complex, as there are three effects to quantify - pixel to pixel variations of the detector, the slow variation in spectral response with wavelength, and the large scale spatial variations (illumination correction). We are able to obtain most of this information from the flat field exposures using the halogen lamp.

The zig-zag pattern of the slitlets leads to a different angle of incidence of the light from odd and even slitlets at the grating, leading to a slightly different efficiency for different slitlets. The average spectrum within each slitlet was computed for the flatfield exposure. Smooth, high order, polynomial fits were made to these average spectra thus simultaneously removing the instrument spectral response and the unknown spectrum of the halogen lamp. The illumination correction (spatial flat field) was then determined by scaling the four slitlets to the same value at a fiducial wavelength.

The flat field thus constructed is then normalised and the data divided by it.

Producing the Data Cube

The goal of the data reduction is to convert the raw data into a regularly gridded data cube, which represents intensity as a function of x, y and λ. Two interpolations are carried out to achieve this result. As described in Section 5.1, a better algorithm that involves only a single interpolation would provide a better result, as each interpolation produces noise enhancement. This method is employed later, however, we were not able to implement this method on the dataset here due to the limited time available to get a result for the EPICS Phase A review.

[§]For each detector pixel, the stack of exposures are sorted, the lowest and highest value are rejected, and the rest combined (using a mean) to form a master frame.

Interpolation # 1 Trace correction (correction for spectral curvature) was carried out using the `apextract` routine in IRAF. This was done individually for each slit, with a fixed aperture size as a function of wavelength (keystone distortion was not considered). A spectrum of the central pinhole was used to determine the trace.

Interpolation # 2 Wavelength calibration used the standard IRAF routines `identify`, `reidentify`, `fitcoords` and `transform` to produce a wavelength calibrated and re-aligned frame with uniform wavelength steps, as shown in Figure 6.30.

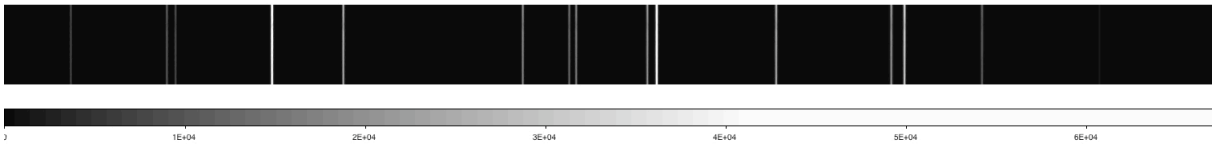

Figure 6.30: View of a single slitlet over the full wavelength range, after wavelength calibration

The dark subtracted, flat fielded, trace corrected, wavelength calibrated data were then re-arranged to form a data cube. The wavelength range is 730 - 980 nm, with a channel spacing of 0.1 nm. The vectors used to stack the slitlets to form a two dimensional image were obtained from fits to the five pinhole scan with white light illumination. The axis ratio ($\sim 2.3 : 1$ due to the finer sampling of the CCD pixels to that of the width of the slices) by which the image needed to be squashed along the slices was computed using the test data taken with the Canon CCD of the five pinhole pattern at the slicer input focal plane. The squashing was performed simultaneously with the wavelength resampling, in order to minimize the number of interpolations performed. The scattered light contribution was determined by looking at an area of the field of view away from the speckle and the zeroth diffracted order and this was then subtracted from each slice in the data cube.

The five sets of exposures were mosaiced to form a single data cube. Due to the overlap of one slice between mosaiced exposures and the fourth slice looks more uniform in the flat field image, the bottom slice (of the four active slices) was discarded in favor of the top slice when combining individual cubes to form the mosaic. Small errors arising from the non-orthogonality of the pinhole movement to the slicing direction can be corrected at this stage.

6.3.4 Results and Discussion

The datacube of our simulated speckle is shown in Figure 6.31. In this figure three typical wavelength slices have been selected at the wavelengths 750, 830 & 910nm, note it is a log scale look up table, the same scale and colour bars are used for each panel. The original datacube can be seen in the top row of panels followed by the result after scaling the datacube such that the speckle should be the same size at all wavelengths. The residuals left over after performing spectral deconvolution can be seen in the third panel down. In this middle panel a faint residual signature of the speckle can still be seen, however is does look to be fairly random. The fourth panel down shows the scaled datacube after binning by 10 channels in the wavelength direction to give a new sampling of $\Delta\lambda = 1nm$. There is an artefact seen in the top left corner of the first Airy ring. This artefact does not appear to be a ghost or a secondary speckle as its position seems to scale exactly with that of the speckle; it is always located at the same point on the first Airy ring. As such it is correctly fit out by the spectral deconvolution method and is not seen in the residuals. The residuals are also binned up to a wavelength spacing of 1nm and the result is seen in the bottom row of panels. An effect of the Fourier ringing can now be seen in the left hand side image, however, the left over signal due to the speckle still only seems to be slightly higher than that of the noise in the observation and therefore likely to be limited by photon noise.

One dimensional cuts are shown in Figure 6.32. These are made vertically across the slices, horizontally along slices and at 45° to the slices to the residuals at the three wavelengths marked and are shown for the case of $\Delta\lambda = 1nm$. The purpose is to compare the horizontal cut to the diagonal cut with the aim of noting the characteristics to see if secondary speckles are detected as they will only be present along the slices containing the core of the speckle. The vertical cut should not be used for this comparison as it is contaminated by the zeroth order and the Fourier ringing from the speckle. The results show, if anything, more noise on the diagonal cut. The residual left over due to the zeroth order's different spectrum can be clearly seen in the 910nm cut.

Radial profiles for the three slices, at a wavelength spacing of $Delta\lambda = 1nm$, centered on the zeroth order are shown in Figure 6.33.The top black curve shows the maximum value in each radial bin of the scaled datacube, the blue curve is the RMS value of the same cube, the bottom red curve is the RMS value for the residuals for the top panels and the residuals after convolving with a Gaussian of 2 pixels per FWHM for

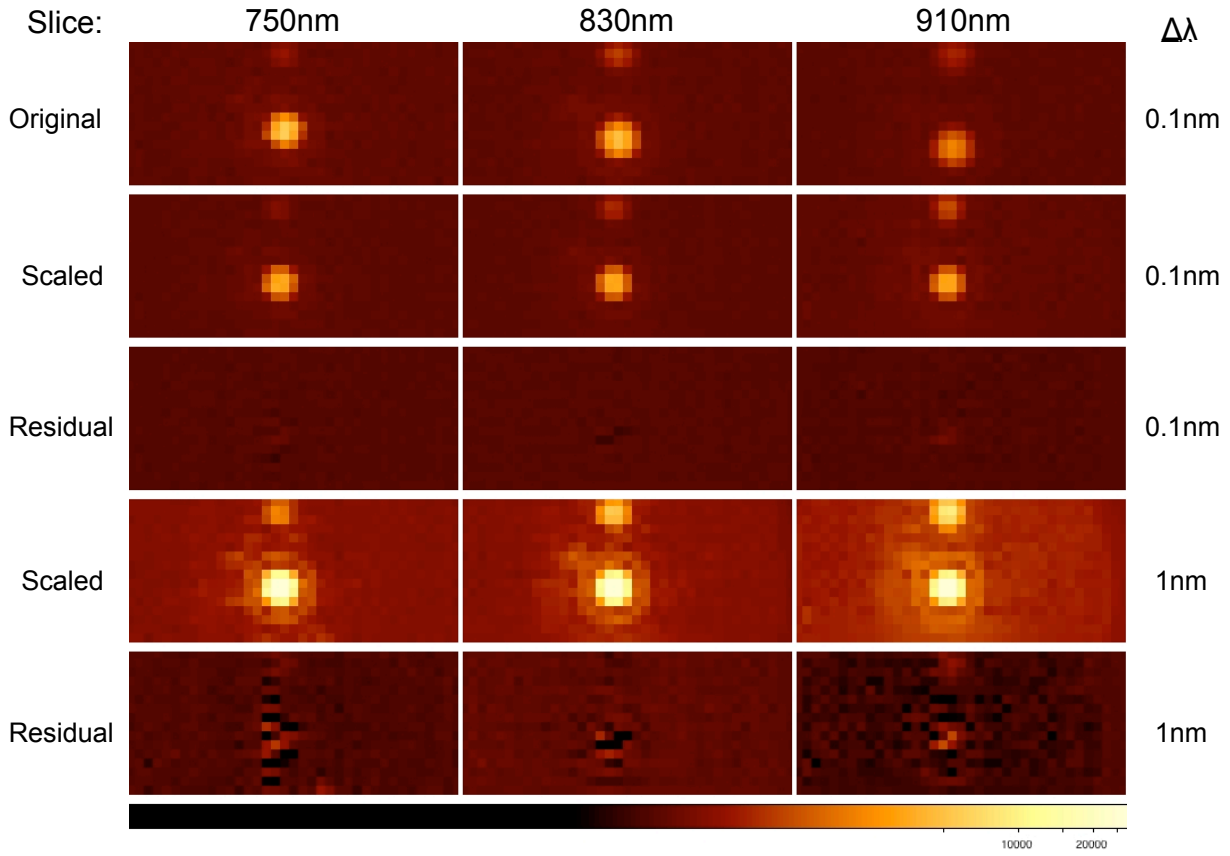

Figure 6.31: Datacube From The Prototype Slicer IFU Before And After Spectral Deconvolution: Results are split into three columns, each of which represents a single wavelength channel, from left to right these are 750nm 830nm and 910nm. Titles to the left of the images indicate what stage in the reduction is being shown: Original - the original datacube, Scaled - the datacube after each slice has been scaled with respect to wavelength and Residual - what is left over after performing spectral deconvolution. Titles to the right of the images indicate whether the original wavelength sampling ($\Delta\lambda = 0.1$nm) or the binned up wavelength sampling ($\Delta\lambda = 1$nm) is being shown.

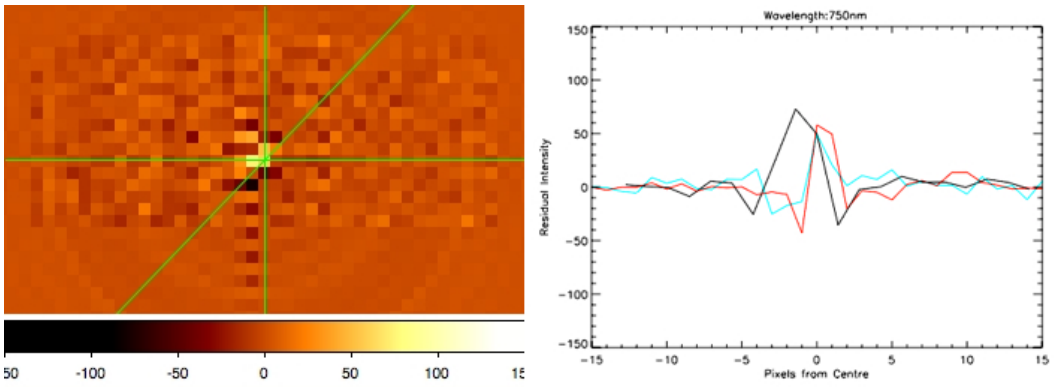

(a) 750nm

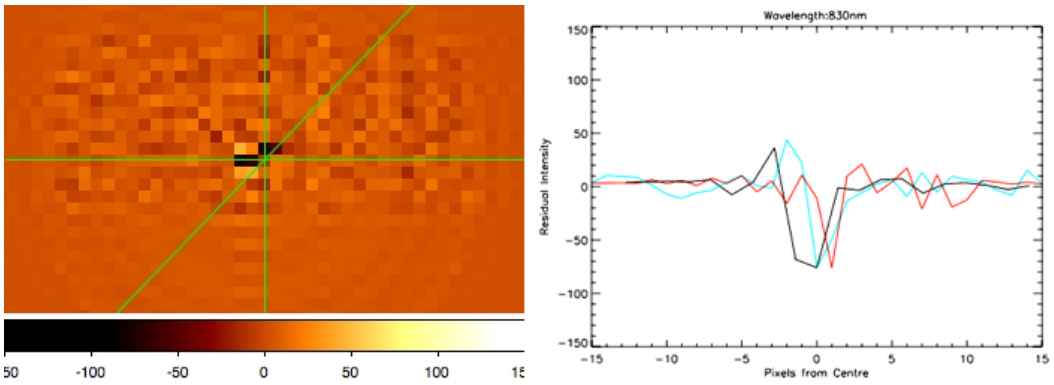

(b) 830nm

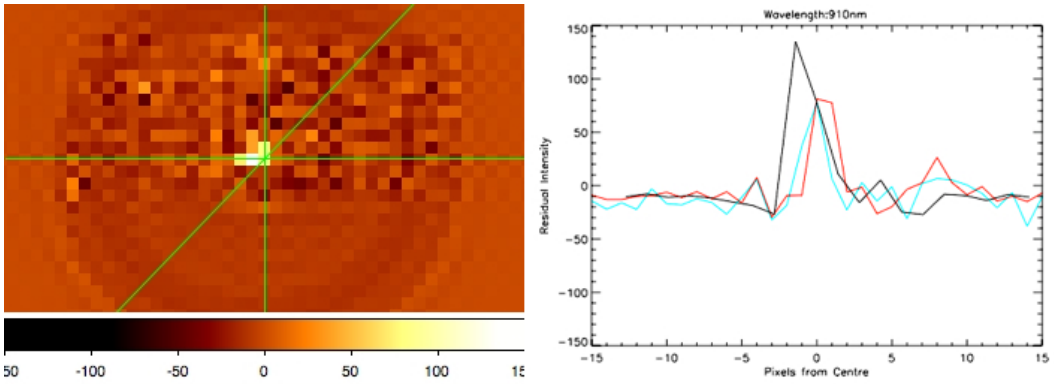

(c) 910nm

Figure 6.32: One Dimensional Cuts Across The Field Of View: Cuts made on the residuals after spectral deconvolution for three wavelength channels each of $\Delta\lambda = 0.1$nm (same as the middle row of Figure 6.31) are shown. Three cuts, passing through the centre of the speckle, are shown for each wavelength channel, as depicted by the green lines in the right hand images. Red - vertical cut, Blue - horizontal cut and Black - diagonal cut.

the bottom panels. The signal from the speckle is seen to be weak, only slightly higher than the background noise, and this difference is likely to be the order of the photon noise.

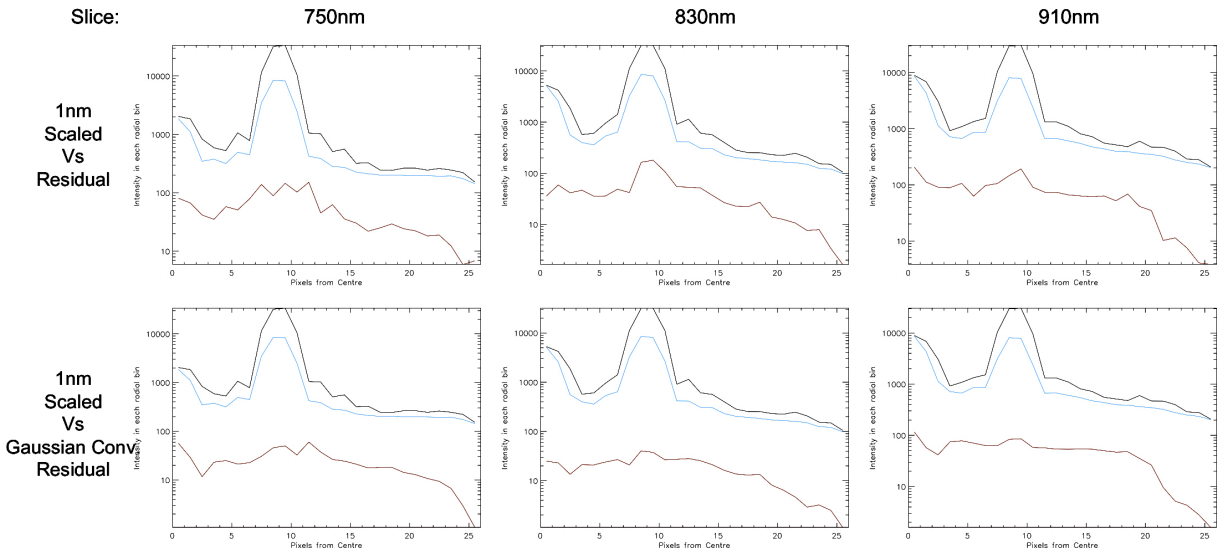

Figure 6.33: Azimuthal Profiles Centered on the Zeroth Order: showing, for the binned datacube of $\Delta\lambda = 1nm$, the values in annular bins centered on the zeroth order of; the maximum value of the scaled datacube (black curve), the RMS value of the scaled datacube (blue curve) and the RMS of the residuals after spectral deconvolution (red curve). These values are shown for the normal residuals (top panels) and the result after convolving with a 2 pixel per FWHM Gaussian (bottom pannels).

Figure 6.34 displays the speckle rejection factor, calculated via the ratio of the RMS values of the 4 core speckle pixels in the scaled datacube to the same pixles in the residual datacube. This is shown for the original and binned wavelength sampling before and after convolving with a Gaussian. The average value of the speckle rejection factor is displayed at the top of each image. The result for the same calculation of the speckle rejection factor, but after the datacubes have been collapsed along the wavelength dimension, is shown in Figure 6.35. Table 6.3 shows the rejection factors achieved in each each.

No secondary speckle noise was seen in the resultant datacube, however, the minimum required rejection factor of 100 as dictated by the EPICS design study is not achieved, in the way we have calculated it here, for the case of the $\Delta\lambda = 0.1\&1$nm, non-Gaussian convolved datacube. The reason behind this is thought to be due to the photon noise of the experiment as the residuals found are very close to the noise seen in the rest of the image as shown by the radial profiles. This prompted further investigation.

	Speckle Rejection Factor	
Binning	**Normal**	**Convolved with Gaussian**
$\Delta\lambda = 0.1nm$	63	234
$\Delta\lambda = 1nm$	73	279
Flattened	250	519

Table 6.3: Table of the rejection factors achieved

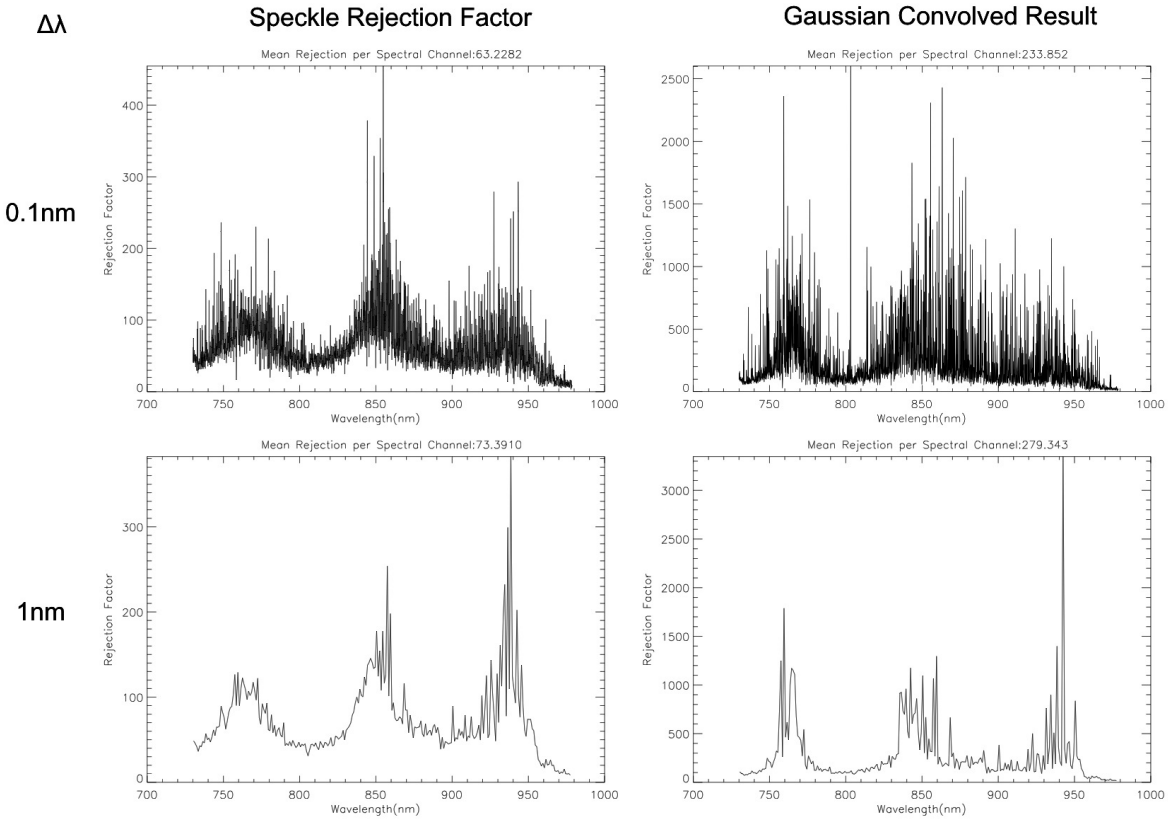

Figure 6.34: Speckle Rejection Factor: Calculated as the ratio of the RMS value of the scaled datacube to its residuals (left) and Gaussian, 2 pixels per FWHM, convolved residuals (right) over the 4 pixels containing the speckles core. Values are shown for original wavelength sampling of $\Delta\lambda = 0.1nm$ (top) and binned sampling $\Delta\lambda = 1nm$ (bottom).

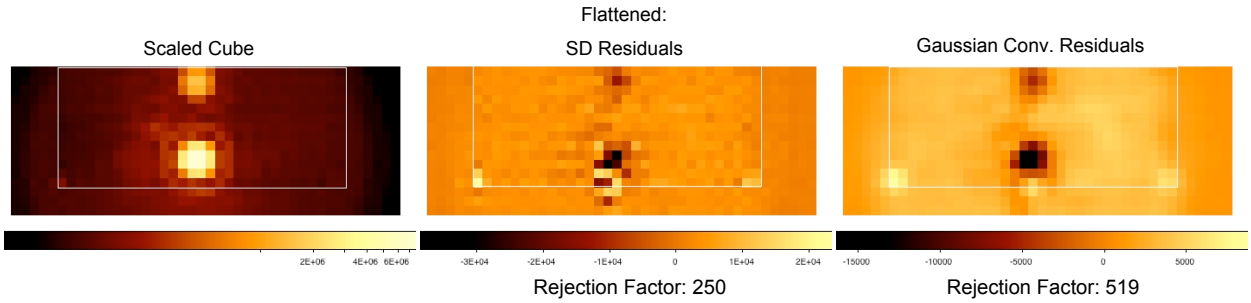

Figure 6.35: Flattened Datacubes: The scaled, residuals and Gaussian (2 pixels per FWHM) convolved residuals datacubes are collapsed along the wavelength axis to produce the figures seen here. The white box dictates the area that is common to all wavelength slices (due the the scaling needed for spectral deconvolution). The speckle rejection factor is shown beneath, calculated as the ratio of the 4 core speckle pixels in the flattened scaled cube to to that of the residuals and Gaussian convolved residuals respectively.

6.4 Tests Using the SWIFT Slicer IFU

Results from the previous dataset were presented at the EPICS Phase A review which prompted the question, what is the ultimate contrast achievable with a slicer based IFS.

6.4.1 Modifications to the Instrumental Setup

In this section we shall describe modifications that were made to the instrumental setup in order to achieve a better signal to noise of the speckle observations including the swapping of the prototype slicer for the full SWIFT slicer.

Light Source

As was mentioned in Section 6.3.1 the amount of flux we could get on to the detector during the observations was limited due to overheating of the integration sphere limiting exposure times. Further analysis of the data obtained showed that the amount of flux changed quite significantly as the lamp heated up and as components in the integrating sphere expanded, this was not ideal. We decided to change the setup such that the top port of the integrating sphere had a cylindrical pipe attached that went straight up out of the baffle. By doing this hot air could escape the integrating sphere through this chimney thus avoiding overheating. The lamp housing was also upgraded such that it could hold a more powerful 100W bulb. However, the full power of this bulb was never used, again due to overheating.

Pre-Optics Stability

Even with the added chimney, the integrating sphere has to find an equilibrium temperature that was suitably low. It was essential that we determine the stability of the pre optics so as to not be affected by temporal effects. To do this a full field illumination of the slicer was performed and a 10 second integration was taken every minute for 90 minutes, the sequence was started just after switching on the lamp. Bad pixels and those below a certain threshold were rejected and a mean count value of the image was determined for each exposure. Results can be seen in Figure 6.36. The shape of the curve produced is a result of the warming up of the preoptics, this includes the warming of the halogen bulb and of the reflective coating inside the integrating sphere. We can clearly see that the system stabilises after approximately 40 minutes,

the structure after this is just due to noise in the images. Consequently, all subsequent measurements were made more than 40mins after switching on the lamp. A PT100 temperature sensor was also attached to the exit baffle holding the focal plane mask from which readings could be checked to ensure stability.

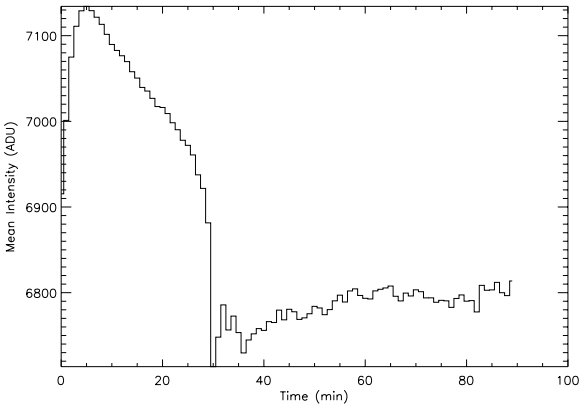

Figure 6.36: Temporal stability of the pre-optics light source

CCD Cooling

In an addition to the preoptics over heating, the CCD enclosure also heated up quite dramatically during the tests. Since we were hoping to integrate for longer periods this issue needed to be addressed to prevent the CCD temperature from creeping up. Light tight baffling was made that let air flow through the baffle, this was helped along by two fans that were used to draw air out of the enclosure. By doing this we were also able to set the CCD to a lower temperature ($-12°C$ instead of $-10°C$) thus reducing the dark current (for the measurements detailed in Section 6.3.2 the CCD was also set to $-12°C$).

Baffelling and Scattered Light

As has been pointed out in Section 6.3.2, there was a low level light leak that needed to be stopped. Problem areas were found using a torch and baffled accordingly. Further baffling was put in place in the preoptics to prevent any scattered light from entering the system after the addition of the chimney.

A test was made whereby the lamp was switched on but the baffle in front of the integrating sphere was turned to block off the open pinholes and full field parts of the focal plane mask. Figure 6.37 shows the

resultant dark and scattered light images. The standard deviation of the clean meaned, dark subtracted, bad pixel corrected, scattered light images was found to be $\sigma = 4.63$ADU. Using the measurements of the read and dark noise calculated in Section 6.1.5, this works out to be 1.86ADU or $2.29e^{-1}$ for a 10 minute exposure which is suitably low not to cause us problems. However, it should be noted that this is a minimum value of the scattered light as the amount of scattered light when the slicer stack is illuminated will increase, how much it increases is hard to measure.

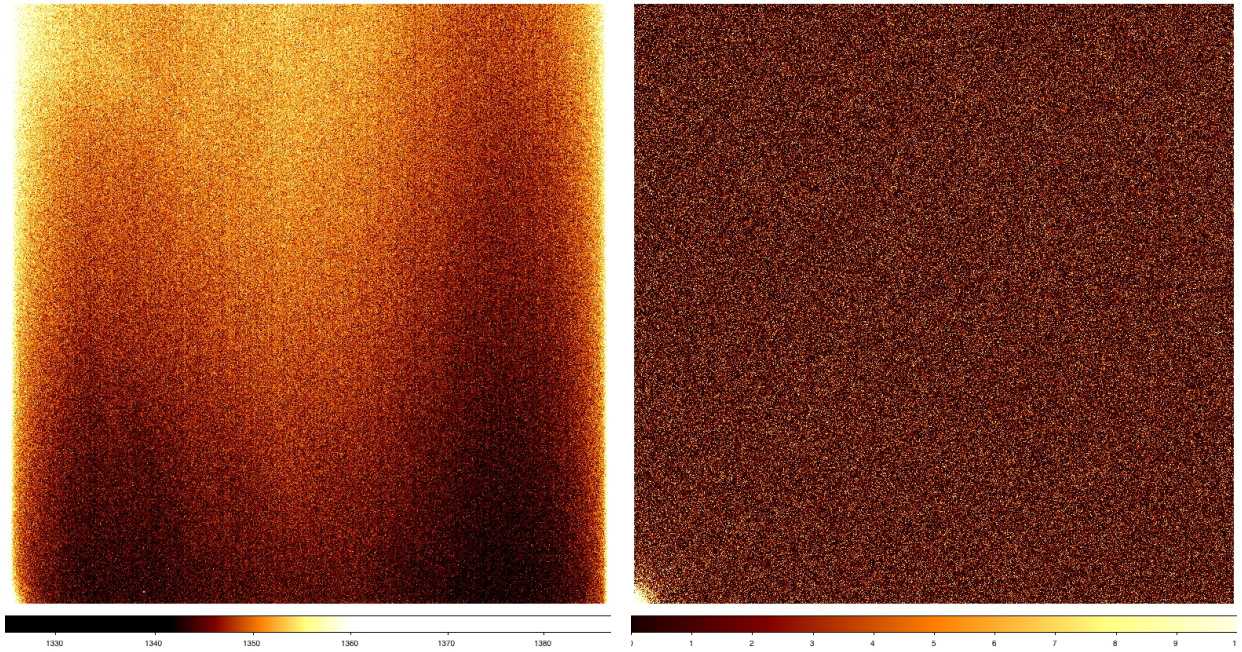

(a) Dark (b) Scattered Light

Figure 6.37: Image of 10 combined dark frames and 10 combined scattered light frames. The low level light leak seen in Figure 6.26 is no longer there. The average scattered light across the CCD was determined to be 1.86 ADU / 10 min.

Switching the Slicers

The SWIFT instrument returned to Oxford in the Summer of 2010, while the PALAO adaptive optics system was being upgraded. This provided a great opportunity to use a full slicer instead just the four slices we have been using up until now thus we would be able to take an image of the entire field of interest in one exposure thus eliminating the risk of temporal variations between mosaiced fields. This was known to be a possibility and as such the base plate of the prototype were made to be identical to SWIFTs. Mechanical

stops were also put in place to enable us to switch the slicers without having to re-calibrate the preoptics.
The slicer was replaced and the CCD was moved to a nominal focus.
Tests showed that the collimator and the spectrograph needed no further adjustment.
The optimal focus for all of the slices was found using the arc lamp with the pin hole mask and the oversized pupil stop to produce point sources on the ccd that could be focused.

Vignetting & Diffraction Grating

The edges of the bottom 3-4 slices appear to be vignetted (visible in Figure 6.38), we think due to the footprint on the field lens, see Figure 6.5. We do not use the edges of these slices for the purposes of the tests, however, incase this vignetting has come about by some more malicious way, we decided to flip the diffraction grating around by 180° and re-align the integrating sphere such that our simulated speckle was now dispersed across the top half of the slicer stack and the zeroth order was now imaged on the bottom four slices. This is why the data cube appears to be flipped with respect to the previous dataset.

6.4.2 Observations and Signal to Noise Calculation

For a 10 minute exposure of the described setup we obtain a peak core speckle intensity of $\sim$ 6000ADU and a minimum of $\sim$ 1000ADU per CCD pixel. This is a decent amount of flux and from the calculation in Section 6.3.2 we will not be running into the dark noise of the CCD.
To determine how many observations we should make we first need to determine the noise we will be facing;

$$N_{total} = \sqrt{S} + N_R + N_D + N_S \tag{6.4}$$

Where N_{total} is the combined noise for a pixel, *sqrtS* is the photon noise on the flux incident on that pixel, N_R is the read noise ($9.5e^-$ ascalculated in Section 6.1.5), N_D is the noise on the dark ($3.5e^-$ as calculated in Section 6.1.5) and N_S is the added noise due to scattered light ($2.29e^-$ as calculated in Section 6.4.1). This value of the noise can then be divided by the square root of the number of observations performed and by the square root of the number of pixels used to create the resampled datacube pixels, whereby we have a factor of 2.3:1 pixels in the spatial direction of each slice due to the sampling of the CCD relative to the slicer stack and a factor of 10:1 if we bin up our datacube to have $\Delta\lambda = 1nm$ instead of $0.1nm$. The results

of this signal to noise calculation showed that 40x10 min exposures (plus one used to remove cosmic rays) would provide a decent signal to noise, as shown in Table 6.5;

	Signal to Noise of the Speckle		
		Intensity on Pixel e^-	
$\Delta\lambda$	**Binning Factor**	**6000**	**1000**
0.1nm	**1**	460	154
0.1nm	**2.3**	701	232
1nm	**23**	2218	736

Table 6.4: Table of calculated SNR of observations.

It was decided that a separate set observations should be made at the same time of the test setup without the diffraction grating in place to see how good a rejection we achieve when the object being observed does not move. Due to the increased signal of the source without the diffraction grating the time for exposures was reduced to 7 minutes such that the observed intensity was roughly equal to that of the speckle. 41 exposures at this integration time would be taken and combined as with the normal observations so as to achieve the same SNR.

It is vital that when looking for such high signal to noise of the speckle we are not limited by the noise on the flat field correction frame. We use flats of an exposure length 7 seconds so as to provide roughly the same amount of flux per spaxel as that of the core of the speckle, thus reducing any effect of non-linearity that may be present, see Section 6.1.5. If we are not to be affected by the noise on this flat field a reasonable assumption would be that the number of flats, N_{Flat}, at this intensity would have to be;

$$N_{FLAT} = R_{F:S}^2 \times N_{Speckle} \tag{6.5}$$

Where $R_{F:S}$ is the ratio of signal to noise of the flat field to that of the speckle observation and $N_{Speckle}$ is the number of observations of the speckle. Therefore, we decided to take a series of 200 flats at this intensity (plus one used to reject cosmic rays) giving us a SNR ratio of the flat to that of the science frame of $\sqrt{5} = 2.2$.

Taking this flat field noise into account we calculate our SNR on the speckle signal to now be;

	Signal to Noise of the Speckle		
		Intensity on Pixel	
$\Delta\lambda$	**Binning Factor**	**6000**	**1000**
0.1nm	**1**	318	106
0.1nm	**2.3**	482	160
1nm	**23**	1525	507

Table 6.5: Table of calculated SNR of observations.

Observations

The preoptics was warmed up and the CCD cooled down and no observations were taken until the instrument was stable. The observations without the diffraction grating in were taken first followed by a thermal cycling of the CCD to remove persistance. Darks frames needed for the test data were then taken with the shutter closed. The observations of the speckle were then made. Following an additional thermal cycle, dark frames for the flat field images were taken followed by the flats themselves. The high signal to noise flat field can be seen in Figure 6.38, note that the structure that is seen running along the wavelength direction is due to dust on the slicer stack whereas the dark blobs are due to dirt on optics close to the CCD focus.

6.4.3 Data Reduction Improvements

The method of datacube reduction was improved such that the key stone distortion of the slices was corrected for and the whole reduction could be performed with a single interpolation on the data;

One interpolation

Here I shall describe the step by step method that was followed, enabling the cube creation to be made with one interpolations;

- Aperture extraction of the slitlets is performed using IRAFs `apall` routine fit to the center of the 5 traces (see Figure 6.39)extracting a fixed width either side of it, however, preferences were set such that a nearest neighbour algorithm is used for extraction resulting in a very chunky but not interpolated aperture for each slitlet.

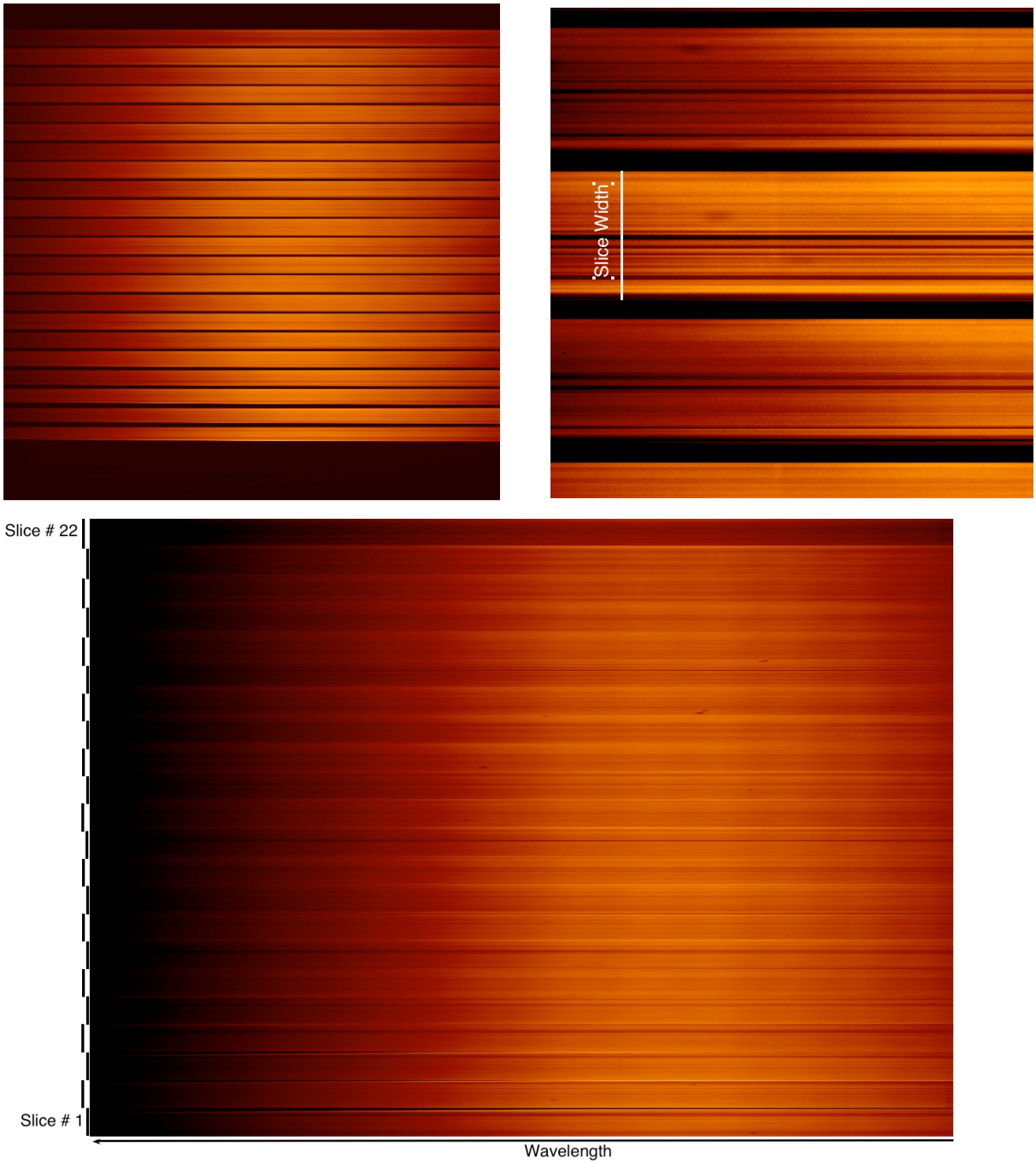

Figure 6.38: Flat Field: Image of the high signal to noise flat field produced by combining 200 individual images and removing a high SNR dark frame. The top left image shows the raw combined image, the top right is a zoom in on the center of the image showing the structure on a slice which is produced from dust on the slicer stack. The bottom image is the result after interpolation on to a spatially aligned wavelength calibrated grid.

- The key stone distortion of each slice is corrected for by using IRAFs `identify` and `reidentify` routines to fit to the spacings between each of the central 3 traces on each slice (note that the two outer traces could not be used for this due to their location being right on the edge of a slice-not a good enough centroid fit). During this coordinate fit, the required location of the central trace and separation between the three traces is made constant for all slices. Therefore, each slice is now fit to a common coordinate system. Results from these fits were run through the `fitcoords` routine to produce a resampling surface of coordinates that would be used later to produce the required transformation.

- The wavelength calibration was carried out much in the same way as before using the arc frames, see Figure 6.40. However, only up to the production of the fit coordinate surface produced by IRAFs `fitcoords`.

- The two produced fitcoords files can then be combined into a single interpolation using IRAFs `transform` routine in which you specify the sampling in the spatial and wavelength directions you desire, thus taking into account the binning of 2.3:1 needed to correct for the sampling of the CCD pixels relative to the slicer stack sampling.

Thus the new data cube is able to be produced via a single interpolation of the raw data frame.

Flat Field Correction

The flat field correction was performed in the following manner;

- The combined science frame was divided though by the combined flat field before the data cube production, thus correcting for pixel to pixel variations.

- the flat field was processed into the form of a datacube itself.

- this flat field datacube was then multiplied by the produced science datacube there by producing an illumination correction.

Re-sampled Datacube

The result is a set of flat field corrected data from each slice that has been resampled onto the same spatial and wavelength coordinate (as seen in the case of out speckle science frame in Figure 6.41) system which

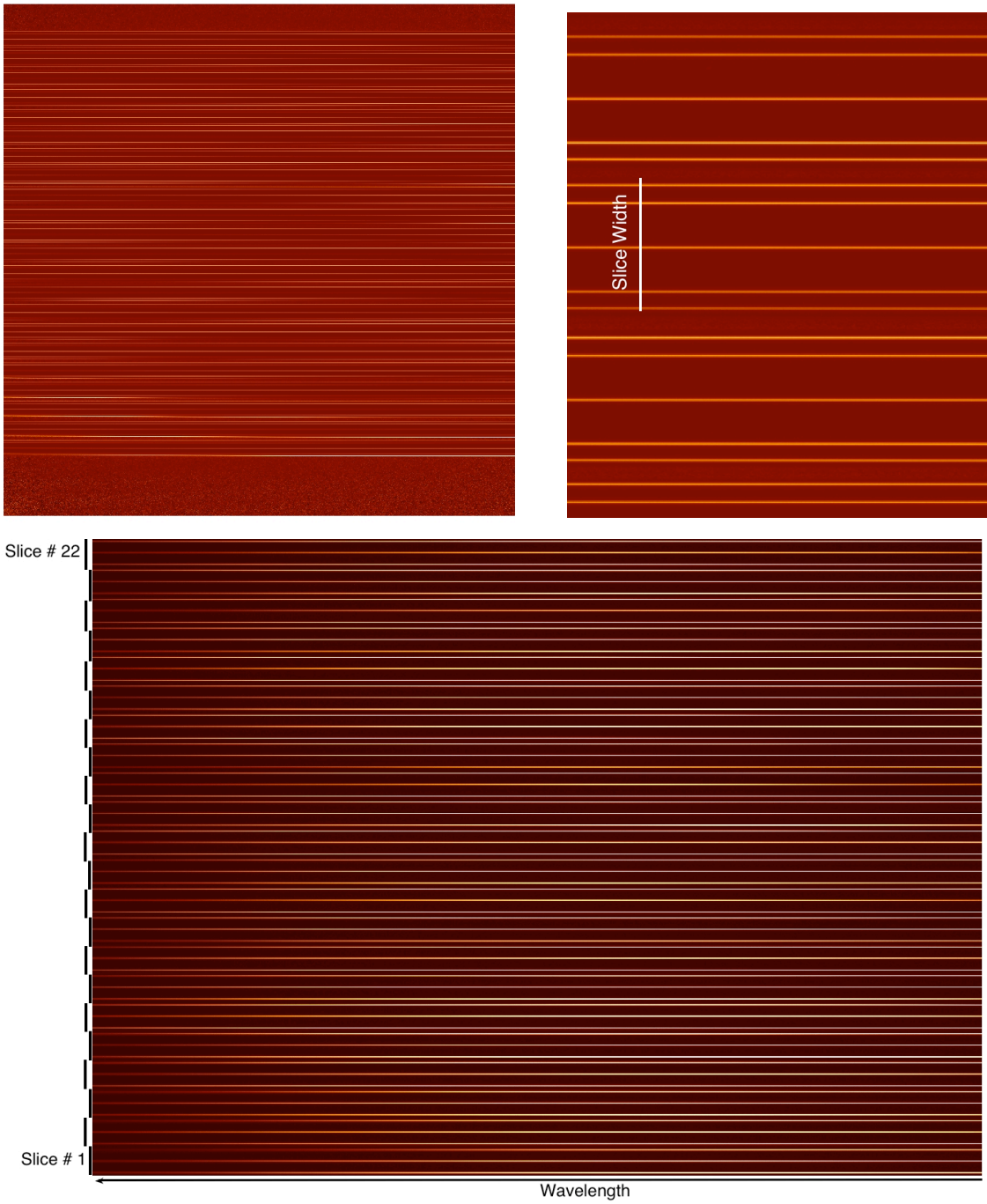

Figure 6.39: Spatial Trace Correction: Image of the pin hole mask illuminated by the halogen lamp whist the integrating sphere was translated vertically to produce a trace across slices, used for spatial calibration. The top left image shows the raw combined image minus dark, the top right is a zoom in on the center of the image showing the traces produced from the 5 pin hole mask . The bottom image is the result after interpolation on to a spatially aligned wavelength calibrated grid. Note that the five lines fo each slice seen in the top right images reduces to three per slice in the bottom image, this is due to us cropping the field of view during aperture extraction such that these areas of the slices are not used in our tests.

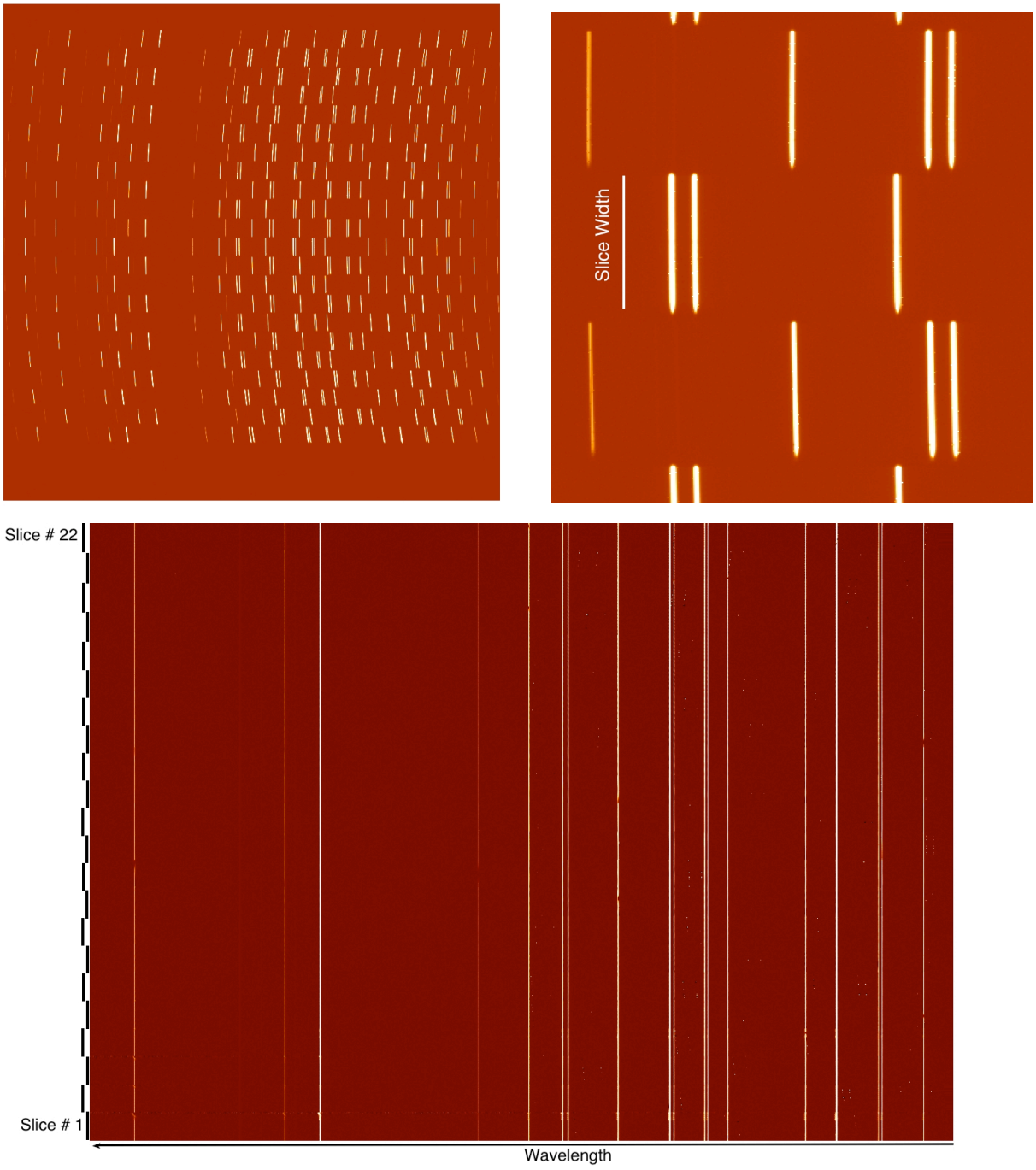

Figure 6.40: Wavelength Correction: Image of the full field illumination with the arc lamp, used for wavelength calibration. The top left image shows the raw combined image minus dark, the top right is a zoom in on the center of the image showing a few of the central arc lines. The bottom image is the result after interpolation on to a spatially aligned wavelength calibrated grid. Note the staggered pattern of the slices in the raw frame and how they are aligned in the processed cube. Slight discrepancies in the calibration are seen at the edges of the bottom 3-4 slices due to the vignetting described in Section 6.4.1, however, this part of the field of view is not used for our tests.

can then simply be re ordered to form the datacube.

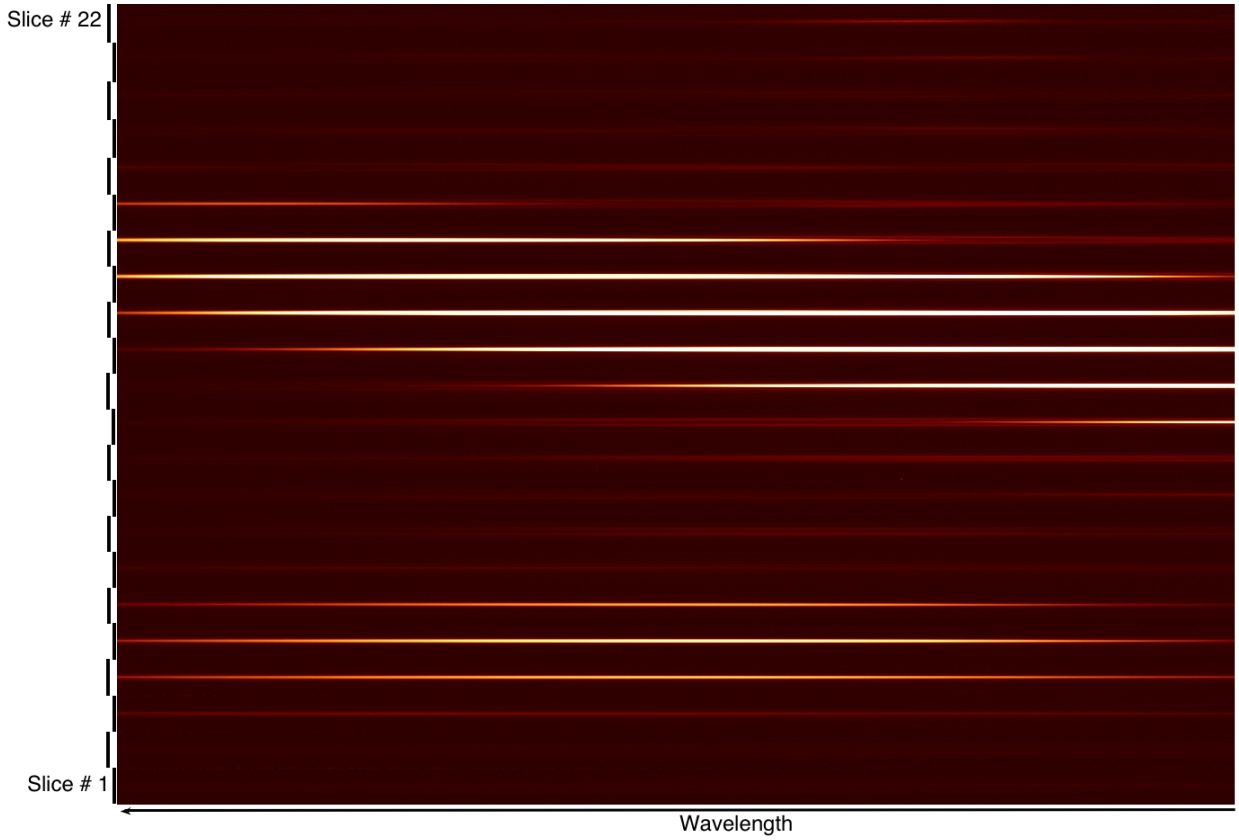

Figure 6.41: Speckle Cube: Image of the combined, dark subtracted, flat field corrected, wavelength and spatially calibrated observations of our simulated speckle before reordering to form a datacube. The zeroth order is seen in the bottom slices and the speckle can be seen as the diagonal trace running across the middle-top slices with wavelength. Note the wavelength axis is reversed (left-red, right-blue).

Possible Limitation

The observed FWHM of the traces, used to correct for the keystone effect and alignment of the slices onto a common coordinate grid, on the CCD is not full Nyquist sampled. At the blue end we find an average of ~ 1.5 pixels per FWHM expanding gradually with diffraction to ~ 2.1 pixels per FWHM at the red end. This can introduce some error into the accuracy of the fits made to the scaling and centering of each slice.

6.4.4 Results and Discussion

Observations With the Diffraction Grating

The same analysis procedure was followed as with the previous data, the resultant images can be seen in Figures 6.42 - 6.46.

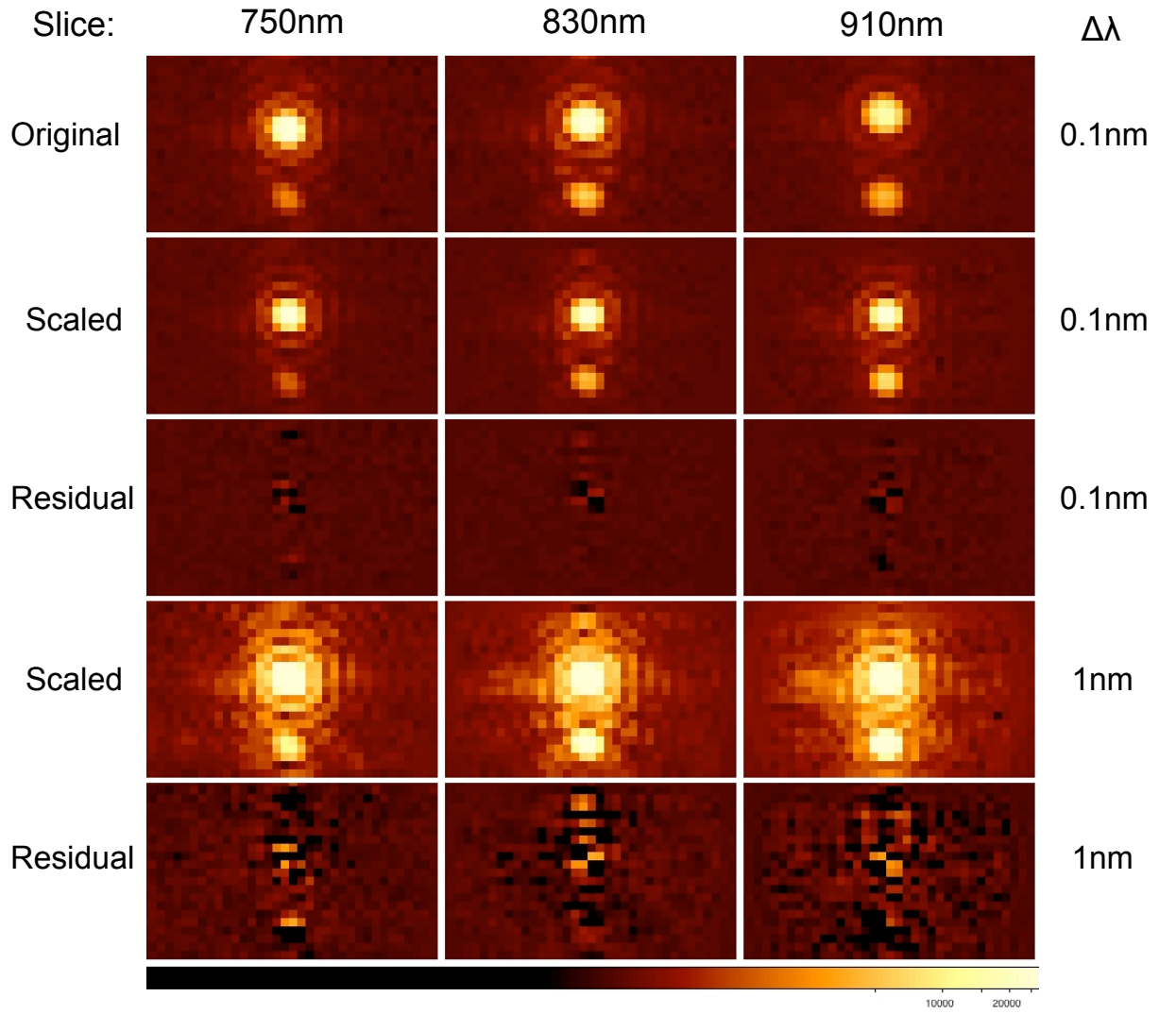

Figure 6.42: Datacube From The SWIFT Slicer IFU Before And After Spectral Deconvolution: Results are split into three columns, each of which represents a single wavelength channel, from left to right these are 750nm 830nm and 910nm. Titles to the left of the images indicate what stage in the reduction is being shown: Original - the original datacube, Scaled - the datacube after each slice has been scaled with respect to wavelength and Residual - what is left over after performing spectral deconvolution. Titles to the right of the images indicate whether the original wavelength sampling ($\Delta\lambda = 0.1$nm) or the binned up wavelength sampling ($\Delta\lambda = 1$nm) is being shown.

The speckle pattern looks to not be rejected to the level of the photon noise in this case, however, these higher SNR observations provide more insight into the distribution of the residuals after spectral deconvolution. The pattern appears to alternate between being too bright and too faint along a slice about the center of the speckle, this is clearly seen in the bottom row of panels in Figure 6.42.

A visual analysis of the new data set shows a very nice high signal to noise Airy pattern of our simulated speckle in which a possible secondary speckles can now be seen as the streak to the left of the speckle in the fourth row of panels in Figure 6.42. It appears, as predicted only when the slice contains the core of the speckle and, at a maximum, its intensity is approximately 1/300th of that of the core of the speckle. However, it shows no wavelength dependance in its position along the slice at all. If this was a secondary speckle it should move relative to the primary speckle with wavelength as discussed in Section 5.3. Since this is not seen we believe this not to be a secondary speckle at all but rather scattered light. In addition to this a brighter, what looks to be diffraction limited, blob can be seen above the speckle at the edge of the field of view. This is not thought to be a secondary speckle at all due to a couple of factors; there is no other light incident on the slice with which to make the secondary speckle, it has a physical extent over more than one slice which is not possible for a secondary speckle due to the lack of coherence across the slices. It is possible that the blob is the second diffracted order of the diffraction grating in the preoptics, however, if this was the case its position such that it is stationary in the scaled cube which is not seen here. These factors considered we believe this to be a ghost image that has propagated though our system.

The scattered light appears to be well fit out by the spectral deconvolution method due to its smooth and slow change with wavelength however the ghost image is not. Signal from the zeroth order is also left after spectral deconvolution due to the difference between its spectra and that of the first order.

The one dimensional cuts shown in Figure 6.43 show that we do not appear to have considerable (if any) secondary speckle noise, seen by comparing the horizontal to diagonal cuts. The vertical cut highlights the residual signals of the zeroth order and the ghost, Fourier noise also seems apparent in the 830nm slice.

The radial profiles seen in Figure 6.44 clearly show the residual signal from the zeroth and first orders as well as the ghost image although the signal from our speckle appears to be rejected by a large factor.

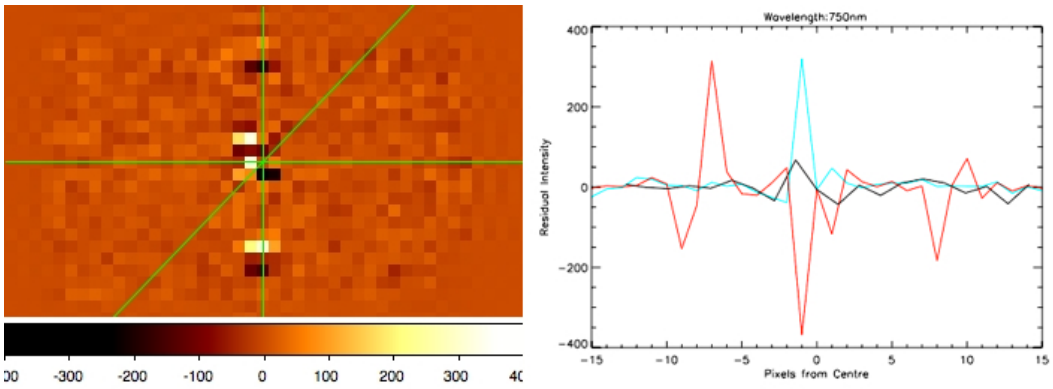

(a) 750nm

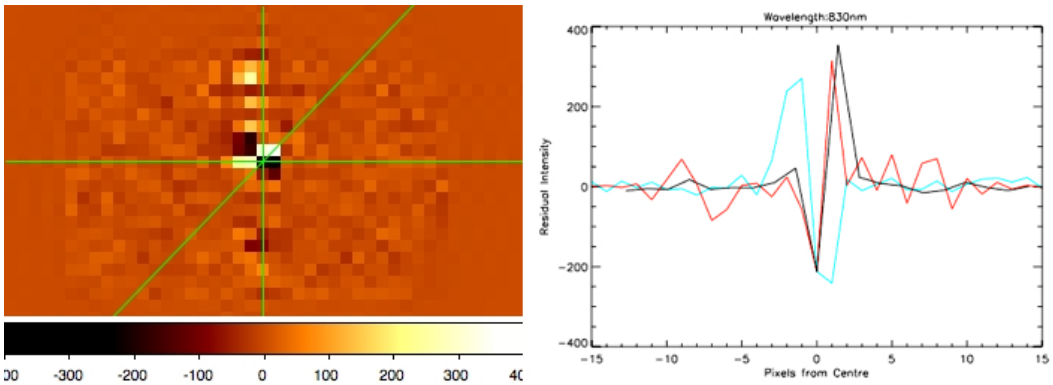

(b) 830nm

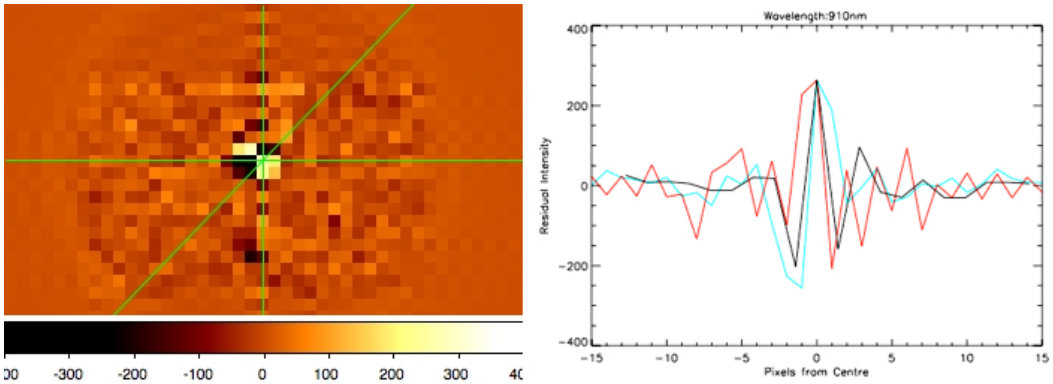

(c) 910nm

Figure 6.43: One Dimensional Cuts Across The Field Of View: Cuts made on the residuals after spectral deconvolution for three wavelength channels each of $\Delta\lambda = 0.1$nm (same as the middle row of Figure 6.42) are shown. Three cuts, passing through the centre of the speckle, are shown for each wavelength channel, as depicted by the green lines in the right hand images. Red - vertical cut, Blue - horizontal cut and Black - diagonal cut.

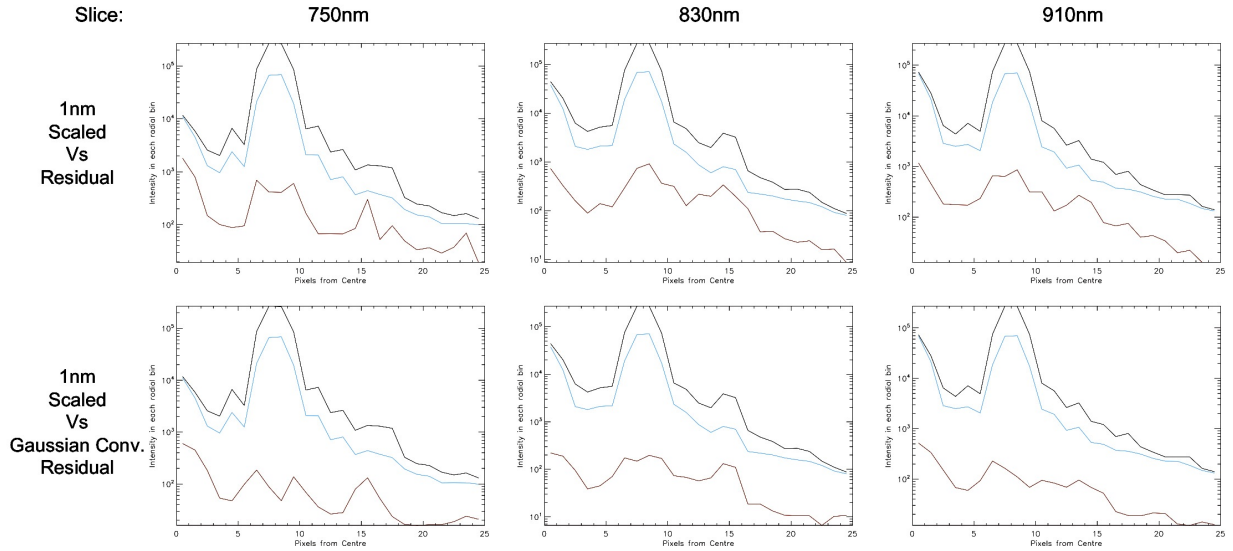

Figure 6.44: Azimuthal Profiles Centered on the Zeroth Order: showing, for the binned datacube of $\Delta\lambda = 1nm$, the values in annular bins centered on the zeroth order of; the maximum value of the scaled datacube (black curve), the RMS value of the scaled datacube (blue curve) and the RMS of the residuals after spectral deconvolution (red curve). These values are shown for the normal residuals (top panels) and the result after convolving with a 2 pixel per FWHM Gaussian (bottom pannels).

Figure 6.45 shows the rejection factors achieved for the regular and re-binned cased both before and after convolution with a Gaussian, Figure 6.46 shows the same but for the flattened datacubes.

Table 6.6 shows the achieved speckle rejection factor in all of these cases previously explained. Although there are residuals left over the rejection factor is still quite high, always surpassing the 100 mark and even reaching the factor of 1000 in each wavelength channel of the Gaussian convolved residuals.

	Speckle Rejection Factor	
Binning	**Normal**	**Convolved with Gaussian**
$\Delta\lambda = 0.1nm$	146	948
$\Delta\lambda = 1nm$	160	1148
Flattened	1052	4657

Table 6.6: Table of the rejection factors achieved

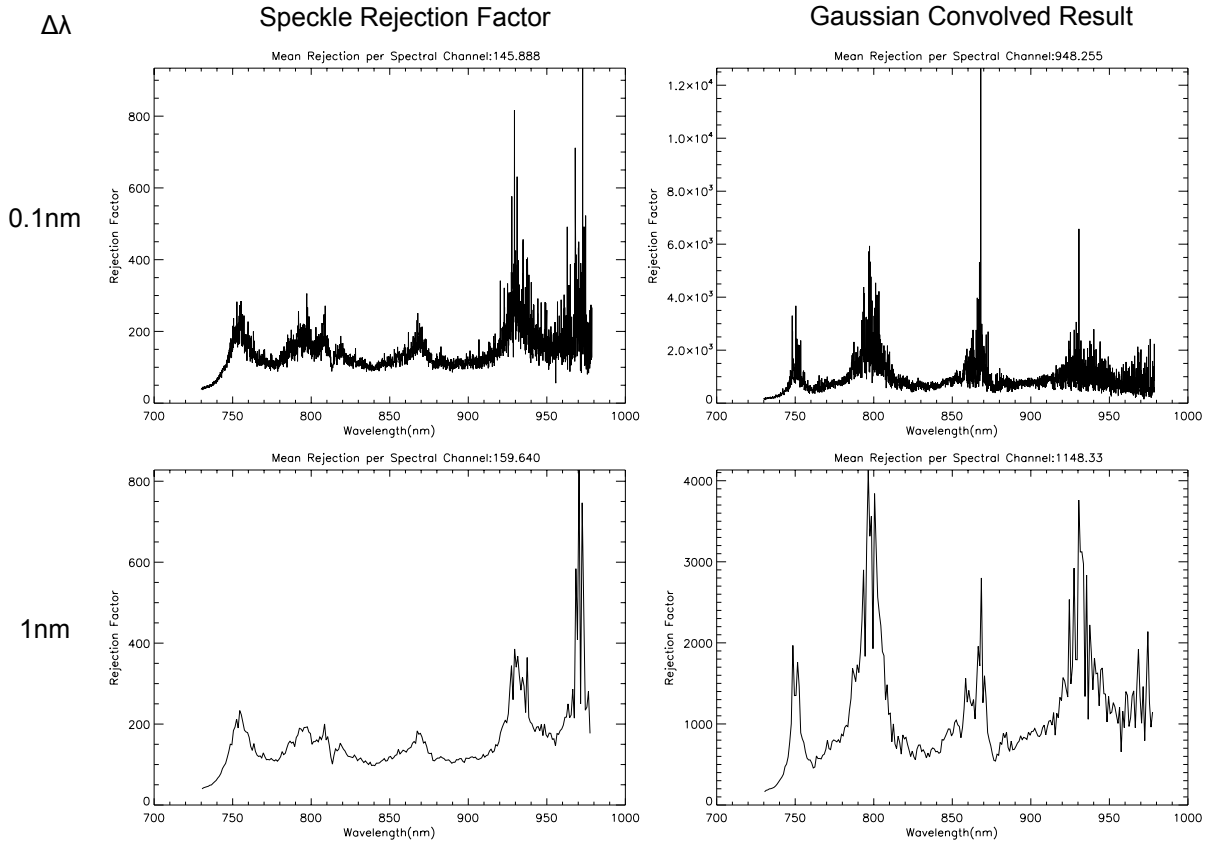

Figure 6.45: Speckle Rejection Factor: Calculated as the ratio of the RMS value of the scaled datacube to its residuals (left) and Gaussian, 2 pixels per FWHM, convolved residuals (right) over the 4 pixels containing the speckles core. Values are shown for original wavelength sampling of $\Delta\lambda = 0.1nm$ (top) and binned sampling $\Delta\lambda = 1nm$ (bottom).

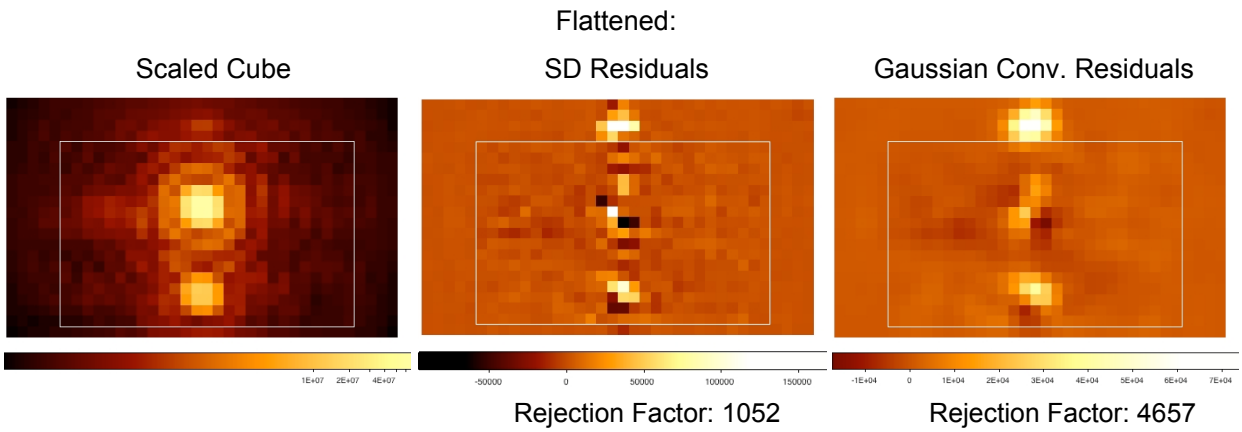

Figure 6.46: Flattened Datacubes: The scaled, residuals and Gaussian (2 pixels per FWHM) convolved residuals datacubes are collapsed along the wavelength axis to produce the figures seen here. The white box dictates the area that is common to all wavelength slices (due the the scaling needed for spectral deconvolution). The speckle rejection factor is shown beneath, calculated as the ratio of the 4 core speckle pixels in the flattened scaled cube to to that of the residuals and Gaussian convolved residuals respectively.

Observations Without the Diffraction Grating

The same analysis procedure was followed as with the previous data sets, the resultant images can be seen in Figures 6.48 - 6.52.

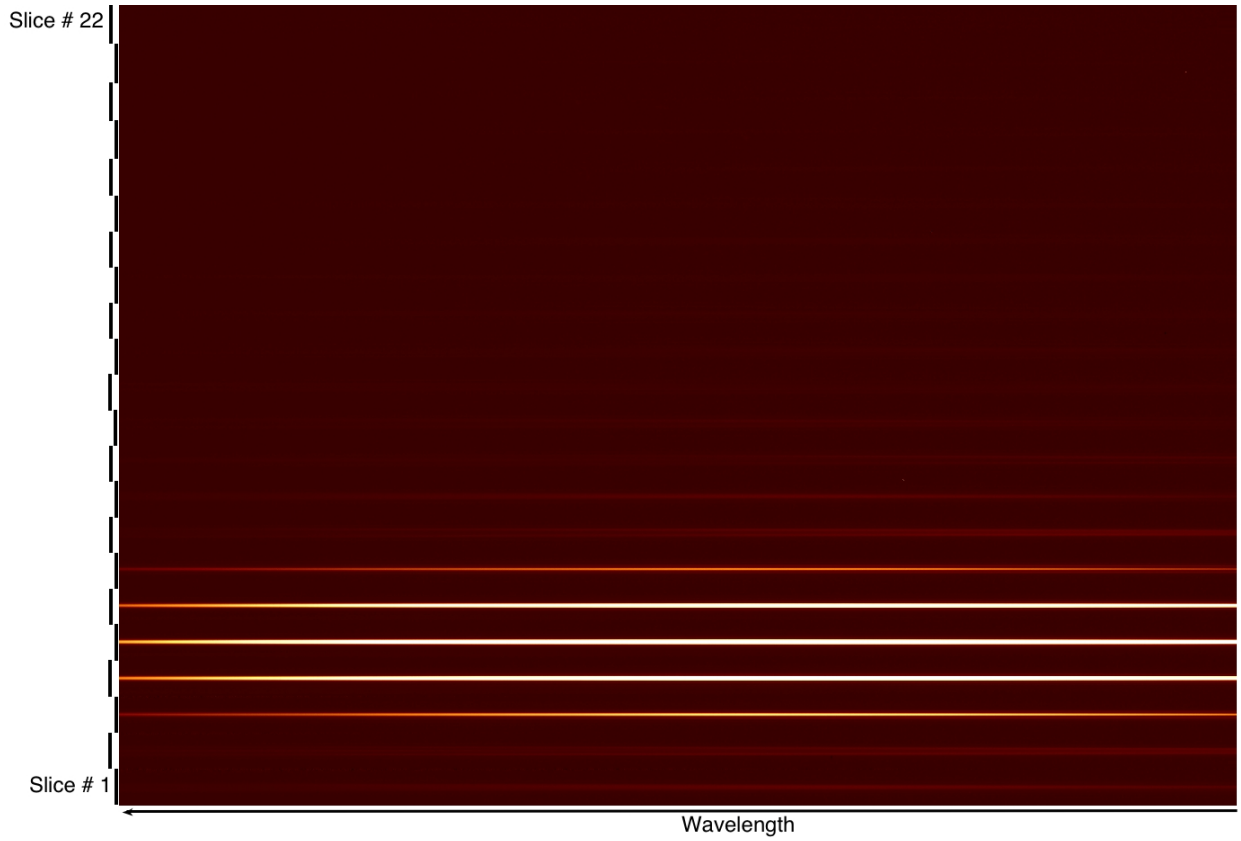

Figure 6.47: Observations without the diffraction grating: Image of the combined, dark subtracted, flat field corrected, wavelength and spatially calibrated observations of our test setup without the diffraction grating in place before reordering to form a datacube. The zeroth order is seen in the bottom slices and the speckle can be seen as the diagonal trace running across the middle-top slices with wavelength. Note the wavelength axis is reversed (left-red, right-blue).

A visual inspection of the results shows that we suffered less from the scattered light in this data set and that is was again very well behaved and fit out well by applying spectral deconvolution. We did, however, seem to suffer from Fourier ringing more in this dataset as can be seen in the fourth row of panels in Figure 6.48. This was likely due to the sources close proximity to the edge of the field of view. Residuals seen here are lower that in the previous data set although they still show the alternating bright, faint trend along the

slice centered on the speckle. The ghost seen in the previous dataset is no longer present which leads us to believe it came from the diffraction grating.

The cuts shown in Figure 6.49 again show no signs of secondary speckles. The vertical cut does however show the Fourier noise, seen to be more intense at the shorter wavelengths due to the greater sampling at longer wavelengths (i.e. as the diffraction limited spot increases in size).

The radial plots seen in Figure 6.50 show very nicely our decreasing signal to noise ratio with wavelength as the speckle gets dimmer due to the QE of the detector (seen as the elevated red line in the 910nm plot) the large rejection factor achieved is also apparent.

Figures 6.51 & 6.52 show the rejection factors that were calculated in the same way as the other two data sets.

Table 6.7 shows all of the achieved speckle rejection factors that were achieved via different methods. The very impressive rejection factors and the plots previously mentioned show that we are not at all being limited by secondary speckles being produced by the slicer, however, they do suggest we are being limited by something due to the speckle moving from slice to slice.

	Speckle		**No Diffraction Grating**	
	Rejection Factor			
Binning	Normal	Convolved with Gaussian	Normal	Convolved with Gaussian
$\Delta\lambda = 0.1nm$	146	948	456	1666
$\Delta\lambda = 1nm$	160	1148	632	2133
Flattened	1052	4657	6262	11779

Table 6.7: Table of the rejection factors achieved

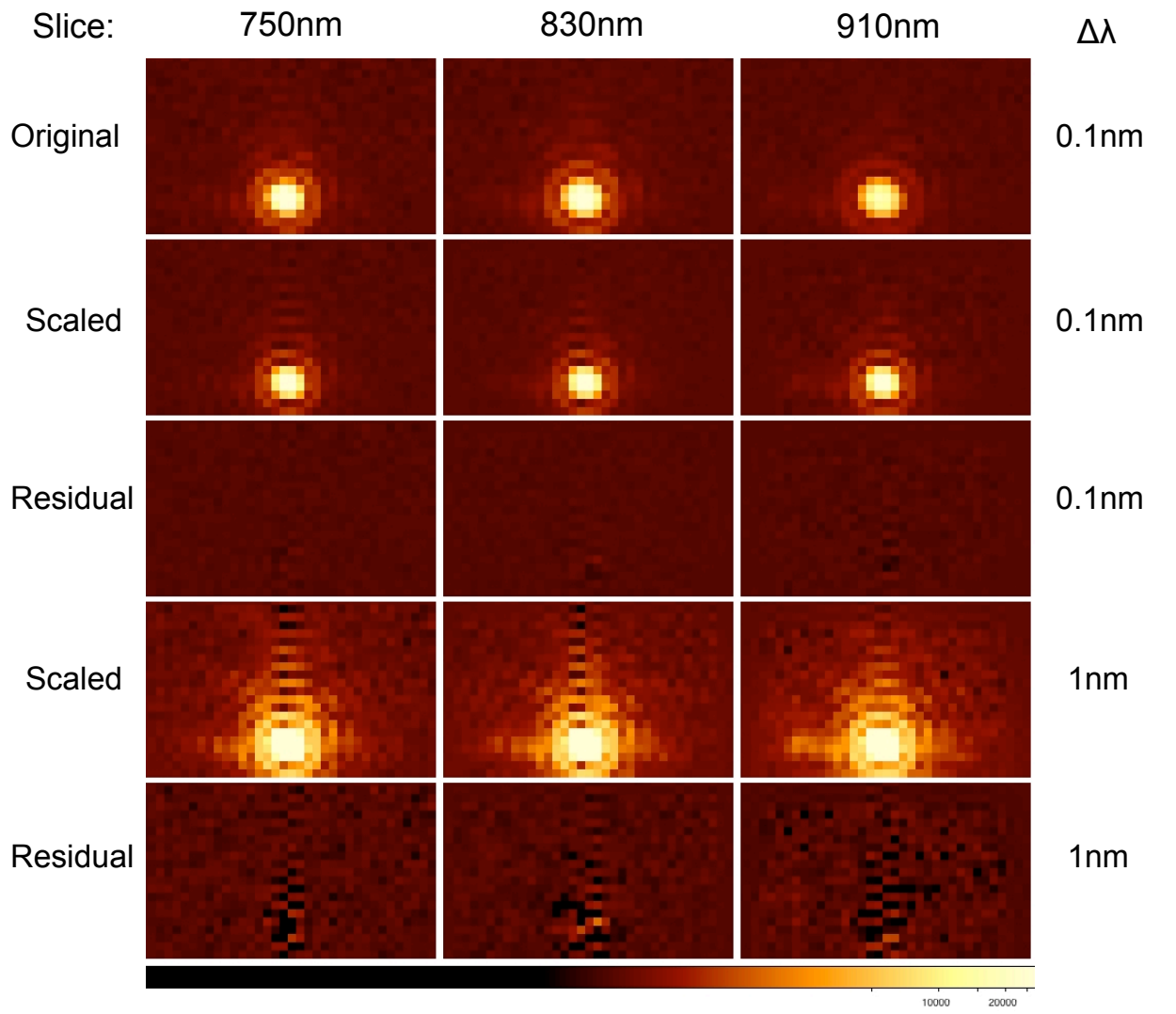

Figure 6.48: Datacube From The SWIFT Slicer IFU (without the diffraction grating) Before And After Spectral Deconvolution: Results are split into three columns, each of which represents a single wavelength channel, from left to right these are 750nm 830nm and 910nm. Titles to the left of the images indicate what stage in the reduction is being shown: Original - the original datacube, Scaled - the datacube after each slice has been scaled with respect to wavelength and Residual - what is left over after performing spectral deconvolution. Titles to the right of the images indicate whether the original wavelength sampling ($\Delta\lambda = 0.1$nm) or the binned up wavelength sampling ($\Delta\lambda = 1$nm) is being shown.

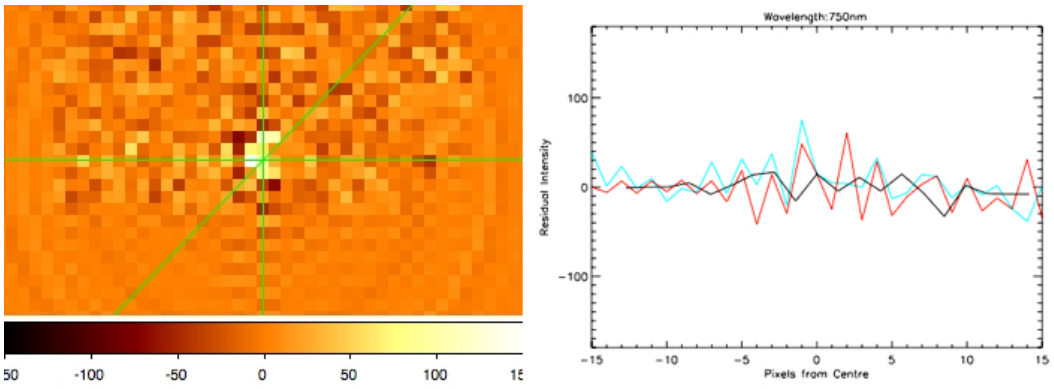

(a) 750nm

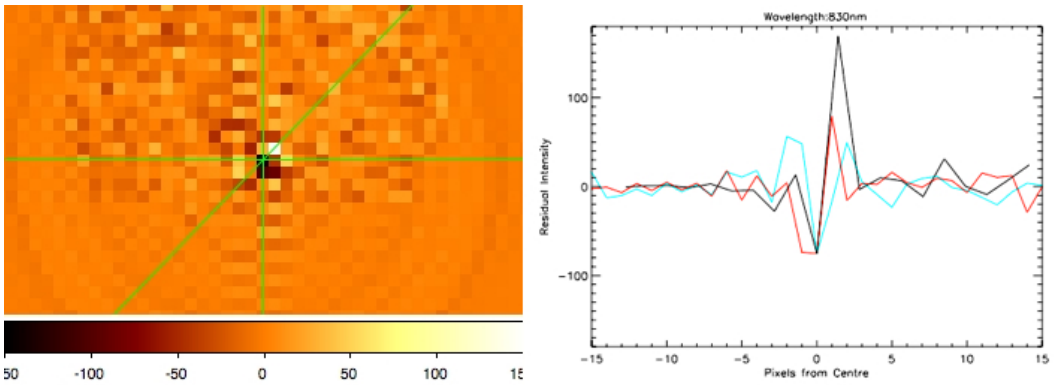

(b) 830nm

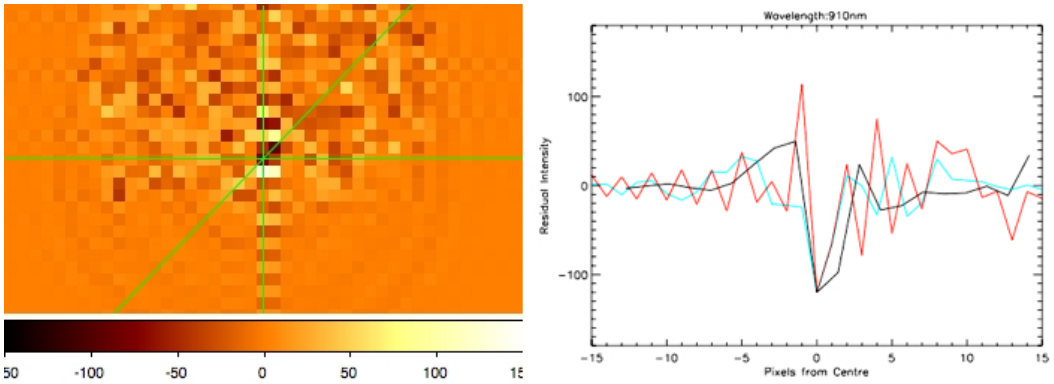

(c) 910nm

Figure 6.49: One Dimensional Cuts Across The Field Of View: Cuts made on the residuals after spectral deconvolution for three wavelength channels each of $\Delta\lambda = 0.1$nm (same as the middle row of Figure 6.48) are shown. Three cuts, passing through the centre of the speckle, are shown for each wavelength channel, as depicted by the green lines in the right hand images. Red - vertical cut, Blue - horizontal cut and Black - diagonal cut.

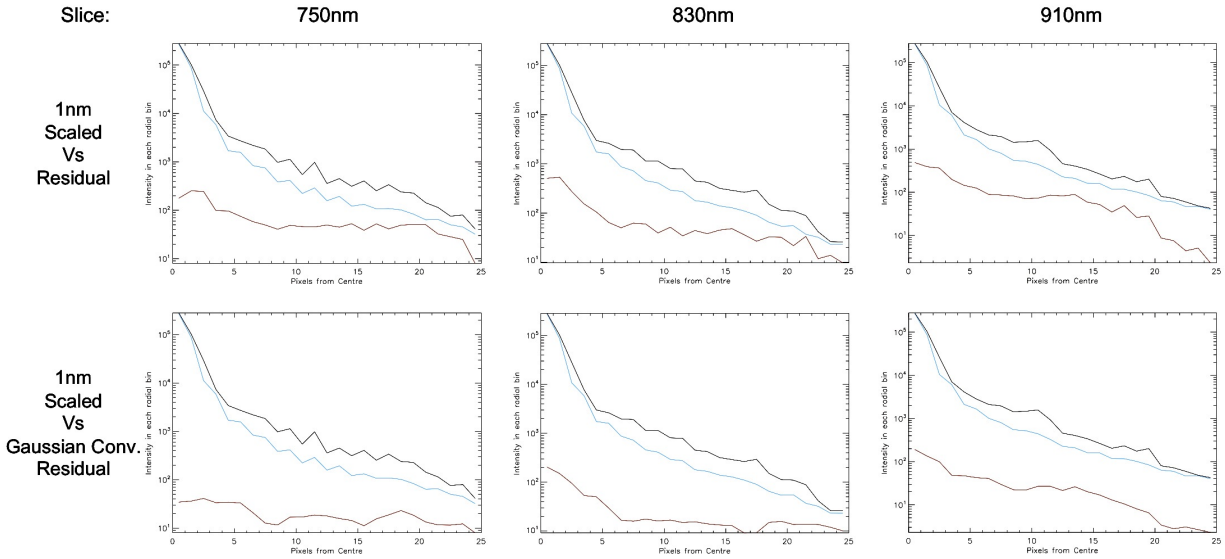

Figure 6.50: Azimuthal Profiles Centered on the Zeroth Order: showing, for the binned datacube of $\Delta\lambda = 1nm$, the values in annular bins centered on the zeroth order of; the maximum value of the scaled datacube (black curve), the RMS value of the scaled datacube (blue curve) and the RMS of the residuals after spectral deconvolution (red curve). These values are shown for the normal residuals (top panels) and the result after convolving with a 2 pixel per FWHM Gaussian (bottom pannels).

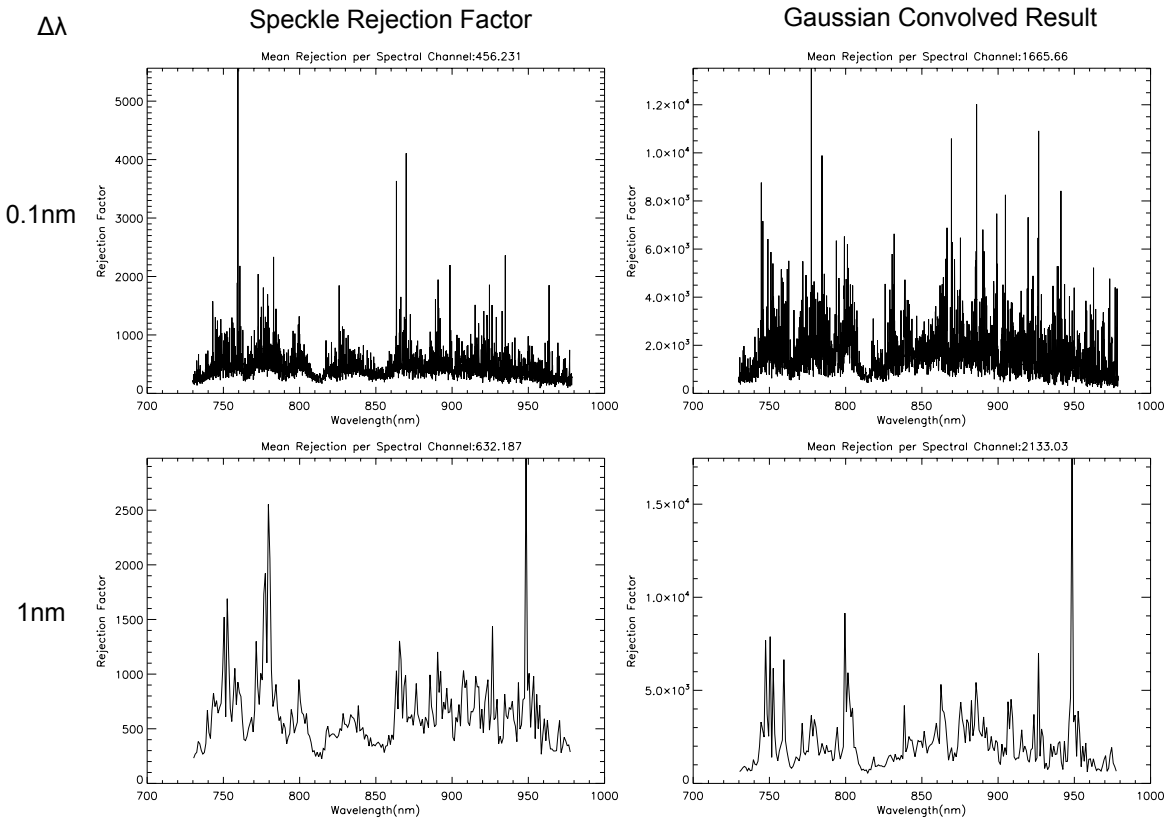

Figure 6.51: Speckle Rejection Factor: Calculated as the ratio of the RMS value of the scaled datacube to its residuals (left) and Gaussian, 2 pixels per FWHM, convolved residuals (right) over the 4 pixels containing the speckles core. Values are shown for original wavelength sampling of $\Delta\lambda = 0.1nm$ (top) and binned sampling $\Delta\lambda = 1nm$ (bottom).

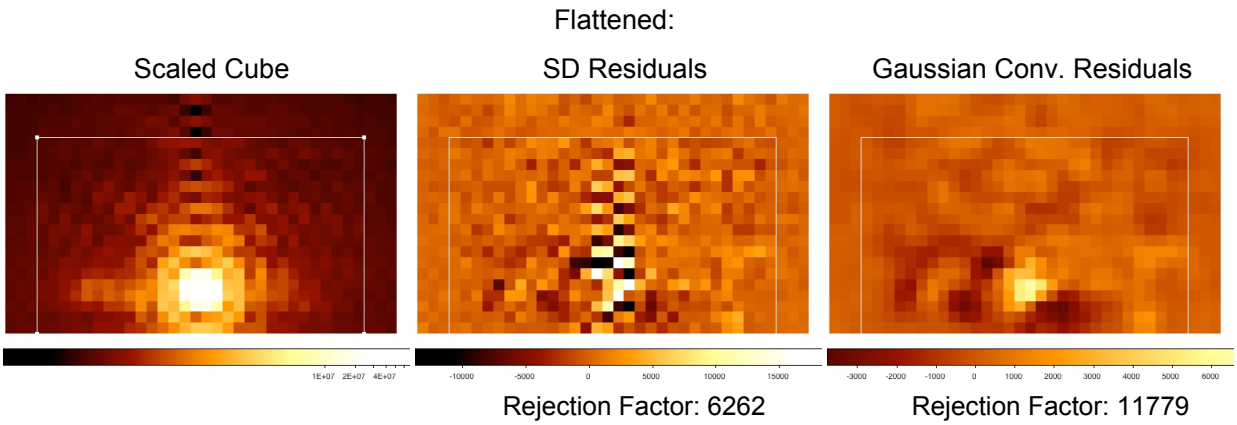

Figure 6.52: Flattened Datacubes: The scaled, residuals and Gaussian (2 pixels per FWHM) convolved residuals datacubes are collapsed along the wavelength axis to produce the figures seen here. The white box dictates the area that is common to all wavelength slices (due the the scaling needed for spectral deconvolution). The speckle rejection factor is shown beneath, calculated as the ratio of the 4 core speckle pixels in the flattened scaled cube to to that of the residuals and Gaussian convolved residuals respectively.

Possible Source of the Errors

As previously mentioned in Section 6.4.3, the trace observations seen in Figure 6.39 were sub Nyquist sampled, resulting in a possible slight centering error, and to a lesser extent scaling error, of the slices.

The centroid of the speckle has to be found (using Gaussian fitting) for the scaling of the datacube. Plots of the identified centroid can be seen in Figure 6.53. As can be seen in the centering along the slice (i.e. X Center), there is quite a systematic change at the level of 0.05 pixels. By comparing to the centering across the slices, it is seen that the minimum and maximum of the x decenter coincide with when the speckle is centered on two slices and on one slice respectively.

Mal-centering and scaling of each slice relative to one another, due to the sub-Nyquist sampled traces, would indeed produce the type of residuals that are seen, due to either too much or too little flux being put into pixels either side of the center of the speckle.

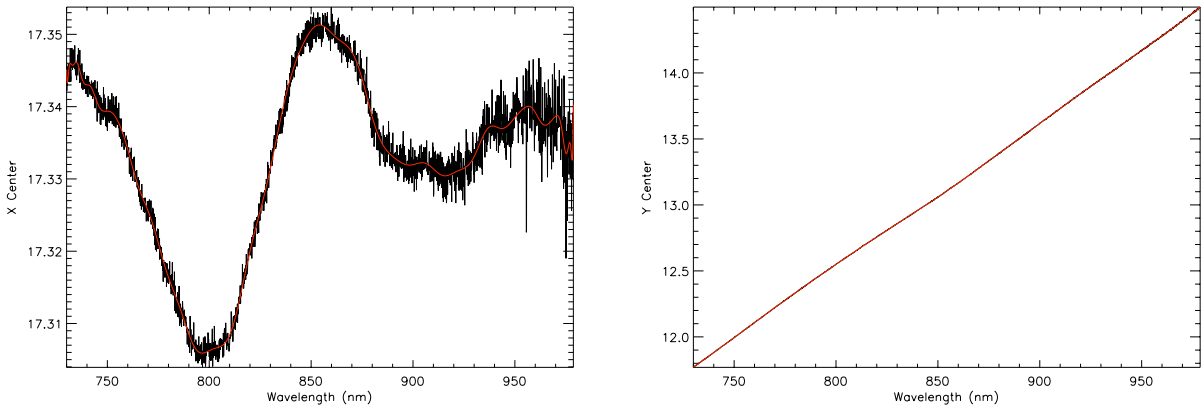

(a) Along Slices

(b) Across Slices

Figure 6.53: Plots of the calculated centroid of the speckle.

6.5 Conclusions from Experiments

Achieved speckle rejection factors appear to be limited by imperfect calibrations. A visual inspection of the residuals almost always shows a positive-negative step change in residual intensity along each slice centered on the speckle. The residuals do not have the same characteristic across the slices, suggesting it is an error in the relative centerings of the slices.

The structure seen in the plots of the speckle rejection factor with wavelength suggests some periodic or systematic variation in the data that is causing a limitation. This effect is seen to a lesser extent in the factor achieved from the data set without the diffraction grating in place, suggesting it is an error in relative slice calibration, rather than wavelength calibration, since our "speckle" in this case is stationary. This theory of systematic noise is also supported by the results after binning up 10 spectral channels to form a datacube with $\Delta\lambda = 1nm$, as the results do not improve by a factor of $\sqrt{10}$. In fact, they improve very little in our simulated speckle observations, however, it does have more of an impact on the results from the data set without the diffraction grating (thus also suggesting it is due to some spatial, rather than wavelength , mis-calibration).

Despite being limited by calibration errors, very impressive speckle rejection factors have been achieved. Performance needed by SPHERE of approximately a factor of 10 out of the speckle rejection is very easily achievable using a slicer based IFS. Results detailed here show that rejection factors of over 100 for individual spectral channels is fairly routinely achievable. However, the push to a factor of 1000 per spectral channel looks to be more difficult, as you really do need to worry about all of the small things such as the interpolation errors, accuracy of calibrations, highly accurate flat fields etc. and a minor error in any of these is likely to be a show stopper.

Far greater rejection factors are achievable if prior information about the spatial extent of an observed real object is taken into account. This is shown via the results after convolving with a Gaussian of 2 pixels per FWHM. The alternating peak-trough nature of the noise along a slice is then blended out due to its limited physical extent, the effect on signal from a real object would be less so due to its diffraction limited size.

No secondary speckles are observed in any of our observations. This is an essential result. The concern about the continued one dimensional coherence up to the detecter looks to have been dispelled. As has been previously stated this is most likely due to the tight tolerances already in place on the spectrograph design and the vast over sizing of the optics helping to negate the effects of diffraction. This supports the results from simulations that show there to only be significant secondary speckle noise produced when the spectrograph contains a large amount of WFE.

On a final note, it should be pointed out that the achieved speckle rejection fits well with the factor of 100-1000 required from the IFS for EPICS to achieve its goals. Although the prototype image slicer and the spectrograph (identical in design to the SWIFT spectrograph) are not optimized for high contrast operation, we do obtain the required contrast.

6.5.1 Future Tests

There are a couple of additional tests that could be performed with this setup to further the understanding of the achievable rejection factors with a slicer IFS. These are;

By opening up the holes in the focal plane mask and using a large pupil stop a set of well sampled traces can be made from which more accurate calibrations would hope to eliminate the residual noise we are seeing.

By rotating the diffraction grating by 90° we can disperse a speckle along the slices instead of across them. This will give us insight into whether or not it is the movement of the speckle or the calibration of relative slices that is limiting us.

Chapter 7

High Contrast Observations with SINFONI

In this chapter we discus the application of spectral deconvolution to on sky SINFONI data, a slicer based IFS on ESO's Very Large Telescope (VLT).

Details of the design of SINFONI and its capabilities are presented, followed by a review of the SINFONI observations of AB Dor C performed by Thatte et al. (2007). These results were one of the major reasons for reinvestigating the use of a slicer based IFS for high contrast observations. The analysis of our observations of Speedy Mic using SINFONI are then detailed whereby the method of data reduction, application of spectral deconvolution and achieved contrast are described.

7.1 Spectrograph for Integral Field Observations in the Near Infrared

* SINFONI is the near infrared integral field spectrograph at the VLT. It comprises of the SPIFFI slicer based IFS that is fed by a curvature sensing adaptive optics module. The instrument offers a choice of 4 gratings and 3 pixels scales which are detailed in Tables 7.1 and 7.2.

A photographs of the layout of the instrument and of the slicer can be seen in Figures 7.1 and 7.2 respectively. The SINFONI instrument has not been designed with high contrast imaging in mind, however, the following sections detail how SINFONI has shown significant promise in this area.

*Details and figures in this section have been drawn from the SINFONI User Manual VLT-MAN-ESO-14700-3517 provided by ESO

Field of view	Spaxel size on the sky
8"x8"	125mas x 250mas
3"x3"	50mas x 100mas
0.8"x0.8"	12.5mas x 25mas

Table 7.1: SINFONI Pixel Scales

Band	Dispersion	FWHM of line	Resolution(λ_{min})	Wavelength Range
J	0.15nm/pix	$\sim 4pix$	~ 2000	$1.10-1.40\mu m$
H	0.20nm/pix	$\sim 3pix$	~ 3000	$1.45-1.85\mu m$
K	0.25nm/pix	$\sim 2pix$	~ 4000	$1.95-2.45\mu m$
H+K	0.50nm/pix	$\sim 2pix$	~ 1500	$1.45-2.45\mu m$

Table 7.2: SINFONI Gratings

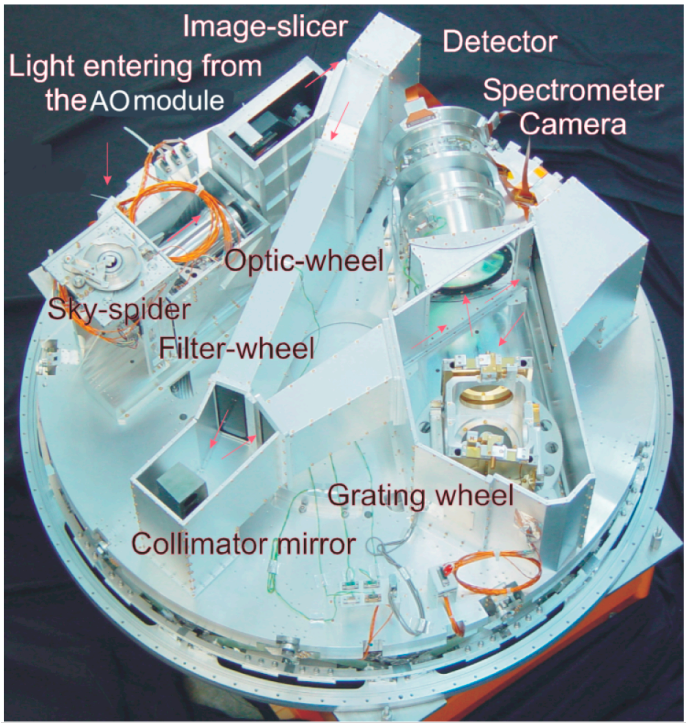

Figure 7.1: An inside view of SPIFFI: The cryostat cover and the reinforcing structure have been removed to provide a free view on the opto-mechanical components of SPIFFI. The light enters from the top, and passes the sky-spider. The pre-optics with a filter-wheel and interchangeable lenses provides three different image scales. The image slicer re-arranges the two-dimensional field into a pseudo-long slit, which is perpendicular to the base plate. Three diamond turned mirrors collimate the light onto the gratings. In total, four gratings are implemented on the grating drive. A multiple-lens system then focuses the spectra on a Rockwell HAWAII array. The diameter of the instrument is 1.3m.

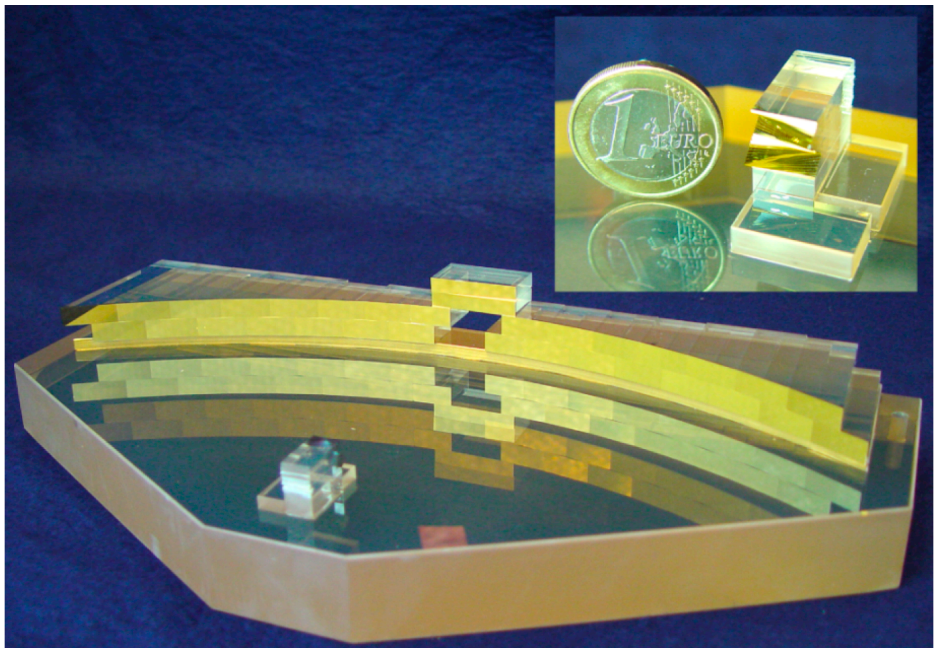

Figure 7.2: SPIFFI image slicer: The light enters through the hole in the large bank of slicer mirrors and is imaged onto the slicer stack containing 32 small mirrors (shown in the sub-panel shown with a 1 Euro coin for scale). From here each sliced image is redirected towards its corresponding second slicer mirror in the large bank of slicer mirrors, which then re-arranges the slitlets into a 31 cm long pseudo-slit.

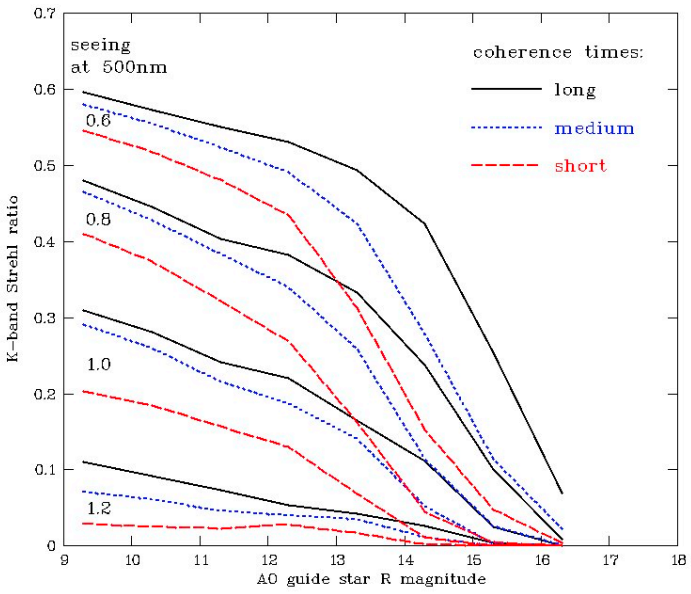

Figure 7.3: Natural Guide Star performance of the adaptive optics system in SINFONI, this is the mode used for high contrast observations as the primary star can be used as the guide star. Performance is shown for a range of optical seeing values and for short medium and long coherence times in the atmosphere

7.2 A Reason for Further Investigation : AB Dor C

† It has been mentioned in previous sections a very good result from using spectral deconvolution on sky with SINFONI has already been obtained by Thatte et al. (2007) using observations of AB Doradus. In the following section I will give a brief overview of what they managed to achieve.

The following results were obtained from 20 minutes of on sky data using SINFONI in the H+K grating mode with a pixel scale of $12.5mas \times 25mas$ (exposures were dithered to give $12.5mas \times 0.125mas$ resolution). A mean Strehl ratio of 0.37 delivered by SINFONI's AO system for the period of observation and seeing varied between 0.58 and 0.74 arcsec. The target was AB Doradus, a local young K dwarf which was previously known to have an M dwarf companion (AB Dor C) at a relative contrast of $\Delta K = 5mag$ only 0.2arcsec away (Nielsen et al., 2005a). AB Dor A was an ideal guide star candidate as it has a K-band magnitude of 4.6. The reason behind this observation was to demonstrate, for the first time, the application of the spectral deconvolution technique to ground based data sets.

It should be noted that AB Dor C is located within the bifurcation radius of this setup, described in Section 2.3.3. As such the process had to be modified slightly, using a iterative procedure to identify the companion and extract its spectrum.

Figure 7.4 shows plots of a single wavelength channel before applying any post processing, the same but with an azimuthally averaged PSF removed to show up the quasi static speckles and finally the same again, after having applied the spectral deconvolution technique. The result is very impressive and the corresponding extracted spectrum can be seen in Figure 7.5, which also shows a comparative spectrum of AB Dor C that was previously found using NACO AO long slit spectroscopy. A point to be made here is that by obtaining the whole H+K spectrum in one go they were able to accurately determine the continuum slope of AB Dor C which is not the case for the NACO observations which are affected by varying slit filling factors. The achieved contrast for a single wavelength channel, after binning up the datacube to a spectral resolution of ~ 400, is shown in Figure 7.6. They manage to get a contrast of ~ 9mag at 0.2 arcsec and ~ 11mag at 0.5 arcsec. These are very impressive contrasts considering there is no coronograph in SINFONI. The lack of a coronograph can be seen as an advantage in some respects as it enables access to smaller inner working radii. The ~ 1mag offset from the photon noise seen in the contrast curve is suggested to be due to errors

†Details and figures in this section have been drawn from Thatte et al. (2007)

from the interpolations required to create the datacube.

It was these results that spurred the effort to reinvestigate the use of slicer based integral field units for future instruments for the detection of exoplanets.

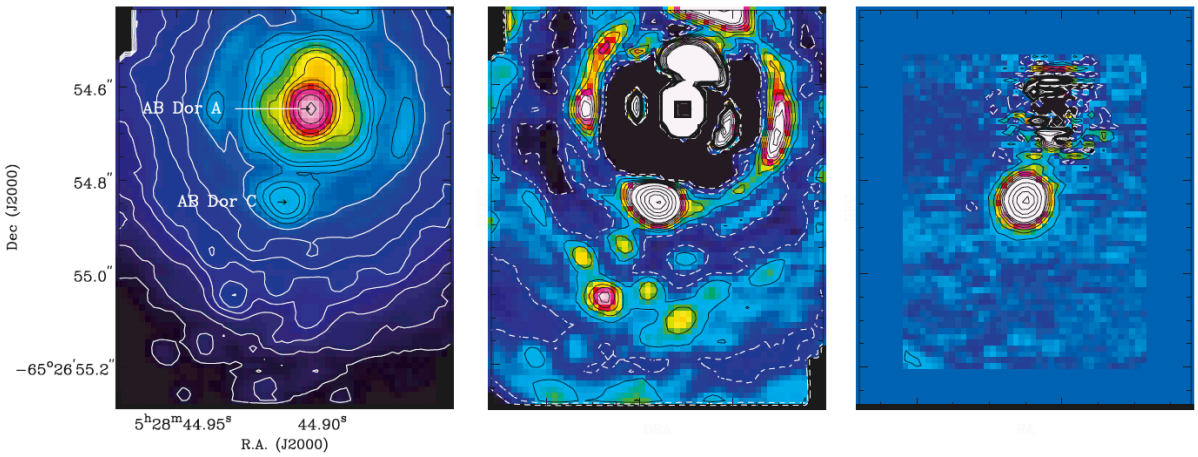

Figure 7.4: Illustration showing the efficacy of the SD technique at removing both PSF artefacts and super-speckles from the SINFONI IFS data cube for the AB Dor system. The left-hand frame shows one wavelength slice of the observed data cube at $2.2\mu m$. Note that the entire vertical extent of the image is only 0.9 arcsec. The colour table is logarithmic (minimum 10^1, maximum 10^4). The contours are logarithmic, from 0.9 to 2.3 in steps of 0.1, and from 2.3 to 4.0 in steps of 0.2. The middle frame shows the same data, but with a radial profile fitted and subtracted, so as to highlight the PSF imperfections. The super-speckles are easily confused with real sources in this narrow-band image. The colour table is now linear (minimum -10, maximum 25), with contours from -12.5 to 32.5 in steps of 5, and from 32.5 to 150 in steps of 20. The four-fold symmetry of the Airy pattern arises from the superposition of the diffraction spikes of the secondary support structure on the Airy rings. The right-hand frame shows the same wavelength slice of the data cube, after applying the SD technique iteratively. Colour table and contours are the same as for the middle frame. Super-speckles are completely absent at the lowest contour level of ± 2.5, corresponding to a 1σ error of ≤ 1 unit. Taken from Thatte et al. (2007)

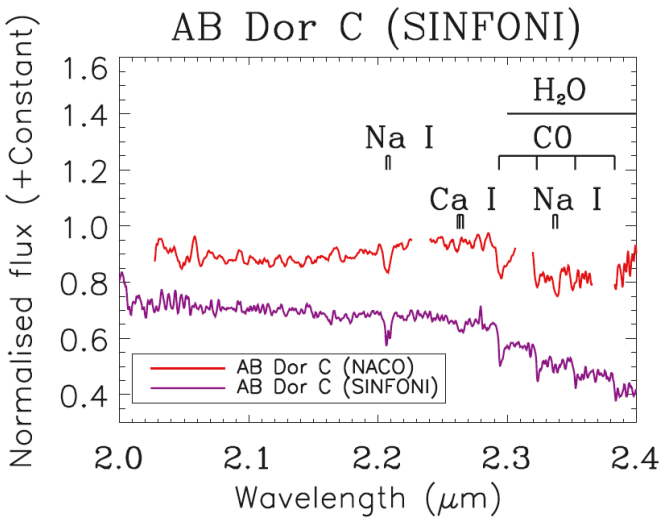

Figure 7.5: The K-band extracted spectrum of AB Dor C, with some of the prominent stellar features marked. The K-band spectrum obtained by NACO AO long-slit spectroscopy, at 0.150 arcsec separation (Nielsen et al., 2005b) is also shown for comparison. Note that the spectrum obtained by Thatte et al also correctly recovers the continuum slope, vital for deriving the spectral type of this young object. The 'emission' feature just shortward of the first CO bandhead is a residual telluric feature that was not correctly subtracted out. Taken from Thatte et al. (2007)

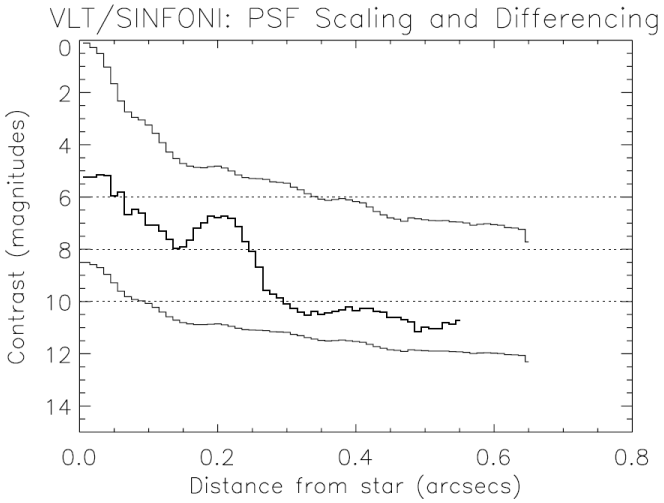

Figure 7.6: The plot shows three curves - the top curve is the radial profile of AB Dor A. The bottom curve is the square root of the top curve, thus representing the photon noise limit. The middle curve is the standard deviation in the SD result frame, so it is a measure of the residual noise. The horizontal lines at 6, 8 and 10 mag are for reference. The large bump at 0.2 arcsec in the SD result frame is due to AB Dor C. The achieved contrast is 9 mag at 0.2 arcsec, and 11 mag at 0.5 arcsec, in 20 min exposure time at $R_{eff} = 400$. As no coronagraph is used, very high contrasts can be obtained at small inner working radii. Taken from Thatte et al. (2007)

7.3 Speedy Mic

In this section I will describe the results obtained from applying the spectral deconvolution technique, with all of our improvements as described in earlier Chapters, to on-sky data of the star HD 197890.

HD 197890, also referred to as BO Mic or by its nickname "Speedy Mic", is a close by , very rapidly rotating, active K 0-2 V star. Its properties are listed in Table 7.3.

We obtained a set of SINFONI observations of Speedy Mic covering the H & K bands with a spectral resolution of ~ 1500 (from $1.493 - 2.455\mu m$ with $\Delta\lambda = 0.0005\mu m$) using the 0.025" pixel scale giving a field of view of 0.8" for a single observation. Observations requirements were such that the seeing was to be no worse than 0.6" and a Strehl Ratio of at least 59% should be achieved, see Figure 7.3. Observations were split into four main pointings each one with Speedy Mic located in a different corner, see Figure 7.9(a). Each of these pointing was made up of 24 dithered pointings which in turn were made up of 11x5 second read outs. This gave us a total of 22mins on source for each quadrant (88mins total on-sky time).

Speedy Mic	
Distance	$44.4pc$
Spectral Type	K 0-2 V
Mass	$0.9 \pm 0.05 M_{sun}$
Age	$3.3 \pm 0.5 \times 10^7 Gyr$
Radius	$0.9 \pm 0.05 R_{sun}$
Effective Temperature	$4750 \pm 50K$
Inclination Angle	$70 \pm 10^\circ$
Equatorial Rotation Velocity	$143^{+23}_{-17} kms^{-1}$

Table 7.3: Properties of Speedy Mic, taken from Wolter et al. (2005) & Wood et al. (2000)

The data were reduced in the standard way using ESO's SINFONI pipeline by Roberto Abuter, and I would like to thank him for producing the data cube that was used in the analysis.

The same implementation of the spectral deconvolution algorithm as was used in the analysis of the experiments described in Chapter 6 was followed in the analysis of this data set, only the residuals after performing SD were re-scaled back to the original frame of reference so as to look for companions, as is described in Section 2.3.3.

The calculated spectrum of Speedy Mic, nessesary for normalising the spectrum of the speckles, can be seen

in Figure 7.7. The region shaded red in this plot is an area of low SNR caused by atmospheric absorption. Data in this region was masked out during the fitting of the speckles so as not to influence the result.

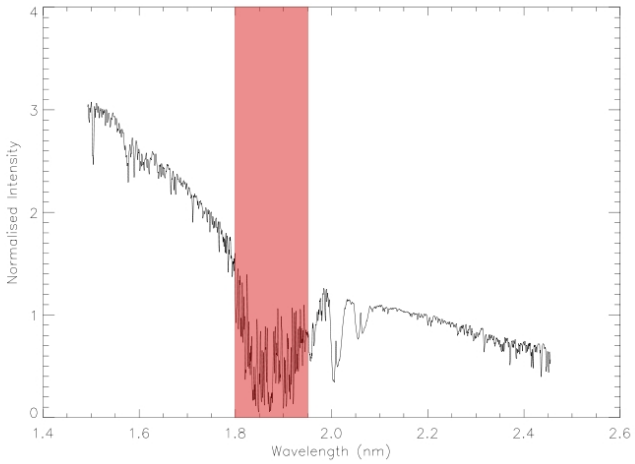

Figure 7.7: Spectrum of Speedy Mic extracted from the scaled data cube. Used for normalising the speckle spectra. The region shaded red in this plot is an area of low SNR caused by atmospheric absorption, for this reason the data in this region were masked out during the fitting of the speckles so as not to influence the result.

An image of a single datacube slice (at $1.65\mu m$) before and after the application of spectral deconvolution, along with a radial contrast curve for the slice is shown in Figure 7.8. The structure left after spectral deconvolution, seen in Figure 7.8(b) and in the corners of (a), is not regular speckle noise as its pattern completely changes when looking at neighbouring wavelength channels. In fact it looks to be completely random when moving through the cube in wavelength. It is also not likely to be secondary speckle noise produced by the IFS for this reason and due to it having a spatial extent of greater than one slice width.

All 1925 wavelength channels of our datacube (from $1.493-2.455\mu m$ with $\Delta\lambda = 0.0005\mu m$) before and after applying spectral deconvolution were summed together to give the plots seen in Figure 7.9, essentially creating a broadband image. The random noise seen in Figure 7.8 is now very nicely smoothed out, lowering the noise floor. However, artefacts of the imperfect calibration of the SINFONI data are clearly seen in Figure 7.9 (b) as the offsets in intensity of individual slices. The noise at the edges of the FoV are an artefact of the Fourier transforms used when performing spectral deconvolution. Figure 7.9(c) shows the radial contrast found from the datacubes collapsed along the wavelength axis. In an attempt to get around

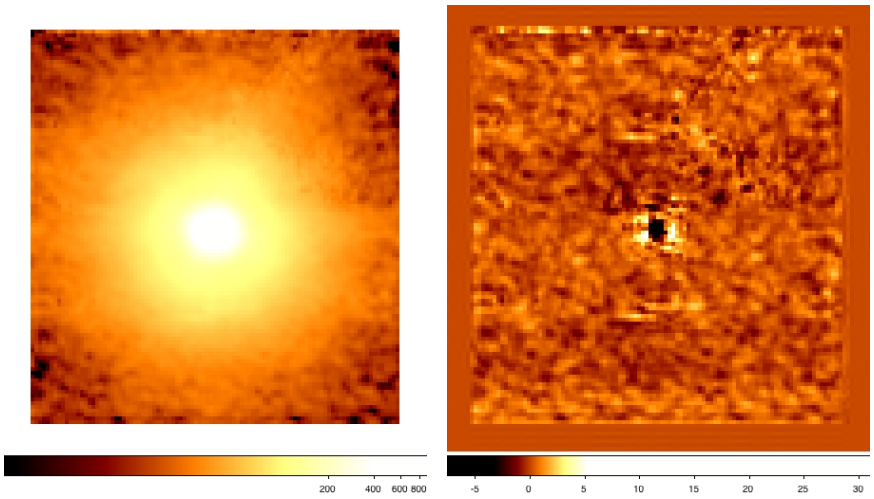

(a) Original Slice (b) Post Spectral Deconvolution

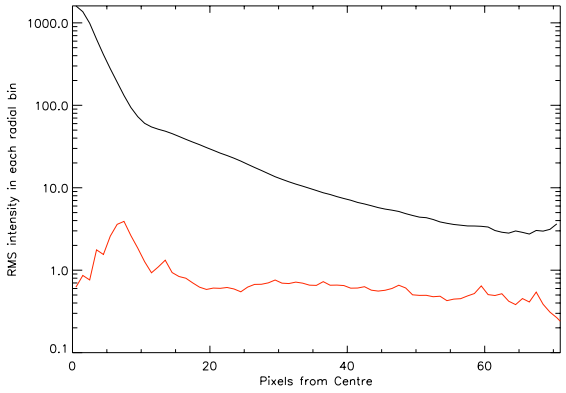

(c) Radial Contrast (40pix = 0.5")

Figure 7.8: Results from a single wavelength slice (1.65μm) FoV = 1.2"x1.3": (a) shows the original slice (log stretch), (b) shows the same slice after applying spectral deconvolution. (c) shows the average intensity for 1pixel wide annular bins centered on Speedy Mic. The black curve is the original radial profile and the red curve is the result after applying spectral deconvolution (1 pixel = 0.0125").

the calibration errors an average value of the intensity for each slice in each quadrant is calculated from a typical region of the image (i.e. a region not covering the core of Speedy Mic or the noisy edges) and removed. The result can be seen in Figure 7.9(d). Figure 7.9(e) highlights a tenuous detection of a possible companion. It's extent is suggestive of a real point source and the negative dips radially either side of the object are a tell tale sign of something real, see Section 5.2. However, we shall not look into this detection any further here.

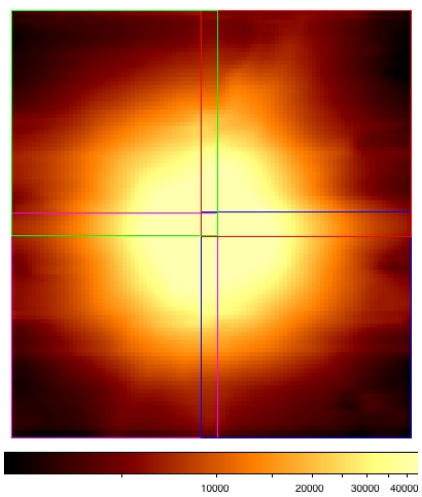

(a) Flattened Original Cube

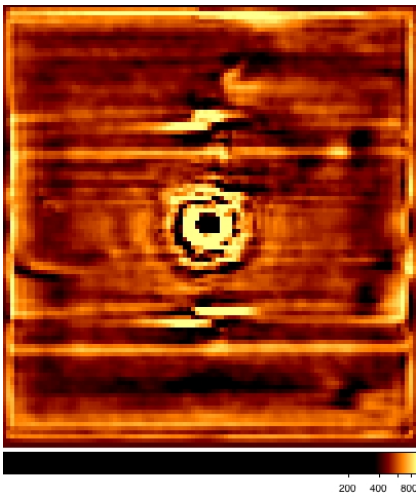

(b) Post Spectral Deconvolution

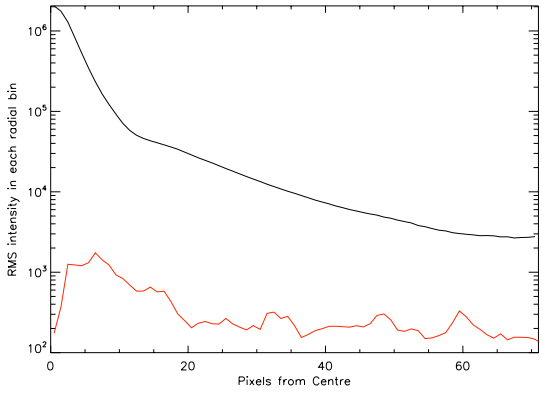

(c) Radial Contrast (40pix = 0.5")

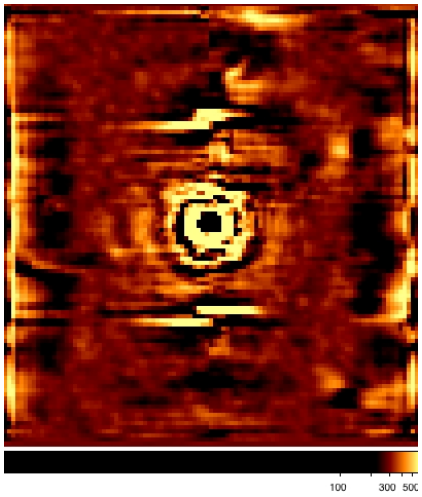

(d) Calibration Corrected

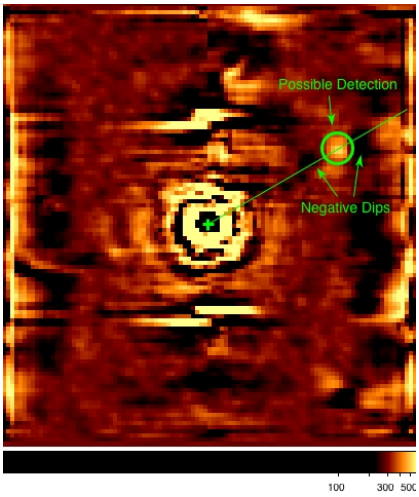

(e) Possible Detection

Figure 7.9: Results after collapsing the data cubes along the wavelength axis(all plots are on a log stretch) FoV = 1.2"x1.3":(a) shows the flattened original datacube with the locations of the four pointings marked with the multicoloured regions, (b) shows flattened cube after spectral deconvolution has been performed. (c) shows the average intensity for 1pixel wide annular bins centered on Speedy Mic. The black curve is the original radial profile and the red curve is the result after applying spectral deconvolution(1 pixel = 0.0125"). (d). A lot of the structure that is seen in (b) appears to be relative calibration errors between the slices. (d) shows the result after removing an average slice value for each slice in each quadrant. A possible detection candidate is pointed out in (e)

7.3.1 Conclusion from SINFONI Observations

Results seen in Figures 7.8 & 7.9 show that we are achieving 1σ contrasts of $\sim 1 \times 10^3$ for an individual wavelength channel and $\sim 1 \times 10^4$ for the broadband image at a separation of 0.25". The noise that we are left with does not look to be caused by the quasi static speckles, which are very well removed, or be due to additional speckles produced in the slicer IFS (due to the shape and completely random distribution of the noise with wavelength). It is most likely due to errors in the production of the data cube. On top of this, errors due to imperfect calibration of the slices relative to each other add up to give an impressive effect in the cube image collapsed along the wavelength axis, see Figure 7.9. Modifications to the data reduction to help this are discussed in the following section. Overall the quasi static speckle noise is very well removed from this data set and any modification of the speckles or production of secondary speckle noise as a result of using a slicer IFU is not seen here.

7.4 Future Modifications of the Method of SINFONI Data Reduction

It is obvious from the appearance of the resultant images after application of spectral deconvolution, seen in Figures 7.8 &7.9, that we are being limited by the accuracy of the reduction to make the original data cube. In this section I will outline the current method of datacube production followed by the SINFONI pipeline and detail a new way of reducing the data to provide more accurate results.

7.4.1 SINFONI Pipeline Data Reduction Technique

The standard pipeline reduction has to make six interpolations to produce the final data cube:

1. Wavelengths are aligned to a reference frame to remove any shift due to flexure
2. Global key stone correction is made using trace frames
3. Wavelengths are resampled to the requires values
4. Sub pixel shifts are needed to align each slice relative to one another in the creation of a data cube
5. Correction for atmospheric dispersion

6. Combining dithered data cubes

Added onto this are the interpolations needed in the application of the spectral deconvolution algorithm.

7.4.2 Modifications

Reduction of the Number of Interpolations

I can foresee no problem in reducing this number of interpolations down to just two:

1. Key stone correction of the slices. This can be corrected for by one interpolation of the readout as a whole using the North-South fiber tests as reference points with which the distortion can be calculated.

2. Wavelength calibration and relative slice centering can then be performed in another interpolation in the same way that has been done for the experiments described in Chapter 6.

These calibration steps should be performed on each dithering position individually (producing a cube for each).These cubes can then be resampled individually, to adjust for the dithering pattern and atmospheric diffraction, in the same interpolations that are needed for the application of the spectral deconvolution algorithm. Therefore negating the need for an additional interpolation.

Calibration Data

The accuracy of the flat fields and the dark frames becomes very important when moving to the high contrast regime. Master flats and darks with very high SNR should be made and used for calibration of the data.

Chapter 8

Conclusions & Future Work

All work performed in this thesis supports the suggestion that slicer based integral field spectrographs do not inherently limit the contrast achievable;

Experimental tests described in Chapter 6 show that, despite being limited by calibration errors, very impressive speckle rejection factors have been achieved. Performance needed by SPHERE of approximately a factor of 10 out of the speckle rejection is very easily achievable using a slicer based IFS. Results detailed here show that rejection factors of over 100 for individual spectral channels is fairly routinely achievable. However, the push to a factor of 1000 per spectral channel looks to be more difficult, as you really do need to consider all of the small things such as the interpolation errors, accuracy of calibrations, highly accurate flat fields etc. and a minor error in any of these is likely to be a show stopper.

The tests also demonstrated that far greater rejection factors are achievable if prior information about the spatial extent of an observed real object is taken into account. This is shown via the results after convolving with a Gaussian of 2 pixels per FWHM. The alternating peak-trough nature of the noise along a slice is then blended out due to its limited physical extent, the effect on signal from a real object would be less so due to its diffraction limited size.

The concern about the continued one dimensional coherence up to the detecter looks to have now been dispelled;

Simulations described in Chapter 5 show that significant secondary speckles are formed only when a large

amount of differential WFE is added. In contrast to the 100nm of differential WFE needed to bring out the secondary speckles in the simulations, spectrographs built for this purpose will be diffraction limited and therefore, by definition, they should have no more than $\lambda/14$ of RMS WFE.
None of the experimental tests showed any secondary speckles to be present. Thus confirming the simulated result. As has been previously stated this is most likely due to the tight tolerances already in place on the spectrograph design and the vast over sizing of the optics helping to negate the effects of diffraction.

It should be pointed out that the achieved speckle rejection from experiments fits well with the factor of 100-1000 needed from the IFS for EPICS to achieve its goals. Although the image slicer and the spectrograph used were not optimised for high contrast operation, we still obtain the required rejection. This means that a slicer designed IFS is a viable option for the EPICS instrument. Although the BIGRE based design is favourable due to the experience gained through SPHERE development and consequently its more advanced opto-mechanical design, the slicer based design has several advantages;

- potentially offers a larger field of view
- can provide a higher spectral resolution while still in an integral field mode (not possible for a BIGRE design)
- spectra can be packed closer together on the detector providing a better detector fill factor
- slicer based design provides a higher efficiency than the BIGRE design.

However, as addressed in Chapter 4, the speckle pattern is only stable for $\sim$10-20 minutes, and so over hundreds of exposures, they would be randomly distributed. Therefore, the degree to which spectral deconvolution can reject them will establish the noise floor for the planet detection. This is a problem due to the limited life time of the speckles; We may integrate for the amount of time required to theoretically detect a given planet but the speckles observed may not exist long enough for us to get a measurement with a high enough SNR. Therefore, it may not be the type of IFS design that limits the speckle rejection factor but rather the photon noise of the speckle itself.

Results from our application of the spectral deconvolution method to on-sky data, seen in Chapter 7, show that standard calibrations are not good enough when entering the high contrast regime and highlight the point that meticulous attention to error sources is needed when reducing data. That having been said, we still achieve a contrast of $>10^3$ at 0.25" separation for a single wavelength channel.

8.1 Future Work

8.1.1 Simulations

The AO modelling group at LAOG have prepared some new simulations that will have an increased FoV. The current simulations have a very small FoV and suffer extensively from Fourier noise during the interpolations. The new simulations include a more realistic E-ELT pupil (i.e. containing spider arms and artefacts from the gaps between mirror segments).

We intend to make the added WFEs more realistic by using those calculated from the optical design and adding in an additional WFE for each slitlet that varies slowly with wavelength, representing the spectra of the slitlets being dispersed through the spectrograph.

We intend to use the simulations to probe parameter space by increasing the range of errors added to the system and also to determine the optimum spectral and spatial resolutions required to produce the best results.

8.1.2 Experimental Tests

There are a couple of additional tests that could be performed with this setup to further the understanding of the achievable rejection factors with a slicer IFS. These are;

By opening up the holes in the focal plane mask and using a large pupil stop a set of well sampled traces can be made from which more accurate calibrations would hope to eliminate the residual noise we are seeing.

By rotating the diffraction grating by 90° we can disperse a speckle along the slices instead of across them. This will give us insight into whether or not it is the movement of the speckle or the calibration of relative slices that is limiting us.

8.1.3 Working with On-Sky Data

Improvement of SINFONI Data Cube Reduction Procedure

As is detailed in Section 7.4, we intend to improve the method of SINFONI data reduction by reducing the number of interpolations performed and increasing the signal to noise of calibration frames. Thus, we intend to see how far we can push the capabilities of SINFONI.

ADI with SINFONI

There is also the possibility of using SINFONI in an ADI mode, whereby the pupil de-rotator is switched off. By doing this we can try combining the spectral deconvolution and angular differential imaging techniques to see what new levels of contrast are achievable.

SWIFT Diffraction Limited Scale

As mentioned in Chapter 6, the SWIFT instrument is currently back in Oxford. We now have a design for an additional diffraction limited pixel scale that could be implemented with very little effort. Our intention is to add in some sort of focal plane mask at the slicer to block out the central star as well as possibly inserting an apodizer into the pupil located within the PALM3K instrument. The result would be an on-sky demonstration of the speckle rejection factors achievable by the first diffraction limited, slicer based, integral field spectrograph behind a very high order adaptive optics system (PALM3K on the Hale 200" telescope). This would also provide a comparison to the Project 1640 TIGER based high contrast IFS, also located at the Hale 200".

Bibliography

ADEL, A., 1937. A Determination of the amount of Carbon Dioxide above the Reflecting Layer in the Atmosphere of the Planet Venus. Astrophys. J., **85**, 345–+.

ADEL, A. & SLIPHER, V. M., 1934. The Atmospheres of the Giant Planets. Nature, **134**, 148–149.

ANTICHI, J., DOHLEN, K., GRATTON, R. G., MESA, D., CLAUDI, R. U., GIRO, E., BOCCALETTI, A., MOUILLET, D., PUGET, P. & BEUZIT, J., 2009. BIGRE: A Low Cross-Talk Integral Field Unit Tailored for Extrasolar Planets Imaging Spectroscopy. Astrophys. J., **695**, 1042–1057.

BACON, R., COPIN, Y., MONNET, G., MILLER, B. W., ALLINGTON-SMITH, J. R., BUREAU, M., CAROLLO, C. M., DAVIES, R. L., EMSELLEM, E., KUNTSCHNER, H., PELETIER, R. F., VEROLME, E. K. & DE ZEEUW, P. T., 2001. The SAURON project - I. The panoramic integral-field spectrograph. MNRAS, **326**, 23–35.

BÉJAR, V. J. S., ZAPATERO OSORIO, M. R., PÉREZ-GARRIDO, A., ÁLVAREZ, C., MARTÍN, E. L., REBOLO, R., VILLÓ-PÉREZ, I. & DÍAZ-SÁNCHEZ, A., 2008. Discovery of a Wide Companion near the Deuterium-burning Mass Limit in the Upper Scorpius Association. Astrophys. J. Lett., **673**, L185–L189.

BEUZIT, J., FELDT, M., DOHLEN, K., MOUILLET, D., PUGET, P. ET AL., 2006. SPHERE: A 'Planet Finder' Instrument for the VLT. *The Messenger*, **125**, 29–+.

BEUZIT, J., FELDT, M., DOHLEN, K., MOUILLET, D., PUGET, P. ET AL., 2008. SPHERE: a planet finder instrument for the VLT. In *Society of Photo-Optical Instrumentation Engineers (SPIE) Conference Series*, vol. 7014 of *Society of Photo-Optical Instrumentation Engineers (SPIE) Conference Series*.

BILLER, B. A., LIU, M. C., WAHHAJ, Z., NIELSEN, E. L., CLOSE, L. M. ET AL., 2010. The Gemini NICI Planet-finding Campaign: Discovery of a Close Substellar Companion to the Young Debris Disk Star PZ Tel. Astrophys. J. Lett., **720**, L82–L87.

BOWLER, B. P., LIU, M. C., DUPUY, T. J. & CUSHING, M. C., 2010. Near-infrared Spectroscopy of the Extrasolar Planet HR 8799 b. Astrophys. J., **723**, 850–868.

CASEWELL, S. L., DOBBIE, P. D., HODGKIN, S. T., MORAUX, E., JAMESON, R. F., HAMBLY, N. C., IRWIN, J. & LODIEU, N., 2007. Proper motion L and T dwarf candidate members of the Pleiades. Mon. Not. R. Ast. Soc., **378**, 1131–1140.

CHALLIS, J., 1863. On the Indications by Phenomena of Atmospheres to the Sun, Moon and Planets. Mon. Not. R. Ast. Soc., **23**, 231–+.

CHAUVIN, G., LAGRANGE, A., DUMAS, C., ZUCKERMAN, B., MOUILLET, D., SONG, I., BEUZIT, J. & LOWRANCE, P., 2004. A giant planet candidate near a young brown dwarf. Direct VLT/NACO observations using IR wavefront sensing. Astron. Astrophys., **425**, L29–L32.

CHAUVIN, G., LAGRANGE, A., ZUCKERMAN, B., DUMAS, C., MOUILLET, D., SONG, I., BEUZIT, J., LOWRANCE, P. & BESSELL, M. S., 2005. A companion to AB Pic at the planet/brown dwarf boundary. Astron. Astrophys., **438**, L29–L32.

CHRISTENSEN, P. R. & PEARL, J. C., 1997. Initial data from the Mars Global Surveyor thermal emission spectrometer experiment: Observations of the Earth. J. Geophys. Research, **102**, 10875–10880.

COWAN, N. B., AGOL, E., MEADOWS, V. S., ROBINSON, T., LIVENGOOD, T. A., DEMING, D., LISSE, C. M., A'HEARN, M. F., WELLNITZ, D. D., SEAGER, S., CHARBONNEAU, D. & THE EPOXI TEAM, 2009. Alien Maps of an Ocean-bearing World. Astrophys. J., **700**, 915–923.

COX, A. N. & PILACHOWSKI, C. A., 2000. Allen's Astrophysical Quantities. *Physics Today*, **53**(10), 100000–+.

DE ZEEUW, P. T., ALLINGTON-SMITH, J. R., BACON, R., BUREAU, M., CAROLLO, C. M., COPIN, Y., DAVIES, R. L., EMSELLEM, E., KUNTSCHNER, H., MILLER, B. W., MONNET, G., PELETIER, R. F. & VEROLME, E. K., 2000. The One Eye that Sees All: Integral Field Spectroscopy with SAURON on the WHT. *The Newsletter of the Isaac Newton Group of Telescopes*, **2**, 11–15.

DODSON-ROBINSON, S. E., VERAS, D., FORD, E. B. & BEICHMAN, C. A., 2009. The Formation Mechanism of Gas Giants on Wide Orbits. Astrophys. J., **707**, 79–88.

DOHLEN, K. & BEUZIT, J.-L., 2004. VLT Concept Feasibility Study: System Analysis ans Error Budgets. *System Analysis Reoprt V1.0 - VLT-TRE LAO-14690-0008*.

DOYLE, L. R., 2008. Overview of extrasolar planet detection methods. In H. Deeg, J. A. Belmonte, & A. Aparicio, ed., *Extrasolar Planets*, 1–+.

EISENHAUER, F., ABUTER, R., BICKERT, K., BIANCAT-MARCHET, F., BONNET, H. ET AL., 2003. SINFONI - Integral field spectroscopy at 50 milli-arcsecond resolution with the ESO VLT. In M. Iye & A. F. M. Moorwood, ed., *Society of Photo-Optical Instrumentation Engineers (SPIE) Conference Series*, vol. 4841 of *Presented at the Society of Photo-Optical Instrumentation Engineers (SPIE) Conference*, 1548–1561.

FORTNEY, J. J., MARLEY, M. S., SAUMON, D. & LODDERS, K., 2008. Synthetic Spectra and Colors of Young Giant Planet Atmospheres: Effects of Initial Conditions and Atmospheric Metallicity. Astrophys. J., **683**, 1104–1116.

GAUDI, B. S., BENNETT, D. P., UDALSKI, A., GOULD, A., CHRISTIE, G. W. ET AL., 2008. Discovery of a Jupiter/Saturn Analog with Gravitational Microlensing. *Science*, **319**, 927–.

GIBSON, N. P., PONT, F. & AIGRAIN, S., 2010. A new look at NICMOS transmission spectroscopy: no conclusive evidence for molecular features. *ArXiv e-prints*.

GRATTON, R., BEUZIT, J. L., BOCCALETTI, A., BONAVITA, M., DESIDERA, S., HUBIN, N., KASPER, M., KERBER, F., REBOLO, R., THATTE, N., TINETTI, G., SCHMID, H. M., STAM, D., VERINAUD, C. & WOLF, S., 2010. Top Level Requirements. *EPICS Phase A Study - E-PLA-ESO-556-0194*.

HINKLEY, S., OPPENHEIMER, B. R., BRENNER, D. & PARRY, I. R., 2009. A New Integral Field Spectrograph and Coronagraph for Exoplanetary Science at Palomar. In *Bulletin of the American Astronomical Society*, vol. 41 of *Bulletin of the American Astronomical Society*, 398–+.

HINKLEY, S., OPPENHEIMER, B. R., BRENNER, D., PARRY, I. R., SIVARAMAKRISHNAN, A., SOUMMER, R. & KING, D., 2008. A new integral field spectrograph for exoplanetary science at Palomar. In *Society of Photo-Optical Instrumentation Engineers (SPIE) Conference Series*, vol. 7015 of *Society of Photo-Optical Instrumentation Engineers (SPIE) Conference Series*.

HINKLEY, S., OPPENHEIMER, B. R., SOUMMER, R., SIVARAMAKRISHNAN, A., ROBERTS, JR., L. C., KUHN, J., MAKIDON, R. B., PERRIN, M. D., LLOYD, J. P., KRATTER, K. & BRENNER, D., 2007. Temporal Evolution of Coronagraphic Dynamic Range and Constraints on Companions to Vega. Astrophys. J., **654**, 633–640.

IRELAND, M. J., KRAUS, A. L., MARTINACHE, F., LAW, N. M. & HILLENBRAND, L. A., 2010. Two Wide Planetary-Mass Companions to Solar-Type Stars in Upper Scorpius. *ArXiv e-prints*.

JANSON, M., BERGFORS, C., GOTO, M., BRANDNER, W. & LAFRENIÈRE, D., 2010. Spatially Resolved Spectroscopy of the Exoplanet HR 8799 c. Astrophys. J. Lett., **710**, L35–L38.

KALAS, P., GRAHAM, J. R., CHIANG, E., FITZGERALD, M. P., CLAMPIN, M., KITE, E. S., STAPELFELDT, K., MAROIS, C. & KRIST, J., 2008. Optical Images of an Exosolar Planet 25 Light-Years from Earth. *Science*, **322**, 1345–.

KALAS, P., GRAHAM, J. R. & CLAMPIN, M., 2005. A planetary system as the origin of structure in Fomalhaut's dust belt. Nature, **435**, 1067–1070.

KALTENEGGER, L. & SELSIS, F., 2008. ESA White paper: Atmospheric modeling: Setting Biomarkers in context. *ArXiv e-prints*.

KASPER, M., AMICO, P., POMPEI, E., AGEORGES, N., APAI, D., ARGOMEDO, J., KORNWEIBEL, N. & LIDMAN, C., 2009. Direct Imaging of Exoplanets and Brown Dwarfs with the VLT: NACO Pupil-stabilised Lyot Coronagraphy at 4 microns. *The Messenger*, **137**, 8–13.

KASPER, M. & BEUZIT, J., 2010. EPICS: An Exoplanet Imaging Camera and Spectrograph for the E-ELT. *The Messenger*, **140**, 24–25.

KASPER, M., BEUZIT, J., VERINAUD, C., GRATTON, R. G., KERBER, F. ET AL., 2010. EPICS: direct imaging of exoplanets with the E-ELT. In *Society of Photo-Optical Instrumentation Engineers (SPIE) Conference Series*, vol. 7735 of *Society of Photo-Optical Instrumentation Engineers (SPIE) Conference Series*.

KASPER, M. & GRATTON, R., 2010. Executive Summary. *EPICS Phase A Study - E-PLA-ESO-556-0626*.

LAFRENIÈRE, D., JAYAWARDHANA, R. & VAN KERKWIJK, M. H., 2008. Direct Imaging and Spectroscopy of a Planetary-Mass Candidate Companion to a Young Solar Analog. Astrophys. J. Lett., **689**, L153–L156.

LAGRANGE, A., BONNEFOY, M., CHAUVIN, G., APAI, D., EHRENREICH, D., BOCCALETTI, A., GRATADOUR, D., ROUAN, D., MOUILLET, D., LACOUR, S. & KASPER, M., 2010. A Giant Planet Imaged in the Disk of the Young Star β Pictoris. *Science*, **329**, 57–.

LAGRANGE, A., GRATADOUR, D., CHAUVIN, G., FUSCO, T., EHRENREICH, D., MOUILLET, D., ROUSSET, G., ROUAN, D., ALLARD, F., GENDRON, É., CHARTON, J., MUGNIER, L., RABOU, P., MONTRI, J. & LACOMBE, F., 2009. A probable giant planet imaged in the β Pictoris disk. VLT/NaCo deep L'-band imaging. Astron. Astrophys., **493**, L21–L25.

LENZEN, R., CLOSE, L., BRANDNER, W., BILLER, B. & HARTUNG, M., 2004. A novel simultaneous differential imager for the direct imaging of giant planets. In A. F. M. Moorwood & M. Iye, ed., *Society of Photo-Optical Instrumentation Engineers (SPIE) Conference Series*, vol. 5492 of *Society of Photo-Optical Instrumentation Engineers (SPIE) Conference Series*, 970–977.

LOPEZ-MORALES, M., 2010. Exoplanet atmospheres: a brand-new and rapidly expanding research field. *ArXiv e-prints*.

LUNINE, J. I., FISCHER, D., HAMMEL, H. B., HENNING, T., HILLENBRAND, L., KASTING, J., LAUGHLIN, G., MACINTOSH, B., MARLEY, M., MELNICK, G., MONET, D., NOECKER, C., PEALE, S., QUIRRENBACH, A., SEAGER, S. & WINN, J. N., 2008. Worlds Beyond: A Strategy for the Detection and Characterization of Exoplanets Executive Summary of a Report of the ExoPlanet Task Force Astronomy and Astrophysics Advisory Committee Washington, DC June 23, 2008. *Astrobiology*, **8**, 875–881.

MACINTOSH, B. A., GRAHAM, J. R., PALMER, D. W., DOYON, R., DUNN, J., GAVEL, D. T., LARKIN, J., OPPENHEIMER, B., SADDLEMYER, L., SIVARAMAKRISHNAN, A., WALLACE, J. K., BAUMAN, B., ERICKSON, D. A., MAROIS, C., POYNEER, L. A. & SOUMMER, R., 2008. The Gemini Planet Imager: from science to design to construction. In *Society of Photo-Optical Instrumentation Engineers (SPIE) Conference Series*, vol. 7015 of *Society of Photo-Optical Instrumentation Engineers (SPIE) Conference Series*.

MADHUSUDHAN, N. & SEAGER, S., 2010. On the Inference of Thermal Inversions in Hot Jupiter Atmospheres. Astrophys. J., **725**, 261–274.

MAROIS, C., 2004. *La recherche de naines brunes et d'exoplanètes: développement d'une technique d'imagerie multibande*. Ph.D. thesis, Université de Montréal.

MAROIS, C., DOYON, R., NADEAU, D., RACINE, R., RIOPEL, M. & VALLEE, P., 2003. TRIDENT: an infrared camera optimized for the detection of methanated substellar companions of nearby stars. In A. B. Schultz, ed., *Society of Photo-Optical Instrumentation Engineers (SPIE) Conference Series*, vol. 4860 of *Society of Photo-Optical Instrumentation Engineers (SPIE) Conference Series*, 130–137.

MAROIS, C., DOYON, R., NADEAU, D., RACINE, R., RIOPEL, M., VALLÉE, P. & LAFRENIÈRE, D., 2005. TRIDENT: An Infrared Differential Imaging Camera Optimized for the Detection of Methanated Substellar Companions. Pub. Astron. Soc. Pac., **117**, 745–756.

MAROIS, C., DOYON, R., RACINE, R. & NADEAU, D., 2000. Efficient Speckle Noise Attenuation in Faint Companion Imaging. Pub. Astron. Soc. Pac., **112**, 91–96.

MAROIS, C., LAFRENIÈRE, D., DOYON, R., MACINTOSH, B. & NADEAU, D., 2006. Angular Differential Imaging: A Powerful High-Contrast Imaging Technique. Astrophys. J., **641**, 556–564.

MAROIS, C., MACINTOSH, B., BARMAN, T., ZUCKERMAN, B., SONG, I., PATIENCE, J., LAFRENIÈRE, D. & DOYON, R., 2008. Direct Imaging of Multiple Planets Orbiting the Star HR 8799. *Science*, **322**, 1348–.

MAROIS, C., ZUCKERMAN, B., KONOPACKY, Q. M., MACINTOSH, B. & BARMAN, T., 2010. Images of a fourth planet orbiting HR 8799. *ArXiv e-prints*.

MAYOR, M. & QUELOZ, D., 1995. A Jupiter-mass companion to a solar-type star. Nature, **378**, 355–359.

MAYOR, M., UDRY, S., LOVIS, C., PEPE, F., QUELOZ, D., BENZ, W., BERTAUX, J., BOUCHY, F., MORDASINI, C. & SEGRANSAN, D., 2009. The HARPS search for southern extra-solar planets. XIII. A planetary system with 3 super-Earths (4.2, 6.9, and 9.2 M_E). Astron. Astrophys., **493**, 639–644.

MOHANTY, S., JAYAWARDHANA, R., HUÉLAMO, N. & MAMAJEK, E., 2007. The Planetary Mass Companion 2MASS 1207-3932B: Temperature, Mass, and Evidence for an Edge-on Disk. Astrophys. J., **657**, 1064–1091.

MOUILLET, D. & BEUZIT, J.-L., 2004. VLT Concept Feasibility Study: Science Analysis Report. *Science Analysis V1.0 - VLT-TRE LAO-14690-0022*.

MURRAY-CLAY, R. A., CHIANG, E. I. & MURRAY, N., 2009. Atmospheric Escape From Hot Jupiters. Astrophys. J., **693**, 23–42.

NEUHÄUSER, R., GUENTHER, E. W., WUCHTERL, G., MUGRAUER, M., BEDALOV, A. & HAUSCHILDT, P. H., 2005. Evidence for a co-moving sub-stellar companion of GQ Lup. Astron. Astrophys., **435**, L13–L16.

NIELSEN, E. L., CLOSE, L. M., GUIRADO, J. C., BILLER, B. A., LENZEN, R., BRANDNER, W., HARTUNG, M. & LIDMAN, C., 2005a. AB Doradus C: age, spectral type, orbit, and comparison to evolutionary models. *Astronomische Nachrichten*, **326**, 1033–1039.

NIELSEN, E. L., CLOSE, L. M., GUIRADO, J. C., BILLER, B. A., LENZEN, R., BRANDNER, W., HARTUNG, M. & LIDMAN, C., 2005b. AB Doradus C: age, spectral type, orbit, and comparison to evolutionary models. *Astronomische Nachrichten*, **326**, 1033–1039.

OPPENHEIMER, B. R. & HINKLEY, S., 2009. High-Contrast Observations in Optical and Infrared Astronomy. Ann. Rev. Astron. Astrophys, **47**, 253–289.

PERRYMAN, M., HAINAUT, O., DRAVINS, D., LEGER, A., QUIRRENBACH, A., RAUER, H., KERBER, F., FOSBURY, R., BOUCHY, F., FAVATA, F., FRIDLUND, M., GILMOZZI, R., LAGRANGE, A., MAZEH, T., ROUAN, D., UDRY, S. & WAMBSGANSS, J., 2005. Report by the ESA-ESO Working Group on Extra-Solar Planets. *ArXiv Astrophysics e-prints*.

PERRYMAN, M. A. C., 2000. Extra-solar planets. *Reports on Progress in Physics*, **63**, 1209–1272.

RACINE, R., NADEAU, D. & DOYON, R., 1999. Defeating Speckle Noise in Faint Companion Imaging. In D. Bonaccini, ed., *European Southern Observatory Conference and Workshop Proceedings*, vol. 56 of *European Southern Observatory Conference and Workshop Proceedings*, 377–+.

ROWE, J. F., MATTHEWS, J. M., SEAGER, S., MILLER-RICCI, E., SASSELOV, D., KUSCHNIG, R., GUENTHER, D. B., MOFFAT, A. F. J., RUCINSKI, S. M., WALKER, G. A. H. & WEISS, W. W., 2008. The Very Low Albedo of an Extrasolar Planet: MOST Space-based Photometry of HD 209458. Astrophys. J., **689**, 1345–1353.

SALTER, G., THATTE, N., TECZA, M. & CLARKE, F., 2010a. Slicer Prototype Breadboard Experiment Test Report. *EPICS Phase A Study - E-TRE-UOX-556-0001*.

SALTER, G., THATTE, N., TECZA, M., CLARKE, F., VERINAUD, C., KASPER, M. & ABUTER, R., 2008. Exploring high contrast limitations for image slicer-based integral field spectrographs. In *Society of Photo-Optical Instrumentation Engineers (SPIE) Conference Series*, vol. 7015 of *Presented at the Society of Photo-Optical Instrumentation Engineers (SPIE) Conference*.

SALTER, G. S., THATTE, N. A., TECZA, M., CLARKE, F., VERINAUD, C. & KASPER, M. E., 2010b. High-contrast observations with slicer-based integral field spectrographs 1: simulations. In *Society of Photo-Optical Instrumentation Engineers (SPIE) Conference Series*, vol. 7735 of *Society of Photo-Optical Instrumentation Engineers (SPIE) Conference Series*.

SALTER, G. S., THATTE, N. A., TECZA, M., CLARKE, F., VERINAUD, C. & KASPER, M. E., 2010c. High-contrast observations with slicer-based integral field spectrographs 2: experimental tests. In *Society of Photo-Optical Instrumentation Engineers (SPIE) Conference Series*, vol. 7735 of *Society of Photo-Optical Instrumentation Engineers (SPIE) Conference Series*.

SCHMIDT, T. O. B., NEUHÄUSER, R., SEIFAHRT, A., VOGT, N., BEDALOV, A., HELLING, C., WITTE, S. & HAUSCHILDT, P. H., 2008. Direct evidence of a sub-stellar companion around CT Chamaeleontis. Astron. Astrophys., **491**, 311–320.

SEAGER, S. & DEMING, D., 2010. Exoplanet Atmospheres. Ann. Rev. Astron. Astrophys, **48**, 631–672.

SOZZETTI, A., 2010. Astrometry and Exoplanets: the Gaia Era, and Beyond. *ArXiv e-prints*.

SPARKS, W. B. & FORD, H. C., 2002. Imaging Spectroscopy for Extrasolar Planet Detection. Astrophys. J., **578**, 543–564.

TECZA, M., THATTE, N., CLARKE, F., FOGARTY, L., GOODSALL, T., SALTER, G., FREEMAN, D. & SALAUN, Y., 2008. SWIFT de-magnifying image slicer: diffraction limited image slicing at optical wavelengths. In *Society of Photo-Optical Instrumentation Engineers (SPIE) Conference Series*, vol. 7018 of *Society of Photo-Optical Instrumentation Engineers (SPIE) Conference Series*.

THATTE, N., ABUTER, R., TECZA, M., NIELSEN, E. L., CLARKE, F. J. & CLOSE, L. M., 2007. Very high contrast integral field spectroscopy of AB Doradus C: 9-mag contrast at 0.2arcsec without a coronagraph using spectral deconvolution. Mon. Not. R. Ast. Soc., **378**, 1229–1236.

THATTE, N., TECZA, M., CLARKE, F., GOODSALL, T., LYNN, J., FREEMAN, D. & DAVIES, R. L., 2006. The Oxford SWIFT integral field spectrograph. In *Society of Photo-Optical Instrumentation Engineers (SPIE) Conference Series*, vol. 6269 of *Society of Photo-Optical Instrumentation Engineers (SPIE) Conference Series*.

TODOROV, K., LUHMAN, K. L. & MCLEOD, K. K., 2010. Discovery of a Planetary-mass Companion to a Brown Dwarf in Taurus. Astrophys. J. Lett., **714**, L84–L88.

TOOMEY, D. W. & FTACLAS, C., 2003. Near Infrared Coronagraphic Imager for Gemini South. In M. Iye & A. F. M. Moorwood, ed., *Society of Photo-Optical Instrumentation Engineers (SPIE) Conference Series*, vol. 4841 of *Society of Photo-Optical Instrumentation Engineers (SPIE) Conference Series*, 889–900.

TURNBULL, M. C., TRAUB, W. A., JUCKS, K. W., WOOLF, N. J., MEYER, M. R., GORLOVA, N., SKRUTSKIE, M. F. & WILSON, J. C., 2006. Spectrum of a Habitable World: Earthshine in the Near-Infrared. Astrophys. J., **644**, 551–559.

VERINAUD, C., GRATTON, R., THATTE, N. & SALTER, G., 2010a. IFS Trade-off. *EPICS Phase A Study - E-TRE-LAO-556-0004*.

VÉRINAUD, C., HUBIN, N., KASPER, M., ANTICHI, J., BAUDOZ, P. ET AL., 2006. The EPICS project for the European Extremely Large Telescope: outcome of the Planet Finder concept study for OWL. In *Society of Photo-Optical Instrumentation Engineers (SPIE) Conference Series*, vol. 6272 of *Presented at the Society of Photo-Optical Instrumentation Engineers (SPIE) Conference*.

VERINAUD, C., KASPER, M., FEDRIGO, E., RABOU, P., PREIS, O., MELANIE, O., STADLER, E., GRATTON, R., VENEMA, L. & HANENBURG, H., 2010b. EPICS Conceptual Design. *EPICS Phase A Study - E-TRE-LAO-556-0001*.

WEBSTER, D. L., 1927. Meteorological, Geological, and Biological Conditions on Venus. Nature, **120**, 879–880.

WOLSZCZAN, A. & FRAIL, D. A., 1992. A planetary system around the millisecond pulsar PSR1257 + 12. Nature, **355**, 145–147.

WOLTER, U., SCHMITT, J. H. M. M. & VAN WYK, F., 2005. Doppler imaging of Speedy Mic using the VLT. Fast spot evolution on a young K-dwarf star. Astron. Astrophys., **435**, 261–273.

WOOD, B. E., AMBRUSTER, C. W., BROWN, A. & LINSKY, J. L., 2000. The Mg II and Lyα Lines of Nearby K Dwarfs: Interstellar Medium Components and Flux Measurements. Astrophys. J., **542**, 411–420.

Prescription of the Pre-Optics Setup

```
System/Prescription Data

Title: EPICS slicer test
Date : 13/12/2010
Configuration 1 of 3

LENS NOTES:

System magnification: 3x
PSF FWHM = 2px @ 700nm for f/1344: pupil diameter = 228um
Airy radius @ 830nm = 1319um

Dispersion of pre-optics grating: 1.085 px / 100nm

Useful wavelength range ~720-900nm

field positions correspond to mask positions

GENERAL LENS DATA:

Surfaces                :              14
Stop                    :               7
System Aperture         : Float By Stop Size = 0.057
Glass Catalogs          : SCHOTT
Ray Aiming              : Paraxial Reference, Cache On
X Pupil shift           :              0
Y Pupil shift           :              0
Z Pupil shift           :              0
X Pupil compress        :              0
Y Pupil compress        :              0
Apodization             : Uniform, factor =   0.00000E+000
Temperature (C)         :    2.00000E+001
Pressure (ATM)          :    1.00000E+000
Adjust Index Data To Environment  : Off
Effective Focal Length  :       -55.58871 (in air at system temperature and pressure)
Effective Focal Length  :       -55.58871 (in image space)
Back Focal Length       :         306.628
Total Track             :         668.356
Image Space F/#         :         56.8309
Paraxial Working F/#    :        1314.404
Working F/#             :        1313.245
Image Space NA          :    0.0003804004
Object Space NA         :     0.001140254
Stop Radius             :           0.057
Paraxial Image Height   :         10.2301
Paraxial Magnification  :       -2.997513
Entrance Pupil Diameter :       0.9781424
Entrance Pupil Position :        385.6449
Exit Pupil Diameter     :       0.1209787
Exit Pupil Position     :        158.7337
Field Type              : Object height in Millimeters
Maximum Radial Field    :        3.412863
Primary Wavelength      :           0.855 ţm
Lens Units              :   Millimeters
Angular Magnification   :       -8.049454

Fields          : 5
Field Type              : Object height in Millimeters
 #        X-Value        Y-Value         Weight
 1      -3.085280       1.459000       1.000000
 2       3.085280       1.459000       1.000000
 3       0.000000       0.000000       1.000000
 4      -2.194500      -1.585000       1.000000
 5       2.194500      -1.585000       1.000000

Vignetting Factors
 #       VDX       VDY       VCX       VCY       VAN
 1  0.000000  0.000000  0.000000  0.000000  0.000000
 2  0.000000  0.000000  0.000000  0.000000  0.000000
```

```
 3  0.000000  0.000000  0.000000  0.000000  0.000000
 4  0.000000  0.000000  0.000000  0.000000  0.000000
 5  0.000000  0.000000  0.000000  0.000000  0.000000

Wavelengths     : 3
Units: µm
 #          Value         Weight
 1       0.730000       1.000000
 2       0.855000       1.000000
 3       0.980000       1.000000

SURFACE DATA SUMMARY:

Surf     Type         Radius      Thickness                Glass      Diameter          Conic   Comment
 OBJ STANDARD       Infinity        43.2689                           6.825726              0
   1 COORDBRK              -              0                                  -              - x-y stage
   2 STANDARD         161.05              4                 SFL6           25              0 edmund 45-803
   3 STANDARD          28.45              8               LAKN22           25              0 edmund 45-803
   4 STANDARD         -31.69             37                                25              0 edmund 45-803
   5 COORDBRK              -              0                                  -              - x-y-stage
   6 STANDARD       Infinity             10                  BK7     1.025579              0 grating substrate
 STO DGRATING       Infinity              5                            0.114              0 newport 54-*-906R
   8 STANDARD       Infinity       286.0231                           0.8028749             0
   9 STANDARD          86.84             11               LAKN22           50              0 edmund f47-318
  10 STANDARD         -86.84            5.5                 SFL6           50              0 edmund f47-318
  11 STANDARD         -894.7       139.8329                                50              0 edmund f47-318
  12 STANDARD       Infinity            162                           26.11376             0 slicer stack
  13 STANDARD       Infinity           -162                                4.2             0 slicer pupil
 IMA STANDARD       Infinity                                           26.11376             0 slicer stack

SURFACE DATA DETAIL:

Surface OBJ STANDARD
Surface   1 COORDBRK x-y stage
Decenter X     :                0
Decenter Y     :                0
Tilt About X   :                0
Tilt About Y   :                0
Tilt About Z   :                0
Order          : Decenter then tilt
Surface   2 STANDARD edmund 45-803
Aperture       : Floating Aperture
Maximum Radius :             12.5
Surface   3 STANDARD edmund 45-803
Aperture       : Floating Aperture
Maximum Radius :             12.5
Surface   4 STANDARD edmund 45-803
Aperture       : Floating Aperture
Maximum Radius :             12.5
Surface   5 COORDBRK x-y-stage
Decenter X     :                0
Decenter Y     :                0
Tilt About X   :                0
Tilt About Y   :                0
Tilt About Z   :                0
Order          : Decenter then tilt
Surface   6 STANDARD grating substrate
Aperture       : Rectangular Aperture
X Half Width   :               30
Y Half Width   :               30
Surface STO DGRATING newport 54-*-906R
Lines / µm     :                0
Diffract Order :                0
Aperture       : Rectangular Aperture, Pickup From Surface 6
X Half Width   :               30
Y Half Width   :               30
Surface   8 STANDARD
Surface   9 STANDARD edmund f47-318
Tilt/Decenter  :      Decenter X      Decenter Y          Tilt X          Tilt Y          Tilt Z          Order
Before surface :               0           4.729               0               0               0Decenter, Tilt
Aperture       : Floating Aperture
Maximum Radius :              25
Surface  10 STANDARD edmund f47-318
Aperture       : Floating Aperture
Maximum Radius :              25
Surface  11 STANDARD edmund f47-318
Tilt/Decenter  :      Decenter X      Decenter Y          Tilt X          Tilt Y          Tilt Z          Order
After surface  :               0           5.189               0               0               0Decenter, Tilt
Aperture       : Floating Aperture
Maximum Radius :              25
Surface  12 STANDARD slicer stack
Aperture       : Rectangular Aperture
X Half Width   :              11
Y Half Width   :           10.34
Surface  13 STANDARD slicer pupil
Surface IMA STANDARD slicer stack
Aperture       : Rectangular Aperture, Pickup From Surface 12
X Half Width   :              11
```

```
Y Half Width   :         10.34

COATING DEFINITIONS:


EDGE THICKNESS DATA:

Surf          X-Edge          Y-Edge
 OBJ       43.268904       43.268904
   1        0.485831        0.485831
   2        6.407321        6.407321
   3        2.537393        2.537393
   4       39.569456       39.569456
   5        0.000000        0.000000
   6       10.000000       10.000000
 STO        5.000000        5.000000
   8      289.699541      289.699541
   9        3.647215        3.647215
  10        8.827045        8.827045
  11      140.182204      140.182204
  12      162.000000      162.000000
  13     -162.000000     -162.000000
 IMA        0.000000        0.000000

MULTI-CONFIGURATION DATA:

Configuration   1:

  1 Param 2     7 :              0
  2 Param 1     7 :              0

Configuration   2:

  1 Param 2     7 :              1
  2 Param 1     7 :          0.035

Configuration   3:

  1 Param 2     7 :             -1
  2 Param 1     7 :          0.035

SOLVE AND VARIABLE DATA:

 Semi Diameter   2      : Fixed
 Semi Diameter   3      : Fixed
 Semi Diameter   4      : Fixed
 Semi Diameter   7      : Fixed
 Semi Diameter   9      : Fixed
 Semi Diameter  10      : Fixed
 Semi Diameter  11      : Fixed
 Semi Diameter  13      : Fixed

INDEX OF REFRACTION DATA:

System Temperature:   20.0000 Celsius
System Pressure   :    1.0000 Atmospheres
Absolute air index:    1.000270 at wavelength 0.855000 ţm
Index data is relative to air at the system temperature and pressure.
Wavelengths are measured in air at the system temperature and pressure.

Surf                  Glass    Temp    Pres     0.730000   0.855000   0.980000
   0                           20.00    1.00   1.00000000 1.00000000 1.00000000
   1              <CRD BRK>                    1.00000000 1.00000000 1.00000000
   2                   SFL6   20.00    1.00   1.78920423 1.78132651 1.77605407
   3                 LAKN22   20.00    1.00   1.64478316 1.64134164 1.63882078
   4                           20.00    1.00   1.00000000 1.00000000 1.00000000
   5              <CRD BRK>                    1.00000000 1.00000000 1.00000000
   6                    BK7   20.00    1.00   1.51230442 1.50975207 1.50778529
   7                           20.00    1.00   1.00000000 1.00000000 1.00000000
   8                           20.00    1.00   1.00000000 1.00000000 1.00000000
   9                 LAKN22   20.00    1.00   1.64478316 1.64134164 1.63882078
  10                   SFL6   20.00    1.00   1.78920423 1.78132651 1.77605407
  11                          20.00    1.00   1.00000000 1.00000000 1.00000000
  12                          20.00    1.00   1.00000000 1.00000000 1.00000000
  13                          20.00    1.00   1.00000000 1.00000000 1.00000000
  14                          20.00    1.00   1.00000000 1.00000000 1.00000000

THERMAL COEFFICIENT OF EXPANSION DATA:

Surf                  Glass     TCE *10E-6
  0                           0.00000000
   1              <CRD BRK>                  0.00000000
  2                   SFL6     9.00000000
  3                 LAKN22     6.60000000
  4                           0.00000000
   5              <CRD BRK>                  0.00000000
  6                    BK7     7.10000000
  7                           0.00000000
```

```
  8                            0.00000000
  9                  LAKN22    6.60000000
 10                    SFL6    9.00000000
 11                            0.00000000
 12                            0.00000000
 13                            0.00000000
 14                            0.00000000

GLOBAL VERTEX COORDINATES, ORIENTATIONS, AND ROTATION/OFFSET MATRICES:

Reference Surface: 12

Surf           R11             R12             R13                 X
               R21             R22             R23                 Y
               R31             R32             R33                 Z

  0   1.0000000000   0.0000000000   0.0000000000  0.000000000E+000
      0.0000000000   1.0000000000   0.0000000000 -9.918000000E+000
      0.0000000000   0.0000000000   1.0000000000 -5.496249084E+002

  1   1.0000000000   0.0000000000   0.0000000000  0.000000000E+000 x-y stage
      0.0000000000   1.0000000000   0.0000000000 -9.918000000E+000
      0.0000000000   0.0000000000   1.0000000000 -5.063560046E+002

  2   1.0000000000   0.0000000000   0.0000000000  0.000000000E+000 edmund 45-803
      0.0000000000   1.0000000000   0.0000000000 -9.918000000E+000
      0.0000000000   0.0000000000   1.0000000000 -5.063560046E+002

  3   1.0000000000   0.0000000000   0.0000000000  0.000000000E+000 edmund 45-803
      0.0000000000   1.0000000000   0.0000000000 -9.918000000E+000
      0.0000000000   0.0000000000   1.0000000000 -5.023560046E+002

  4   1.0000000000   0.0000000000   0.0000000000  0.000000000E+000 edmund 45-803
      0.0000000000   1.0000000000   0.0000000000 -9.918000000E+000
      0.0000000000   0.0000000000   1.0000000000 -4.943560046E+002

  5   1.0000000000   0.0000000000   0.0000000000  0.000000000E+000 x-y-stage
      0.0000000000   1.0000000000   0.0000000000 -9.918000000E+000
      0.0000000000   0.0000000000   1.0000000000 -4.573560046E+002

  6   1.0000000000   0.0000000000   0.0000000000  0.000000000E+000 grating substrate
      0.0000000000   1.0000000000   0.0000000000 -9.918000000E+000
      0.0000000000   0.0000000000   1.0000000000 -4.573560046E+002

  7   1.0000000000   0.0000000000   0.0000000000  0.000000000E+000 newport 54-*-906R
      0.0000000000   1.0000000000   0.0000000000 -9.918000000E+000
      0.0000000000   0.0000000000   1.0000000000 -4.473560046E+002

  8   1.0000000000   0.0000000000   0.0000000000  0.000000000E+000
      0.0000000000   1.0000000000   0.0000000000 -9.918000000E+000
      0.0000000000   0.0000000000   1.0000000000 -4.423560046E+002

  9   1.0000000000   0.0000000000   0.0000000000  0.000000000E+000 edmund f47-318
      0.0000000000   1.0000000000   0.0000000000 -5.189000000E+000
      0.0000000000   0.0000000000   1.0000000000 -1.563328566E+002

 10   1.0000000000   0.0000000000   0.0000000000  0.000000000E+000 edmund f47-318
      0.0000000000   1.0000000000   0.0000000000 -5.189000000E+000
      0.0000000000   0.0000000000   1.0000000000 -1.453328566E+002

 11   1.0000000000   0.0000000000   0.0000000000  0.000000000E+000 edmund f47-318
      0.0000000000   1.0000000000   0.0000000000 -5.189000000E+000
      0.0000000000   0.0000000000   1.0000000000 -1.398328566E+002

 12   1.0000000000   0.0000000000   0.0000000000  0.000000000E+000 slicer stack
      0.0000000000   1.0000000000   0.0000000000  0.000000000E+000
      0.0000000000   0.0000000000   1.0000000000  0.000000000E+000

 13   1.0000000000   0.0000000000   0.0000000000  0.000000000E+000 slicer pupil
      0.0000000000   1.0000000000   0.0000000000  0.000000000E+000
      0.0000000000   0.0000000000   1.0000000000  1.620000000E+002

 14   1.0000000000   0.0000000000   0.0000000000  0.000000000E+000 slicer stack
      0.0000000000   1.0000000000   0.0000000000  0.000000000E+000
      0.0000000000   0.0000000000   1.0000000000  0.000000000E+000


GLOBAL Surface CENTER OF CURVATURE POINTS:

Reference Surface: 12

Surf            X              Y              Z
  0             -              -              -
  1             -              -              - x-y stage
  2   0.0000000000  -9.9180000000 -345.3060045674 edmund 45-803
  3   0.0000000000  -9.9180000000 -473.9060045674 edmund 45-803
  4   0.0000000000  -9.9180000000 -526.0460045674 edmund 45-803
  5             -              -              - x-y-stage
```

```
  6              -              -              - grating substrate
  7              -              -              - newport 54-*-906R
  8              -              -              -
  9   0.0000000000  -5.1890000000 -69.4928565674 edmund f47-318
 10   0.0000000000  -5.1890000000 -232.1728565674 edmund f47-318
 11   0.0000000000  -5.1890000000 -1034.5328565674 edmund f47-318
 12             -              -              - slicer stack
 13             -              -              - slicer pupil
 14             -              -              - slicer stack

ELEMENT VOLUME DATA:

For centered elements with plane or spherical circular faces, exact
volumes are computed by assuming edges are squared up to the larger
of the front and back radial aperture.

For all other elements, approximate volumes are numerically integrated
to 0.1% accuracy. Zero volume means the volume cannot be accurately computed.

Single elements that are duplicated in the Lens Data Editor
for ray tracing purposes may be listed more than once yielding
incorrect total mass estimates.

                             Volume cc   Density g/cc         Mass g
Element surf   2 to   3       2.541721       3.370000       8.565600
Element surf   3 to   4       2.607827       3.730000       9.727196
Element surf   6 to   7      36.000000       2.510000      90.360000
Element surf   9 to  10      14.431904       3.730000      53.831003
Element surf  10 to  11      14.039549       3.370000      47.313279
Total Mass:                                               209.797079

F/# DATA:

F/# calculations consider vignetting factors and ignore surface apertures.

             Wavelength:       0.730000           0.855000           0.980000
#                 Field       Tan       Sag      Tan       Sag      Tan       Sag
1   -3.0853, 1.4590 mm:1295.3948 1288.93051292.1330 1285.52011288.3333 1281.4396
2    3.0853, 1.4590 mm:1295.3948 1288.93051292.1330 1285.52011288.3333 1281.4396
3    0.0000, 0.0000 mm:1314.9048 1316.32941312.5048 1313.98721309.5197 1311.0403
4  -2.1945, -1.5850 mm:1316.7186 1304.16981314.2789 1301.46591311.1121 1298.0676
5   2.1945, -1.5850 mm:1316.7186 1304.16981314.2789 1301.46591311.1121 1298.0676

CARDINAL POINTS:

Object space positions are measured with respect to surface 1.
Image space positions are measured with respect to the image surface.
The index in both the object space and image space is considered.

Object Space         Image Space
W = 0.730000
Focal Length          :           55.583271          -55.583271
Focal Planes          :          -61.770074          166.889707
Principal Planes      :         -117.353346          222.472978
Anti-Principal Planes :           -6.186803          111.306436
Nodal Planes          :         -117.353346          222.472978
Anti-Nodal Planes     :           -6.186803          111.306436

W = 0.855000(Primary)
Focal Length          :           55.588715          -55.588715
Focal Planes          :          -61.813851          166.795153
Principal Planes      :         -117.402566          222.383868
Anti-Principal Planes :           -6.225136          111.206438
Nodal Planes          :         -117.402566          222.383868
Anti-Nodal Planes     :           -6.225136          111.206438

W = 0.980000
Focal Length          :           55.731341          -55.731341
Focal Planes          :          -61.920497          167.263482
Principal Planes      :         -117.651837          222.994823
Anti-Principal Planes :           -6.189156          111.532141
Nodal Planes          :         -117.651837          222.994823
Anti-Nodal Planes     :           -6.189156          111.532141
```